Université de Strasbourg

UNIVERSITÉ DE STRASBOURG

École Doctorale des Sciences de la Terre et de l'Environnement

ITES (UMR 7063)

THÈSE présentée par :

Julien PORTÉ

Soutenue le : **09 décembre 2021**

pour obtenir le grade de : **Docteur de l'université de Strasbourg**

Discipline/ Spécialité : Géophysique

Imagerie 3-D de la résistivité complexe à partir de données électromagnétiques à source contrôlée

---

THÈSE dirigée par :
  Mr GIRARD Jean-François   Professeur, Université de Strasbourg, Strasbourg, France
  Mr BRETAUDEAU François (co-encadrant)   Ingénieur-chercheur, BRGM, Orléans, France

RAPPORTEURS :
  Mr GÜNTER Thomas   Directeur de recherche, LIAG, Hanovre, Allemagne
  Mr BROSSIER Romain   Maître de conférences, Université Grenoble Alpes, Grenoble, France

AUTRES MEMBRES DU JURY :
  Mr SCHAMPER Cyril   Maître de conférences, Sorbonne Universités, Paris, France
  Mr MARQUIS Guy   Professeur, Université de Strasbourg, Strasbourg, France

Université de Strasbourg

ÉCOLE DOCTORALE DES SCIENCES DE LA TERRE ET DE L'ENVIRONNEMENT

ITES (UMR 7063)

THÈSE

présentée par Julien PORTÉ

soutenue le 9 décembre 2021

pour obtenir le grade de: **Docteur de l'Université de Strasbourg**

Discipline/Spécialité: **Géophysique**

Imagerie 3-D de la résistivité complexe à partir de données électromagnétiques à source contrôlée

THÈSE dirigée par:

Pr. GIRARD Jean-François	Professeur, Université de Strasbourg, Strasbourg, France
Dr. BRETAUDEAU François	Ingénieur-Chercheur , BRGM, Orléans, France

RAPPORTEURS :

Dr. GÜNTHER Thomas	Directeur de recherche, LIAG, Hanovre, Allemagne
Dr. BROSSIER Romain	Maître de conférences, ISTerre, Grenoble, France

EXAMINATEURS :

|	
Dr. SCHAMPER Cyril	Maître de conférences, Sorbonne Universités, Paris, France
Pr. MARQUIS Guy	Professeur, Université de Strasbourg, Strasbourg, France

INVITÉS :

|	
Dr. KESSOURI Pauline	Ingénieure-Chercheure, BRGM, Orléans, France

Résumé étendu du manuscript

1 Introduction

L'imagerie de la résistivité électrique du sous-sol par prospection géophysique électrique est une technique bien établie dans l'étude de la proche surface. Elle permet l'accès aux propriétés électriques du milieu car fortement corrélée à la porosité et aux propriétés électriques du fluide en présence et donc à sa salinité. Dans certains cas, lors de prospections électriques, des phénomènes de polarisation provoquées (PP) par l'application d'un courant dans le milieu peuvent être observés. La relaxation d'un courant résiduel dans le milieu après coupure de l'injection est observée à des temps plus ou moins longs. Ces phénomènes traduisent les effets de chargeabilité du sol et sont décrits par une résistivité complexe (RC) pouvant varier avec la fréquence avec une signature spectrale cacactéristique. Plusieurs méchanismes de polarisation interviennent aux basses fréquences intéressant les méthodes d'imagerie de résistivité (1 mHz à 100 kHz) et sont dus au transport des charges libres et à leur accumulation réversible aux interfaces entre la matrice rocheuse et la solution electrolytique. Ces méchanismes de polarisation sont les effets de Maxwell-Wagner, la polarisation de la double couche électrique (Couche de Stern et couche diffuse, figure 1a), la polarisation de membrane (figure 1b) et la polarisation d'électrodes en lien avec la présence de particules métalliques (Kemna et al., 2012).
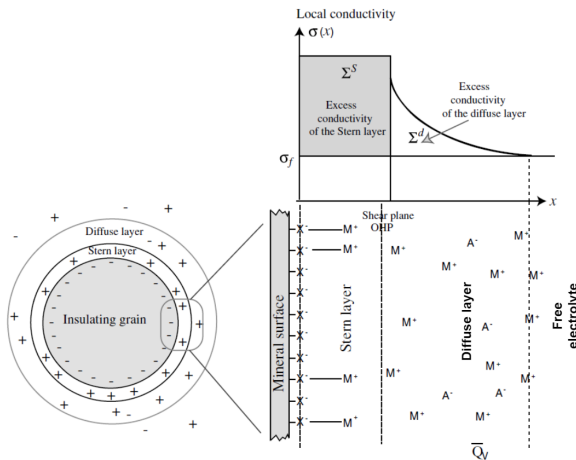
(a) *Illustration de la structure de la double couche électrique (EDL) à l'interface grain/électrolyte. Image modifiée de Revil and Florsch (2010)*
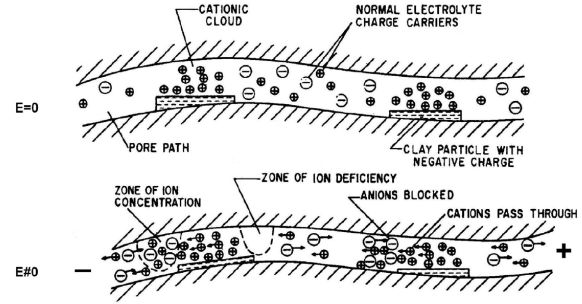
(b) *Illustration de la polarisation de membrane d'un conduit de pore contenant des particules d'argiles chargées négativement, à l'équilibre (haut) et lors de l'application d'un champ électrique (bas). Image de Ward and Fraser (1967).*

Historiquement la détection et la discrimination du type de particules métalliques disséminées fut le moteur des développements dans ce domaine (Pelton et al., 1978). Un intérêt nouveau a par la suite fortement été porté vers ses applications hydrogéologiques et environnementales afin de remonter aux propriétés hydrologiques (Binley et al., 2005; Börner et al., 1996) du milieu, ainsi que pour le suivi de contaminant. Plus récemment, le domaine de la bio-géophysique s'intéresse tout particulièrement aux effets PP dans le

milieu pour étudier les processus de bio-remédiation et de biofilm dans le milieu (Kessouri et al., 2019). L'étude des effets PP et de sa signature spectrale est par conséquent cruciale avec des enjeux économiques pouvant être importants.

La résistivité complexe $\rho^*(\omega)$ est habituellement étudiée par prospection électrique dans le domaine temporel ou spectral. Elle possède donc une partie réelle $\rho_r(\omega)$ et une partie imaginaire $\rho_q(\omega)$ et s'exprime sous sa forme exponentielle à l'aide d'une norme $|\rho^*(\omega)|$ et d'une phase $\phi_{cpx}(\omega)$:

$$\rho^*(\omega) = \rho_r(\omega) + i\rho_q(\omega) \tag{1}$$

$$\rho^*(\omega) = |\rho^*(\omega)|e^{i\phi_{cpx}(\omega)} \quad \text{with} \quad \begin{cases} |\rho^*(\omega)| = \sqrt{\rho_r^2(\omega) + \rho_q^2(\omega)} \\ \phi_{cpx}(\omega) = \arctan\left(\frac{\rho_q(\omega)}{\rho_r(\omega)}\right) \approx \frac{\rho_q(\omega)}{\rho_r(\omega)} \end{cases} \tag{2}$$

Dans le domaine temporel un signal carré 50% duty-cycle est habituellement utilisé pour étudier la RC afin d'étudier la relaxation du courant dû aux effets PP lors de la coupure de l'injection (figure 1). Les effets PP peuvent également être étudiés lors de la période de charge du sous-sol au moment de l'injection du courant. Les effets PP peuvent être quantifié en mesurant la chargeabilité M du milieu (Seigel, 1959) par le ratio V_s/V_0 entre le voltage mesuré après coupure du courant et le voltage mesuré lors de l'injection du courant à l'équilibre, ou en calculant la chargeabilité intégrée M_{int} à partir de l'aire sous la courbe entre deux bornes temporelles t_1 et t_2 après coupure du courant.
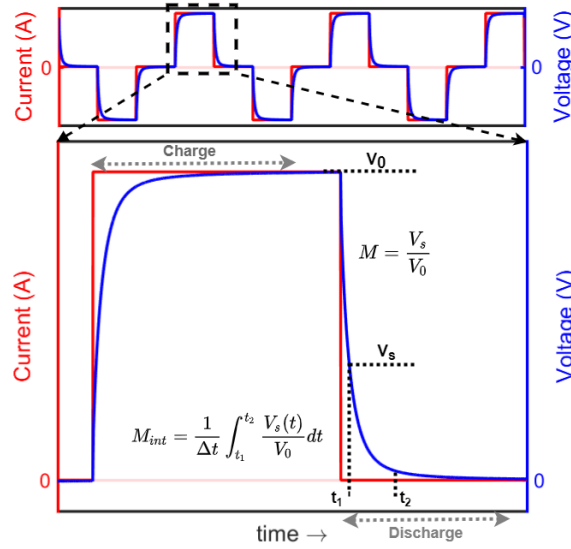

Figure 1: *Illustration d'une mesure de polarisation provoquées dans le domaine temporel (TDIP) par l'injection d'un signal carré 50% duty-cycle avec un zoom sur une demi-période positive pour illustrer la période de charge et de décharge due à la présence d'effets de polarisation provoquées. La chargeabilité M peut être calculé par le ratio V_s/V_0 ou en calculant la chargeabilité intégrée M_{int} à partir de l'aire sous la courbe entre deux bornes temporelles t_1 et t_2 après coupure du courant.*

Les mesures dans le domaine fréquentiel (communément méthode SIP, dérivée de l'anglais, *spectral induced polarization*) habituellement réalisées en laboratoire sur échantillon, se font en étudiant l'amplitude et le déphasage du voltage mesuré à différentes fréquences (figure 2). Un coefficient géométrique permet de remonter à la RC du milieux. En l'absence d'effet PP, aucune phase n'est mesurée dans le cas où l'hypothèse courant continu des méthodes geo-électriques est respectée.
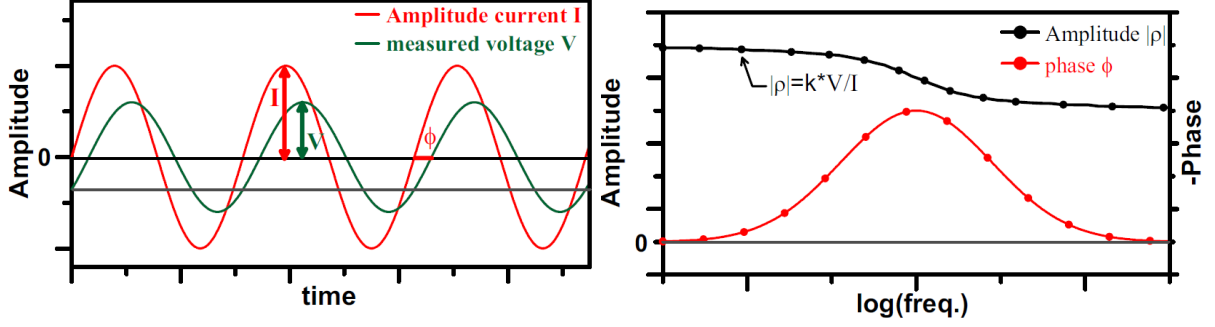

Figure 2: *Illustration d'une mesure de polarisation provoquées dans le domaine fréquentiel (SIP) à partir de l'injection d'un signal sinusïdale dans le domaine temporel (Gauche). Spectre de la norme et de la phase de la RC (Droite) obtenu à l'aide d'un coefficient géométrique (Images de Ghorbani (2007))*

En effet, une hypothèse courant continu (DC) est utilisée malgré l'utilisation d'un courant alternatif basse fréquence (1000 s à 10 kHz) lors des mesures afin d'étudier la signature spectrale des effets PP. Il est alors nécessaire de travailler à des fréquences suffisamment faibles et des géométries d'acquisition adaptées à l'échelle du terrain afin de pouvoir négliger les effets de couplage électromagnétique (EM) intervenant à plus haute fréquence et pour des dispositifs à grand espacement.

Des techniques variées cherchent à gérer la présence d'effets EM contenus dans les données PP afin de réduire les limitations de la méthode. Elles reposent souvent sur des approximations cherchant à séparer empiriquement les effets EM (Routh and Oldenburg, 2001). Les méthodes électromagnétiques à source contrôlée (CSEM) résolvent les équations complètes de Maxwell, au prix cependant de temps de calcul beaucoup plus conséquent. L'information fréquentielle contenue dans l'onde EM est utilisée en sus des effets géométriques pour contraindre l'imagerie du sous-sol. Les méthodes CSEM prennent en compte une résistivité généralement supposée réelle et constante avec la fréquence. Ces méthodes dans le domaine fréquentiel sont particulièrement bien adaptées à la prise en compte des effets PP. Il n'existe cependant que peu de travaux prenant en compte en simultané les effets PP et EM afin de résoudre les propriétés de résistivité complexe du milieu et de sa dépendance fréquentielle.

Les travaux de cette thèse portent sur l'implémentation d'une résistivité complexe dépendante de la fréquence au code POLYEM3D (Bretaudeau et al., 2021), un code tridimensionnel (3D) de modélisation et d'inversion local de données CSEM permettant ainsi la prise en compte des effets de couplage de PP et d'induction électromagnétique dans le processus d'imagerie du sous-sol. Il est question ici d'établir en premier lieu la

sensibilité des données CSEM dans le domaine fréquentiel aux effets de polarisation provo-
quées intervenant à l'échelle du terrain. Cette phase fait alors place à l'élaboration d'une
stratégie d'inversion adaptée à la sensibilité des données et au problème multi-paramètre.
En effet, la résolution du problème inverse souffre de la multiplication du nombre de
paramètres avec l'introduction d'une résistivité complexe dépendante de la fréquence et
donc l'augmentation du nombre de modèles équivalent résultant. Déterminer des moyens
de contraindre efficacement le problème inverse en forçant l'information apriori à minima
est crucial. Pour cela, la première phase de ce travail se base sur un module d'inversion
1D de la RC permettant des développements à moindre frais de calculs. Une stratégie
d'inversion multi-étape est mise en avant dans ce travail afin de contraindre l'inversion
efficacement vers la solution la plus probable en se basant sur les différences de sensibilités
des données aux différents paramètres PP. La méthode d'inversion établie est testée sur
divers exemples synthétiques 1D avant d'être transposée au problème 3D. Un exemple
synthétique 3D complet est ensuite présenté, ainsi que les limitations liées à la faible sen-
sibilité des effets PP. Dans une dernière partie les développements réalisés lors de cette
thèse sont appliqués sur deux jeux de données CSEM réels présentant des effets PP: 1) un
jeu de données 2.5D CSEM acquis près de Schleiz (Allemagne) et partagé par l'Institut
de Géophysique et Météorologie de l'université de Cologne et 2) un jeu de données acquis
dans le cadre de cette thèse et du projet ANR EXCITING sur l'ancien site minier de
La-Porte-Aux-Moines (Côtes-d'Armor, France).

2   Étude de sensibilité

Le code POLYEM3D résouds les équations de Maxwell en formulation champ électrique
avec une approche séparant le champ primaire du champ secondaire (Eq.3) (Newman
and Alumbaugh, 1995). Le champ électrique primaire $\boldsymbol{E_p}$ définit par le champ électrique
pour un milieu de référence de conductivité σ_p est habituellement obtenu pour un milieu
1D à l'aide d'un code de modélisation 1D semi-analytique (1DSA) (rapide et précis) basé
sur les routines du code *EM1D* (Kim et al., 1997; Lee et al., 2011; Song et al., 2002).

$$\nabla \times \nabla \times \boldsymbol{E_s} + i\omega\mu_0\sigma\boldsymbol{E_s} = -i\omega\mu_0(\sigma - \sigma_p)\boldsymbol{E_p} \qquad (3)$$

Le champ électrique secondaire $\boldsymbol{E_s}$ est obtenu par la résolution du systeme d'équation
par la méthode des différences finies (FD) sur une grille Cartésienne irrégulière basé sur
le schéma de (Streich, 2009). Le nombre imaginaire est noté i, ω représente la fréquence
angulaire et μ_0 la perméabilité magnétique dans le vide.

L'introduction d'une conductivité complexe au code prenant en compte originalement
une conductivité σ^r et une permittivité ϵ réelle et constante $\sigma = \sigma^r + i\omega\epsilon$ a été réalisée
de manière directe par simple reformulation du problème. Une permitivité effective ϵ_{eff}
regroupant la permitivité du milieu et la partie imaginaire de la conductivité σ^q est
introduite. Dans le domaine fréquentiel, la modélisation de la dépendance fréquentielle

de la résistivité est réalisée fréquence par fréquence.

$$\sigma(\omega) = \overbrace{\sigma^r(\omega) + i\sigma^q(\omega)}^{\sigma^*} + i\omega\epsilon \tag{4}$$

$$= \sigma^r(\omega) + i\omega\epsilon_{eff}(\omega) \qquad \text{with } \epsilon_{eff} = \epsilon + \frac{\sigma^q(\omega)}{\omega} \tag{5}$$

Dans un premier temps, la sensibilité des données CSEM aux effets PP a donc été étudiée en 1D à l'aide du code de modélisation 1DSA. Dans cette partie, une approche étudiant des milieux de résistivité complexe 1D à complexité croissante est réalisée. Plusieurs configurations de sources communément utilisées pour les méthodes CSEM sont considérées. Les effets PP introduit dans les données CSEM par une résistivité complexe pouvant varier avec la fréquence sont comparés à la réponse d'un milieu équivalent sans effet PP et donc a résistivité réelle et constante.

La considération de la réponse du champ magnétique ou de la réponse du milieu à l'excitation d'une source magnétique limite la fenêtre de fréquence pouvant être étudiée car les composantes du champ EM disparaissent ou ne sont plus sensibles aux variations de resistivité du milieu dans le cas d'une source inductive. L'étude de la réponse du champ électrique d'un milieu de résistivité complexe excité par une source galvanique a donc été préférée.

Il a été montré que l'ajout d'une résistivité imaginaire constante dans un modèle constant et réel n'impacte de manière significative que la partie imaginaire du champ électrique ou sa phase en raison de la relaxation du voltage résiduel due à la chargeabilité du milieu (figure 3). L'amplitude du champ électrique est donc contrôllée majoritairement par la partie réelle de la RC et sa norme $|\rho^*(\omega)|$ ($\rho^r \gg \rho^q$).
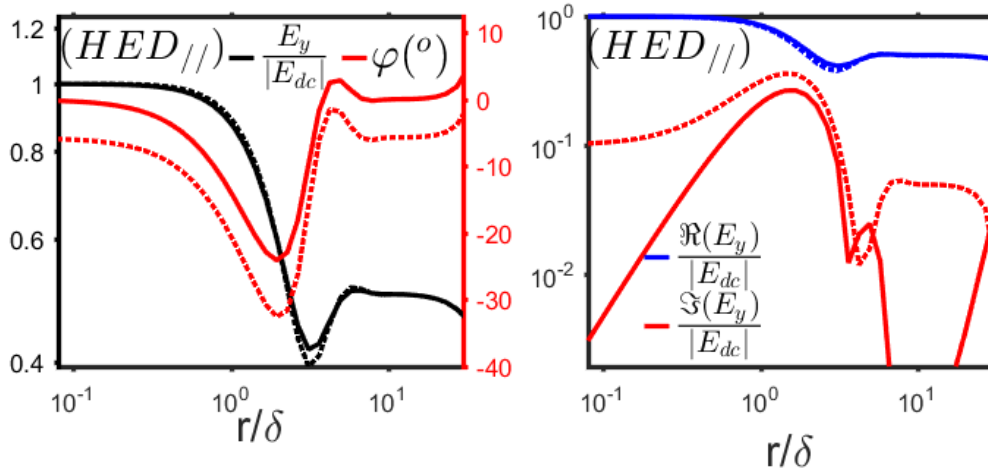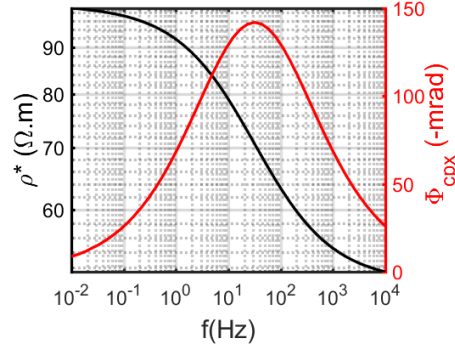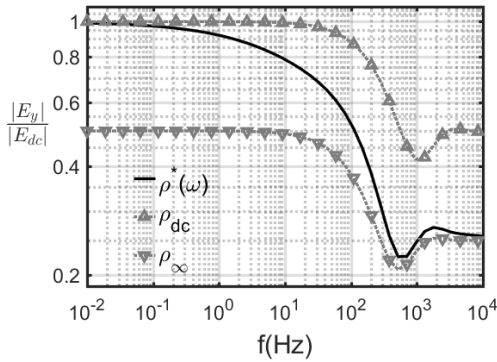
Figure 3: *Réponse du champ électrique (Amplitude normalisée et phase (gauche) ou partie réelle et imaginaire (droite)) en fonction de l'écartement r normalisé par l'épaisseur de peau δ, paralèlle à un dipôle électrique horizontal pointant vers le profil de récepteurs ($HED_{//}$, i.e. configuration dipôle-dipôle), pour un demi-espace homogène de résistivité constante avec (pointillé) et sans (ligne pleine) partie imaginaire (i.e. une phase de résistivité de -100 mrad).*

Dans le cas d'une résistivité variant avec la fréquence, comme présenté en figure 4 pour un milieu homogène variant selon un modèle de resistivité Cole-Cole (Pelton et al., 1978), les variations de la norme de la RC avec la fréquence impactent directement les variations de l'amplitude du champ électrique. La phase du champ électrique est quand à elle impactée à la fois par les variations de la norme de la résistivité et de sa phase.

(a) *Modèle Cole-Cole* $(\rho_0 = 100\Omega.m, \rho_\infty = 50\Omega.m, m = 0.5, \tau = 0.01s, c = 0.5)$

(b) *Amplitude du champ électrique*
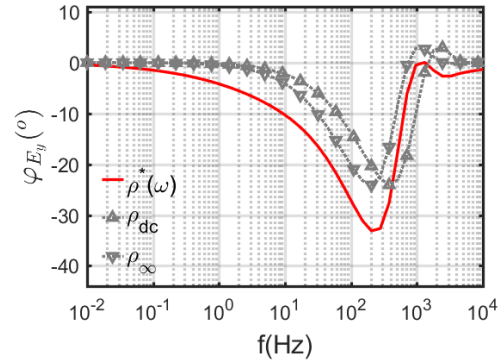
(c) *Phase du champ électrique*

Figure 4: *Réponse du champ électrique (Amplitude normalisée (b) et phase (c)) en fonction de la fréquence, pour un dipôle électrique horizontal pointant vers un recepteur à 500 mètres, pour un demi-espace homogène polarisable selon (c) un modèle Cole-Cole* $(\rho_0 = 100\Omega.m, \rho_\infty = 50\Omega.m, m = 0.5, \tau = 0.01s, c = 0.5)$. *Le champ est normalisé par sa valeur dans le cas statique (pour un milieu de résistivité* ρ_{dc}). *Les réponses pour un milieu de résistivité réelle et constante dans le cas statique* ρ_{dc} *et fréquence infinie* ρ_∞ *sont représentées en gris.*

Plusieurs conclusions ont pu être tirées lors de cette phase d'étude de sensibilité :

❏ les effets PP sont relativement faibles comparés à l'induction EM.

❏ les effets PP liés aux variations de la norme $|\rho^*(\omega)|$ et de la phase $\phi_{cpx}(\omega)$ de la RC peuvent être séparés au premier ordre dans les données du champ électrique.

❏ un milieu sans variation fréquentiel de la norme $|\rho^*(\omega)|$ de la RC présentera moins d'effets PP dans la donnée EM.

❏ dans le cas de corps polarisables en profondeur, les effets d'inductions EM seront plus important à haute fréquence et peuvent compliquer l'accès à la réponse PP (relativement plus faible). De plus la sensibilité en profondeur diminue également avec la fréquence (effet de peau, $\delta = 503\sqrt{\frac{\rho}{f}}$). Ces deux effets cumulés compliquent l'accès à la RC des cibles en profondeur à plus haute fréquence.

3   Inversion de la RC

Le problème inverse consiste à remonter aux paramètres du milieu inconnus à partir de données mesurées et donc *observées*. Il consiste en l'opération *inverse* de la modélisation des données à partir d'un milieu décrit par un certain nombre de paramètres connus (figure 5). L'imagerie de la résistivité cherchent donc à reconstruire un modèle possédant une distribution de résistivité expliquant les données EM observées selon différentes contraintes.
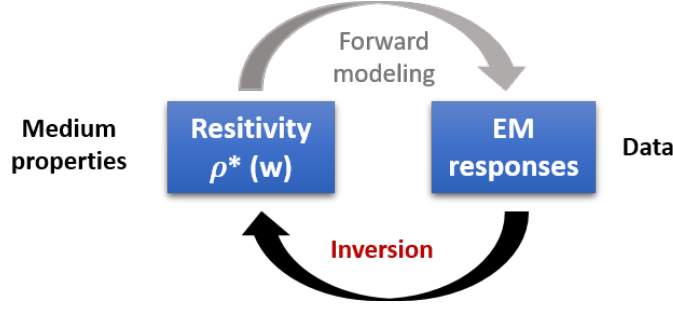

Figure 5: *Schéma résumant les relations entre modélisation et inversion*

L'inversion consiste en un problème d'optimisation local cherchant à minimiser une fonction coût χ de manière itérative. Elle comporte une partie associée aux données χ_d, cherchant à minimiser l'écart entre les données modélisées et les données observées (généralement la norme L2, pondérée par la matrice diagonale des covariances des données W_d) et une partie associée au modèle χ_m qui consiste à régulariser le problème inverse. λ est un coefficient cherchant à balancer le poids entre le terme associé aux données et aux contraintes sur le modèle.

$$\chi = \chi_d + \lambda \chi_m \quad \text{with} \quad \begin{cases} \chi_d = \frac{1}{2}||W_d(d^{cal} - d^{obs})||_2^2 \\ \chi_m = \frac{1}{2}||W_m(m - m^{ref})||_2^2 \end{cases} \tag{6}$$

Le terme χ_m contient entre autres les informations a priori du modèle. Dans les travaux de cette thèse, aucune information a priori n'a été utilisée. Une condition cherchant à minimiser la rugosité (condition de lissage maximum, $W_m = \Delta$ l'opérateur Laplacien) ou la norme L2 (condition de norme minimale, $W_m = I$) entre le modèle à l'itération k et le modèle à l'itération précédente $k - 1$ (Grayver et al., 2013).

Différentes méthodes d'optimisation sont considérées (Descente de gradient ou Gauss-Newton) afin de résoudre la direction de descente Δ_m :

$$m_{k+1} = m_k + \alpha_k \Delta m_k, \tag{7}$$

α_k étant le pas de déscente optimal, un facteur réel entre 0 et 1 déterminé par une récherche linéaire (*line search*) (Nocedal and Wright, 2006).

Stratégie multi-étape et paramétrisation polynomiale
Faisant suite à l'étude de sensibilité, une stratégie d'inversion multi-étape est mise en avant dans ce travail afin de contraindre l'inversion efficacement vers la solution la plus

probable. Dans une première étape, la norme du modèle de résistivité pouvant varier avec la fréquence est recherchée par l'inversion des données d'amplitude du champ électrique, peu affecté par la présence d'une partie imaginaire de la résistivité. A partir du modèle obtenu, une seconde étape résout le modèle de phase $\phi_{cpx}(\omega)$ de la résistivité à partir du résiduel restant sur la phase des données de champ électrique et dû aux phénomènes transitoires liés aux effets de PP.

Le problème inverse 3D étant généralement fortement sous-déterminé et le problème numérique large, réduire le nombre de paramètres lors de l'inversion des données est essentiel. Afin de réduire ce nombre, plusieurs modèles de relaxation empiriques peuvent être envisagés afin de décrire les variations de la résistivité, tel que l'un des plus utilisé, le modèle Cole-Cole (Cole and Cole, 1941), mais ces modèles, bien que pratique et directement en lien avec certaines propriétés du milieu, restent spécifiques et peuvent ne pas être adaptés à certains jeux de données. Ce travail fait le choix d'utiliser une paramétrisation polynomiale de la RC. Deux polynômes de 2nd ordre décrivent la résistivité complexe dans le problème inverse, ce qui permet de conserver ainsi une description générale et versatile du problème. La norme de la résistivité complexe $|\rho^*(\omega)|$ et sa phase $\Phi_{cpx}(\omega)$ sont alors paramétrisés selon les coefficients des polynomes sous la forme :

$$
\left.
\begin{array}{ll}
log(|\rho^*|) & = \sum_{j=0}^{n=2} p_j * log_{10}(f)^j \\
log(\Phi_{cpx}) & = \sum_{j=0}^{n=2} q_j * log_{10}(f)^j
\end{array}
\right\}
\qquad
m = \begin{pmatrix} p^0 \\ p^1 \\ p^2 \\ q^0 \\ q^1 \\ q^2 \end{pmatrix}
\qquad (8)
$$

1D inversion

Lors de la procédure d'inversion multi-étape jouant sur les différences de sensibilité entre la norme et la phase de la résistivité sur les données CSEM, chacun des polynômes est inversé séparément, réduisant ainsi le problème à 3 paramètres par cellule à résoudre simultanément. La méthode d'inversion suggérée a été développée à nouveau à partir de travaux à une dimension (1D), puis testée sur divers exemples synthétiques.

Pour illustrer la stratégie d'inversion, la figure 6 présente les résultats de l'inversion de données synthétiques CSEM pour 13 fréquences logarithmiquement réparties entre 10^{-2} Hz et 10 kHz (un profil de récepteurs mesurant le champ électrique in-line d'un dipôle électrique horizontale (HED) orienté dans la direction du profil) pour un modèle 1D comprenant une couche conductrice polarisable selon un modèle Cole-Cole avec un temps de relaxation relativement court ($\rho_0 = 100\Omega.m, \rho_\infty = 50\Omega.m, m = 0.5, \tau = 0.001s, c = 0.5$). Les effets PP sont ainsi fortement couplés aux effets EM. La procédure multi-étape et la paramétrisation polynomiale ont été utilisées afin de reconstruire la norme et la phase de la résistivité ainsi que sa signature spectrale. La norme $|\rho^*|$ de la RC obtenue en figure 6a) provient de l'étape (1) démarrant d'un milieu homogène de résistivité moyenne et une phase de RC négligeable (-1 $mrad$, constante durant l'étape 1), tandis que le modèle de phase Φ_{cpx} est le résultat de l'étape (2) démarrant du modèle obtenue en étape (1)
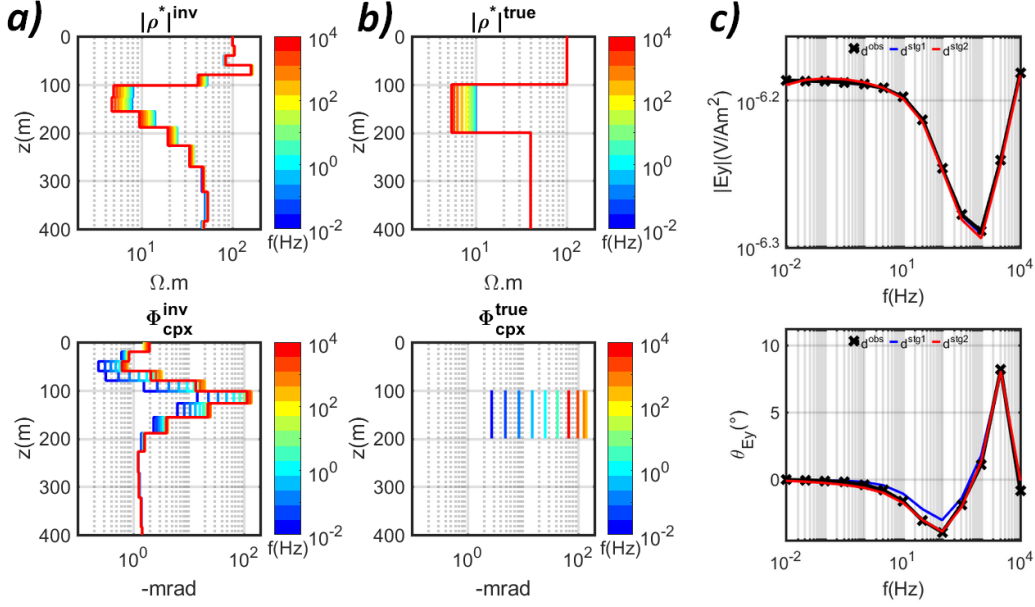
Figure 6: *Résultats de l'inversion multi-étape d'un modèle à 3 couches avec une seconde couche conductrice polarisable selon un modèle Cole-Cole avec un temps de relaxation court utilisant les données d'un profil de 21 récepteurs répartie sur 500 mètres pour une source horizontale électrique in-line (à 50 mètres du premier récepteur). a) Modèle de résistivité inversé la norme $|\rho^*|$ est obtenu en étape 1) et la phase Φ_{cpx} en étape 2), b) modèle de résistivité vraie et c) Fits sur les données en amplitude et phase à la fin de l'étape 1 et 2 pour le récepteur à 250 m de la source.*

ayant résolue la norme de la RC et ses variations fréquentielles. La figure 6c) montre un exemple de l'avancée du fit à chaque étape de l'inversion. Il est clair sur ces figures que le modèle de norme de résistivité obtenue en étape (1) explique en quasi-totalité les données d'amplitude du champ électrique mesuré tandis que seul un déphasage résiduel reste à expliquer en résolvant le modèle de phase de la résistivité en seconde étape.
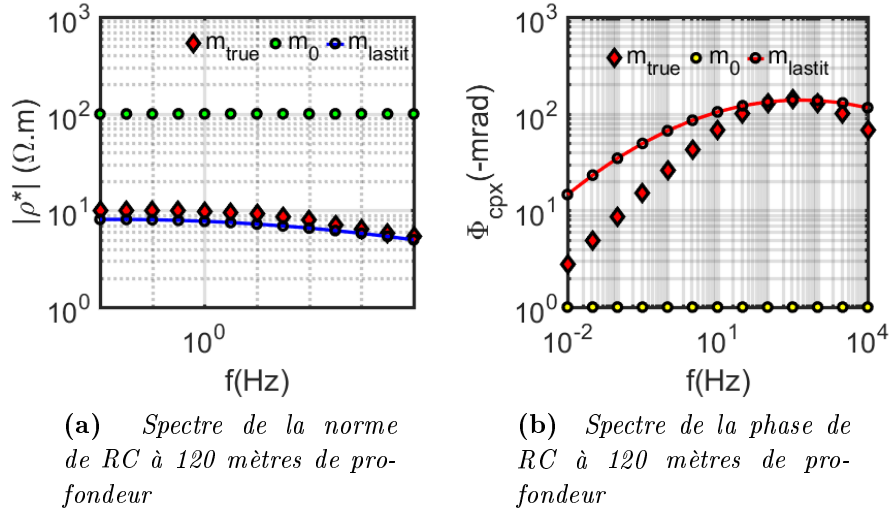
(a) *Spectre de la norme de RC à 120 mètres de profondeur*

(b) *Spectre de la phase de RC à 120 mètres de profondeur*

Figure 7: *Résultats de l'inversion du modèle 1D d'une couche polarisable selon un modèle CC ($\rho_0 = 100\,\Omega.m, \rho_\infty = 50\,\Omega.m, m = 0.5, \tau = 0.001s, c = 0.5$)*

La figure 7 présente le spectre de RC extrait dans la couche à 120 mètres de profondeur. La forme du spectre de RC obtenue est cohérente avec celle du modèle vrai tandis que la géométrie de la couche correctement résolue. Les valeurs de phases les plus faibles sont mal résolues malgré des données parfaitement expliquées, dues à une faible sensibilité des effets PP, tandis qu'à plus haute fréquence la sensibilité diminue également due à l'effet de peau.

3D inversion

Une fois la méthode développée et validée sur des exemples synthétiques 1D, la transposition au problème 3D est présentée dans les travaux de thèse ainsi que son application sur données synthétiques. L'inversion des données d'un modèle synthétique complet est présenté à la suite. Le modèle est composé d'un encaissant homogène de résistivité réelle et constante $100\,\Omega.m$. Deux cibles polarisables (cubes de 200x200 mètres) sont introduites à une profondeur de 100 mètres (toit des cubes). Le premier cube est une cible similaire à la couche conductrice polarisable présentée précédemment avec un temps de relaxation différent ($\rho_0 = 10\,\Omega.m$ $m = 0.5$ $\tau = 1\,s$ $c = 0.5$). Le second cube présente un faible constraste de résistivité avec l'encaissant, cependant il présente une résistivité variable avec la fréquence avec une variation de sa norme et une phase conséquente ($\rho_0 = 100\,\Omega.m$ $m = 0.5$ $\tau = 0.01\,s$ $c = 0.5$). La figure 8 présente la géométrie d'acquisition utilisée, ainsi que les spectres de RC des deux cubes. Le problème 3D étant beaucoup plus complexe et couteux en ressources de calcul, uniquement 7 fréquences logarithmiquement réparties entre 10^{-2} Hz et 10 kHz ont été utilisées.

Le modèle de résistivité complexe résultant de l'inversion suivant la procédure multi-étape et utilisant une paramétrisation polynomiale est présenté en figure 9. Le modèle obtenue fait ressortir les cubes de l'encaissant de différentes façons. Le cube 1, conducteur et polarisable est correctement résolu par le coefficient p^0 décrivant la partie constante
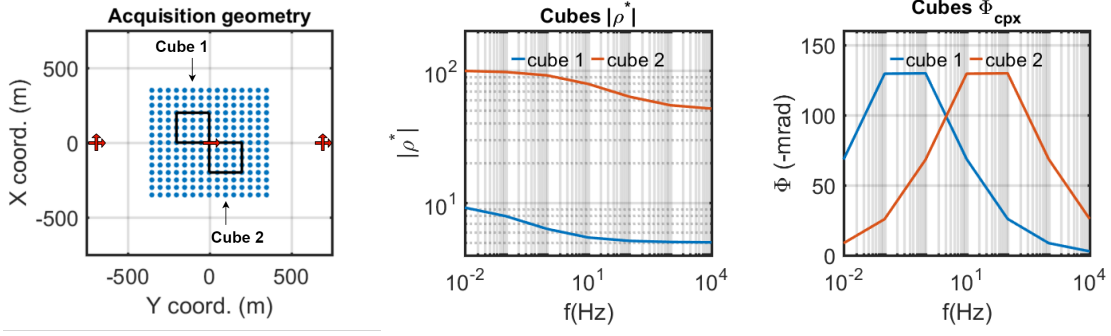
Figure 8: *Géométrie d'acquisition en surface (gauche) utilisant une grille de récepteurs (points bleus) mesurant le champ électrique horizontal (orienté selon x et y) provenant de 5 sources électriques horizontales (flèches rouges), les contours des cubes sont projetés en surface (traits noirs). La norme et la phase de RC des cubes sont présentées dans l'image du centre et de droite (cube 1, $\rho_0 = 10\,\Omega.m$ $m = 0.5$ $\tau = 1\,s$ $c = 0.5$ et cube 2, $\rho_0 = 100\,\Omega.m$ $m = 0.5$ $\tau = 0.01\,s$ $c = 0.5$)*

de la norme de la RC. Le cube 2 ne ressort pas correctement de l'image due à son faible contraste avec l'encaissant. Le cube 2 est cependant correctement résolue par les coefficient décrivant les variations fréquentielles de la norme de la RC (p^1 et p^2), contrairement au cube 1 laissant place à plusieurs artéfacts sur ces paramètres. Les données étant correctement résolues, les solutions sont équivalentes illustrant les problèmes de non-unicité de la solution. En seconde étape[a], la phase de la RC et ses variations fréquentielles sont résolues. Le coefficient q^0 est correctement résolu pour les deux cubes, regroupant cependant les deux cubes sous la forme d'une seule anomalie allongée. Le coefficient q^1 décrivant la pente de la phase permet cependant la discrimination des deux structures, l'une ayant une pente positive et l'autre un pente négative dues à la différence de temps de relaxation. Le coefficient q^2 n'est pas correctement résolu, la perturbation introduite dans le modèle n'étant pas significative, malgré des données correctement expliquées.

Il est montré à l'aide de cet exemple qu'à partir de la stratégie d'inversion développée sur synthétique 1D, un modèle de résistivité complexe imageant plusieurs cibles polarisables 3D a pu être extrait. La localisation des anomalies ainsi que l'extraction de certaines informations PP ont pu être obtenues, permettant ainsi la discrimination des cibles chargeables de l'encaissant non chargeable. De plus, le comportement spectral distinct des deux cibles a pu être différencié. Malgré des données correctement expliquées, ces travaux illustrent cependant la complexité du problème posé par la reconstruction d'un modèle de résistivité complexe et de sa dépendance fréquentielle. Les difficultés sont à la fois liées à la faible sensibilité des effets PP et à l'aspect multi-paramètre du problème.

---

[a]Dans le cas 3D, une étape dite "zéro", précédent l'étape (1), inversant les données identiquement à l'étape (1) (Amplitude du champ électrique) pour une norme de résistivité constante est réalisée, les effets EM étant largement supérieurs aux effets PP dans les données. L'inversion est stoppée manuellement lorsque le résiduel sur le fit des données est considéré du même ordre de grandeur que les effets PP potentiels.
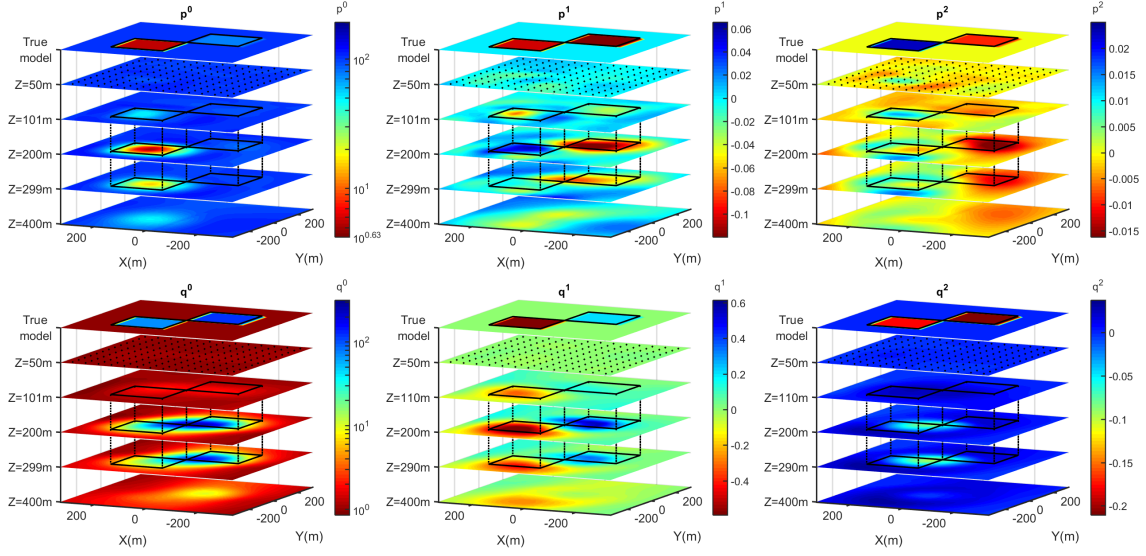
Figure 9: *Résultats d'inversion pour le modèle à deux cubes. Chaque image représente un coefficient de polynome p^n (haut) ou q^n (bas) allant du degré zéro au second degré de gauche à droite pour plusieurs coupes horizontales du modèle inversé à Z=50, 110, 200, 290 et 400 mètres. La coupe en surface représente le modèle vrai pour une coupe passant par le cube. Les coefficients p^n sont obtenus lors de la première étape et les coefficients q^n lors de la seconde étape*

En effet, la sensibilité des données CSEM aux effets PP pour des cibles à ces profondeurs est limitée avec des effets PP et ne permet de retrouver que la principale tendance des variations fréquentielles de la RC. Des données de grandes qualités et l'apport potentiel de contraintes a priori supplémentaires seront nécessaire à la résolution de données réelles pour des cibles profondes. Des cibles chargeables moins profondes impliqueraient une meilleure sensibilité aux effets PP, cependant la présence d'effets EM serait également réduit. Dans ce cas, la méthode SIP classique avec l'utilisation d'une méthode de retrait des effets EM devra être considéré sérieusement en fonction de l'apport des effets EM au problème d'imagerie étant donné l'importance des coûts de calcul supplémentaires liés à la résolution des équations de Maxwell en 3D.

4   Applications sur cas réels

Dans une dernière partie les développements réalisés lors de cette thèse sont appliqués sur deux jeux de données CSEM réels présentant des effets PP: 1) un jeu de données 2.5D CSEM acquis près de Schleiz (Allemagne) et partagé par l'Institut de Géophysique et Météorologie de l'université de Cologne et 2) un jeu de données acquis dans le cadre de cette thèse et du projet ANR EXCITING sur l'ancien site minier de La-Porte-Aux-Moines (Côtes-d'Armor, France).

Données de Shleiz (Allemagne)

Le premier jeu de données est extrait d'une campagne de mesures CSEM 2.5D réalisée pour le projet DESMEX en 2016 et 2017 dans une ancienne région minière exploitant de l'antimoine près de la ville de Schleiz en Allemagne. Les données ont été traitées et inversées dans le domaine temporel et fréquentiel dans les travaux de Mörbe et al. (2020) et consiste en un profil long de 8.5 km avec 52 récepteurs mesurant le champ électrique perpendiculaire au profil ainsi que de 6 positions de sources constituées de long câbles mis à la masse d'une longueur d'environ 1000 mètres centrés approximativement sur le profil et déployés orthogonalement. Les données rassemblent des mesures allant de 0.25 Hz à 20 kHz et sont de très bonnes qualités jusqu'à quelques kiloHertz.

Quelques stations présentant de fort effets PP au-dessus d'une anomalie conductrice, ont été extraites de ce jeu de données afin d'y réaliser des inversions 1D. Les résultats d'inversion suivant la procédure multi-étape et la paramétrisation polynomiale de la station présentant les effets PP les plus important sont présentés en figure 10.
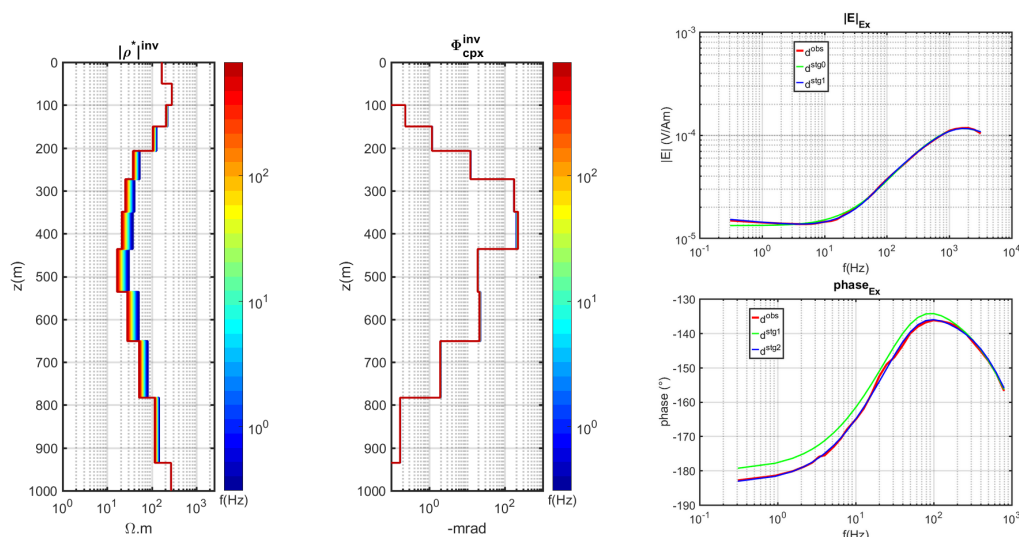

Figure 10: *Résultats d'inversion suivant la procédure multi-étape pour le RX928 du jeu de données partagé de Schleiz (Allemagne). Le RX928 est à l'aplomb d'une anomalie PP fortement conductrice. Le modèle de RC obtenu est présenté à gauche et les fits à chaque étape sont présentés à droite.*

Une variation de la norme de la résistivité de l'anomalie conductrice a pu être obtenu avec une tendance décroissante avec la fréquence. Cette anomalie conductrice est corrélée à une phase de RC importante dépassant $-100\ mrad$. Lors des deux étapes une amélioration du fit considérable est obtenue. Aucune variation supplémentaire de la phase avec la fréquence n'a cependant pu être retrouvée, les données étant déjà correctement expliquées, pointant à nouveau du doigt la faible sensibilité des effets PP. Ce résultat est corrélé à celui d'une station voisine présentant des anomalies similaires, mais possédant un fit de moins bonne qualité dû à ce qui est interprété comme des effets 2D voir 3D. Ces résultats encourageant restent néammoins faiblement contraints, les inversions prenant en compte les données combinant plusieurs sources/récepteurs n'ayant pas convergés dues aux complexités de la géologie incompatible avec une hypothèse 1D.

Données de La Porte-Aux-Moines (Côtes-d'Armor, France)

Un second cas d'application est présenté sur le jeu de données CSEM de La Portes-Aux-Moines (PAM). Les données ont été acquises durant cette thèse en décembre 2020 dans le cadre du projet ANR EXCITING. La zone d'étude est également un ancien site minier faisant partie de l'ancien PERM (Permis Exclusif de Recherche Minière) de Merléac. La zone présente un gisement important d'amas sulfurés avec de fortes concentrations d'éléments Zn, Cu, Pb, Ag et de pyrites (Aye, 1983). Ce gisement découvert au début des années 1970, de nombreuses campagnes geophysiques réalisées entre 1975 et 1980 ont démontré la présence de forts effets PP (forte phase et effets de fréquences) liés à cet amas ainsi qu'à la présence de graphites. Une campagne CSEM a donc été dimensionnée et réalisée sur le site en recouvrant la zone d'intérêt. 5 sources et 66 récepteurs mesurant le champ électrique N/S et E/W ont été déployés. La réponse du champ électrique allant d'une période de 128 s à une fréquence de 800 Hz est mesurée. La géométrie d'acquisiton est présentée en figure 11a.
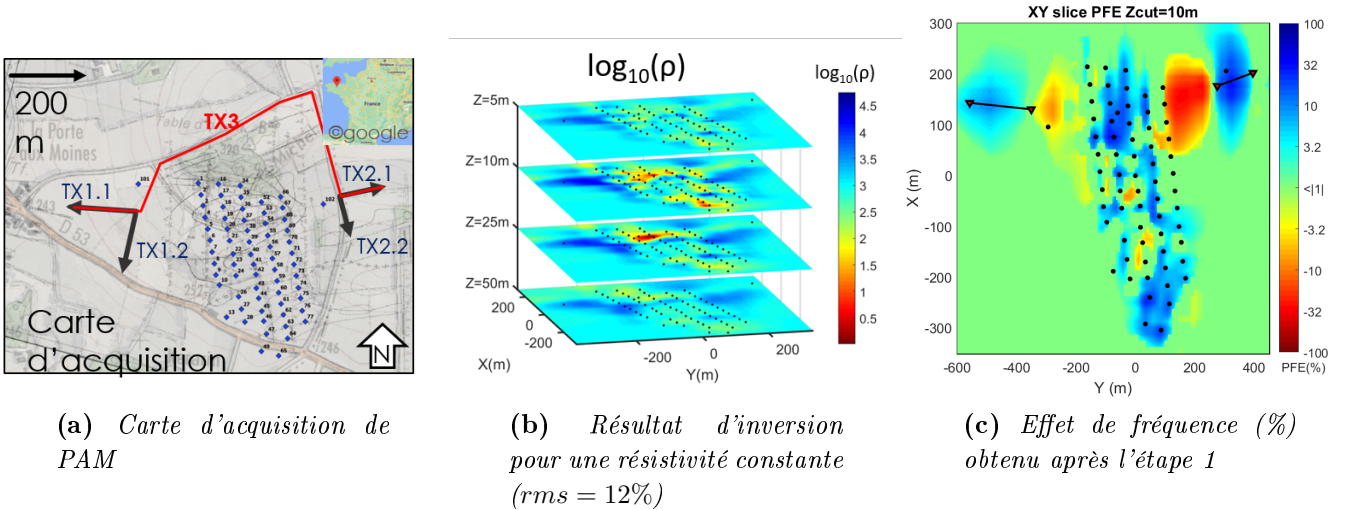

(a) *Carte d'acquisition de PAM*

(b) *Résultat d'inversion pour une résistivité constante (rms = 12%)*

(c) *Effet de fréquence (%) obtenu après l'étape 1*

Figure 11: *Présentation des résultats de l'inversion des données de la campagne CSEM de La Porte-Aux-Moines. La variation fréquentielle de la norme de RC est présentée sous forme d'effet de fréquence car seul un comportement linéaire a pu être retrouvé en l'état actuel. Le travail doit cependant être poursuivi pour améliorer la convergence (rms = 10.64%).*

Les données de la campagne sont d'une extrême qualité malgré la suppression d'un nombre important de données due à des problèmes instrumentaux ($\approx 23\%$ des données) et présentent des effets PP très important. Plusieurs tentatives d'inversions ont été réalisées combinant plusieurs sources entre elles. Les différentes inversions ont cependant montré de grandes difficultés de convergence dues a une géologie 3D très complexe avec des variations de résistivité très importantes sur plusieurs ordres de grandeur ($\rho \in [0.1\Omega.m - 100k\Omega.m]$). L'introduction d'anomalies fortement résistantes entre les sources et la zone d'étude sont nécessaires afin d'expliquer les observations de variations brutales du champ électriques. Ces anomalies restent néanmoins mal contraintes due

à un manque de données. La figure 11b présente le modèle de résistivité réelle et con-
stante le plus satisfaisant en inversant les données en considérant une résistivité constante.
L'étape (1) de l'inversion multi-paramètre faisant suite et prenant en compte une norme
de résistivité variant avec la fréquence n'a cependant pas convergé suffisamment malgré
une amélioration du fit des données. Ces problèmes de convergences peuvent être liés
à l'introduction d'importante anomalies d'effet de fréquence ($\propto p^1$) proches des sources
dans des zones mal contraintes. Le résultat de cette étape est présenté en figure 11c sous
la forme d'une carte préliminaire d'effet de fréquence, le coefficient de second ordre p^2 ne
présentant pas de variation significative. Les zones présentant les effets de fréquences les
plus important dans la zone de réception sont cohérentes avec la localisation attendue
des anomalies PP (amas sulfuré au nord et zone à graphites au sud) et avec la présence
d'anomalies conductrices.

Ces résultats encourageant sont cependant à relativiser avec la faible amélioration
du fit à ce stade. Un travail supplémentaire sur ce jeu de données est nécessaire.
Une meilleure compréhension des effets EM intervenant dans les données à plus haute
fréquence est nécessaire. En effet, ces dernières présentent dans certains cas des résiduels
important ne pouvant pas être attribués aux effets PP. De plus, afin d'améliorer la con-
vergence de l'étape 1, une contrainte supplémentaire peut être nécessaire afin de pondérer
la sensibilité proche des sources et l'introduction d'artéfacts importants.

5 Conclusion

La méthode SIP a été largement utilisée pour accéder indirectement aux propriétés du milieu, les effets PP étant étroitement liés aux caractéristiques texturales du milieu et de son contenu en fluide. Historiquement, elle a été popularisée par ses applications pour l'exploration minière, mais aussi pour les études hydrologiques, la caractérisation des argiles et plus récemment dans le domaine de la bio-géophysique. La motivation de ce travail de thèse était l'amélioration de l'imagerie de résistivité complexe, la méthode SIP utilisant une extension de la tomographie de résistivité électrique avec une hypothèse de DC, qui ne prend pas en compte la présence d'effets EM. L'induction EM intervient avec l'augmentation de la fréquence, de l'espacement source/récepteur, de la conductivité et de la disposition des câbles, limitant ainsi l'accès au spectre de RC. D'autre part, le contenu des données EM est riche en information pouvant aider à la reconstruction du milieu. Les effets PP se traduisent par une résistivité complexe pouvant varier avec la fréquence dans les équations de Maxwell, cependant les codes 3D ayant la capacité d'inverser une RC sont rares, ou ne prennent pas en compte explicitement sa variation fréquentielle. Par conséquent, ce travail s'est concentré sur l'implémentation d'une RC dépendante de la fréquence dans un code de modélisation et d'inversion CSEM 3D. Suite à une étude de sensibilité des données CSEM aux effets PP, une stratégie d'inversion décomposant le problème en plusieurs étape a été proposée afin de contraindre efficacement l'inversion multi-paramètre. Dans un premier temps, une étape centrée sur l'inversion des données d'amplitude du champ électrique est réalisée. En effet, l'amplitude du champ électrique est contrôlée principalement par la variation de la norme de la RC, la présence d'une phase de la RC impactant faiblement l'amplitude de la réponse du champ électrique. La seconde étape de la stratégie d'inversion consiste en l'inversion du résidu restant sur la phase du champ électrique, qui concentre l'effet PP dû à la présence d'une phase significative de la RC. Il a été montré qu'en utilisant la stratégie multi-étape, la complexité de l'inversion des données pouvait être réduite en séparant ainsi les effets sur les observables associés aux variations de la norme de la RC et à sa phase. Une paramétrisation polynomiale de la RC a été proposée afin de décrire le comportement spectral et de gérer le nombre croissant de paramètres avec l'augmentation du nombre de fréquences. La norme et la phase de la RC sont décrites par les coefficients de deux polynômes indépendants. Par conséquent, aucun modèle particulier de RC liant les variations de la norme à la phase de la RC n'est supposé dans l'inversion. Cette nouvelle stratégie d'inversion des données CSEM/PP a donc été proposée et appliquée sur plusieurs jeux de données synthétiques 1D et 3D. Cependant, les effets PP restent relativement faibles par rapport aux effets EM, surtout lorsque l'on considère des cibles profondément enfouies. Il est donc crucial d'avoir des données d'une extrême qualité, avec des méthodes de traitement robustes. Malgré une sensibilité aux effets PP limitée, les inversions synthétiques 3D présentées dans ces travaux ont montrées être capable d'extraire suffisamment d'information pour discriminer les cibles considérées de l'encaissant ainsi que de séparer leur comportement spectral. Pour finir, la stratégie d'inversion a été appliqué sur deux jeux de données. Dans cette partie du travail, des inversions 1D ont été présentées sur le jeu de données Schleiz. Des anomalies PP cohérentes ont été récupérées, cependant la complexité géologique a

conduit à se limiter à des inversions 1D mono-récepteur, par conséquent mal contraintes verticalement. Un travail d'inversion 2.5D basé sur le code 3D a été entrepris, cependant aucune conclusion définitive n'a été atteinte dans le laps de temps de la thèse. Dans le cadre de la campagne CSEM de PAM certaines difficultés ont été rencontrées, parmi lesquelles la complexité du cadre géologique ainsi que d'important contrastes de résistivité mal contraints en dehors de la grille de réception (notamment sous les sources) et un manque de résolution vertical qui a pu restreindre la convergence de l'inversion vers un modèle de résistivité expliquant correctement les données. Une tentative de récupération de la variation de la norme de la RC a été menée et a conduit à des résultats prometteurs, cependant, des travaux supplémentaires doivent être poursuivis pour mieux contraindre l'inversion sous les sources et pondérer les données hautes fréquences partiellement expliquées. Ces applications mettent en évidence la complexité de l'inversion d'un milieu de RC prenant en compte simultanément l'induction EM ainsi que les effets PP. Ce travail de thèse sur l'imagerie 3D de la RC a permis d'améliorer l'accès au comportement spectral d'une cible profondément enfouie, ce qui nécessite notamment de prendre en compte l'induction EM pour étudier des offsets plus importants. Pour les cibles moins profondes, pour lesquelles l'approximation DC est suffisante, il permet d'améliorer l'étude des variations de RC à plus haute fréquence où l'induction EM se produit même à court offset dans les milieux conducteurs. Les développements réalisés au cour de cette thèse contribueront à établir une meilleure stratégie d'inversion des données EM afin d'inverser simultanément les informations EM et IP contenant chacunes des informations essentielles sur le milieu. Pour les cibles enfouies, la récupération d'informations quantitatives sur la RC reste cependant un défi en raison de la faible amplitude des effets PP, néanmoins les données peuvent être suffisamment sensibles aux effets PP pour aider à la discrimination entre différents comportements spectraux, même à grande profondeur comme démontré sur modèle synthétique. Pour les cibles moins profondes, ou les cibles plus proches des récepteurs (*i.e.*, mesures en puits) une comparaison sérieuse avec les techniques de suppression des effets EM doit être envisagée afin de comparer leurs performances en fonction des résultats attendus, car l'induction EM est moins sensible à court offset et contient moins d'informations supplémentaires sur le milieu environnant, tandis que les coûts de calculs supplémentaires nécessaires à sa prise en compte sont important. Parmi les perspectives liées à ces travaux, le travail peut être poursuivi sur l'implémentation d'autres paramétrisation de la RC à des fins de comparaison et/ou afin d'être utilisées lorsque suffisamment de contraintes sont connues afin de préciser le comportement fréquentiel. De plus, le lien entre l'inversion des mesures de terrain intégrant un grand volume avec des informations partielles aux propriétés du milieu in-situ à plus petite échelle doit être évalué de plus près à l'aide de techniques de réduction d'échelle. De toute évidence, le travail prometteur sur le jeu de données de PAM doit être poursuivi ainsi que le travail sur le jeu de données complet 2.5D de Schleiz. Compte tenu des réponses PP observées dans l'ensemble du jeu de données de PAM, l'acquisition des données CSEM/ERT supplémentaires pour combler certaines lacunes dans les données pourrait être justifiée et envisagée pour contraindre et compléter l'inversion existante. Tout au long de ce travail, les limites de sensibilité des données CSEM aux effets PP ont été passées en revue sur les inversions de données synthétiques et de terrain. Malgré des résultats encourageants, la faisabilité

de ce type de travaux est à mettre en perspective avec d'autres problématiques courantes rencontrées sur le terrain ayant des sensibilités similaires ou supérieures, comme les effets topographiques, ou la présence d'une anisotropie de résistivité. En effet, j'ai travaillé ici avec la résistivité isotrope, cependant de nombreux milieux géologiques sont anisotropes en raison des stratifications sédimentaires et des processus de déformation, ce qui aurait un impact sur les données ainsi que sur la PP. La perspective de mélanger les deux effets dans la formulation du code dans une prochaine étape est d'un grand intérêt, mais rendrait encore plus complexe une procédure d'inversion.

Contents

_____

Acknowledgements

This thesis was carried out within the framework of the ANR project EXCITING and was conducted in two places starting in April 2018. The first half of my thesis was carried out at the French Geological Survey (BRGM,*i.e. Bureau de Recherche Géologiques et Minières*) in Orléans, France, whereas the second half took place back to Strasbourg where I conducted all my studies, at the Institute of Earth an Environment of Strasbourg (ITES - former IPGS). I would like to thank in the following, each person or entity that participated in the achievement of this work. The first part will be in English as the rest of this manuscript, whereas the second part will be more personal and will thus be written in French for my non-English speaker relatives.

Acknowledgements

First of all, I would like to thank both of my great supervisor, **Jean-François Girard** (ITES -University of Strasbourg) and **François Bretaudeau** (BRGM) for their continuous support at every stage of this research project. I am deeply grateful that you took me on as a PhD student and continued to have faith in me over all of these years.

I would like to thank the French **National Research Agency (ANR)** that funded this work within the framework of the project **EXCITING** (ANR-17-CE06-0012), as well as the **BRGM** and the **ITES (University of Strasbourg)** which welcomed me into their organization and offer me the means to succeed this work. Furthermore, I am grateful to GENCI (Grand Equipement de Calcul Intensif) and CINES (Centre Informatique National de l'enseignement Supérieur) supercomputing facilities on which large scale 3-D EM modelling and inversion were performed using the Occigen supercomputer.

I would like to show gratitude to all my jury members that accepted to evaluate my PhD work. I am grateful to my main examiners: **Thomas Günther** and **Romain Brossier**, my examiners: Cyril Schamper and Guy Marquis, and as a guest: **Pauline Kessouri**, for their time and for carefully evaluating my work.

To conclude, I would like also to offer my special thanks to **Wiebke Mörbe** and **Pritam Yogeshwar** from the Institute of Geophysics and Meteorology at the University of Cologne, Germany, for the sharing of the Schleiz dataset and their interest into my work.

Remerciements

En premier lieu je souhaite exprimer à nouveau toute ma gratitude à **Jean-François** et **François**, mes directeurs de thèses, pour m'avoir accompagné durant tout ce temps entre

Orléans et Strasbourg. Merci à François, pour m'avoir (ré-)accueilli au BRGM au début de cette thèse et virtuellement sur sa machine, le fameux *Kirikou*, petit mais rapide ! Je le remercie pour tout le temps qu'il a pris pour m'expliquer les tréfonds de POLYEM' jusqu'à pouvoir participer à son développement. Merci ensuite à Jean-François que j'ai pu rejoindre à Strasbourg en deuxième partie de thèse, début 2020. Je le remercie à nouveau pour son soutien indéfectible durant toute cette thèse mais aussi pour tout ce qu'il avait déjà pu m'apprendre en tant que Professeur lors de mon parcours à l'EOST et pour m'avoir fait confiance dès mes stages de fins d'études. Mon retour à Strasbourg resta cependant relativement discrets avec très vite l'arrivée du Covid-19 nous renvoyant tous à la maison et que je ne remercie pas en passant !

Merci à toute l'**équipe IGT** pour leur accueil chaleureux au BRGM et tous les merveilleux échanges que j'ai pu y avoir. Je remercie tout spécialement l'équipe *Chantal* (*aka* la team EM) avec qui j'ai pu constamment échanger scientifiquement, ou non, et partager de nombreuses missions toutes plus intéressantes que les autres. Sans oublier bien sûr la bonne humeur toujours au rendez-vous, à en faire oublier les nombreuses difficultés rencontrées sur le terrain (Big Up! au Cafard d'Anses-Caffard ! **Pierrot** le champion du troubleshooting le plus improbable). Merci aussi à **Florent Beau"Doigt"**, le Super Tech' (futur ingénieur) des missions CSEM (entre autres),... à quand le prochain concours de tirage/enroulage de câble ? *Safety-first!* nous rappelle **Mathieu**, que je n'oublie pas de remercier pour son soutien et de m'avoir fait confiance à mes débuts au BRGM lors de mon stage ingénieur du côté de DGR à l'époque ! Je tiens à mentionner tout spécialement **Nico'** qui m'a accueilli dans son bureau les quasi deux années passées au BRGM. Je le remercie pour ses précieux conseils et les divers échanges que nous avons pu avoir, notamment en matière de randonnées et qui ont été à l'origine de mes projets de vadrouilles en solitaire avec notamment la découverte de la West Highland Way !

Côté ITES, je tiens à remercier chaleureusement **Guy Marquis** qui n'était jamais très loin pour nous raconter une énième anecdote toujours plus intéressante que la précédente ! Je le remercie aussi lui et **Cyril Schamper** pour leur aide précieuse afin de perfectionner l'anglais de mon manuscrit.

Je tiens également à remercier **Pascale** au BRGM ainsi que Dilek et Binta à l'ITES pour leur aide précieuse dans toutes les démarches administratives !

Vient enfin la partie des remerciements concernant mes proches sans qui cette thèse n'aurait sûrement pas abouti, leur soutien ayant été d'une importance capitale !

Je remercie tout d'abord mes parents, **Elisabeth et Martial Porté**, qui ont toujours été là pour moi durant ces nombreuses années d'études. Je remercie plus généralement **ma famille** pour leur amour inestimable, leur confiance, leur soutien et toutes les valeurs qu'ils ont su m'inculquer.

Je tiens enfin à remercier chaleureusement ma piti'te **Sam'** qui fait mon bonheur tous les jours et qui m'a soutenu au quotidien dans les moments les plus difficiles de ces travaux sans jamais sourciller. (Patate <3)

Un grand Merci aussi à **Thomas** qui à pu m'accompagner une grande partie de mes années Strasbourgeoises et qui m'a toujours été d'un soutien primordial depuis le lycée,

en passant par la période STUE jusqu'à aujourd'hui encore ! *ps: j'attends encore les photos de Florence ;)*

Pour finir j'aimerais remercier mes amis, **Flora et Xavier** (et coucou Berlioz !) à Strasbourg, ainsi que **Karine** et **Cyril** du côté d'Orléans (big up! à la Bonne Pioche et à ce premier Festicolor exceptionnel !)

Enfin, que tous ceux qui, de loin ou de près, ont participé à la réussite de ce travail et qui n'ont malheureusement pas été cités trouvent ici l'expression de ma sincère gratitude.

Introduction

_____

Some Earth materials exhibits a typical late time relaxation after the application of a current into the ground. This phenomenon is called *provoqued polarization* or more commonly *induced polarization* and originates from electrochemical interfacial interactions between an electrolyte and the mineral grain and pore. The study of induced polarization (IP) became a very popular geoelectrical method throughout the years due to the sensitivity of these phenomena to various highly-valuable properties of the medium related to the pore space interfaces. Among other applications, IP method was particularly successful to access to the content of disseminated metallic particle and their discrimination in the frequency domain, whereas many hydrological application were carried out to estimate hydraulic permeability from IP parameters.

This PhD work takes place within the framework of the ANR *EXCITNG* program (ANR-17-CE06-0012). The main objective of the project is to improve the characterization of electrical properties of different clay minerals and mixtures from the laboratory scale to the field scale. Indeed, the characterization of clay material is of high interest for major economical and risk reduction issues considering their leading role as impermeable barriers in various domains of application. Clays usually present a higher IP response than surrounding rocks and recent works have shown that the different clay minerals present specific electrical signatures.

IP effects are described mathematically by a frequency-dependent complex resistivity (CR) and therefore needs measurements at several frequencies. Generally, interpretation is performed applying a theory of direct current hypothesis. Indeed, electromagnetic induction or coupling are thus neglected or removed using empirical methods. Therefore, strong limitations can appear to recover a complex resistivity spectrum in the field at large scale due to EM induction perturbation that arises with frequency and offset from the source.

The purpose of this work was therefore to improve the imagery of a frequency-dependent CR by fully taking into account EM induction in the modelling when inverting for IP data. This work is thus placed at the scale of the field (from several tenth of meters to several kilometers), the larger scale considered in the EXCITING project. The frequency window available for CR spectral characterization would be improved as well as the use of longer offset to study deeper targets. Furthermore, the EM information content of the data would participate to the resistivity medium reconstruction.

This thesis work relies mainly on a 3D finite-differences modelling and inversion code for frequency domain controlled-source electromagnetic (CSEM) and magnetotelluric (MT) data developed in the EM geophysicist team of the Bureau de Recherches Géologiques et Minières (BRGM, *i.e.* the french geological survey) where the first half

of this thesis was conducted. The pre-existing CSEM code takes into account a real and constant resistivity, neglecting by the way the IP effects that can occur in the data, nevertheless this assumption is valid in the vast majority of CSEM application as EM induction magnitude overcomes IP effects.

The strategy adopted to undertake this work was therefore to adapt the pre-existing 3D code for a frequency-dependent CR formulation. An evaluation of the CSEM data sensitivity to CR parameters and IP effect is carried out at first to develop an appropriate inversion strategy. The inversion is at first adapted to the multi-parameter problem and tested following a 1D approach before a complete implementation to the computationally expensive 3D problem.

The manuscript is structured in six chapters:

❏ The first chapter presents the origin of induced polarization from a brief historical review to a description of induced polarization mechanism. The parameters and models used to describe these phenomenon are discussed.

❏ The second chapter is a presentation of resistivity imaging methods. The basics of the electrical resistivity tomography method are presented followed by the extension to the method of induced polarisation in time and frequency domain. Then the bases of EM theory are presented with a CSEM method presentation.

❏ The third chapter is about the POLYEM3D code itself. The forward problem is presented as well as the inverse problem theory and gradient calculation.

❏ The fourth chapter deals with a sensitivity study of CSEM data to IP effects. The straightforward implementation of the CR to the CSEM code is presented with some validation works. Then it follows the sensitivity study with 1D and 3D modelling in a workflow increasing gradually the complexity.

❏ The fifth chapter presents in a first section the multiparameter inversion strategy developed to recover a frequency-dependent CR, which was developed through a 1D inversion module and tested on synthetics examples. In the second section, the 3D adaptation of the CSEM inversion code is presented with a complete 3D synthetic example.

❏ The last and final chapter presents the applications of the inversion code to real datasets. Several difficulties are arising in this work and limitations of the CR study on real dataset are discussed.

An accepted paper including supplementary work carried out partially during this thesis and dealing for the characterization of the transition zone between the sedimentary cover and the basement of deep sedimentary basin for geothermal exploitation in Alsace is presented in appendix B. The work carried out in the framework of this paper is not related to IP, however it concerns resistivity imaging using CSEM method with similar tools as used in this PhD work.

Complex resistivity and induced polarization phenomenon

Frequency-dependent complex resistivity (CR) describes physically the so-called induced polarization (IP) phenomenon linked to the delayed voltage response in Earth materials when a low-frequency current injected into the ground. In this first chapter, inspired from the work of Sumner (1984) and from the very rich and relatively recent historical review of Seigel et al. (2007), an introduction to IP and complex resistivity is presented. A brief recall of induced polarization history is presented first to place in its context the emergence of the IP method, until to present-day applications. The physical origins of the phenomena are then discussed, as well as the common models that describe IP at the field scale to link IP parameters to medium properties for geological interpretation and hydrogeological characterization. Induced polarization prospecting method is introduced in more detail in the next chapter on resistivity imaging.

I.1 Induced polarization method, a brief history of its origin

Induced polarization was first mentioned by Conrad Schlumberger in its pioneering work of 1920 (Schlumberger, 1920, see Chapter XIII), a true foundation of geophysics. He describes the effect of a slow residual voltage relaxation after the current injection turn-off (Figure I.1), which cannot be attributed to electrode polarization. He named this effect "*polarisation provoquée*" (in French), or in english *induced polarization* which also took the name of *over-voltage phenomenon* (concerning metallic conductors) during the early years of the method[a].

---

[a]Induced polarization term introduced later can be misleading, nevertheless this term was commonly accepted by the geophysical community.
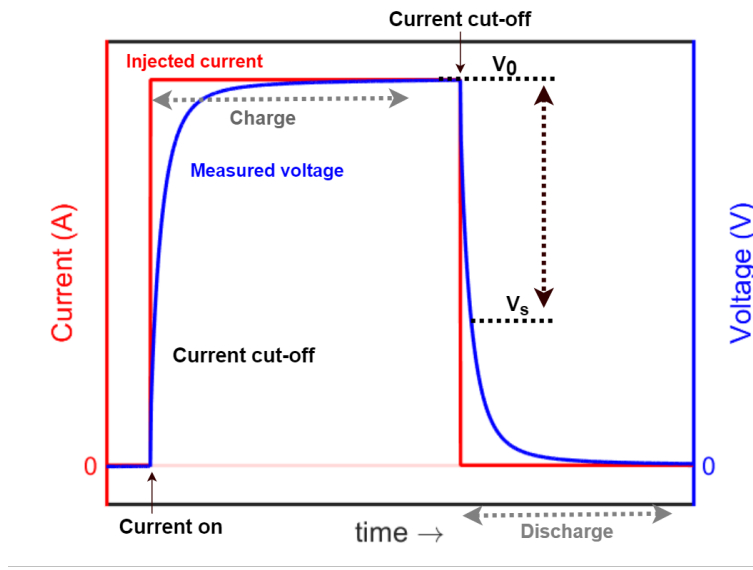
Figure I.1: *Illustration of the time-domain relaxation occurring in induced polarization measurements when a current is injected to the ground. A charge and a discharge phase due to induced polarization effect are appearing. The effect can be quantified using the ratio between the voltage after the current shut-off and the voltage measured during injection when the steady state condition is reached V_s/V_0, this measurement refers to the chargeability introduced in the following.*

Various attempts followed the work of Schlumberger, who was contracted by the former Soviet Union for an extensive logging program of some oil fields, where among which he studied the application of induced polarization. Concrete advances in the method arose thirty years later around the 1950's, after World War II. A reference publication starting this period of interest is the work done by Bleil (1953), with his publication of a part of his PhD work dealing with IP laboratory experiments and field data measurements over ore deposits. It pointed out interest for mineral exploration and IP in following years. In parallel from 1946 to 1958, the team at *Newmont Exploration Limited*, under the lead of Arthur Brant, largely developed the IP method on their side, keeping their developments confidential for several years. They made important advances from theory, laboratory measurements, instrumentation to field application. Wait (1959) resumes in a collection of papers these fundamental works. Among it, figures the development of the mathematical formulation of IP response from Seigel (1959) [b] for a medium with a given *chargeability* which is a parameter quantifying the voltage decay due to IP. Concerning non-metallic origin of IP, Vacquier et al. (1957) apply the IP method for groundwater prospecting measurements on artificial clay and sand mixtures. They point out a link between the grain size, hydraulic permeability and the characteristic relaxation times of the IP response as well as the origin of a *membrane polarization* due to a constriction of the charges in pore throats. The clay content is a key parameter of IP response due to its high cation exchange capacity (CEC). Marshall and Madden (1959) developed a theoretical model for the membrane polarization playing a large role in clay mixtures. In

---

[b]The work of Seigel was originally part of its PhD work (Seigel, 1949), that was kept confidential for several years at the request of Newmont.

the following years, IP pursued its development and was largely studied in laboratory as well as applied to the field, especially for mineral exploration. Spectral induced polarization, the study of the variation of resistivity with frequency, arose mainly during this period. A review of the method for this period by Madden and Cantwell (1967) suggested some capabilities of the IP method for mineral discrimination considering their spectral behaviour, nevertheless at this point the theoretical understanding of the physics was too limited.

Later, Pelton et al. (1978) demonstrated in their work the use of Cole-Cole models (Cole and Cole, 1941), originally used for complex permittivity, in order to discriminate between various disseminated metallic particles of ore body that present characteristic CR spectral shapes. In addition, to palliate to the strong limitation of IP method due to EM coupling, they proposed a combination of two models for EM induction removal as they intervene generally at different characteristic times. The use of Cole-Cole models for IP study imposes itself over years as one of the reference model for interpretation of IP phenomena at the field scale, even though many others relaxation models are used (for a list and comparison of several circuit analogue models, see Dias, 2000; Liu et al., 2016). IP method was largely used for oil exploration in the 1980's, Sternberg (1991) presented in his paper a review of his work (mainly with his colleague D. Oehler) on this period for hydrocarbon exploration and points out the success and limitation that they encountered with the method in this context. Indeed, Olhoeft (1985) points three main sources of IP in these context as the presence of disseminated metallic particles (pyrite or magnetite), specific reactions involving organic materials and the specific response of clay interactions and its high CEC. Vinegar and Waxman (1984) focused their interest on the IP response of shaly sands and following the work of Waxman and Smits (1968) for a real conductivity, they developed a model based on similar petrophysical parameters to account for *shaliness* (*i.e.* the CEC), salinity, and oil saturation in the description of the imaginary part of the conductivity.

In more recent years with the improvement of the instrumentation, the IP method was widely applied to environmental studies in order to recover hydrogeological properties, as the hydraulic permeability and textural properties with the works of Binley et al. (2005); Börner et al. (1996); Maurya et al. (2018b); Weller et al. (2015). Vanhala (1997) used IP method for contaminants mapping in soils, in particular for organic pollutant that influences less the real part of the resistivity but can have a significant effect on the imaginary part of the resistivity (see also Börner et al., 1993). With the necessity of nuclear waste storages arising with years, it can be mentioned that IP method found many application in this field for clay cap characterization acting as permeability barriers (Okay, 2011; Okay et al., 2014, and references within). Revil et al. (2019) present in their case a recent application of IP method to the study of clay cap in geothermal fields. Lately, IP method gained a large interest in *biogeophysics* (Atekwana and Slater, 2009), that link geophysical observations to biological organism or related phenomena (bioremediation processes, biofilm formation, plant-root system processes,...). A recent review of IP applied to this domain is presented by Kessouri et al. (2019).

I.2   Induced polarization mechanisms

Earth materials' electrical properties can be influenced by three domains: the rock matrix where electric conduction is generally neglected (excepted in metallic ore bodies where electronic conduction dominates), the fluid in the pore space that implies electrolytic conduction and the interfaces between both where charges can accumulate. In most earth materials, electrolytic conduction is dominant if present (see Chapter 2). Induced polarization has thus several origins in the low frequency range concerning EM resistivity imaging (0.001 Hz to 100 kHz). IP relies on the transport of charge carriers and reversible accumulation at the interfaces of the electrolyte and the surface of the rock matrix. The polarization implies thus a frequency-dependent complex resistivity or conductivity. In the recent review of Kemna et al. (2012), they identified several underlying polarization mechanisms that can overlap in the low-frequency range:

Maxwell-Wagner polarization

Maxwell-Wagner polarization comes from the heterogeneities in the medium. Due to a difference of relaxation times τ ($\tau = \epsilon/\sigma$) between two materials, a charge accumulation at the interface appears when a current is applied (Iwamoto and Bhushan, 2012). Maxwell-Wagner effects are controlled by the relaxation times of both materials, tortuosity and volume fractions of the different phases (Kemna et al., 2012). They are nevertheless independent of the grain and pore sizes (Lesmes and Morgan, 2001). These effects occur mainly at high frequencies compared to the other mechanisms (above the kiloHertz (Kemna et al., 2012; Leroy et al., 2008)).

Electrical double layer polarization

The electronic double layer (EDL) comes from the fixed charge density located at the surface of a mineral, generally with negative charges excess (Leroy et al., 2008). The EDL counterbalances the effect of the mineral surface attracting charges of the electrolyte to restore electro-neutrality. It is composed of two[c] distinct layers, the Stern and the diffuse layer (Figure I.2). The Stern layer is composed of an *immobile* layer (charges still can move tangentially to the grain surface (Schwarz, 1962) of electrolytic charges that are directly adsorbed to the mineral surface. On the other hand, the diffuse layer is composed of the electrolyte volume of mobile charge carriers affected by the concentration of charges in the Stern layer until a given distance. The volume of electrolyte far enough from the Stern layer and unaffected by excess charge is called the free electrolyte. Both layers can be deformed by the application of an external current and thus give arise to polarization phenomena. Their associated dipole moment are in opposition with the applied current and their polarization will depend on the type of materials, in the sense of colloidal suspensions, granular porous medium or a continuous solid phase (Revil and Cosenza, 2010). Indeed, as the solid phase becomes more and more dominant, the diffuse, then the Stern layer, between mineral grains becomes continuous. Therefore, their contribution progressively decreases.

---

[c]Three layers actually exist, nevertheless only two are generally considered in IP application, inner and outer Stern layers considered as one.
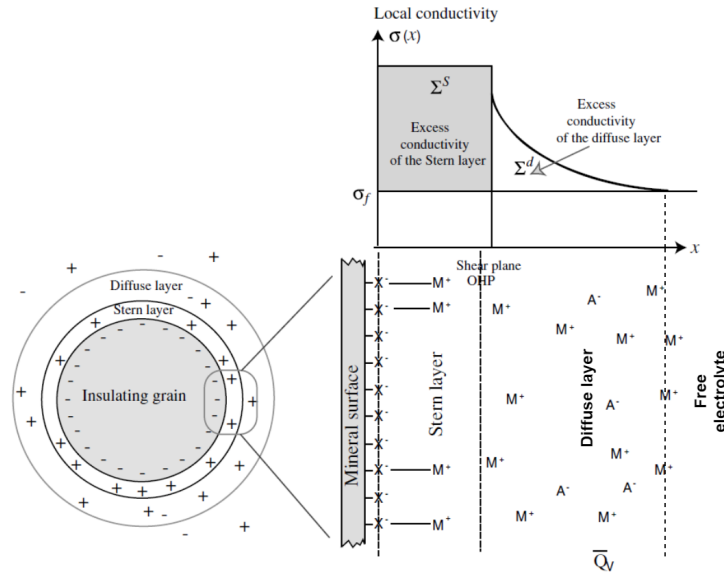
Figure I.2: *Illustration of the electrical double layer structure at the mineral interface with an electrolytic solution. The EDL is responsible of an excess of surface conductivity with respect to the fluid conductivity and illustrate in the upper right of the image. Modified from* Revil and Florsch (2010)

Membrane polarization

In their early work, Marshall and Madden (1959) described one of the main origin of IP, the so-called *membrane* polarization. Membrane polarization arises from the difference of mobility of charge carriers at the grain interface and to the constriction of charges (the larger anions) in pore throats. When a current is applied, it deforms the diffuse layer of the EDL with an accumulation and depletion of mobile ions (Figure I.3), that produces a back-diffusion of charge carriers at the grain interface. It generates a difference of salinity (or concentration) between both sides of the grain because the constriction occurs at the pore throat, which induces a polarization phenomenon similar to an equivalent dipole opposed to the applied current.
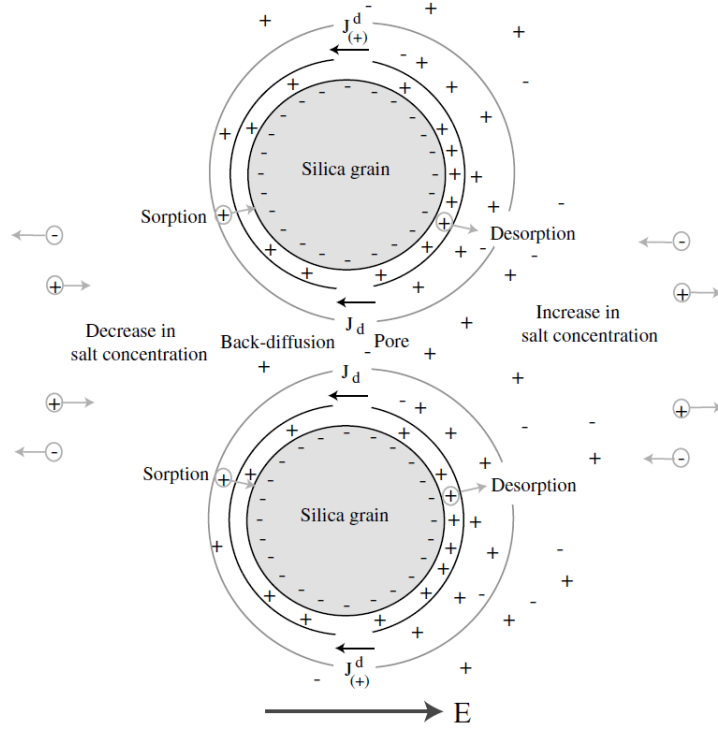
Figure I.3: *Illustration of the membrane polarization for a pore constricted between two grains from* Revil and Florsch (2010)

The membrane polarization and its constriction origin can be better depicted and understood in pore throat configuration. This phenomenon is particularly enhanced by the presence of clay particles with a negatively charged surface in pore throat as depicted in figure I.4. The presence of the clay particle results in a diffuse layer forming a positively charged cationic cloud at the clay interface. When a current is applied, the difference of mobility of charge carriers will create an ion selective *membrane* due to the constriction of the larger anions that are unable to pass easily through the cationic cloud concentration, which is not the case for smaller cations (Ward, 1988). It results in charges accumulation and depletion that return to equilibrium at the current turn-off.
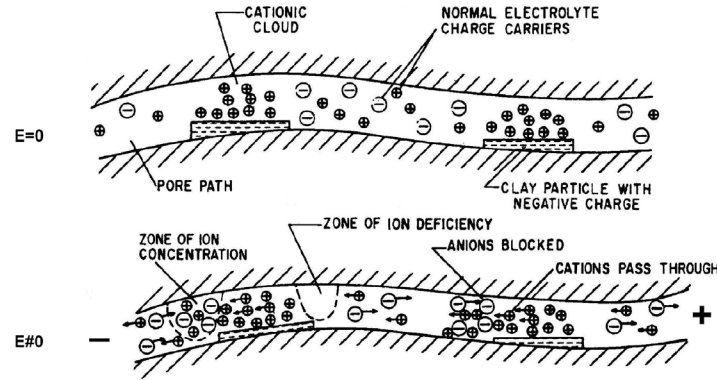
Figure I.4: *Illustration of the membrane polarization for a pore throat containing clay particles negatively charged from* Ward and Fraser (1967). *a) at steady state, b) in presence of an electric field*

.

Electrode polarization

The last polarization mechanism that impacts IP method, is the first to be described in the early literature, as Schlumberger (1920), which associates *provoked polarization* to the presence of metallic ore bodies. This is the electrode polarization, which happens in rock materials acting as semi-conductor or metallic conductor, thus for media containing disseminated conductive minerals or massive metallic ore body. Generally these effects generate the largest observable IP effects. They arise from two effects related to metallic particle properties. Charge carriers are migrating and accumulating at interfaces inside the metallic particles with no charge transfer across the interface and creating a secondary dipole that polarizes therefore the metallic grain outer layer. On the other hand, when an external current is applied, the contact with an electrolyte creates redox electrochemical reactions with charge transfer at metallic grain interfaces (Revil et al., 2015; Wong, 1979) which will act as a battery cell.

I.3 IP parameters

I.3.1 Complex resistivity $\rho^*(\omega)$

Induced polarization is physically described in EM governing equation by a complex conductivity or a complex resistivity. The electrical conductivity or the electrical resistivity, describes the ability of a medium to carry, or inversely to resist to, an electric current flow. Resistivity applications and ranges in Earth materials are discussed in more details in Chapter 2 concerning resistivity imaging. The focus is given at first to the description of induced polarization parameters:

The complex conductivity of a medium σ^* is described as follow :

$$\sigma^*(\omega) = \sigma_r(\omega) + i\sigma_q(\omega) \tag{I.1}$$

It consists of a real, or in-phase part σ_r and an imaginary, or quadrature phase part σ_q, with $i = \sqrt{-1}$ the imaginary number. **Each terms of σ^* are positive** and can be frequency-dependent (noted with respect with the angular frequency $\omega = 2\pi f$, f being the frequency in Hertz). The conductivity value of the in-phase part is larger than the conductivity of the quadrature part which represents only a fraction of the total conductivity, thus $\sigma_r \gg \sigma_q$. In this work, the resistivity parameter is preferred for the description of the Earth electrical properties. Indeed, Earth materials are generally considered as insulators due to a weak conductivity (see Chapter 2) explaining the commonly used term of resistivity instead of conductivity with field-scale geophysical methods, nevertheless using conductivity or resistivity can be seen as equivalent. The resistivity is simply the reciprocal of the conductivity:

$$\rho^*(\omega) = \frac{1}{\sigma^*(\omega)} \tag{I.2}$$

As $\sigma^*(\omega)$ is a complex number, a special attention should be paid due to fundamental properties of complex numbers. Indeed, the imaginary part of the conductivity is of opposite sign to the imaginary part of the resistivity. Furthermore, the real part of the resistivity **is not** equal to the reciprocal of the real part of the conductivity as demonstrated below:

$$
\begin{aligned}
\rho^*(\omega) &= \frac{1}{\sigma^*(\omega)} \\
&= \frac{1}{\sigma_r(\omega) + i\sigma_q(\omega)} \times \frac{\overline{\sigma^*(\omega)}}{\overline{\sigma^*(\omega)}} \\
&= \frac{\sigma_r(\omega) - i\sigma_q(\omega)}{\sigma_r(\omega)^2 + \sigma_q(\omega)^2} \\
&= \frac{\sigma_r(\omega) - i\sigma_q(\omega)}{|\sigma^*(\omega)|^2},
\end{aligned}
$$

with $\overline{\sigma*}$ the complex conjugate of the conductivity. The real and imaginary part of the resistivity can thus be expressed according to the imaginary conductivity by identifying the real and imaginary part of the previous equation as:

$$\rho_r(\omega) = \frac{1}{|\sigma^*(\omega)|^2}\sigma_r(\omega) \quad \text{and} \quad \rho_q(\omega) = -\frac{1}{|\sigma^*(\omega)|^2}\sigma_q(\omega) \tag{I.3}$$

If the complex resistivity is defined as :

$$\rho^*(\omega) = \rho_r(\omega) + i\rho_q(\omega) \tag{I.4}$$

It is demonstrated that the imaginary resistivity is therefore a negative parameter $\rho^q < 0$. Other sign convention can be used.

The resistivity can be expressed under its exponential form, with a CR norm $|\rho^*(\omega)|$ and a CR phase $\Phi_{cpx}(\omega)$[d]:

$$\rho^*(\omega) = |\rho^*(\omega)|e^{i\phi_{cpx}(\omega)} \quad \text{with} \quad \left\{ \begin{array}{l} |\rho^*(\omega)| = \sqrt{\rho_r^2(\omega) + \rho_q^2(\omega)} \\[2mm] \phi_{cpx}(\omega) = \arctan\left(\frac{\rho_q(\omega)}{\rho_r(\omega)}\right) \approx \frac{\rho_q(\omega)}{\rho_r(\omega)} \end{array} \right. \tag{I.5}$$

Notice again that the CR phase is negative, which is not the case for the complex conductivity phase.

I.3.2 Classic IP parameters

Before computing a CR spectrum using spectral induced polarization methods, several quantities were used to estimate and quantify IP response. These parameters were developed at the early stages of IP method and are mainly related to mineral exploration. Their origins come partially from instrumental limitations and from the particularity of time-domain IP measurement (Slater and Lesmes, 2002). In order to access these parameters, a current is applied to the ground and a geometric coefficient is used to determine the resistivity. The slow voltage decay curve (instead of an abrupt decrease) observed at the current turn-off and due to IP effect is used to estimate the *chargeability* introduced below. These measurements can be carried out for several charging times to obtain the parameter at several frequencies. The IP method is described in more detail in Chapter II concerning EM imaging.

Chargeability (M)

In order to quantify this relaxation phenomena, the chargeability M was introduced and commonly attributed to Seigel (1959). The chargeability of the medium is estimated by evaluating the ratio between the measured secondary voltage V_s after a short delay from the current turn-off and the voltage during the steady-state injection V_0 (equation (I.6)). Therefore, it can be a dimensionless quantity, but is commonly expressed in mV/V due to the obvious magnitude difference between the steady-state voltage and the residual voltage. A short delay between the current shut down and the secondary measured voltage has to be respected to avoid EM induction in the measurements (early-time effect).

$$M = \frac{V_s}{V_0} \tag{I.6}$$

Another way to determine the chargeability is to evaluate the area under the voltage decay curve between two time limits with equation (I.7). Generally, this quantity refers to the integral chargeability, but some ambiguities can exist as referred by Kemna (2000).

$$M_{int} = \frac{1}{\Delta t} \int_{t_1}^{t_2} \frac{V_s(t)}{V_0} dt \tag{I.7}$$

---

[d]The norm or amplitude of the CR $|\rho^*(\omega)|$ and its phase $\Phi_{cpx}(\omega)$ should not be confused with the amplitude and the phase of EM fields. CR norm and phase are properties of the medium, whereas EM fields amplitude and phase are geophysical observables (measurements)

Kemna (2000) points out that in a first approximation the chargeability M can be linearly related to the CR phase Φ_{cpx}.
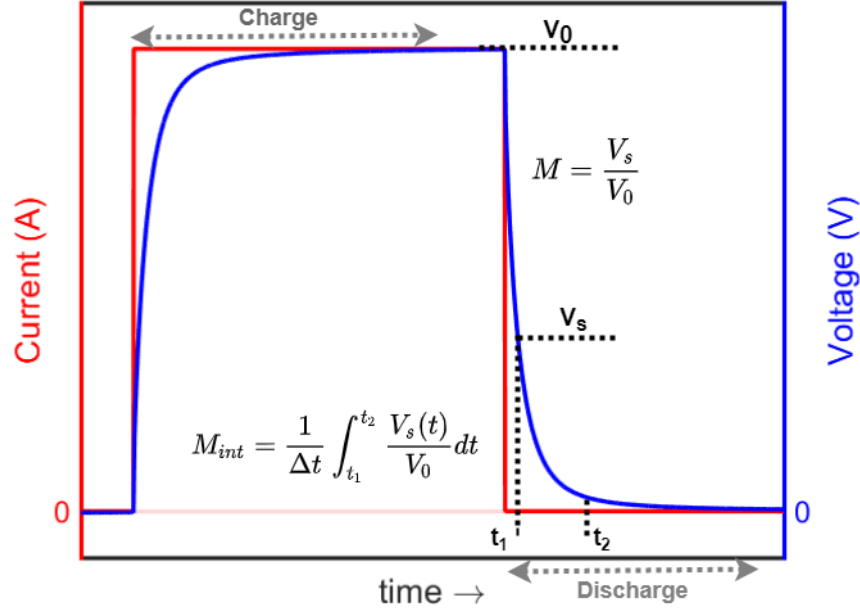

Figure I.5: *Time-domain induced polarization measurement illustration during the charge and the discharge phases due to induced polarization effect when a current is applied. Chargeability is calculated using the ratio between the voltage after the current cut-off (respecting a slight delay to avoid EM coupling at short time) and the voltage during injection when the steady state condition is reached V_s/V_0, or using the area under the relaxation curve between t_1 and t_2.*

Frequency effect (FE)

As IP phenomena are frequency-dependent, a common IP parameter is the frequency effect FE, which measures the variation of the resistivity norm between the early time and the late time, *i.e.* using ideally the zero frequency and the infinite frequency:

$$FE = \frac{|\rho_0| - |\rho_\infty|}{|\rho_\infty|} \tag{I.8}$$

The FE is commonly expressed in percentage and thus being referred as the percentage frequency effect ($PFE = 100FE$). In practice, two frequencies are used with a low and a high frequency replacing the ideal limits ρ_0 and ρ_∞.

Metal Factor (MF)

The last common IP parameter is the metal factor (MF), which got obviously its name from mineral applications due to its correlation with metallic content (Marshall

and Madden, 1959).

$$MF = s \left(\frac{|\rho_0| - |\rho_\infty|}{|\rho_0||\rho_\infty|} \right) = a \frac{FE}{|\rho_0|} \tag{I.9}$$

a is an arbitrary constant, taken to be equal to $2\pi \times 10^{-5}$ by Marshall and Madden (1959).

Normalized parameters

These parameters can be written under a normalized form. Indeed, Keller (1959) introduced the normalized chargeability) MN as the *specific capacity*. The time-domain chargeability (from equation (I.6)) is normalized by the real part of the resistivity (including the bulk and the surface resistivity of the rock).

$$MN = \frac{M}{\rho^r} \tag{I.10}$$

The Metal Factor as stated by Marshall and Madden (1959) is already a normalized parameter. These parameters enhance the relationships between structural properties, surface polarization processes and IP measurements especially in samples with high pore fluid conductivity (Lesmes and Frye, 2001; Slater and Lesmes, 2002).

I.4 Relaxation models: insight of theoretical versus empirical model

I.4.1 Insight on IP theoretical model

IP method seeks to determine the CR of the medium and to link its value and spectral characteristic to the properties of the medium and underlying geochemical processes. The CR is frequency-dependent and its spectral response is rich in information. To understand the link between CR and the properties of the medium (clay content, hydraulic permeability, grain/pore sizes, surface properties,...), a robust physical understanding of the IP phenomena described in section I.2 is required with theoretical models able to predict the CR variation with frequency. However, IP phenomena are very complex and so is the task to account for a physical-mathematical model. Reasons of these complexities are the numerous parameters (porosity, specific surface, CEC, excess of charge Q_v, partition coefficient f_v, temperature, pH, surface site densities,*etc.* (Leroy and Revil, 2009; Okay et al., 2014)) that intervene from the nano-scale to the macro-scale as well as that several polarization mechanisms can co-exist simultaneously with various magnitudes (Kemna et al., 2012; Revil and Florsch, 2010). Hypotheses on the polarization mechanisms that dominate the IP response have to be made and depend on the type of material. For example, the work on water-saturated pack of glass beads of Leroy et al. (2008) can be mentioned: they developed a model taking into account the Stern layer polarization and Maxwell-Wagner effect followed by the work of Leroy and Revil (2009) where they extended the application to clay particles. Related works following these developments for a better understanding of IP are presented by Revil (2012, 2013); Revil and Florsch (2010) among others.

No further consideration of such mechanistic models will be made in this work as their application to field scale are limited (concerning the resistivity imaging problem) due to the large number of parameters and unknowns of the investigated medium. Although they are essential to the phenomenological understanding of IP and for going further into quantitative interpretation, imaging problem requires however a simple relaxation model with a minimum number of parameters for CR description with frequency variation.

I.4.2   Empirical relaxation model

In order to explain the slow decay voltage after current cut-off related to IP phenomenon, *empirical* relaxation models are used. These models are based on analogue circuits, by approximating the geological medium response as a succession of electronic components (resistor, capacitor, Warburg impedance element, etc.) and thus link the observable to a frequency-dependent CR to explain the relaxation phenomenon. An exhaustive presentation and comparison of 12 of these models developed at one of the early stage of IP history (between 1959 and 1979) are presented in details by Dias (2000), where he proposed an actualisation of his former model (Dias, 1968, 1972). In the following, the more common empirical models are presented with a discussion about the important role of the relaxation time in IP prospection.

Cole-Cole model (Cole and Cole, 1941; Pelton et al., 1978)

In order to characterize a relaxation phenomena, the simplest model of CR and its frequency dependence can be derived from the Debye relaxation model (Debye, 1929) originally formulated for dielectric permittivity. Cole and Cole (1941) introduced later a supplementary exponent to the Debye formulation to explain a broader frequency range of the dispersion and a smaller maximal absorption observed on experimental dielectric spectra. Its equivalent for CR is the most used CR model by the IP community. The Cole-Cole (CC) model can be explained in its CR form (equation (I.11)). The popularization of the Cole-Cole model originates from the work of Pelton et al. (1978), where they demonstrated that the Cole-Cole model was able to fit a variety of CR spectra and showed that the associated Cole-Cole parameters were able to discriminate between certain type of mineralization.
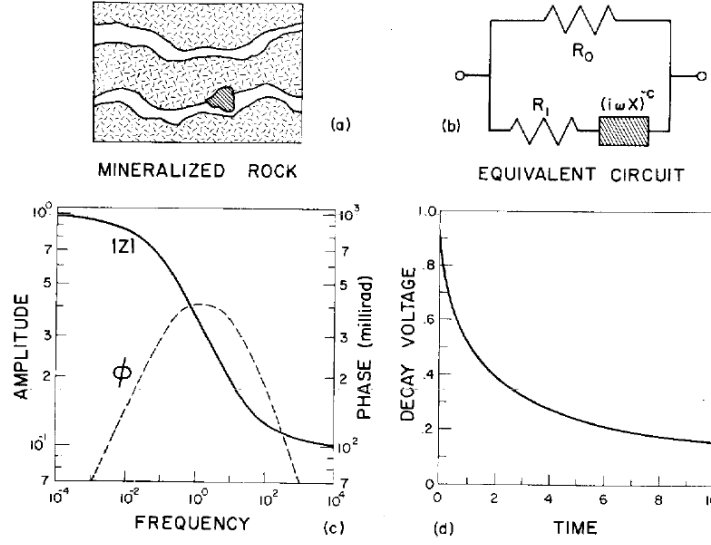
Figure I.6: *Original presentation of the Cole-Cole model equivalent circuit presented by Pelton et al. (1978). a) A small section of a mineralized rock which has both blocked and unblocked pore passages. b) An equivalent circuit for the mineralized rock. c) Typical frequency domain response for the equivalent circuit ($|Z|$ Impedance norm, Φ Impedance phase). d) Time-domain relaxation response corresponding to the frequency domain response plotted in (c)*

.

The equivalent circuit describing the CC model is presented in the original figure presented in Pelton et al. (1978) (Figure I.6). The circuit attempts to simulate a mineralized rock with both blocked and unblocked pore passages using a simplified circuit. It is composed of two parallel paths, with a resistor simulating the rock matrix resistance and a resistor representing the electrolyte resistance coupled to a complex impedance element $(i\omega X)^{-c}$ simulating the metallic-ionic interface. The CC model equation for its resistivity formulation is:

$$\rho^*(\omega) = \rho_0 * \left[1 - m \left(\frac{1}{1 - \frac{1}{1+(i\omega\tau)^c}} \right) \right] \tag{I.11}$$

CC model is described by four parameters ruling the shape of the CR spectrum:

❏ ρ_0 (or ρ_{dc}) defined by the resistivity at zero frequency. It corresponds to the low frequency asymptote of the CR spectrum and has no effect on the CR phase.

❏ m, the intrinsic chargeability (Seigel, 1959) that determines the step between the low and high frequency asymptotes and is therefore defined as :

$$m = \frac{\rho_0 - \rho_\infty}{\rho_0} \tag{I.12}$$

❏ τ, the characteristic time constant of the relaxation that determines the frequency position of the CR phase maxima (or CR norm inflexion point) in the spectrum. In

time domain, it determines the duration of the relaxation of the decay voltage. This parameter is linked to the characteristic length of the grain or pores of the medium. The relaxation time is commonly proportional to the square of the characteristic length.

❏ c, the frequency dependence exponent, that impacts the frequency range of the dispersion of the CR spectrum. The higher the parameter c, the shorter is the frequency range from which $\rho^*(\omega)$ switches from ρ_0 to ρ_∞. c values are generally between 0.2 to 0.5. c is linked to the grain/pore size distribution. For a broad distribution of grain/pore size, thus a broad distribution of relaxation times, the phase peak tends to vanish (Chelidze and Gueguen, 1999; Hallof and Klein, 1983).

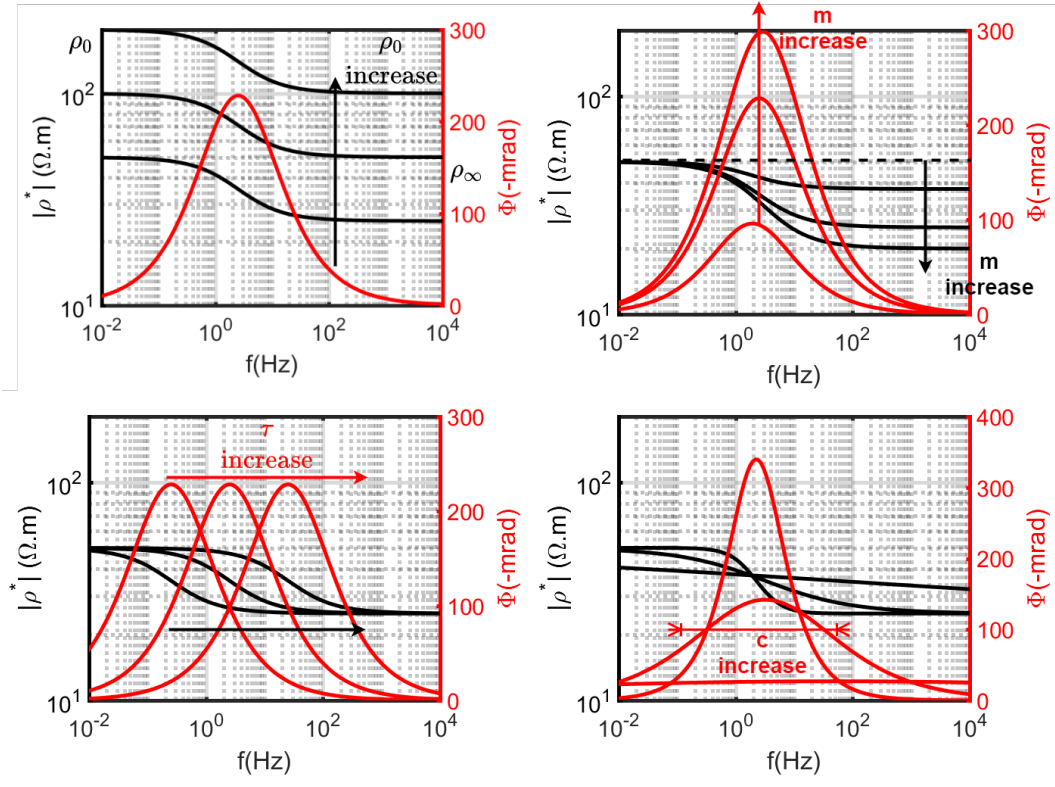Effects of each parameters on the CR spectrum are resumed in figure I.7

Figure I.7: *Influence of each CC parameters on the norm and phase of the CR spectrum*

.

The frequency of the phase peak is given by $f_{peak} = \frac{1}{2\pi\tau}\frac{1}{(1-m)}^{\frac{1}{2c}}$. Some differences exist with the CC parameters using the complex conductivity formulation and are discussed in Tarasov and Titov (2013). Fiandaca et al. (2018) proposed in a recent work a re-parametrization of the CC model to decrease correlation existing between CC parameters in imaging problem.

A double Cole-Cole model can be used as an EM removal method as presented by Pelton et al. (1978). Indeed, EM coupling can be modelled at first order using a second

Cole-Cole model with shorter relaxation time and higher value of exponent c (close to 1), than the *first* Cole-Cole model associated to IP mechanism.

Constant-Phase Angle (CPA) model

In some cases (*e.g.* Börner (1991); Börner et al. (1993); Vinegar and Waxman (1984); Weller et al. (1996)), IP responses do not present a phase peak. A constant phase is observed, the real and imaginary parts of the CR present a frequency dependence following a similar power law (similarly to dielectric permittivity as proposed by Jonscher (1977)). This behaviour is described by the Constant Phase Angle (CPA) model presented in figure I.8 and respecting equation:

$$\rho^*(\omega) = \rho_{f_0} \left(\frac{i\omega}{\omega_{f_0}} \right)^{-a} \tag{I.13}$$

with ρ_{f_0} the resistivity at a given reference frequency ω_{f_0}. b characterizes the frequency dependence and takes values in the range of $0 < a < 0.05$ (Borner and Schon, 1991; Kemna, 2000).
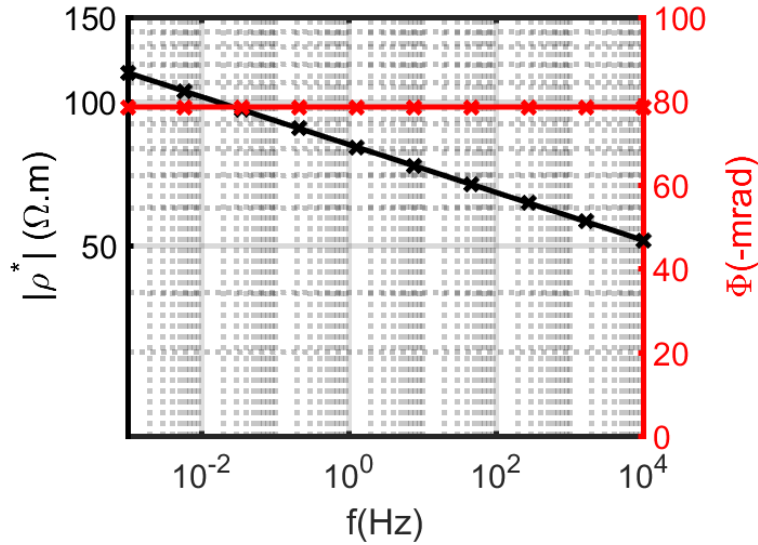
Figure I.8: *Example of CR spectrum for the CPA model using $\rho_{f_0} = 100\,\Omega.m$, $a = 0.05$, and $f_0 = 0.1\,Hz$.*

The CPA model presents a low decrease with frequency of the CR norm.

Generalized Cole-Cole model

The previous models are the most commonly cited in the IP literature (Weller et al., 1996). A last model is presented here for its practicality. Indeed, measured dispersion spectra can be asymmetrical as noted and modeled by Davidson and Cole (1951). A

similar model was thus derived by Pelton (1983) and a generalized Cole-Cole model[b] can be expressed as:

$$\rho^*(\omega) = \rho_0 * \left[1 - m \left(\frac{1}{1 - \frac{1}{1+(i\omega\tau)^c}} \right)^a \right] \tag{I.14}$$

Interest of this formulation is that under this form, several models can be obtained:

❏ if $m = 1$ and $a = 1$ and $c = 1$, the Debye relaxation model is obtained.

❏ $a = 1$ corresponds to the simple Cole-Cole model.

❏ $c = 1$ corresponds to the Davidson-Cole model (Davidson and Cole, 1951).

❏ $c = 1$ and $m = 1$ the CPA model is obtained. Equation (I.13) is not totally equivalent to this form, some differences exist at low frequencies if $f < \tau$, as presented in figure I.9.
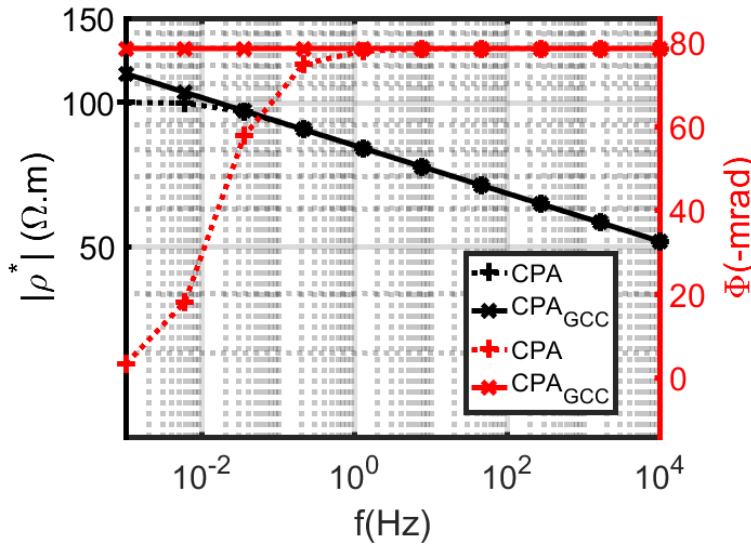

Figure I.9: *Example of CR spectrum for the CPA model using $\rho_{f_0} = \rho_0 = 100\,\Omega.m$, $a = 0.05$, and $f_0 = 0.1\,Hz$ and $\tau = 1/f_0$*
.

Relation to the medium

Induced polarization is a valuable tool to access critical properties of the medium linked to the polarization mechanisms described previously. These mechanisms mainly occur at the interface between the grain/pore and an electrolyte. Consequently, IP effects are closely linked to textural properties. Some notable relationships with medium properties with high interest for field-scale investigation can be related. First of all, it can be highlighted that the presence of measurable IP in a dataset at the field scale is

---

[b]Kruschwitz et al. (2010) uses this model for an analysis of textural properties of porous media.

already a valuable information, contrary to the classic resistivity imaging that needs at least a contrast for further interpretation in most cases. On the other hand, the relaxation time is of special interest as a clear link exists with the mean size of the grains or of the pore throats in a medium. Its exact relation is still in discussion and depends on the medium and on the means of determination of the characteristic time. However, generally the relationships describe a proportional link between the time constant and the ratio of the square of the grain or pore throat characteristic size d and a diffusion coefficient D. (Binley et al., 2005; Börner, 1991; Vinegar and Waxman, 1984).

$$\tau \propto d^2 \qquad \tau \propto \frac{d^2}{D} \tag{I.15}$$

(Börner et al., 1996; Vanhala, 1997) demonstrated using the CPA model a relationship between CR phase and granulometry of several sandstone samples as shown in figure I.10.
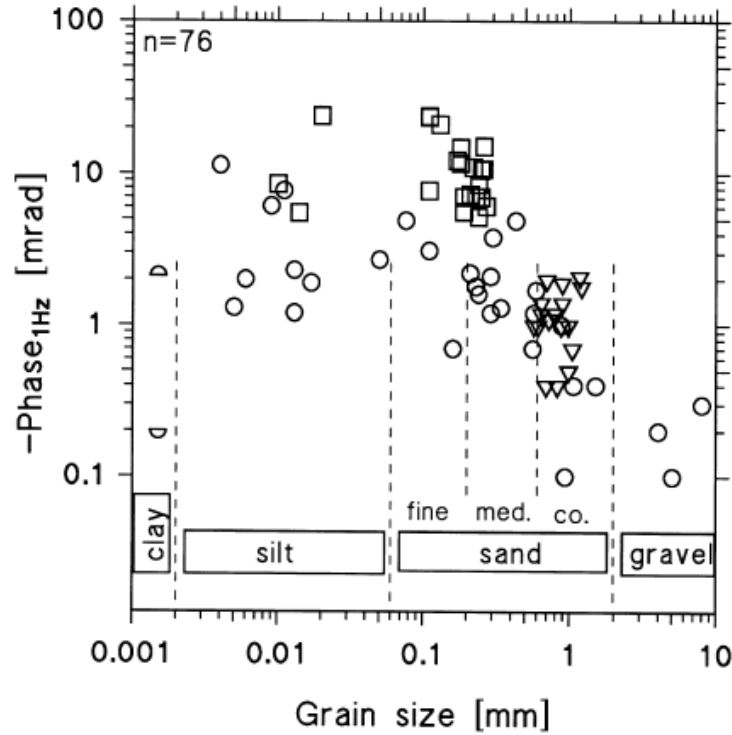
Figure I.10: *Relationship between the measured phase at 1 Hz and the grain size for various samples, from Vanhala (1997)*
.

In the case of metallic particles, the link between the chargeability and the volume fraction within the host was presented by (Pelton et al., 1978). In figure I.11, they presented the link with the time constant and the particle size with m and τ. Furthermore, as mentioned previously, with Hallof and Klein (1983) they pointed out the interest of IP method for metallic particles discrimination, as in the example of discrimination between graphite and sulphide that do not have the same economic interest.
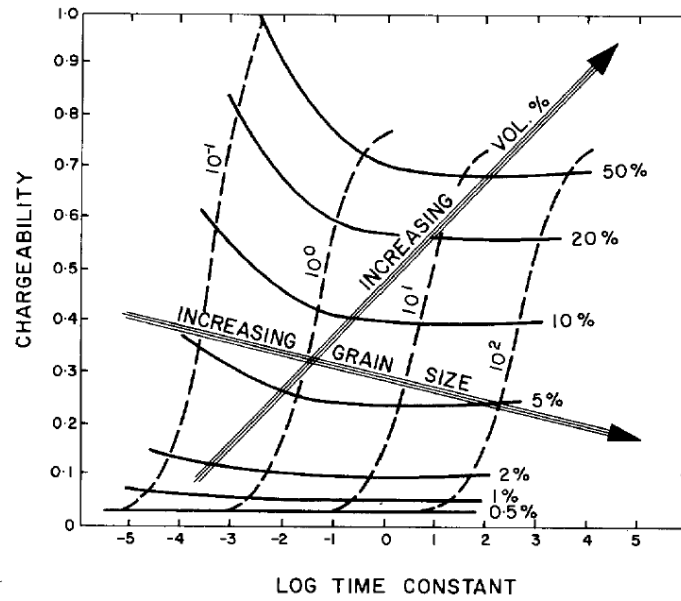
Figure I.11: *Extrapolated trends that links the volume fraction of disseminated metallic particle (sulfide) and their particle size, with the chargeability and the time constant variation from (Pelton et al., 1978).*

Link to the specific surface area was made by (Börner et al., 1996) (Figure I.12). They established thus the link between IP parameters and the hydraulic permeability of a medium and suggested the use of Kozeny-Carman law. IP method applied to the determination of hydraulic permeability is one of the main application of the method in environmental studies. Several applications of IP method followed these results, as the works of (Hördt et al., 2007; Kemna et al., 2004) and more recently (Maurya et al., 2018b) for a recent application that uses a different approach based on (Weller et al., 2015).

Figure I.12: *Link between the specific surface area and the imaginary conductivity for various samples and laboratory measurements* Kruschwitz et al. (2010, *from).*
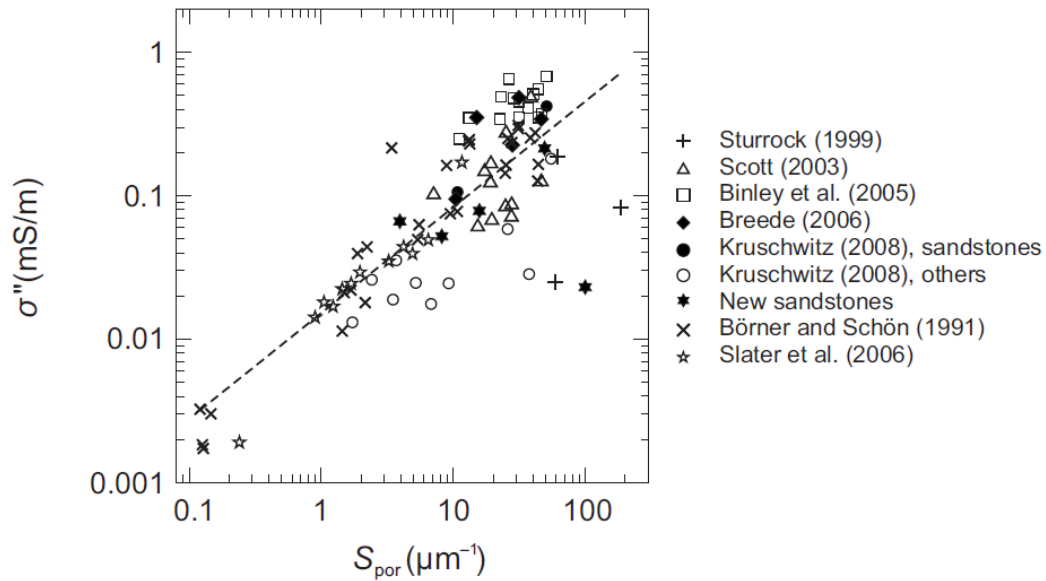
Conclusion

In this first chapter, the highlights of the historyl of induced polarization method was presented. The IP method arises from electrical prospecting with some strong instrumental limitations in its early years. However, the presence of IP mechanisms and the observation of relaxation phenomena in the ground due to the presence of ore bodies were early noticed and subsequent developments were driven by mining applications and associated economic prospectives. It was only several decades later that IP method made a considerable breakthrough, with the development of mathematical and physical models, instrumentation improvements and among other, interest for spectral induced polarization method which allows the access to textural properties of the medium. These links are related to the IP mechanisms intervening at low frequencies. They imply reversible charge migrations due to an external current in a medium, that occur at the interface between the grain/pore and an electrolyte. The description of these phenomena with physics-based models is very complex even concerning laboratory study in controlled environment. This is why field-scale investigations are mainly based on empirical models, based on analogue circuit for medium modelling. Among these models, the CPA and the CC are the most popular and present some critical relations with medium properties that highlight the large interest for the method.

In this chapter, I focused on the relations between IP parameters and the medium, nevertheless the description of IP measurements in the field was set aside with the theoretical background of the method. Indeed, in the next chapter, the resistivity imaging method will be presented in detail with the electrical methods and its extension to time-domain and frequency-domain IP method. Afterwards, electromagnetic theory and methods are

presented introducing EM induction in the imaging process.

CHAPTER II

Resistivity imaging

II.1   Electrical resistivity

A fundamental property of interest in this work considering direct current (DC, zero frequency) to 100 kHz signals, is the electrical resistivity ρ $[\Omega.m]$, or equivalently its reciprocal, the conductivity σ $[S.m^{-1}]$ of the ground. The resistivity corresponds to the electrical resistance R to the current flowing through a medium of a unit area A per unit of length l.

$$\rho = R\frac{A}{l} \tag{II.1}$$

Our interest in resistivity lies in its wide range depending on the material (Figure II.1). Resistivity is sensitive to many physico-chemical properties, especially its fluid content, its salinity and clay content. Indeed, in many resistivity imaging applications, geophysical techniques will be sensitive to the porosity of the host, its fluid saturation and salinity rather than the rock matrix which is in most cases an insulator.
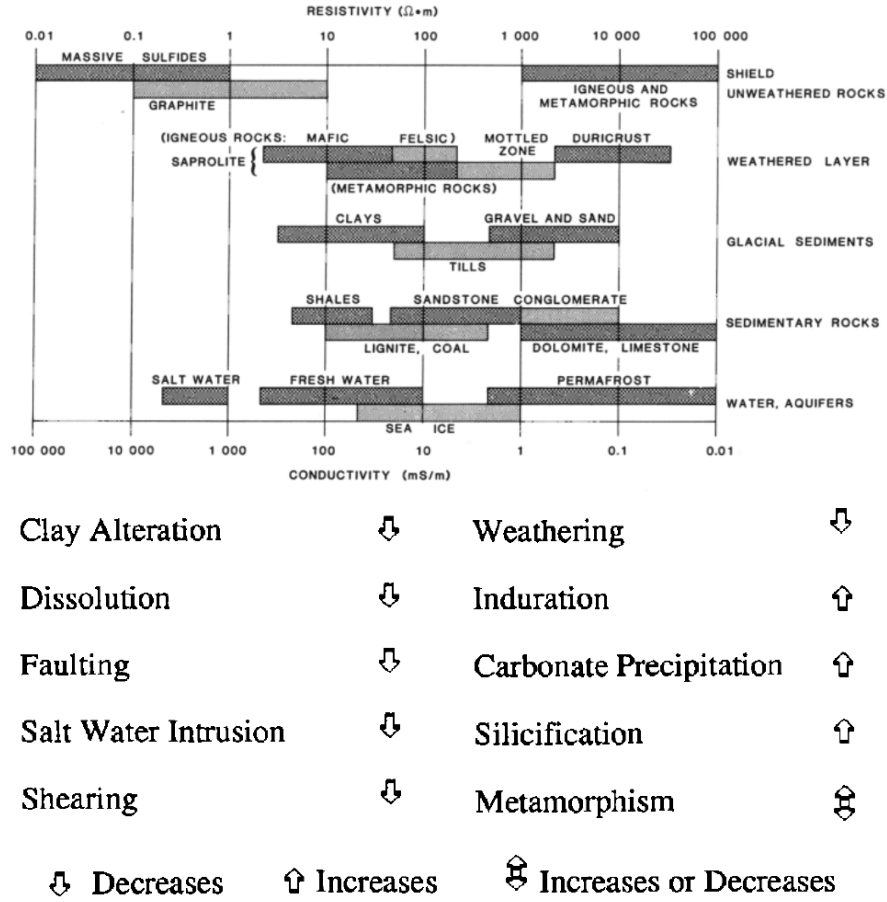
Figure II.1: *Resistivity and conductivity range of typical earth material (from Palacky (1988)) and insight of the effect of various geological processes on resistivity (Ward, 1988)*

Several empirical relationships link the porosity of a medium to its resistivity. Archie's Law (Archie, 1942) establishes a relationship between porosity Φ and resistivity according to the fluid resistivity ρ_{fluid}, its saturation S_w and an exponent m depending of the cementation of the pore matrix. Archie's law does not consider the rock resistivity, and is not valid for a conductive matrix, or in presence of conductive clay fillings. In those cases, the Waxman-Smits relationship (Waxman and Smits, 1968) is preferred linking the bulk conductivity of the medium to fluid conductivity scaled by a formation factor $F = \Phi^{-m}$ and surface conductivity occurring at pore interfaces.

$$\rho = \rho_{fluid}S_wF = \rho_{fluid}S_w\Phi^{-m} \hspace{3cm} \textbf{Archie's Law} \hspace{1cm} (II.2)$$

$$\sigma = \frac{1}{F}\sigma_{fluid} + \sigma_s \hspace{3cm} \textbf{Waxman-Smith relationship} \hspace{1cm} (II.3)$$

Why not ϵ_r and μ ?

On the contrary, when considering other fundamental EM properties of the medium, magnetic permeability μ has a narrower range of variation and is considered in most

application as the magnetic permeability in the free space. Figure II.2 presents the range of magnetic susceptibility χ_m $(\chi_m = 1 + \mu_r)$ of typical Earth materials and reflects that this parameter is mainly sensitive to the fraction of iron oxides.
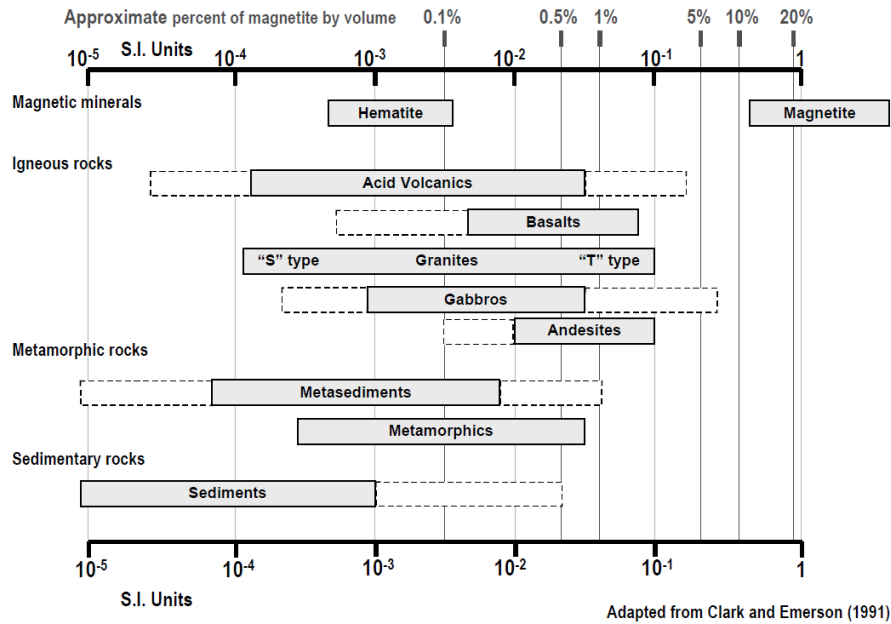
Figure II.2: *Range of magnetic susceptibility χ_m $(\chi_m = 1 + \mu_r)$ for typical Earth media (from Lelièvre (2003) adapted from Clark and Emerson (1991))*

Dielectric permittivity will be taken as its value in free space for applications in the scope of this manuscript as explained in following section. Its range has also a weaker dynamic compared to resistivity. One of its noteworthy characteristics, is its high value in water, which is greatly impacted by water state, *i.e.* its relative value varies from 80 in its liquid phase to approximately 3 in its solid phase (Figure II.3). Water dielectric permittivity studies have large application in ground penetrating radar techniques to identify water content in the ground and monitoring its solid/liquid state in glacier or permafrost applications.

Figure II.3: *Examples of relative dielectric permittivity ϵ_r ($\epsilon = \epsilon_r\epsilon_0$) values and range for typical Earth medium (data from Baker et al. (2007)) for high frequency EM measurement ($\leq 1\,Mhz$)*

II.2   Electrical prospecting
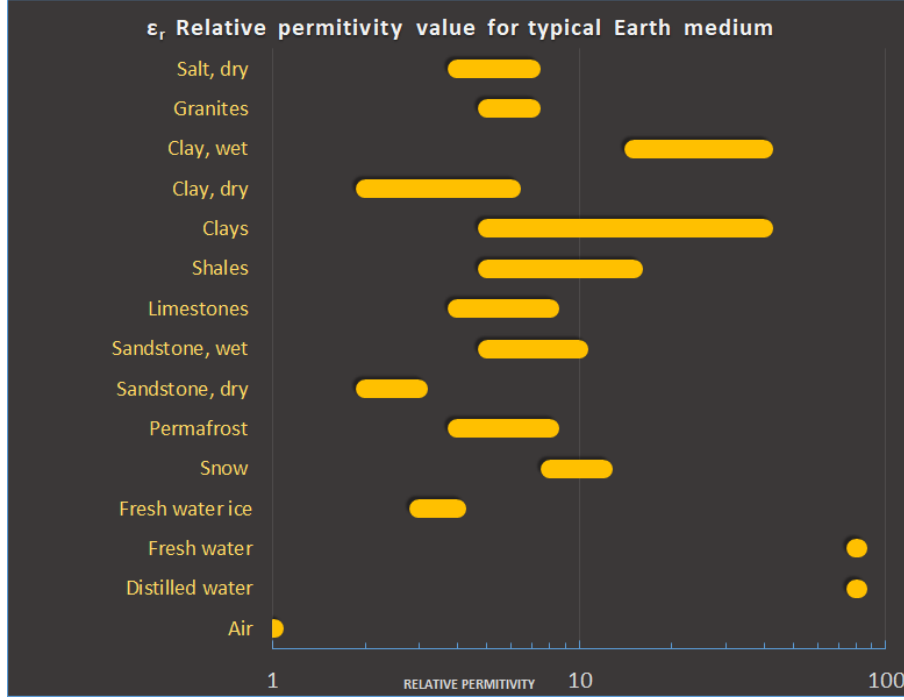
II.2.1   Electrical resistivity method

The electrical prospecting method is generally attributed to the fundamental early XXth century work of Conrad Schlumberger with the help of his brother, on potential mapping method. Started in 1912 and interrupted by the *Great War*, before the publication of his work in 1920 (Schlumberger, 1920), he highlighted the main role of the resistivity of the ground when measuring potential using a continuous current. He pointed out the misconception of the ground resistivity made in some previous work mapping the resistance of the ground, which is biased as the resistance measurement is mainly dependent to the dipole sizes and their direct vicinity instead of the studied area between the measurement electrodes. However, the method was developed and adapted at a fast pace during the 20's to the 30's and has been used ever since. Besides the early Schlumberger brothers developments, a fundamental study to mention is the work of Wenner, who started to work on the measurement of the *effective* resistivity, called later *apparent* resistivity, of the earth using a quadrupole measurement array. The four-electrode array method will give place to many configurations, the most famous ones taking the name of their pioneering inventor as the Wenner, or Schlumberger array.

Ohm's law gives us :

$$V = RI \tag{II.4}$$

The current density J in the radial direction is uniformly distributed in an homo-

geneous half-space and can be expressed at a position from a point source at a radial distance r as :

$$J(r) = \frac{I}{2\pi r^2} \tag{II.5}$$

We obtain the expression for the potential at a point by integrating equation (II.4) considering $\frac{V}{l} = \rho\frac{I}{A} \equiv -\nabla V = \rho j$:

$$V(r) = \frac{\rho I}{2\pi r} \tag{II.6}$$

In practice, to inject a current into the ground, a pair of electrodes must be considered. The potential V^{AB} at a given point P in the ground can be rewritten for the injected current between the electrodes A $(+I)$ and B $(-I)$ as :

$$V^{AB}(P) = V_A + V_B$$
$$V^{AB}(P) = \frac{\rho I}{2\pi}\left(\frac{1}{AP} - \frac{1}{BP}\right) \tag{II.7}$$

Considering now, like its founder Wenner, a four-electrodes array with AB the *current electrodes* where the current is injected, and MN the *potential electrodes* in-between which the potential difference is measured. We can determine the potential difference V^{AB}_{MN} measured between MN due to the current injection between AB as :

$$\Delta V^{AB}_{MN} = V^{AB}(M) - V^{AB}(N) = \frac{\rho I}{2\pi}\left(\frac{1}{AM} - \frac{1}{BM} - \frac{1}{AN} + \frac{1}{BN}\right)$$
$$= \frac{\rho I}{2\pi}K \tag{II.8}$$

In conclusion, we can note that using a quadrupole configuration, we obtain a "resistivity" of the ground using a very simple relationship, using only the measured potential difference between electrodes M and N due to a known injected current between A and B and a geometric factor K, which depends uniquely on the configuration array. Be aware that the obtained **measured resistivity is not the true resistivity** in a heterogeneous medium, but what is named an **apparent resistivity**, which is the resistivity for an equivalent half-space integrated in a volume according to the array geometry. Indeed, the integrated volume highly depends on the array configuration, which implies different sensitivities to geological structure (Figures II.4,II.5).

We can rewrite equation (II.8) according to the apparent resistivity ρ_{app} with respect to the geometric factor as :

$$\rho_{app} = \left(\frac{2\pi}{\frac{1}{AM} - \frac{1}{BM} - \frac{1}{AN} + \frac{1}{BN}}\right)\frac{\Delta V_{MN}}{I} \tag{II.9}$$

A and B current electrodes, M and N potential electrodes
A: spacing between electrodes used in a particular measurement
n: spacing factor (integer values 1-6)
x: distance to "infinite electrodes" in pole-pole array

Figure II.4: *Examples of common four-electrode array configurations and their associate geometric factor (from Samouëlian et al. (2005))*

	Wenner	Wenner–Schlumberger	Dipole–dipole	Pole–pole	Pole–dipole
Sensitivity of the array horizontal structures	++++	++	+	++	++
Sensitivity of the array vertical structures	+	++	++++	++	+
Depth of investigation	+	++	+++	++++	+++
Horizontal data coverage	+	++	+++	++++	+++
Signal Strength	++++	+++	+	++++	++

The labels are classified form (+) to (++++), equivalent at poor sensitivity to high sensitivity for the different array configurations.

Figure II.5: *Characteristics of different 2D array configurations types (from Samouëlian et al. (2005))*
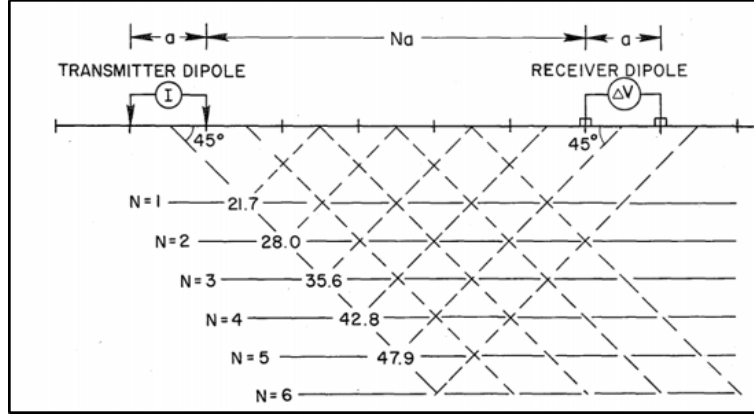
Apparent resistivity pseudo-section

Figure II.6: *Sketch of a Dipole-Dipole array used for Electrical Resistivity Tomography imaging (from Beyer (1977))*

A common application of four-electrode arrays for resistivity imaging is the measurement along a 2D profile using several offsets and electrode combinations. Offset controls the depth of investigation. A direct way to represent the results is an apparent resistivity pseudo-section. Considering a Dipole-Dipole array, ρ_{app} for several combinations of quadrupole is evaluated and reported on a 2D graph at the middle point for a given "pseudo-depth" according to the spacing N (Figure II.6). Rules of thumb allow the estimation of the depth of the measurements but they are approximative. To obtain the depth of investigation and the true resistivity of the medium from apparent resistivity pseudo-sections, a proper inverse problem has to be solved. In order to inverse apparent resistivity, the forward problem of the electrical potential in the medium has first to be solved.

The governing equations of the electrical resistivity method are derived from Maxwell's equations (presented in next section) with a static approximation. As a direct current is used in electrical prospecting, all derivatives with respect to time vanish, simplifying largely the problem. DC method governing equations are:

$$\nabla \cdot (\sigma \nabla V) = -\nabla \cdot J = -I\delta(r - r_s) \tag{II.10}$$

$$\frac{\partial V}{\partial n} = 0 \quad \text{for n normal to free surface (air)} \tag{II.11}$$

$$V = 0 \quad \text{at the boudaries of the domain} \tag{II.12}$$

Equation (II.10) is *Poisson's equation* for a source at the position $r_s(x_s, y_s, z_s)$, with x_s, y_s and z_s the Cartesian spatial coordinates of the source, whereas equations (II.11) and (II.12) are boundary conditions at the air-ground interface and at the boundaries of the modelling domain.

II.2.2 Induced polarization method

Induced polarization effect was first mentioned by Conrad Schlumberger in his pioneering work of 1920, when he noted that the potential difference did not drop instantaneously

after the current cut-off over an ore body. Indeed, induced polarization effect are defined by a late-time transient response that can not be attributed to electromagnetic induction that occurs at shorter time and dissipates quickly. The observed relaxation is due to low-frequency polarization mechanisms presented in Chapter I and intervening at the pore/fluid interfaces. The chargeability of the ground can be studied in time or in frequency-domain. Time and frequency IP chargeability quantities are not strictly equivalent, but can be studied simultaneously. Some authors claim that TDIP and SIP parameters can be qualitatively and quantitatively equivalent (Maurya et al., 2018a). In the spectral domain, capacitive response of the ground induces a phase lag on the voltage measurement (The impedance of the system $Z(\omega) = V(\omega)/I(\omega)$ is complex with an in-phase part and a quadrature phase part) in comparison to the injected current.

Time-domain induced polarization (TDIP)
DC method described in previous section, uses in practice a low frequency alternating current (AC) to measure the in-phase potential difference between MN electrodes and deduce ρ_{app} (real). In TDIP method, a 50 % duty cycle square wave is commonly used in order to study the transient signal when the current is cut-off. In practice, the relaxation is commonly studied at the current step-off during the discharge phase, nevertheless, polarization mechanisms intervene also during the current step-on with an observed charging phase and can be used to estimate IP parameters as well (Figure II.7).
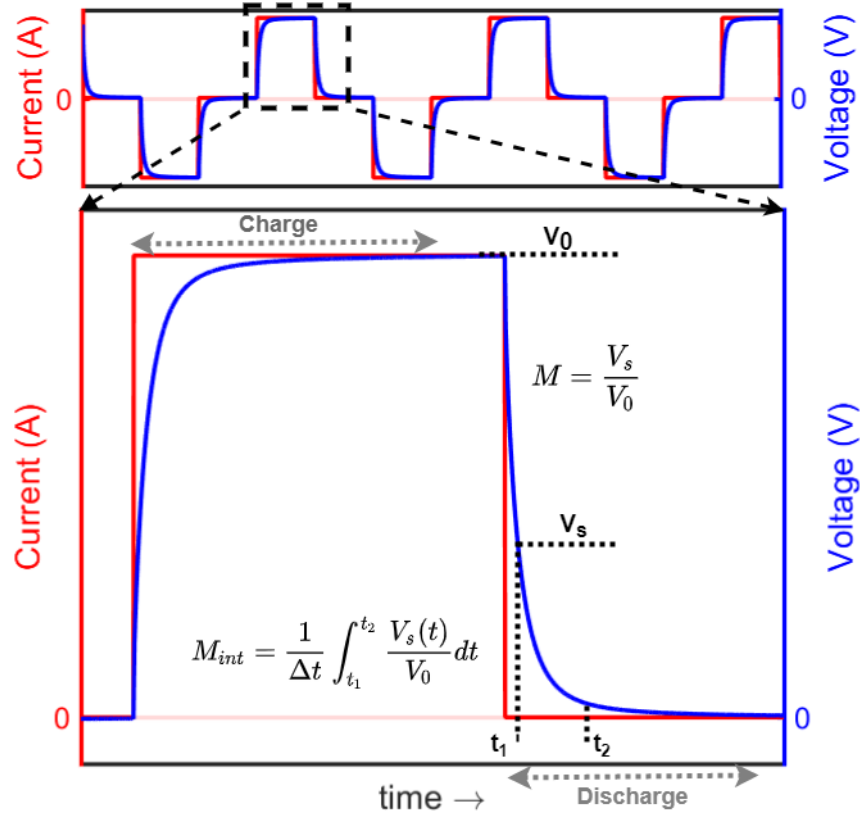
Figure II.7: *Time-domain induced polarization measurement illustration using a 50% duty-cycle square signal injection with a zoom on a positive half-period to highlight the charge and discharge phases due to induced polarization effect. Chargeability is calculated using the ratio between the voltage after the current shut-off (respecting a slight delay to avoid EM coupling at short time) and the voltage during injection when the steady state condition is reached V_s/V_0, or using the area under the relaxation curve between the two time boundaries t_1 and t_2.*

The chargeability of the medium is estimated, considering the discharge phase, by evaluating the ratio or the area under the curve, between the measured voltage V_s after a delay from the current shut off and the voltage at the top of the square signal at the steady state V_0. A short delay between the current shut off and the secondary measured voltage has to be respected to avoid EM induction in the TD measurements. As a reminder, time-domain chargeability is noted M and some ambiguity can exist as it can refer to the simple ratio or its integral form. As induced polarization effects are frequency-dependent, measurements are made for various square periods **to deduce an apparent resistivity and an apparent chargeability at several frequencies** , at least, at a low and a high* frequency (* the term high-frequency has to be taken with caution here, the DC approximation have to be respected, limiting fastly the highest frequency due to apparition of EM induction; 100 Hz is sometimes cited as a higher limit but it highly depends on the acquisition geometry, the conductivity of the medium and wire coupling effects). In time domain, if EM induction is significant a sign reversal can be observed at

early times after the current shut-off. EM information is usually discarded in IP study and recently, Kang and Oldenburg (2017) advocate and demonstrate the usefulness of the information in a decoupling workflow using DC and EM information for a synthetic 3D imaging of resistivity and pseudo-chargeability.

From the apparent resistivity at low and high frequency, the FE, PFE or the MF can be derived according to equations presented in chapter I. A rough approximation of the apparent intrinsic chargeability can also be estimated but all of these parameters will depend on the CR spectrum shape and measurement capability to obtain the longer periods and highest frequencies free of EM induction, as it requires to reach the low and high frequency asymptote of the CR spectrum. In other words, it needs the resistivity for a square signal infinitely long (limited by survey and instrumentation) and resistivity at very short periods where static approximation does not hold anymore (limited by EM coupling).

Spectral or frequency-domain induced polarization (SIP or FDIP)

Spectral induced polarization is an equivalent technique to TDIP using frequency domain to estimate CR parameters. SIP is very common in laboratory at the sample scale and allows to investigate a large frequency range from 1 mHz to 10 kHz. While the estimate is carried out in the frequency domain, the measurement still occurs in the time domain (II.8a). Indeed, similarly to TDIP a current is injected into the ground with a periodic signal. Analyzing measurements in the frequency domain, there is more freedom on the choice of the signal waveform. The same measurement can be used for TDIP and SIP measurements, as long as the full waveforms of the current and the voltage are recorded. The spectral content of the injected waveform allows to build up a signal that concentrates the energy on specific frequency, allowing hence several frequency measurements using the same time series. For example, classic square-wave divides its energy (decreasing) on each odd harmonic $f_h(k) = (2k + 1)f_0$ Hz with $k = 0, 1, 2, ..., n$ (Considering the fundamental f_0 as the first harmonic). High-frequency measurements from a low-frequency waveform can then be obtained, as long as the signal is strong enough, the source stable enough and the record long enough (spectral resolution $=$ $1/$[recorded time]). The signal can differs from a 50% duty cycle square wave to estimate the chargeability on the decay or the charging curves. Indeed, the phase delay introduced by polarization will be investigated. The impedance transfer function $Z(\omega) = \frac{V(\omega)}{I(\omega)}$ is calculated (Figure II.8) and the phase delay will be characterised by the argument between the quadrature (imaginary) and in-phase (real) parts of the spectrum. The resistivity norm of the medium is deduced from the norm of the impedance. Again, caution has to be taken to avoid interpretation in the EM induction domain as presented in figure II.8, where divergence of the measured and true CR occurs at the highest frequencies. This method is essentially used for laboratory SIP measurements on small-scale rock samples where the geometric coefficient is therefore constant and EM effects limited.
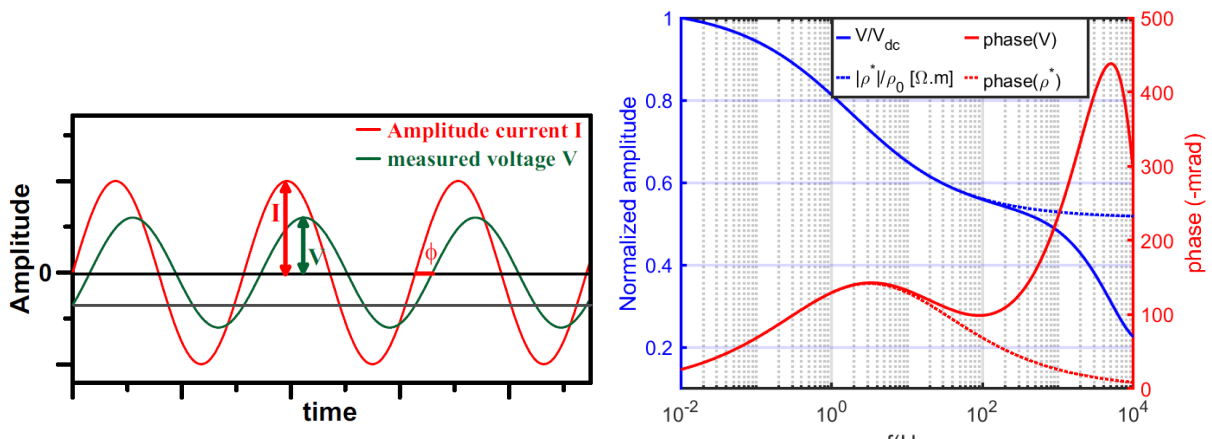
Figure II.8: *Spectral-domain induced polarization measurement using a low-frequency sinusoidal signal injection in the time domain with the phase delay induced by IP effects on the voltage measurement (left, from Ghorbani (2007)); Voltage spectrum example for a dipole-dipole array configuration with an offset of 100 m over a homogeneous half-space ($\rho_0 = 100\Omega.m, m = 0.5, \tau = 0.1s, c = 0.5$) compared to the true Cole-Cole model introduced (right). With increasing frequency, EM induction arises in the medium and the measured resistivity and phase diverge from the true values.*

Obtaining CR norm and phase allow then to estimate the intrinsic chargeability of the medium. CR spectrum can be fitted using specific model (overviewed in chapter I) to determine more IP characteristics of the medium, as the four CC parameters, which allow the evaluation of the properties of the medium. To recall, all parameters obtained in this way are apparent parameters corresponding to equivalent half-space parameters, integrated on the investigated volume. A proper inversion should be carried out to access true parameter distribution. A considerable advantage of the SIP method is that measured CR is totally independent of the time delay after current shut-off, or to a time window integration.

II.3 Electromagnetic method

II.3.1 EM Theory

A brief introduction concerning electromagnetic theory is carried out at first to highlight the base of the Physics and fundamental concepts concerning geophysical electromagnetic methods. The following developments are mainly based on the exhaustive book *Electromagnetic Methods in Applied Geophysics* edited by Nabighian (1988).

Maxwell equations

Macroscopic electromagnetic phenomena are respecting *Maxwell's equations*. Those relations can be written under their differential forms in a medium free of electromagnetic source :

Gauss flux theorem:

$$\nabla \cdot \vec{d} = \rho_{\text{free}} \tag{II.13}$$

Gauss's law for magnetism:

$$\nabla \cdot \vec{b} = 0 \tag{II.14}$$

Faraday's law of induction:

$$\nabla \times \vec{e} = -\frac{\partial \vec{b}}{\partial t} \tag{II.15}$$

Ampère's law:

$$\nabla \times \vec{h} = \vec{j} + \frac{\partial \vec{d}}{\partial t} \tag{II.16}$$

$\vec{d}\,[C/m^2]$ represents the dielectric displacement charges, $\vec{e}\,[V/m]$ is the electric field, $\vec{b}$ $[T]$ the magnetic induction and $\vec{h}\,[T]$ the magnetic field. $\vec{j}\,[A]$ is the current density due to conduction, whereas $\frac{\partial \vec{d}}{\partial t}$ represents the displacement current $\vec{J_D}$. Lower case notation represents the quantities in the time domain, whereas upper-case notation stands for the frequency domain.

Constitutive relations

Relations between current, charge displacement, electromagnetic fields and material properties are given by the constitutive relations for the electrical conductivity σ, the dielectric permittivity and the magnetic susceptibility μ. Each of these parameters are tensors defined for each position of the medium and related to many physical properties as the temperature and the pressure. They are complex parameters that can be frequency-dependent. In this work, anisotropy of the medium or variation in time of these parameters will not be considered.

$$\vec{j} = \sigma \vec{e} \tag{II.17}$$

$$\vec{d} = \epsilon \vec{e} \tag{II.18}$$

$$\vec{b} = \mu \vec{h} \tag{II.19}$$

Wave equation

Wave equation can be deduced from previous equation by applying a curl to the Maxwell-Faraday's and Maxwell-Ampere's law (Equations (II.15) and (II.16)) and using constitutive relations to obtain:

$$\nabla \times \nabla \times \vec{e} + \mu\epsilon \frac{\partial^2 \vec{e}}{\partial t^2} + \mu\sigma \frac{\partial \vec{e}}{\partial t} = 0 \tag{II.20}$$

$$\nabla \times \nabla \times \vec{h} + \mu\epsilon \frac{\partial^2 \vec{h}}{\partial t^2} + \mu\sigma \frac{\partial \vec{h}}{\partial t} = 0 \tag{II.21}$$

Using the identity $\nabla \times \nabla \times x = \nabla\nabla \cdot x - \nabla^2 x$ and considering a homogeneous medium with no conductivity variation, we obtain Helmholtz's equations, the wave equation of electromagnetic fields in the frequency domain ($\frac{\partial}{\partial t} = i\omega$):

$$\Delta \vec{E} + (\mu\epsilon\omega^2 - i\omega\mu\sigma)\vec{E} = 0 \tag{II.22}$$

$$\Delta \vec{H} + (\mu\epsilon\omega^2 - i\omega\mu\sigma)\vec{H} = 0 \tag{II.23}$$

Defining the wave number k as:

$$k^2 = \mu\epsilon\omega^2 - i\omega\mu\sigma \tag{II.24}$$

we obtain:

$$\Delta \vec{E} + k^2\vec{E} = 0 \tag{II.25}$$

$$\Delta \vec{H} + k^2\vec{H} = 0 \tag{II.26}$$

We know the solution for these second order differential equations, expressed here for an electric field sinusoidal wave propagating vertically downward (solution for the magnetic field can be deduced similarly):

$$\vec{e} = \vec{e_0}^+ e^{i(kz-\omega t)} \tag{II.27}$$

We can reformulate under the form considering $k = \alpha - i\beta$:

$$\vec{e} = \vec{e_0}^+ e^{-i\alpha z} e^{i\omega t} e^{-\beta z} \tag{II.28}$$

It highlights that:

❏ $e^{-i\alpha z}$: the wave oscillates with respect to the propagation direction z

❏ $e^{i\omega t}$: the wave oscillates with time

❏ $e^{-\beta z}$: the wave suffers from an attenuation with propagation in z direction

Two main approximations can be distinguished considering the wave number relationship:

➠ Propagative case ($\mu\epsilon\omega^2 >> \omega\mu\sigma$):

$$k \approx \omega\sqrt{\mu\epsilon} \tag{II.29}$$

In the propagative case ($f \gtrsim 10MHz$), or the dielectric limit, the electromagnetic waves propagate as seismic waves. They are not sensitive to the conductivity but are controlled by permittivity. The wave number is purely real (considering a real permittivity). There is weak, or no attenuation of the wave. The wave is characterized by its radian distance δ_R, the distance associated to a phase delay of 1 radian ($\alpha z = 1$ with $z = \delta_R$). It is the range of ground penetrating radar (GPR) techniques.

$$\delta_R = \frac{1}{\Re(k)} = \frac{1}{\omega\sqrt{\mu\epsilon}} \tag{II.30}$$

⇨ Diffusive case ($\mu\epsilon\omega^2 << \omega\mu\sigma$):

$$k \approx \sqrt{-i\omega\mu\sigma} \tag{II.31}$$

In the diffusive case ($f \lesssim 100kHz$) , or the quasi-static limit, the electromagnetic wave is not sensitive to the permittivity and is controlled by conductivity of the medium. EM methods considered in this manuscript are working in the diffusive domain. Considering k solution of (II.31), we have $\alpha = \beta = 1/\delta_{skin}$. δ_{skin} is the skin depth, an important parameter considering the evaluation of sensitivity of EM field with depth in the diffusive regime. The skin depth is defined as the distance where the amplitude of the EM wave is attenuated by a factor of $1/e$, consequently only around 36 % of its amplitude is remaining. It characterizes the EM wave by its attenuation with respect to conductivity and frequency. The energy of the EM waves concentrates into the shallowest layers as the conductivity and the frequency increase, decreasing EM sensitivity to deeper targets. However, this depth is indicative as geometrical considerations are restricting the investigation depth at short offsets with the source of the EM fields.

$$\delta_{skin} = \sqrt{\frac{2}{\omega\mu\sigma}} \simeq 503\sqrt{\frac{\rho}{f}} \tag{II.32}$$

Maxwell's equations with source terms
The previous relationships are valid when no source is present in the medium, but we are interested in active geophysical EM methods. Maxwell's equations with source terms are then the following :

$$\nabla \times \vec{E} + i\omega\mu\vec{H} = -\vec{M}_m \tag{II.33}$$

$$\nabla \times \vec{H} - \sigma\vec{E} = \vec{J}_e \tag{II.34}$$

$\vec{M}_m$ and $\vec{J}_e$ are respectively the magnetic and the electric source terms. These expressions will be used to determine E and H fields due to EM perturbation of a medium by various source configurations.

In presence of an anomaly, two main EM effects in the medium occurs:

Galvanic effect
When a *primary* electric current is applied to a conductivity anomaly within a homogeneous medium, some accumulation of charges are forming at the interfaces. Those effects are seen at a macroscopic scale as current channelling into conductive medium, where the current flows easily. Disparity in charge distribution at interfaces creates current flow into the anomaly. The anomalous body can be seen as a secondary electric source term into the medium.

Considering an infinite parallel plate capacitor model of conductivity σ_0 with a thin plate of conductivity σ_a in-between, we can obtain the secondary field due to charge

concentration at the interface :

$$E_0\sigma_0 = E_a\sigma_a$$
$$E_0\sigma_0 = (E_0 + E_s)\sigma_a$$
$$E_s = E_0\frac{\sigma_0 - \sigma_a}{\sigma_a} \tag{II.35}$$

❏ for a conductive anomaly, in the case $\sigma_0 < \sigma_a$, the secondary electric field is opposed to the primary electric field. A conductive target concentrates the current lines, hence the term of current channelling.

❏ for a resistive anomaly, in the case $\sigma_0 > \sigma_a$, the secondary electric field is in the same direction as the primary electric field. Current flows around the resistive target by favouring the easiest path opposing less resistance.

Figure II.9 illustrates galvanic effect occurring in the medium for a conductive and a resistive anomaly. Galvanic effects are generally associated to the in-phase EM response.
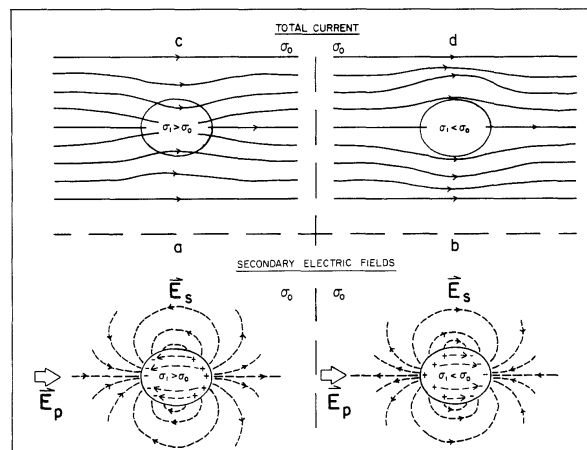

Figure II.9: *Sketch of the galvanic effects occurring in presence of a conductive or resistive anomaly, from Jiracek (1990). Boundary charges form on surface of the anomalous body and form a secondary source of current that results in "current channeling" or "current deflection" of the total field current lines according to an anomaly, respectively more conductive or more resistive than the background.*

Vortex effect, or *Eddy* current
Conductive targets subjected to a time-varying primary magnetic field are subject to an inductive flow of current according to Faraday's law. This vortex effect is also called *Eddy* current. These currents are creating their own secondary magnetic fields out-of-phase with the primary field, hence the anomaly can be seen as a secondary magnetic source in the medium. Induction response of a given target will depends on its induction number which depends on its geometry and conductivity but also on the frequency. The inductive response is bounded between a resistive (low frequency - low conductivity) and an inductive limit (high frequency - high conductivity), with a resonance peak in-between.

The induction number is of great importance in inductive methods as evaluating its characteristic allows the maximization of the target response with an appropriate acquisition geometry and frequency.

At low induction numbers, in the resistive limit, induced currents in the body vanish due to the slow time variations of the primary magnetic field. At high frequency, the induced currents reach a saturation limit determined only by the geometry of the conductive body and its relationship with the acquisition. Eddy currents are flowing at the interface only due to skin effect, so as the secondary magnetic field counterbalance perfectly the primary magnetic field. There is no magnetic field inside the conductor.
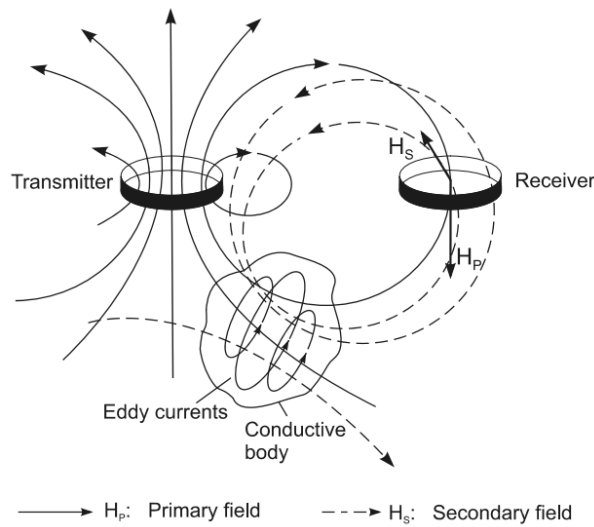

Figure II.10: *Sketch of the vortex effects occurring when a time-varying magnetic field is imposed to a conductive body from Seidel and Lange (2007)*

Both effects may coexist at the same time and be interdependent.

II.3.2   Controlled-source electromagnetic method (CSEM)

CSEM **practical definition**
In theory, Controlled-Source Electromagnetic method (CSEM) is a very general term for active EM method in geophysics. This term is nevertheless more commonly used in a more restricted way. As there are many and various EM methods, from time to frequency domain, from airborne, surface, borehole, or using inductive, galvanic or a mix of both coupling for measurements; some distinction have to be made, even if equations governing each of them are all based on solving Maxwell equations with a source term. Time-domain and airborne electromagnetic methods are commonly designated under their respective acronym of TDEM (or TEM) and AEM. They are therefore easily differentiated in separated categories. An exception of the following definition, will concern CS audio-magnetotelluric (CSAMT) technique, even though they use an active source signal, this method is more similar to magnetotelluric method using plane wave characteristics of the orthogonal electric and magnetic fields to obtain an impedance tensor from their ratio and deduce the Cagniard (Cagniard, 1953) apparent resistivity

of the medium. **In this thesis CSEM method is defined as EM geophysical prospecting methods working in the quasi-static frequency domain ($1\,mHz$ to $100\,kHz$)** ([†], including marine application, not considered further in this work). These methods consider generally the resistivity of the ground as a constant and real parameter neglecting IP effects.

Principles of the method

CSEM is then a geophysical prospecting method looking for resistivity imaging and measuring the EM field responses of the ground from a signal injected by an active source at several frequencies. From 2000's, marine-CSEM method became popular following its commercial success in marine hydrocarbon exploration (Constable, 2010). These developments where highly motivated by the complementarity of EM acquisition looking for medium resistivity variation, sensitive to medium content, and seismic acquisition having a high resolution power in imaging velocity interfaces. This work is more oriented to land-CSEM, but if the field constrains are very different principles of the method are the same and are sketched in figure II.11.
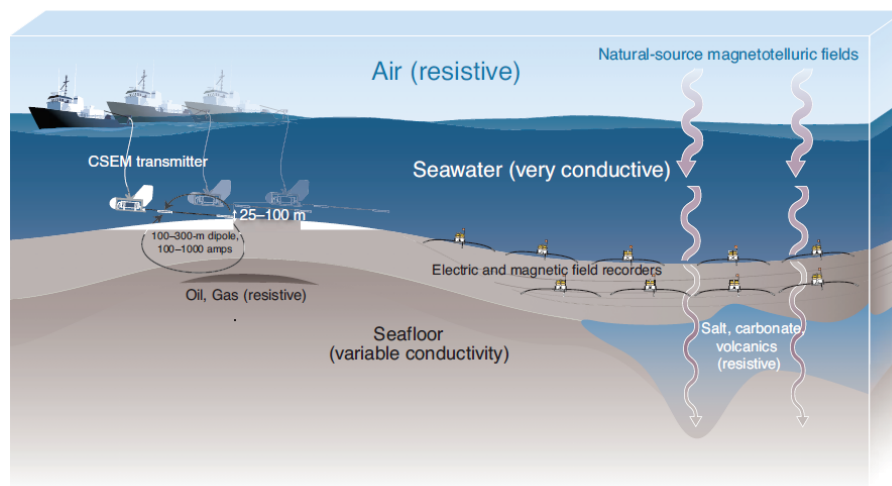
Figure II.11: *Marine CSEM typical survey illustration with an electrical source towed behind a boat in the acquisition area with a grid of sea-floor reception devices measuring electric and magnetic field ,from Constable (2010).*

A CSEM survey consists in measuring electromagnetic field responses to a *controlled* source injection at several positions and at several frequencies. Measurements are made at location covering the area of interest. In marine CSEM, a boat tows the EM source above the seafloor, where a grid of acquisition station where positioned. It results in a high number of transmitter/reception couples with a good illumination of the medium from various offset and direction. A good illumination is necessary to solve the inverse problem. Indeed, as for electric method, offset and direction controls geometrically the depth (and the volume) investigated during the acquisition (Geometrical sounding). Nevertheless, in EM methods a broad range of frequency can be measured, then the depth

to which EM waves are sensitive depends also to the skin depth δ_{skin} ((II.32)). In plane wave methods (CSAMT, MT), the frequency controls totally the depth of investigation (Frequency sounding). CSEM method uses the frequency spectrum from DC to plane wave domain, then geometrical and frequency sounding will have an importance in the medium reconstruction. A considerable advantage is that frequency information helps the medium reconstruction, then a lighter array configuration can cautiously[†] be considered to reduce the number of Tx/Rx couples ([†], frequency information benefit does not counterbalance perfectly geometrical illumination in complex settings). For land CSEM, accessibility is a matter of concern and limits transmitter and/or receiver positions, highlighting the crucial importance of frequency sounding information. Man-made noise is also generally more considerable on land.

As mentioned earlier, the source can be **inductive**, by the injection of a current into a wire loop, or **galvanic** by a direct injection of the current through a grounded wire. Both techniques have their pros and cons: no coupling with the ground is necessary for inductive source with easier installation, but a faster signal decrease and sensitivity highly dependent to the induction number ($\approx$ not sensitive to resistors). On the other hand, large galvanic sources are harder to install, injecting currents into the ground can be difficult in resistive material, but the recovered signals decrease at a lower rate, with a sensitivity to resistivity on the whole frequency domain. More discussion on sensitivity differences between inductive and galvanic transmitters can be found in the chapter IV, section IV.2.

II.3.3   Controlled-source electromagnetic and induced polarisation (CSEMIP)

Lately, following the improvements of instrumentation, computation capability and the availability of several EM modelling codes, the challenging task of taking EM induction effects into account in induced polarization data gained an increasing interest. Code availability for EM/IP modelling and inversion are still nevertheless a crucial need as it is pointed by Kemna et al. (2012) in their review. Recently, Mörbe et al. (2020) present a large land CSEM survey with data contaminated by sufficiently strong IP effects at low frequencies from conductive graptolite shales.

A lot of literature deals with EM induction removal from the SIP data in order to access to IP parameters. In their EM removal work, Routh and Oldenburg (2001) highlighted 3 distinct categories of removal methods:

❏ assuming that the IP phase is constant or described by a linear function, whereas EM coupling respects a power law.

❏ using a double Cole-Cole model for IP and EM induction modelling in SIP data. EM induction effects dissipating quicker than those of IP, a first Cole-Cole model with a short characteristic time explains EM induction and a second at longer characteristic time is obtained to describe IP.

❏ first, modelling full-EM response (solving Maxwell's equations) for an a-priori re-

sistivity model, deduced from the apparent resistivity of the medium or a prior inversion, then subtract EM coupling from SIP data.

Nevertheless, only a few works deal with solving IP and EM effects simultaneously for the inversion of CR. The main limitation is the need for large computational resources to solve complete Maxwell's equations as soon as the dimension of the problem increases. Inversion codes for SIP data that fully take into account EM effects started with the 1D work of Ghorbani et al. (2009). They developed a one-dimensional homotopy inversion algorithm for a Cole-Cole parametrization using the forward modelling code of Ingeman-Nielsen and Baumgartner (2006). Their formulation takes into account finite length wires but is limited to 1D approximations. Later, some EM codes in higher dimensions were developed taking complex resistivity into account: MacLennan et al. (2014) developed a 2.5D inversion code working on crosswell EM data. They evaluated the effect of a CR medium for inductive-inductive crosswell acquisition and demonstrated their method on a synthetic model. They assumed nevertheless a CR independent of the frequency, pointing out that in clayey materials, the frequency effect is weak. Furthermore, as they are working in the frequency domain, they argue that inversion could also be done frequency per frequency otherwise. Using the same approximation, Commer et al. (2011) worked to implement a constant CR into their code detailed in earlier work (Commer and Newman, 2008; Commer et al., 2008). Only a group of authors to our known have developed a 3D inversion code inverting together EM induction and IP effect information considering a frequency-dependent CR using a CR model based on the GEMTIP model (Zhdanov, 2008; Zhdanov et al., 2018; Zhengwei Xu and Zhdanov, 2015).

Conclusion

Resistivity imaging techniques are powerful tools for subsurface characterization, especially to access medium porosity and fluid content. We detailed in this chapter the principles of classic geoelectric resistivity imaging techniques and their static assumption to access an apparent resistivity using a simple geometric factor. At low frequencies, induced polarization occurs and a transient voltage is observed after the current shut-off. Induced polarization, in the time or frequency domain, extends application of the classic electrical prospecting methods to the study of the induced phase delay due to polarization. A complex resistivity is used to model these effects and chargeability of the medium can be deduced from IP measurements. CR frequency variation can be linked to IP relaxation models, which allows then to access to many properties of the pore space geometry and its content. TDIP and SIP methods assume a static approximation of the EM waves, therefore EM induction occurring with increasing frequency, offset, conductivity and wire coupling need to be taken into account. Data impacted by EM coupling are usually neglected, suppressed from the data, or some EM removal techniques are applied. On the contrary CSEM can fully take into account EM induction by solving Maxwell equations. Frequency information contained in the data helps resolving the medium resistivity, but at larger computational cost that can fastly be restrictive. They are nevertheless assuming a real and constant resistivity in most cases. Works including IP EM coupling and

taking both information for the resolution of the inverse problem are scarce. Development of a code able to use both information and solve the multi-parameter problem efficiently is needed.

POLYEM3D

Introduction

Geophysical EM imaging relies on the inversion of data sample at discrete points of a studied domain. The number of data points is obviously limited by several factors. The logistics of a survey can be limited due to time restrictions, staff availability, equipment and each of them are impacting the cost of the survey. In addition, some areas are very challenging such as industrialized areas, or areas with sharp topography. In most geophysical applications, data are obtained on a discrete grid. In order to model these data, a forward problem is needed. The forward problem is a set of equations to solve that describes mathematically the response of a particular model according to its parameters. Considering resistivity imaging, the forward problem is described by Maxwell equations and allows the modelling of the EM field response of a particular resistivity distribution. Forward modelling can be used through a trial and error approach in order to find manually a model that fits the data, but this kind of approach is highly restrictive and limited to very simple medium with only a few parameters. However, the discrete dataset must be *inverted* to obtain a spatial resistivity distribution that explain the data set. Inversion can be seen as the reciprocal of the forward problem (Figure III.1). The dataset is used as an input to retrieve the medium description according to some parameters (i.e. the resistivity here). However to solve the inverse problem, the forward problem resolution is needed.
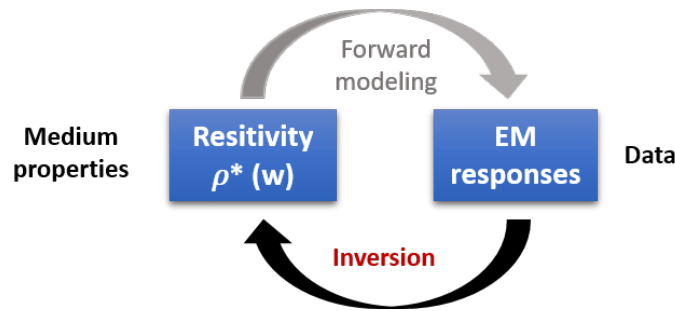
Figure III.1: *Sketch resuming the relation between the modelling and the inversion phase of the problem*

The work of this thesis is based on *POLYEM3D*, a 3D finite-difference modelling and inversion code for frequency-domain controlled-source electromagnetic (CSEM) and magnetotelluric (MT) data. In the first part of this chapter, the formulation of the forward problem is detailed. In a second part, the inverse problem is outlined and POLYEM3D

inversion code essentials are described, with a special care to the gradient of the objective function formulation, for a better understanding of the following chapters.

III.1   Forward problem

The forward problem of the EM resistivity imaging problem is dependent on the resolution of Maxwell's equations with a source term (equation (II.33) and (II.34)). These equations can be separated into a primary/secondary field formulation considering the total field $E^{tot} = E^p + E^s$ being the sum of the *primary* field E^p for a reference model and a secondary field E^s (same for the magnetic field H), due to the scattering of the EM waves by an anomaly of conductivity σ^s within the reference model σ^p ($\sigma = \sigma^p + \sigma^s$). Equations (II.33) and (II.34) are subtracted from the solution in the reference model to obtain an equation without the sources terms M_m and J_e :

$$\nabla \times \vec{E^s} + i\omega\mu\vec{H^s} = 0 \tag{III.1}$$

$$\nabla \times \vec{H^s} - \sigma\vec{E^s} = \overbrace{(\sigma - \sigma^p)}^{\sigma^s} \vec{E^p} \tag{III.2}$$

A secondary source term is obtained and can be noted $J_s = (\sigma - \sigma^p)\vec{E^p}$ which is directly proportional to the primary electric field and the resistivity perturbation in the reference medium (*i.e.*   the secondary resistivity). The critical computation of the primary electric field $\vec{E^p}$ containing the source singularity is therefore separated from the finite-differences problem. $\vec{E^p}$ is calculated separately using a 1D semi-analytical code, but can be any reference solution over a reference model. Finite-wire solutions can be modelled as well as current loop for inductive source modelling.

POLYEM3D uses the **electric field formulation** of the EM problem by taking the curl of equation III.2 and substituting the magnetic field term by the Maxwell-Faraday equation to obtain the vector Helmholtz equation for the secondary electric field:

$$\nabla \times \nabla \times \vec{E^s} + i\omega\mu_0\sigma\vec{E^s} = -j\omega\mu_0(\sigma - \sigma_P)\vec{E^p}. \tag{III.3}$$

The solution of E^s is computed by finite-difference method (or finite-volume through a slight variation in the formulation) and using a discretization of equation III.3 over a specific grid. The grid uses the staggered-grid approach defined by Streich (2009) over an irregular Cartesian grid. The finite-volume formulation consists in a simple scaling by the staggered cell sizes on the right and left-hand sides of equation III.3 to obtain a *"controlled-volume"* (Weiss and Constable, 2006). The finite-volume approach allows to obtain a symmetric system of equations with better numerical properties. Equation III.3 can be expressed according to a system of discretized linear equations:

$$\mathbf{A}\vec{E^s} = \vec{b}, \tag{III.4}$$

with **A** the finite-difference system of equations which discretizes the double curl and the $i\omega\mu\sigma$ factors linked to the medium properties description on the staggered grid, $\vec{E^s}$ the secondary electric field vector on the staggered grid and $\vec{b}$ the source term depending of the

scattered conductivity and the primary electric field. Vectors $\vec{E^s}$ and $\vec{b}$ contain the three components of the electric field in the z, y and x-direction and are of the size $3N_zN_yN_x$ ($N_{z,y,x}$ being the size of the forward grid in the z, y ,and x direction respectively). The primary electric field E^p contained in the right-hand side, must be computed in a prior step at each point of the staggered grid[a]. $\mathbf{A}$ is thus of the size $9N_z^2N_y^2N_x^2$). The staggered grid is defined with the electric field on the faces of the cell, shifted thus by a half cell from the center. The electric field components $\vec{E_z}$, $\vec{E_y}$ and $\vec{E_x}$ are staggered of a half cell in the directions z, y and x. The magnetic field is calculated with the application of a curl operator to electric field. It is defined on the edges of the cells following the staggered formulation shifted thus two times. This formulation is similar to the formulation of Haber et al. (2000) and in opposition to the common formulation of Yee (1966) who considers the electric field on the edge and the magnetic field on the faces of the cell. A sketch of the staggered grid and field positions is presented in figure III.2, with indices (i, j, k) corresponding to axes (z, y, x) respectively, z being the depth.
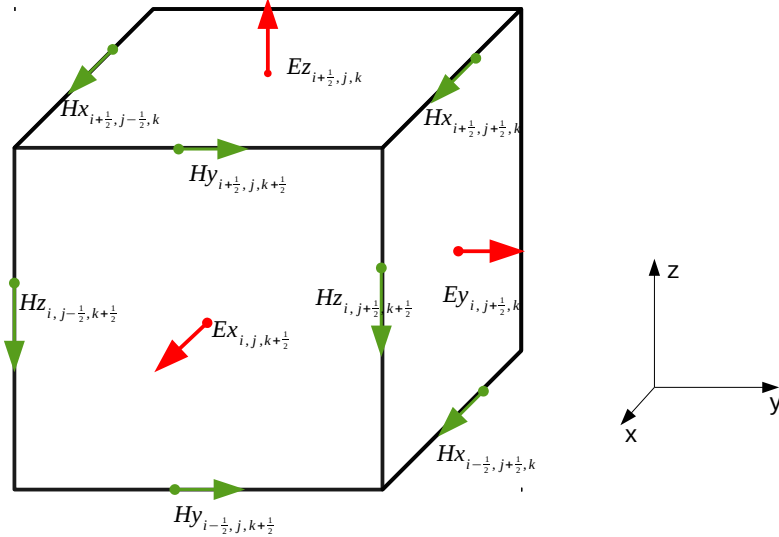

Figure III.2: *Staggered scheme used for electric and magnetic component based on the work of Haber et al. (2000); Streich (2009)*

Conductivity and dielectric permittivity are defined for each cell of the modelling grid. Nevertheless, as the fields are computed at the interfaces of the cell, the properties are discontinuous. A staggered conductivity is therefore defined on the staggered position. A staggered conductivity using harmonic averaging is used and gives as an example in the z direction:

$$\widetilde{\sigma}_{i+\frac{1}{2},j,k} = \Delta z_{i+\frac{1}{2}} \left(\frac{\Delta z_i}{2\sigma_{i,j,k}} + \frac{\Delta z_{i+1}}{2\sigma_{i+1,j,k}} \right)^{-1}. \tag{III.5}$$

Δz_i is the size of cell (i, j, k), and $\Delta z_{i+\frac{1}{2}}$ the size of the corresponding staggered

---

[a]the three components of the electric and magnetic field for each data at the receiver position must be computed as well for interpolation and re-orientation purposes

cell along z, that is the distance between the center of cells (i, j, k) and $(i + 1, j, k)$. Similar notation is used for y, and x components respectively in the j and k increment directions. Harmonic averaging ensures the continuity of the current densities derived from the averaged and non-averaged conductivities across cell boundaries (Streich, 2009).

The system of finite-difference equations describing the Helmholtz equation III.3 for the secondary electric field on the staggered grid is thus defined by the three systems of the electric field, that can be associated to the three diagonal components $E^{z^s}_{i+\frac{1}{2},j,k}$ $E^{y^s}_{i,j+\frac{1}{2},k}$ and $E^{x^s}_{i,j,k+\frac{1}{2}}$ of the system $\mathbf{A}E^s$:

$$
\begin{aligned}
& \frac{1}{\Delta x_k} \left[\frac{E^{x^s}_{i+1,j,k+\frac{1}{2}} - E^{x^s}_{i,j,k+\frac{1}{2}}}{\Delta z_{i+\frac{1}{2}}} - \frac{E^{x^s}_{i+1,j,k-\frac{1}{2}} - E^{x^s}_{i,j,k-\frac{1}{2}}}{\Delta z_{i-\frac{1}{2}}} \right] \\
- \; & \frac{1}{\Delta x_k} \left[\frac{E^{z^s}_{i+\frac{1}{2},j,k+1} - E^{z^s}_{i+\frac{1}{2},j,k}}{\Delta x_{k+\frac{1}{2}}} - \frac{E^{z^s}_{i+\frac{1}{2},j,k} - E^{z^s}_{i+\frac{1}{2},j,k-1}}{\Delta x_{k-\frac{1}{2}}} \right] \\
+ \; & \frac{1}{\Delta y_j} \left[\frac{E^{y^s}_{i+1,j+\frac{1}{2},k} - E^{y^s}_{i,j+\frac{1}{2},k}}{\Delta z_{i+\frac{1}{2}}} - \frac{E^{y^s}_{i,j+\frac{1}{2},k} - E^{y^s}_{i-1,j+\frac{1}{2},k}}{\Delta z_{i+\frac{1}{2}}} \right] \\
- \; & \frac{1}{\Delta y_j} \left[\frac{E^{z^s}_{i+\frac{1}{2},j+1,k} - E^{z^s}_{i+\frac{1}{2},j,k}}{\Delta y_{j+\frac{1}{2}}} - \frac{E^{z^s}_{i+\frac{1}{2},j,k} - E^{z^s}_{i+\frac{1}{2},j-1,k}}{\Delta y_{j-\frac{1}{2}}} \right] \\
+ \; & i\omega\mu_0 \widetilde{\sigma}_{i+\frac{1}{2},j,k} E^{z^s}_{i+\frac{1}{2},j,k} \; = \; -i\omega\mu_0 \left(\widetilde{\sigma}_{i+\frac{1}{2},j,k} - \widetilde{\sigma}^p_{i+\frac{1}{2},j,k} \right) E^{z^p}_{i+\frac{1}{2},j,k}
\end{aligned}
\tag{III.6}
$$

$$
\begin{aligned}
& \frac{1}{\Delta z_i} \left[\frac{E^{z^s}_{i+\frac{1}{2},j+1,k} - E^{z^s}_{i+\frac{1}{2},j,k}}{\Delta y_{j+\frac{1}{2}}} - \frac{E^{z^s}_{i-\frac{1}{2},j+1,k} - E^{z^s}_{i-\frac{1}{2},j,k}}{\Delta y_{i+\frac{1}{2}}} \right] \\
- \; & \frac{1}{\Delta z_i} \left[\frac{E^{y^s}_{i+1,j+\frac{1}{2},k} - E^{y^s}_{i,j+\frac{1}{2},k}}{\Delta z_{i+\frac{1}{2}}} - \frac{E^{y^s}_{i,j+\frac{1}{2},k} - E^{y^s}_{i-1,j+\frac{1}{2},k}}{\Delta z_{i-\frac{1}{2}}} \right] \\
+ \; & \frac{1}{\Delta x_k} \left[\frac{E^{x^s}_{i,j+1,k+\frac{1}{2}} - E^{x^s}_{i,j,k+\frac{1}{2}}}{\Delta y_{j+\frac{1}{2}}} - \frac{E^{x^s}_{i,j+1,k-\frac{1}{2}} - E^{x^s}_{i,j,k-\frac{1}{2}}}{\Delta y_{j+\frac{1}{2}}} \right] \\
- \; & \frac{1}{\Delta x_k} \left[\frac{E^{y^s}_{i,j+\frac{1}{2},k+1} - E^{y^s}_{i,j+\frac{1}{2},k}}{\Delta x_{k+\frac{1}{2}}} - \frac{E^{y^s}_{i,j+\frac{1}{2},k} - E^{y^s}_{i,j+\frac{1}{2},k-1}}{\Delta x_{k-\frac{1}{2}}} \right] \\
+ \; & i\omega\mu_0 \widetilde{\sigma}_{i,j+\frac{1}{2},k} E^{y^s}_{i,j+\frac{1}{2},k} \; = \; -i\omega\mu_0 \left(\widetilde{\sigma}_{i,j+\frac{1}{2},k} - \widetilde{\sigma}^p_{i,j+\frac{1}{2},k} \right) E^{y^p}_{i,j+\frac{1}{2},k}
\end{aligned}
\tag{III.7}
$$

$$
\frac{1}{\Delta y_j} \left[\frac{E^{y^s}_{i,j+\frac{1}{2},k+1} - E^{y^s}_{i,j+\frac{1}{2},k}}{\Delta x_{k+\frac{1}{2}}} - \frac{E^{y^s}_{i,j-\frac{1}{2},k+1} - E^{y^s}_{i,j-\frac{1}{2},k}}{\Delta x_{k+\frac{1}{2}}} \right] \tag{III.8}
$$

$$
- \frac{1}{\Delta y_j} \left[\frac{E^{x^s}_{i,j+1,k+\frac{1}{2}} - E^{x^s}_{i,j,k+\frac{1}{2}}}{\Delta y_{j+\frac{1}{2}}} - \frac{E^{x^s}_{i,j,k+\frac{1}{2}} - E^{x^s}_{i,j-1,k+\frac{1}{2}}}{\Delta y_{j-\frac{1}{2}}} \right]
$$

$$
+ \frac{1}{\Delta z_k} \left[\frac{E^{z^s}_{i+\frac{1}{2},j,k+1} - E^{z^s}_{i+\frac{1}{2},j,k}}{\Delta x_{k+\frac{1}{2}}} - \frac{E^{z^s}_{i-\frac{1}{2},j,k+1} - E^{x^s}_{i-\frac{1}{2},j,k}}{\Delta x_{k+\frac{1}{2}}} \right]
$$

$$
- \frac{1}{\Delta z_k} \left[\frac{E^{x^s}_{i+1,j,k+\frac{1}{2}} - E^{x^s}_{i,j,k+\frac{1}{2}}}{\Delta z_{i+\frac{1}{2}}} - \frac{E^{x^s}_{i,j,k+\frac{1}{2}} - E^{x^s}_{i-1,j,k+\frac{1}{2}}}{\Delta z_{i-\frac{1}{2}}} \right]
$$

$$
+ i\omega\mu_0 \widetilde{\sigma}_{i,j,k+\frac{1}{2}} E^{x^s}_{i,j,k+\frac{1}{2}} = -i\omega\mu_0 \left(\widetilde{\sigma}_{i,j,k+\frac{1}{2}} - \widetilde{\sigma}^p_{i,j,k+\frac{1}{2}} \right) E^{x^p}_{i,j,k+\frac{1}{2}}
$$

The matrix $\mathbf{A}$ derived from previous equations is sparse and has 13 non-zero components per line. Dirichlet conditions are applied imposing a tangential electric field that is vanishing on the boundaries of the forward domain (*i.e.* perfect electric conductor). To ensure this condition the grid boundaries should be sufficiently far from sources. Dirichlet conditions ensure the symmetry of the $\mathbf{A}$ matrix (Newman and Alumbaugh, 1995; Streich, 2009). The system in equation (III.4), as well as the primary field on the 3D grid, are solved through a massively parallel approach using direct solver as the MUlti-frontal Massively Parallel Solver direct solver (MUMPS, Amestoy et al. (2019, 2001)), or the Watson Sparse Matrix Package (WSMP, Gupta (2000)) combined to a Message Passing interface (MPI). Direct solvers are more robust, especially in the case of a model containing an air/ground interface, than iterative methods that may fail to converge and are difficult to apply for solving the Helmholtz equation (see Grayver et al. (2013) and references therein). Solving the problem using a direct solver requires nevertheless a larger amount of memory. The A matrix is factorized in a computationally expensive step at first, then a comparatively inexpensive forward-backward substitution is carried out to solve the system. The factorization is needed for each modelled frequency, nevertheless each additional source needs only one extra forward-backward substitution, less resource-demanding[b].

In order to get the finite volume formulation mentioned above, the equations III.7, III.8 and III.9 are scaled by the volume of the current staggered cell, that is by multiplying both side of each equation respectively by $(\Delta z_{i+\frac{1}{2}}\Delta y_j \Delta x_k)$, $(\Delta z_i \Delta y_{j+\frac{1}{2}} \Delta x_k)$ and $(\Delta z_i \Delta y_j \Delta x_{k+\frac{1}{2}})$.

As the system is solved on the complete staggered grid, the field at the receivers for the given data is obtained by interpolation. The interpolation is done on the secondary electric field improving numerical accuracy. POLYEM3D is a code with a versatile outlook

---

[b]As an example, for a 3D grid of 740096 cells, solved on 256 processes, for 450 data per frequency and source, and using the WSMP direct solver: POLYEM3D code requires approximately 75 seconds for the complete factorization of the $\mathbf{A}$ matrix, then the solution per source took less than a half second.

but was designed mainly for land-CSEM applications, which involves a sharp conductivity boundary at the air-ground interface ($\frac{\sigma_{air}}{\sigma_{ground}} \gg 10^{10}$), where sources and receivers are generally located. Therefore, a rigorous interpolation approach developed by Shantsev and Maaø (2015) is used to interpolate the secondary electric field to the receiver position. The secondary magnetic field is obtained from the electric field on the staggered grid using a discretized curl operator from relation:

$$\mathrm{H^s} \; = \; -\frac{1}{j\omega\mu_0}\nabla \times \mathrm{E^s} \tag{III.9}$$

A simple tri-linear interpolation is used to extract the secondary magnetic field at the receiver, as the magnetic permeability is considered constant for its value in free space μ_0, therefore there are no magnetic field discontinuities.

The formulation of the CSEM forward problem allows then the modelling of the electric and magnetic field responses of a resistivity medium discretized over a finite-difference grid for various source definitions. The grid definition is a critical part of the modelling accuracy. The accuracy of the discretization is dependent of the skin depth in the medium. Plessix et al. (2007) give an estimation of the discretization about 2 to 3 cells per skin depth. For better results, it is common to refine the grid at sharp conductivity discontinuities, near the source position and near the receivers position. It points out the necessity to refine correctly the air layer. However, by using the secondary/primary field approach, although the refinement should be maintained, the source area discretization is less critical than for a total-field formulation. An illustration of a 3D grid built for the modelling of the EM response of a conductive cube in a homogeneous background is presented in figure III.3 for its central area with a fine discretization. An example of the horizontal electric field amplitude calculated on the staggered grid is presented in figure III.4.
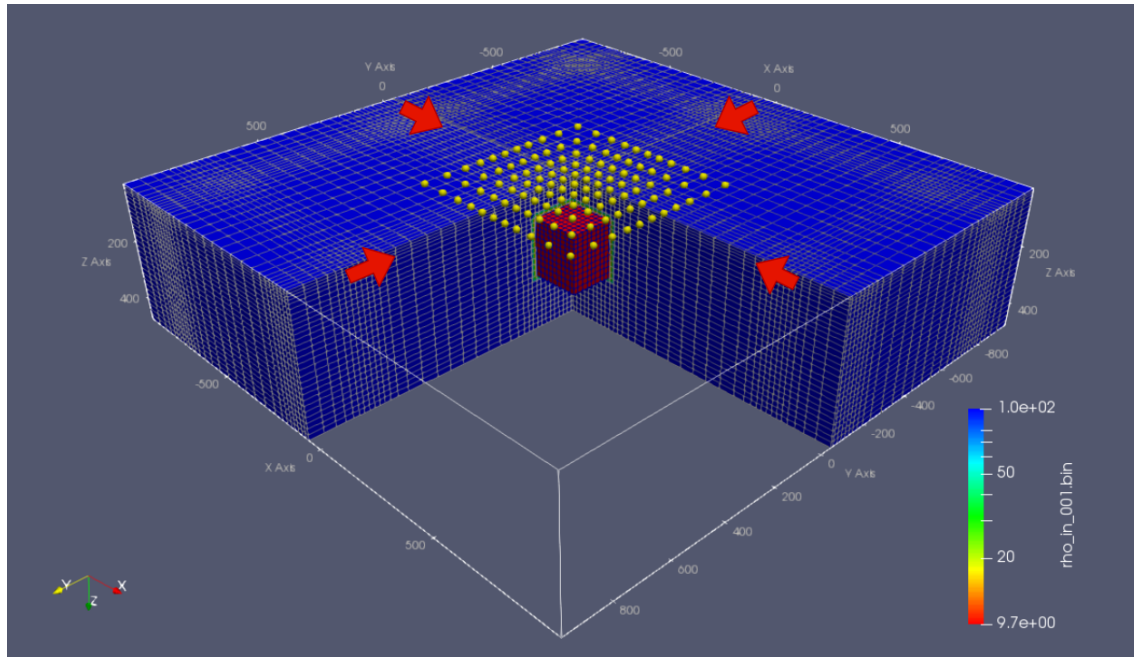
Figure III.3: *Representation of a 3D grid used by POLYEM3D with a resistivity model containing a central anomaly. EM field responses of the 3D cube are computed by finite-difference method based on the present grid using the primary field in the background model calculated on the grid. The figure presents only the central area of the grid with a fine discretization, whereas cell sizes increase progressively towards the boundaries to ensure the Dirichlet condition. A finer discretization of the model is used at the air interface, for the anomaly and at sources position (oriented electric dipoles represented by red arrows). This model accounts for 556400 cells.*
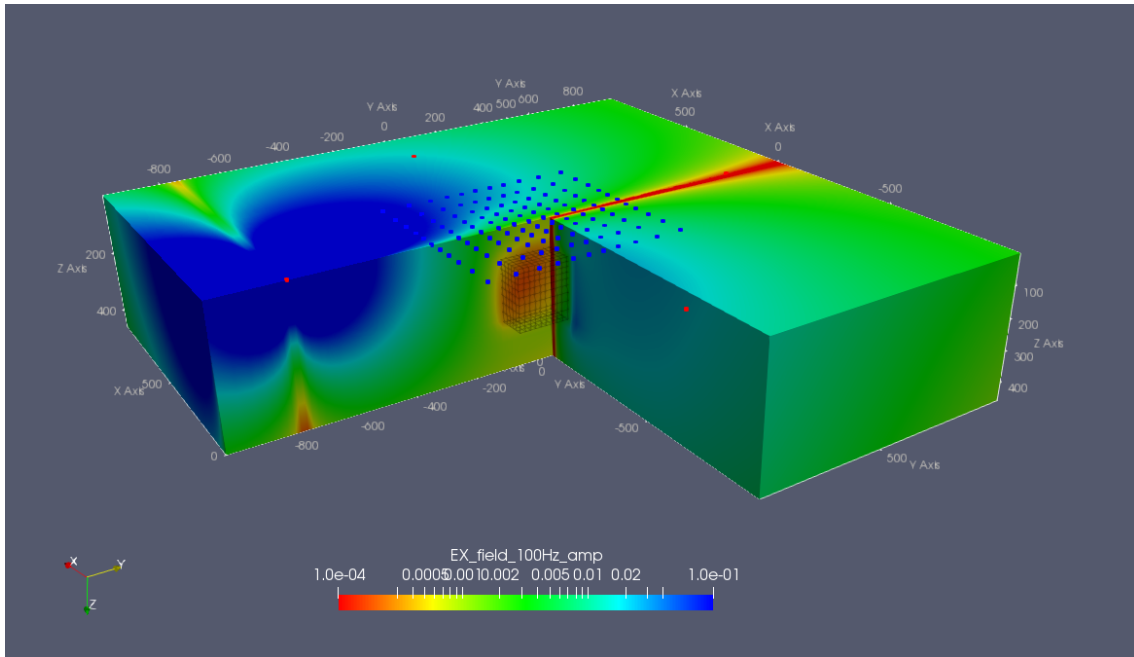
(a) *Ex amplitude*
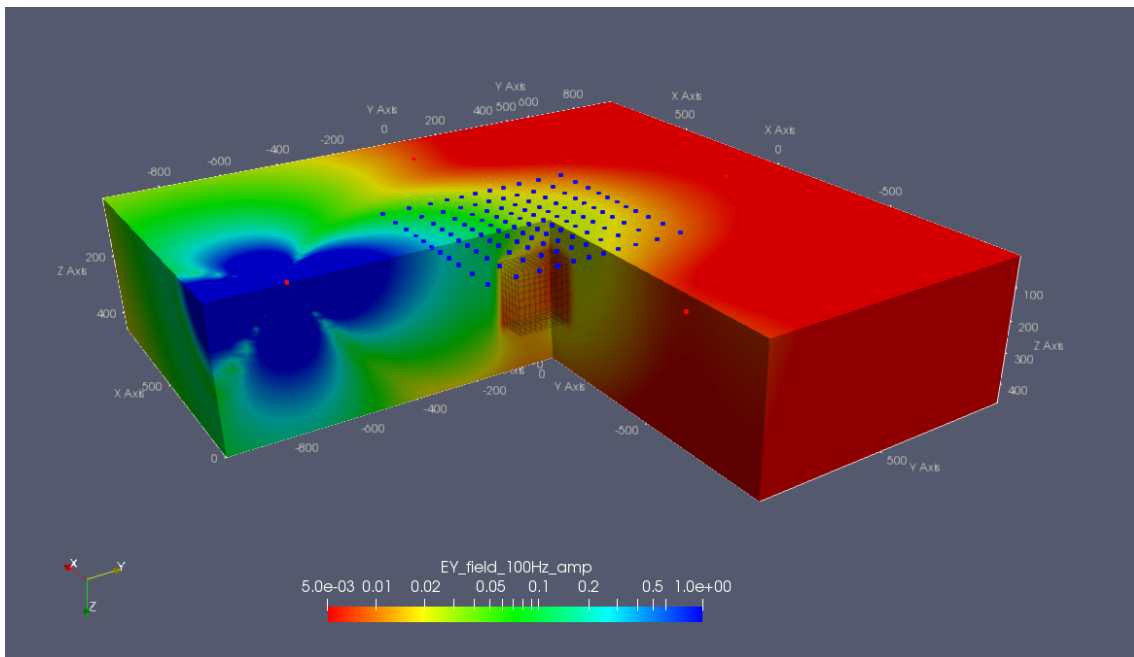
(b) *Ey amplitude*

Figure III.4: *Representation of the horizontal electric field amplitude of one of the sources at 100 Hz for the model response presented in figure III.3. The cube position can be noticed by the sharp decrease of the field at the center due to its higher conductivity and thus current channelling effects.*

III.2   Inverse problem

Modelling the EM responses of the ground allows a better understanding of the effect of the complexity of the resistivity distribution in the medium. Sensitivity of a given

target and acquisition geometry can therefore be established to maximize the response in a planned survey and to estimate the optimal acquisition geometry, or simply its feasibility according to ambient, geometrical (*i.e.* source/receiver positioning errors) or instrumental noises. However, to retrieve the distribution of a given parameter from discrete geophysical observations, an inversion must be carried out. Inversion procedure uses optimization methods to infer a parameter set m describing the physical problem through a forward problem g that gives a modelling solution of a measured data set d. The forward problem is described by :

$$g(m) = d \qquad\qquad (III.10)$$

The inverse problem seeks a distribution of the medium parameters $\tilde{m}$ that explains the observed data d^{obs} according to the forward problem and optimization constraints. In most of the case, the true parameters of the medium cannot be inferred due to non-linearity, or to a problem that is over or under-determined. Considering the resistivity imaging problem, m is a parametrization of the resistivity and d is a set of the observables of the EM fields ($\Re(E_n)$, $\Im(E_n)$, $|E_n|$, $log(E_n)$, ρ_a the apparent resistivity, $\mathcal{Z}_{i,j}$ the impedance tensor, or PE_{max} the maximum of the polarization ellipse, *etc...* with n a given component depending of the coordinate system). In a multi-parameter problem, m contains several types of parameters as for the problem of the intermediate frequency domain seeking the resistivity and the dielectric permittivity of the medium (Busch et al., 2012; Lavoué et al., 2014).

There are two main inverse problem techniques based on a *global* or a *local* resolution of the problem. Indeed, the basis of inverse theory is the minimization[c] of an objective function, in order to find a solution of model parameters $\tilde{m}$ vector that solves the forward problem equation (III.10) whose solution fit the dataset. The objective function takes generally into account several constrains that weight the final result, therefore $\tilde{m}$ is not necessarily the solution that best fits the data due to specific constrains (smoothness of the solution, prior-information, probability density function,...).

Global optimization methods search a *global* minimum, which is thus defined on the entire considered domain. *Global* minimum is opposed to *local* minima that are only defined for a given subset of the domain when the problem is non-linear. On the other hand, local optimization techniques seek for a minimum in the neighbouring of a defined initial state (a given set of $m = m_0$). The non-linear inverse problem is linearised around m_0. Solution of local optimization is not necessarily the global minimum and the optimization can get stuck in a *local* minimum close to the starting model due to non-linearity of the problem. This is why the choice of an appropriate starting model m_0 is critical concerning these methods that *linearise* the inverse problem in the neighbourhood of m_0 (Tarantola and Valette, 1982).

Global optimization seems therefore preferable to avoid local minima, however such methods require a large number of *samples*[d], in order to obtain a *global* mapping of

---

[c]It can equivalently be considered as a maximization using an equivalent formulation of the objective function

[d]solutions of equation (III.10) for a representative set of the model parameters m over the considered domain

the cost function and lead the problem towards the global minimum. This task can be computationally expensive such as the complexity of the forward problem increases. In the case of the 3D finite-difference CSEM problem. The calculation capabilities needed to obtain such a sampling is highly restrictive. POLYEM3D inversion code is based on local optimization algorithm. Two types of inversion methods are available in POLYEM3D:

❏ Preconditioned gradient based methods that use the *Seiscope optimization toolbox*, a reverse communication algorithm, combined with a line search based on a bracketing strategy (Métivier and Brossier, 2016; Nocedal and Wright, 2006)

❏ Gauss-Newton optimization using a Least Squares with QR-factorization (LSQR) algorithm to solve the normal equation (Grayver et al., 2013; Paige and Saunders, 1982) and the same line search.

At first, Gradient-based and Gauss-Newton methods are presented in the following section about local optimization. Then, POLYEM3D inversion code generalities are presented in more details with a brief overview of the parametrization and regularization of the inverse problem, the *Seiscope* optimization toolbox associated to the inversion workflow and line search is presented. The calculation of the cost function of the 3D gradient using the Adjoint State method (Plessix, 2006; Plessix and Mulder, 2008) is presented for a complete understanding of the inversion code.

III.2.1   Local optimization

A Local optimization problem to seeks a model minimizing an objective function χ (III.11), with a data fit associated function χ_d and a model regularisation term χ_m. The data minimization term consists in a measure of the fit between the observed data vector d^{obs} and modelled data vector d^{cal}. The model regularisation term uses an objective function imposing some constraints on the model parameters with λ a Lagrange multiplier parameter controlling the trade-off between data fit and model regularization.

$$\chi = \chi_d + \lambda \chi_m \tag{III.11}$$

In the following developments, the model regularization term is omitted to introduce the inverse problem. However, its implementation follows a similar development. Regularization of the inverse problem is discussed in more detail in section III.2.2.

The optimization problem seeks thus to minimize the objective function χ_d. The fit between the observed data vector d^{obs} and modelled data vector d^{cal} is calculated for a model m by solving the forward problem $g(m)$ in equation (III.10). The objective function, or the misfit function, can take several forms (Menke, 1984; Tarantola, 2005) using different types of norms to quantifying the length of the residual vector. The L_2 norm[e] of the data residuals is commonly used in geophysical applications and is adopted in the following developments :

$$\chi_d = \frac{1}{2} ||(d^{cal} - d^{obs})||_2^2 \tag{III.12}$$

---

[e]Actually, the square of the L_2 norm is commonly taken to drop the square root for simplicity of subsequent developments.

It can be re-written with $\Delta d = d^{cal} - d^{obs}$ the data residual vector as:

$$\chi_d = \frac{1}{2}\Delta d^\dagger \Delta d, \tag{III.13}$$

with † the transposed conjugate operator. The residual of the data is usually weighted using a covariance matrix W_d applied to the data vector. W_d contains usually the reciprocal of the standard deviation of the data. The objective function is thus reformulated: $\chi_d = \frac{1}{2}(\Delta d W_d)^\dagger W_d \Delta d$.

The solution of the inverse problem is expressed as a local iterative method, where a model vector at iteration $k + 1$ with a lower objective function can be obtained from a previous model vector at iteration k through a model update in the descent direction of the objective function, therefore moving closer to the minimum of the objective function $\chi_d(m_{k+1}) < \chi_d(m_k)$:

$$m_{k+1} = m_k + \alpha_k \Delta m_k \tag{III.14}$$

Δm_k is the descent direction along which the update is made and α_k a positive real defining the step length in the descent direction. There are several ways to determine the descent direction Δm_k .

Considering a solution of the inverse problem for a small perturbation $\tilde{m} = m_0 + \Delta m$, the following second-order Taylor series expansion can be derived:

$$\chi_d(\tilde{m}) = \chi_d(m_0 + \Delta m) = \chi_d(m_0) + \Delta m^t \nabla \chi_d + \frac{1}{2}\Delta m^t \mathbf{H} \Delta m, \tag{III.15}$$

with $\nabla_m \chi_d$ the gradient of the cost function with respect to m and H the second order derivative. For simplification of the notation in the following, if no subscript is specified, the differentiation operator ∇ refers to the derivation with respect to the model parameter vector m ($\nabla = \frac{\partial}{\partial m}$) otherwise it designates the derivative with respect to the parameter indicated in subscript. $\mathbf{H}$ is the second order derivative of the cost function with respect to m and is called the *Hessian* matrix ($\mathbf{H} = \frac{\partial^2 \chi_d}{\partial m^2} = \frac{\partial \nabla \chi_d}{\partial m}$).

The gradient of the objective function is given by :

$$
\begin{aligned}
\nabla \chi_d &= \sum_{i=1}^{N_d} \left[\frac{\partial d_i^{cal}{}^\dagger}{\partial m_j}(d_i^{cal} - d_i^{obs}) + (d_i^{cal} - d_i^{obs})^\dagger \frac{\partial d_i^{cal}}{\partial m_j} \right] \\
&= \sum_{i=1}^{N_d} \Re \left[\frac{\partial d_i^{cal}{}^\dagger}{\partial m_j}(d_i^{cal} - d_i^{obs}) \right]
\end{aligned}
\tag{III.16}
$$

, with $j = 1, 2, ..., N_m$ and $i = 1, 2, ..., N_d$. N_m and N_d are respectively the number of parameters m and the number of data d^{cal} or d^{obs}. It can be reformulated in its vector/matrix form (Virieux and Operto, 2009) as :

$$\nabla \chi_d = \Re \left[\frac{\partial d^{cal}{}^\dagger}{\partial m}(d^{cal} - d^{obs}) \right], \tag{III.17}$$

$\frac{\partial d^{cal}}{\partial m}$ is a particular matrix in inverse theory. This is the so-called *Fréchet* derivatives matrix $\mathbf{F}$. It can also take the name of Jacobian or sensitivity matrix. It documents the

sensitivity of the data, that is, the perturbation expected in the data due to a perturbation in the model.

The Hessian matrix is given by:

$$\mathbf{H} = \frac{\partial^2 \chi_d}{\partial m^2} = \Re \left[\mathbf{F}^\dagger \mathbf{F} \right] + \Re \left[(\frac{\partial^2 d^{cal}}{\partial m^2})^t (\Delta d^\dagger, ..., \Delta d^\dagger) \right] \qquad \text{(III.18)}$$

An extra differentiation with respect to m of equation III.15 and neglecting terms beyond the second-order gives:

$$\nabla \chi_d (m_0 + \Delta m) = \nabla \chi_d(m_0) + \nabla^2 \chi_d \, \Delta m \qquad \text{(III.19)}$$

As $m_0 + \Delta m$ is considered a solution of the inverse problem in the neighbouring of m_0, a local minimum is reached for the left-hand side equal to zero. The perturbation of the starting model that solves the problem posed in equation III.14 can be therefore written as:

$$\Delta m = -\mathbf{H}^{-1} \nabla \chi_d \qquad \text{(III.20)}$$

Newton's method

The optimisation problem searching the model update from equation (III.20) is called **Newton's method** . Nevertheless, Δm should be sufficiently small to respect the Taylor series expansion of equation (III.15), thus model m_0 should be sufficiently close to the model solution. The Newton method is an effective algorithm to determine the descent direction. To evaluate the model step, the gradient preconditionned by the inverse Hessian matrix of the cost function is computed as a descent direction. The inverse Hessian contains information on the curvature of the cost function at the evaluated model vector and re-equilibrates the differences of sensitivity that can occur between parameters of different classes in a multi-parameter problem, or due to an impaired illumination(Operto et al., 2013; Pratt et al., 1998).

A line-search is performed to account for the non-linearity of the problem and to ensure the decrease of the objective function according to specific conditions and solve the optimal step α:

$$m_{k+1} = m_k - \alpha_k \underbrace{\mathbf{H}^{-1} \nabla \chi_d}_{\Delta m} \qquad \text{(III.21)}$$

Newton's method has a quadratic rate of convergence in the neighbourhood of the solution (Nocedal and Wright, 2006).

Gauss-Newton method

In most cases, the second term of the Hessian (equation (III.18)) is avoided in large problems. Indeed, its computation requires huge calculation cost for the determination of the differentiation of the Fréchet derivatives matrix. It takes into account the second-order terms of the cost function and is commonly supposed small as the residual is small

and if the problem is quasi-linear (Tarantola, 2005). Indeed, this term is related to the non-linearity of the inverse problem and is zero for a linear problem. Therefore, a variant of the Newton method uses an approximation of the *exact* Hessian (equation (III.18)). This is the **Gauss-Newton method** (GN), where the second order terms are dropped to form the *approximated Hessian* $\mathbf{H^a}$. The approximate Hessian is therefore given as :

$$\mathbf{H^a} = \Re\left[\mathbf{F}^\dagger\mathbf{F}\right] \tag{III.22}$$

The model at iteration $k+1$ is thus obtained from:

$$m_{k+1} = m_k - \alpha_k \underbrace{\mathbf{H^{a-1}}\nabla\chi_{d_k}}_{\Delta m} \tag{III.23}$$

The solution Δm of the system in equation (III.20) can therefore be determined by evaluating the reciprocal of the Hessian $\mathbf{H^{a-1}}$, or a solution can be obtained by solving a system of linear equations through the reformulation :

$$\mathbf{H^a}\Delta m = -\nabla\chi_d \tag{III.24}$$

Therefore several advantages to the GN method (Nocedal and Wright, 2006):

1. As mentioned before, the second order term can be neglected in many situations, therefore the GN gives similar convergence to that of Newton's method with no computation of the non linear part of the Hessian.

2. $\mathbf{H^a}$ is simply evaluated using the Fréchet derivative matrix, which is frequently computed at this point for the gradient evaluation in equation (III.17) and thus can be free of additional expensive computing and storage.

3. Δ_m can be solved iteratively by determining the solution of the problem $\mathbf{J}\Delta m = -\delta d$ (inferred from equation (III.20)) without stocking explicitly $\left[\mathbf{F}^\dagger\mathbf{F}\right]$

4. GN has a convergence rate lower than quadratic but significantly higher than linear in the neighbourhood of the solution.

Steepest-descent method (STD)

The *gradient* of equation (III.12) with respect to the model parameters represents the direction of increase of the objective function at the position of m_k. Therefore, the opposite of the gradient points toward the descent direction. The steepest descent method seeks thus to minimize the objective function by moving simply along the *steepest descent* direction using the gradient of the cost function as :

$$m_{k+1} = m_k - \alpha_k\nabla\chi_{d_k} \tag{III.25}$$

The steepest descent method is equivalent to approximating the Hessian in its simplest form $H = I$ an identity matrix in equation (III.21). Therefore, the optimization relies only on the gradient of the cost function and a line search determining the optimal step

length α_k with a linear rate of convergence. Others optimization methods called Quasi-Newton, are using different estimations of the Hessian matrix for preconditioning the descent direction and improving the convergence. One of the most popular is the ℓ-BFGS method that estimates an approximation of the Hessian matrix from the gradient of ℓ previous iterations (Nocedal and Wright, 2006).

If a model regularization term is taken into account in equation (III.11), the gradient of the model objective function, as well as its Hessian must be added to their corresponding terms ($\nabla\chi = \nabla\chi_d + \lambda\nabla\chi_m$ and equivalently for the Hessian).

Line search

α is an optimal step length determined using **a line-search** (Nocedal and Wright, 2006) to ensure the decrease of the cost function[f]. Several conditions on the step length of the cost function exists and are applied during the line-search, as the *Armijo* (Armijo, 1966) or the *Wolfe conditions* (Wolfe, 1969). They enforces specific update conditions as a sufficient decrease of the cost function and/or an increase of its curvature at the solution. The advantage of this method is its simplicity of implementation. Only the gradient of the cost function is needed to iterate the model towards a solution. The Wolfe condition

mixes-up the *Armijo* condition with a constraint on the curvature[g].

❏ The 1st Wolfe condition is the *Armijo* condition, that ensure the sufficient decrease of the cost function with $c_1 \in [0,1]$. c_1 is a small value set to 10^{-4} as suggested by Nocedal and Wright (2006). p_k is the descent direction ($p_k = -\nabla\chi(m_k)$ for the STD method).

$$\chi(m_k + \alpha p_k) \leq \chi(m_k) + c_1\alpha\nabla\chi_k^t p_k \tag{III.26}$$

❏ The 2nd Wolfe condition is the *curvature condition* that enforces the condition of a sufficient decrease of the cost function by imposing a condition on its slope at the evaluated point. A higher slope is expected to ensure that the convergence could not decrease significantly with a greater step α. $c_2 \in [c_1,1]$ and is set here at 0.9.

$$\chi(m_k + \alpha_k p_k)^t p_k \geq c_2\nabla\chi_k^t p_k \tag{III.27}$$

III.2.2   POLYEM3D inversion code

POLYEM3D is a versatile code with many features available for the inversion user. In this part, the inversion options available in POLYEM3D code are briefly detailed. It was presented previously that the heart of an inverse problem relies on the estimation of the Fréchet derivative matrix, the gradient and the Hessian of the objective function if needed. The code computes the gradient directly and/or the Fréchet derivative matrix through

---

[f]the decrease of the cost function is an essential condition but some algorithm are *non-monotone*, that is, the decrease is not guaranteed at each iteration in an attempt to avoid to be trapped in narrow curved valley of the objective function (Dai, 2002; Nocedal and Wright, 2006).

[g]A visual representation of the right-hand side of the *Armijo* condition and the curvature condition are presented by Nocedal and Wright (2006) in figures 3.3 and 3.4

the adjoint state method (Plessix, 2006; Plessix and Mulder, 2008). For gradient based methods that only need the gradient, the calculation of the computationally expensive Fréchet derivative matrix and storage can thus be avoided. However, GN method still needs the explicit computation of the Fréchet derivative matrix to solve equation (III.24). Considering GN inversion, POLYEM3D does not compute the Hessian and its inverse explicitly and solves a modification of the system of equations III.24 through the LSQR algorithm to obtain the optimal model perturbation Δm. Therefore, the adjoint state method is presented in a following section with insights on the POLYEM3D GN solution.

Seiscope toolbox and line seach

POLYEM3D inversion code relies on the Seiscope optimization toolbox (Métivier and Brossier, 2016), a reverse communication algorithm, combined with an efficient line search based on a bracketing strategy. First order (Steepest descent (STD), nonlinear conjugate gradient (NLCG)) and second-order optimization methods (ℓ-BFGS) are available and require only the computation of the objective function and its gradient at each iteration, or reversed communication step. In the following, the critical part of the toolbox dealing with the general line search strategy is presented. For more details on the toolbox, the reader is referred to the paper of Métivier and Brossier (2016). At each step, the boundaries of the model parameters are checked to ensure to keep the solution at the given iteration in the possible domain, as well as the Wolfe Conditions. If one of the conditions is not respected or a boundary is reached, the step length is adjusted following the bracketing strategy of Bonnans et al. (2006, Section 3.1). The workflow in figure III.5 summarizes the steps followed by the line search.
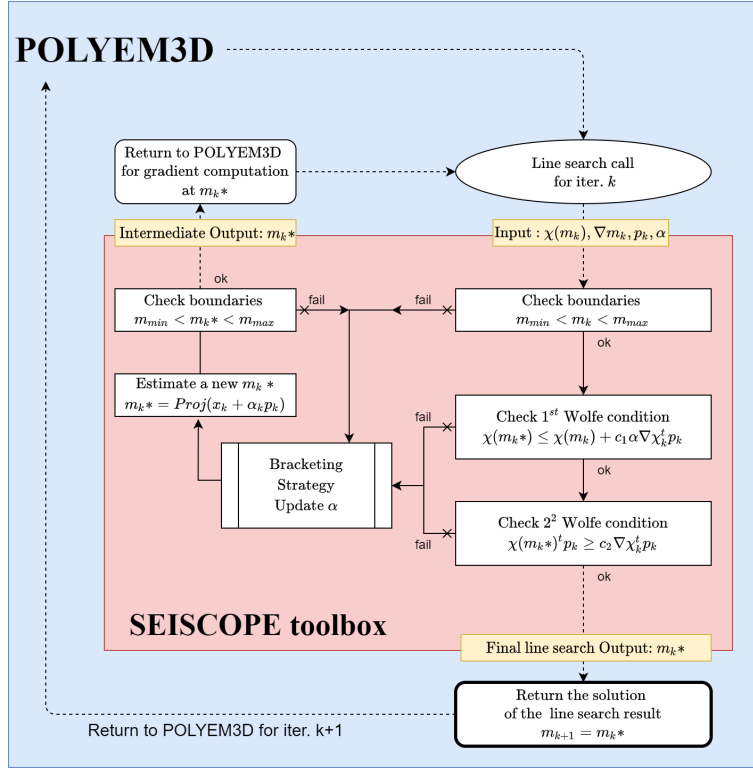
Figure III.5: *Workflow of the general line search algorithm of the Seiscope optimization toolbox (Métivier and Brossier, 2016)*

Adjoint state method for the calculation of the gradient

The gradient of the objective function requires the Fréchet derivative matrix after equation (III.17) in order to undertake a gradient-based optimization. Computing the Fréchet derivative matrix for the 3D EM problem is computationally expensive due to the very large number of model cells needed for an accurate response with a direct solver approach. The calculation of the 3D gradient POLYEM3D does not rely on the Fréchet derivative matrix for gradient-based method (that does not require the approximated Hessian, *i.e.* STD, NLCG, or ℓ-BFGS). A more efficient strategy is implemented for the calculation of the gradient called the *Adjoint state method*. The Adjoint state method applied to our case, is resumed in the following after the recipe proposed by Plessix (2006).

State equations

At first a list of the *state equations* must be established, which are the equations describing the forward problem, as well as the link towards the inversion domain. The state functions are associated to independent state variables. Three state function can be derived from the forward problem described in section III.1 and from forward to inverse domain operator:

❏ the forward problem system, defined as :

$$A(\sigma)E^S = b^S \qquad \text{with} \quad b^S = -i\omega(\sigma - \sigma^P)E^P, \tag{III.28}$$

with $A(\sigma)$ the system of finite-difference equations presented in section III.1. σ is the conductivity vector defined for each cell of the forward grid.

❏ the interpolation operator Q, relating the field calculated on the forward grid to data measured at the receiver positions (Q includes the vector field reorientation, the type of field extracted, the curl operator for magnetic field, *etc...*). Each data recording at a receiver position is considered as an independent data.

$$QE^S = d_{cal} \qquad \text{(III.29)}$$

❏ the operator $C(\sigma)$ that link the forward to the inverted parameter m, which contains the change of variable and the change of grid operators, defined as:

$$C(\sigma) = m \qquad \text{(III.30)}$$

Three state variables are obtained and will be associated to an *adjoint state* variable of same dimensions:

State function	State variable	Adjoint variable
$A(\sigma)E^S = b^S$	E^S	λ_e
$QE^S = d_{cal}$	d_{cal}	λ_d
$C(\sigma) = m$	σ	λ_σ

Augmented functional $\mathcal{L}$ recipe

1. At first, the augmented functional (or associated Lagrangian) $\mathcal{L}$ defining the adjoint state problem introducing the objective function, can be defined following Plessix (2006) as :

$$\begin{aligned} \mathcal{L}(m, \sigma, d_{cal}, E^S, \lambda_\sigma, \lambda_d, \lambda_e) = \chi(d^{cal}) \quad &- < \lambda_\sigma, C(\sigma) - m > \\ &- < \lambda_d, QE^S - d_{cal} > \\ &- < \lambda_e, A(\sigma)E^S - b^s >, \end{aligned} \qquad \text{(III.31)}$$

with $<,>$ representing the dot product notation. The problem of the adjoint state method seeks therefore a solution that minimizes the objective function with respect of m, under the constraints of each state function.

2. The adjoint state equations are then derived looking for the saddle points of $\mathcal{L}$ with respect to each state variable defined previously. <u>**The state variables and the adjoint state variables are considered independent of m**</u> .

   (a) $\frac{\partial \mathcal{L}}{\partial \mathbf{d_{cal}}} = \mathbf{0}$

   $$\begin{aligned} \frac{\partial \mathcal{L}}{\partial d_{cal}} &= \partial_d \chi(d^{cal}) - \partial_d < \lambda_d, QE^S - d_{cal} > \\ 0 &= (d_{cal} - d_{obs}) + \lambda_d \\ \lambda_d &= -\Delta d \end{aligned} \qquad \text{(III.32)}$$

A first adjoint state equation is obtained, which allows the determination of the adjoint-state variable λ_d that corresponds simply to the residual vector:

$$\boxed{\lambda_d = -\Delta d} \tag{III.33}$$

(b) $\frac{\partial \mathcal{L}}{\partial \mathbf{E^S}} = \mathbf{0}$

$$\begin{aligned}
\frac{\partial \mathcal{L}}{\partial E^s} &= -\partial_e < \lambda_e, A(\sigma)E^S - b^s > -\partial_e < \lambda_d, QE^S - d_{cal} > \\
0 &= -(Q)^t \lambda_d - A(\sigma)^\dagger \lambda_e \\
A(\sigma)^\dagger \lambda_e &= (Q)^t \Delta d
\end{aligned} \tag{III.34}$$

The second adjoint state relation is a linear system "$Ax = b$", that can be solved to get the adjoint field λ_e by back-propagating the residual on the grid equivalently to a source term. The matrix A is the same as the forward problem and is already factorized, thus a similar form can be used taking the conjugate (noted $\overline{}$) of the previous relationship to preserve the A matrix :

$$\boxed{A(\sigma)\overline{\lambda_e} = (Q)^t \overline{\Delta d}} \tag{III.35}$$

(c) $\frac{\partial \mathcal{L}}{\partial \sigma} = \mathbf{0}$

$$\begin{aligned}
\frac{\partial \mathcal{L}}{\partial \sigma} &= -\partial_\sigma < \lambda_\sigma, C(\sigma) - m > -\partial_\sigma < \lambda_e, A(\sigma)E^S - b^s > \\
0 &= -\partial_\sigma C(\sigma)^\dagger \lambda_\sigma - \left[\partial_\sigma (A(\sigma)E^S)^\dagger - \partial_\sigma b^\dagger)\right] \lambda_e \\
\lambda_\sigma &= -(\partial_\sigma C(\sigma)^\dagger)^{-1} \left[\partial_\sigma (A(\sigma)E^S)^\dagger - \partial_\sigma b^\dagger)\right] \lambda_e
\end{aligned} \tag{III.36}$$

If no grid transformation a parametrization of m equal to the conductivity medium σ as stated in the forward problem as :

$$m = C(\sigma) = \sigma \tag{III.37}$$

A relation between λ_σ and the adjoint field λ_e is obtained in the last adjoint state function:

$$\boxed{\lambda_\sigma = -\left[\partial_\sigma (A(\sigma)E^S)^\dagger - \partial_\sigma b^\dagger)\right] \lambda_e} \tag{III.38}$$

3. The third step is to evaluate the gradient, which correspond to the derivative of $\mathcal{L}$ with respect to m considering each state variable independent of m (comprising d^{cal} in the cost function):

$$\begin{aligned}
\frac{\partial \mathcal{L}}{\partial m} &= -\partial_m < \lambda_\sigma, C(\sigma) - m > \\
\frac{\partial \mathcal{L}}{\partial m} &= \lambda_\sigma
\end{aligned} \tag{III.39}$$

The gradient is therefore obtained with respect to the adjoint variable λ_σ for which the expression was determined in equation (III.38):

$$\boxed{\partial_m \chi = \lambda_\sigma} \tag{III.40}$$

Gradient solution

Using the adjoint field solution λ_e obtained through the solution of the linear system $Ax = b$ (eq. (III.35)), the gradient can be computed with :

$$\partial_m \chi = \lambda_\sigma = -(\partial_\sigma C(\sigma)^t)^{-1} \left[\partial_\sigma (A(\sigma)E^S)^\dagger - \partial_\sigma b^\dagger) \right] \lambda_e \qquad (III.41)$$

❏ Derivation of A matrix and the source term (equation (III.3) and (III.4)) by σ results in:

$$\partial_\sigma (A(\sigma)E^S)^\dagger = (i\omega\mu)^\dagger E^{S\dagger} \qquad (III.42)$$

❏ and for the source term:

$$\partial_\sigma b^* = (-i\omega\mu)^* E^{P*} \qquad (III.43)$$

The gradient of the objective function is then obtained for a real conductivity parametrization $(m = \sigma^r)$ with :

$$\boxed{\partial_m \chi \quad = \quad - \left[i\omega\mu E^{tot} \right]^\dagger \lambda_e} \qquad (III.44)$$

Gauss-Newton solution

The solution of the Gauss-Newton system is:

$$\begin{aligned}
\mathbf{H^a}\Delta m &= -\nabla\chi_d \\
[\mathbf{F}^\dagger\mathbf{F}]\Delta m &= -\mathbf{F}^\dagger\Delta d
\end{aligned} \qquad (III.45)$$

Solving this system is equivalent to solving in a least square sense the equation:

$$\mathbf{F}\Delta m = -\Delta d \qquad (III.46)$$

It allows the resolution of a linear system of equations to determine the model update as discussed previously with the difference that F is not sparse nor a square matrix ($F_{i,j}$, with $i = 1, ..., N_d$ and $j = 1, ..., N_m$). As the model should be regularized this relation does not hold under this state anymore. Indeed, the complete regularized and weighted problem expressed without regularization in equation III.45 is formulated as:

$$\Re[\mathbf{F}^\dagger\mathbf{F}]\Delta m = -[\Re(\mathbf{F}^\dagger W_d \Delta d) + \lambda\nabla_m\chi_m(m)], \qquad (III.47)$$

with Δd the data residuals vector, λ the Lagrange multiplier in equation III.11 (trade-off between data and model regularization). $\nabla_m\chi_m(m)$ is the gradient of the cost function associated to the model parameters (equations (III.50),(III.51) and (III.49)) which can be rewritten under the form $\nabla_m\chi_m(m) = W_m(m - m_{ref})$ with W_m a model weighting matrix depending on the type of regularization chosen[h]. In order to solve this problem, the following system is solved using the LSQR algorithm (Paige and Saunders, 1982) as presented in the paper of Grayver et al. (2013):

---

[h]$W_m = L$ for the maximum smoothness constrain, $W_m = I$ for the minimum norm and, $W_m = \sqrt{P}$ for the minimum support regularization with the matrix $P_{ii} = (e^2)/(|m_i^{n-1} - m_i^{ref}|^2 + e^2)^2$.

$$\begin{pmatrix} \hat{F} \\ \sqrt{\lambda} W_m \end{pmatrix} \Delta m = - \begin{pmatrix} W_d \hat{\Delta} d \\ \sqrt{\lambda} W_m (m - m_{ref}) \end{pmatrix} \qquad (\text{III.48})$$

Note on the Fréchet solution:

The Fréchet derivative matrix necessary to solve the system of equations (III.48) is evaluated following a similar scheme as the gradient. The adjoint state method is used to compute the Frechet derivative matrix with the back-propagation of a unit residual in equation (III.35) to obtain the solution of the Fréchet for the given data. The drawback is that this step must be done independently for each data to fill the Fréchet derivative lines independently. However, considering the 3D CSEM finite-difference problem, $N_m >> N_d$, this strategy is computationally very efficient compared to a perturbation method that requires to perturb each cell individually and solve the forward finite-difference system of equation (III.4) with a factorization of A at each perturbation. On the contrary, no supplementary factorization is needed to solve the adjoint system of equation (III.35) which has thus to be solved N_d times.

Parametrization and regularization

Model parametrization and inversion grid

The forward problem solved by POLYEM3D is formulated using the conductivity of the medium as presented in section III.1, however the parameterization of the medium properties in the inverse problem can differ from the forward problem parametrization. The choice of parametrization is of crucial importance. It will impact the sensitivity of the parameters and in multi-parameter cases, the cross-coupling that can exist between parameters of different classes can be affected by a different formulation. The logarithm of the resistivity is a popular choice in EM resistivity imaging problem. Several parametrizations of the medium parameter are available in POLYEM3D:

❏ the conductivity σ

❏ the resistivity ρ

❏ the logarithm of the resistivity (or conductivity)

❏ a logarithmic form of a bounded resistivity $log(\frac{\rho - \rho_{min}}{\rho_{max} - \rho})$

The choice of the inversion grid enters also in the parametrization of the inverse problem. Indeed, the grid used to calculate the forward problem (called the *forward grid*) is not necessarily the grid used to parametrize the inverse problem and some change of grid operators can be used. A different grid or support can be chosen and will be named the *inversion grid*. The inversion grid is commonly a coarser grid compared to the forward grid as the latter needs to be sufficiently fine for numerical accuracy. POLYEM3D offers several choices considering the inversion grid and can be based on:

❏ a bounded domain of the forward grid combined to a projection on smooth basis function.

❏ a nearest neighbour interpolation on a defined inversion grid.

❏ a linear or a cubic B-spline parametrization by defining the nodes position (De Boor and De Boor, 1978).

Notice that the spline parametrization imposes an implicit smoothness condition on the inversion result compared to a coarse block grid model.

Model Regularization

Regularization of the inverse problem is generally necessary for a good convergence of the optimization due to an ill-posed problem or perturbation in the data. The regularization is defined by the model objective function χ_m introduced in equation (III.11). The regularization defines *a priori* information and constrains the inverse problem. Many types of regularization are possible, depending on the specificities of the problem and prior information available. Several types of common regularization described in Grayver et al. (2013) [i] are available in POLYEM3D:

❏ a maximum smoothness constraints, that ensures the smoothness of the solution compared to the reference model with **L** the Laplacian operator. If $m^{ref} = 0$ the regularization is similar as the popular Occam algorithm (Constable et al., 1987) that minimize the *roughness* of the solution.

$$\chi_m^{smooth} = \frac{1}{2}||\mathbf{L}(m - m^{ref})||_2^2 \qquad (III.49)$$

❏ a minimum-norm constraints, that restricts the model misfit from a reference model.

$$\chi_m^{norm} = \frac{1}{2}||m - m^{ref}||_2^2 \qquad (III.50)$$

❏ a minimum support stabilizing functional that enforces the concentration of the perturbation in a reduced area compared to a reference model. The constant e stabilizes the functional for $m_j - m_j^{ref} \to 0$ and controls the compactness of the solution.

$$\chi_m^{MS} = \sum_{i=1}^{N_m} \frac{(m_i - m_i^{m^{ref}})^2}{(m_i - m_i^{m^{ref}})^2 + e} \qquad (III.51)$$

Reference model terms can be chosen in several ways as 1) $m^{ref} = m_0$ to constrain the deviation from the starting model or from an *a priori* model, 2) $m^{ref} = m_{n-1}$ to constrain the deviation between each iteration. In following work, the maximum smoothness regularization is preferred, as it respects the diffusive physics of the EM wave in

---

[i] More details are available on these regularization in the paper of (Grayver et al., 2013) as their first and second derivatives needed for the gradient and Hessian estimation.

the quasi-static approximation domain. Furthermore, in my inversion approach I always tend to minimize the use of *a priori* information, therefore a smoother result is generally preferred. Indeed, a focusing regularization could be preferred when a sufficient *a priori* information can justify such a strong constrain on the inversion as underlined by Zhdanov (2009) in his conclusion.

Conclusion

POLYEM3D is a versatile 3D finite-difference modelling and inversion code for frequency-domain controlled-source electromagnetic (CSEM) and magnetotelluric (MT) data. In this chapter, the basics of the 3D code operation were presented. The code follows a finite-volume approach to solve the electrical formulation of the Helmholtz equation on a staggered 3D grid using a massively parallel direct solver. A rigorous interpolation ensures the correctness of the solution at the air/ground interface presenting a strong resistivity discontinuity. It allows the inversion of EM data for various acquisition geometries and provides a large choice of parametrization of the inverse problem. Gradient-based optimization are available, facilitated by the use of a reverse communication algorithm, that essentially takes the gradient in input. Furthermore, a Gauss-Newton optimization methods is implemented using an LSQR algorithm to solve the GN system and determine the model update with a higher convergence rate. The POLYEM3D code presented here is therefore the basis of the following work dealing with the implementation of a CR in order to take into account induced polarization effects as well as EM induction. The implementation into the forward problem and in the inversion part of POLYEM3D are discussed in the following chapter. The structure of the code was preserved in order to be compatible with the original code, whereas the multi-parameter formulation is introduced in a general formulation to facilitate further implementation.

CHAPTER IV

Complex resistivity in CSEM data

This chapter deals with the IP effects observed in CSEM data. A synthetic study of CSEM data sensitivity to CR is carried out for 1D and 3D media. The implementation of the CR to the pre-existing codes is briefly discussed with some validation tests. The sensitivity study is then presented following a modelling framework with gradually increasing complexity.

IV.1 Complex resistivity implementation

IV.1.1 Method

As presented in detail in the previous chapter, to obtain EM responses of a 3D resistivity distribution the POLYEM3D code solves secondary electrical formulation of Maxwell's equations using a scattered field approach. Hence, the primary field $\boldsymbol{E_p}$ containing source information, is solved at first at the 3D staggered grid positions for a reference resistivity medium. A semi-analytical 1D code (SA1D) solves the primary field for a 1D layered medium ensuring an accurate and fast solution. The finite-difference method is then used to solve the secondary electric field for the 3D model containing a resistivity anomaly. In fact, both stages take as input a medium described by resistivity and permittivity value. Indeed, the medium is formulated in the forward problem by a complex vector σ with a constant and real conductivity σ^r and an imaginary part associated to the dielectric permittivity ϵ

$$\sigma = \sigma^r + i\omega\epsilon \qquad\qquad (\text{IV}.1)$$

Implementing a CR in order to take into account induced polarization effects in the forward problem is then straightforward by using a simple change of variable. Indeed, as for CR the permittivity is a complex parameter (that can as well be frequency-dependent). Complex conductivity and complex permittivity can then be seen as effective parameters that gather the real part of one parameter with the imaginary part of the other:

$$\sigma = (\sigma^r + i\sigma^q) + i\omega(\epsilon^r + i\epsilon^q)$$

$$\sigma = (\sigma^r - \omega\epsilon^q) + i\omega\left(\epsilon^r + \frac{\sigma^q}{\omega}\right)$$

$$\sigma = \underbrace{(\sigma^r - \omega\epsilon^q)}_{\sigma_{eff}} + i\omega\underbrace{\left(\epsilon^r + \frac{\sigma^q}{\omega}\right)}_{\epsilon_{eff}} \qquad\qquad\qquad \text{(IV.2)}$$

Both parameters are measured together in EM measurements and are inseparable. Equation (IV.2) shows that polarization mechanisms that occur at low frequencies can thus be seen as a significant propagation term in the quasi static domain. As this work concerns the quasi-static domain essentially, $\sigma_{eff} \simeq \sigma^r$ is considered. On the other hand, the choice to keep a real and constant part of the dielectric permittivity was made to preserve propagation effects that can occurs for longer offsets and higher frequencies. Its value is kept nevertheless to that in free-space. As this work is based on a frequency domain code, each frequency is solved independently for a given model. Adding the frequency dependence of the complex conductivity, it yields finally to a medium parameter σ formulated in the forward problem as :

$$\sigma(\omega) = \sigma^r(\omega) + i\omega\epsilon_{eff}(\omega) \qquad \text{with } \epsilon_{eff} = \epsilon_0 + \frac{\sigma^q(\omega)}{\omega} \qquad\qquad \text{(IV.3)}$$

Using a simple change of variable, the code was efficiently adapted to solve EM responses with induced polarization effects due to a complex conductivity that can be frequency-dependent. The code was separated in two modes to simplify the input files. The first considers a constant CR, adding a vector describing the imaginary part of the resistivity in the medium for each cell, and the second mode considers the frequency dependence. In the latter, the CR medium is described by two matrices instead of a simple vector, with a value in each cell and for each frequency calculated. This description will not hold when looking to recover these parameters by inversion of EM data due to an inverse problem that is already under-determined. Indeed, the size of the problem will grow drastically with the number of frequencies evaluated and some lateral constrains will have to be added on the resistivity spectrum. This problematic will be the subject of the following chapter.

IV.1.2   Validation of the forward problem

To evaluate the correctness of the formulation and the code accuracy some validation were performed. The staggered-grid finite-difference scheme of the code was already validated for the main POLYEM3D code and was not evaluated further. At first the results of the 1D semi-analytic solver (referred as the 1DSA solution) was compared to analytic solutions for an homogeneous half-space with a constant CR. The 1DSA code is based on the routines of the code *EM1D* (Kim et al., 1997; Lee et al., 2011; Song et al., 2002). In a second step, the solution of the 3D code was validated by comparing the 1DSA solution

of a conductive polarizable layer in a homogeneous medium to the 3D finite-difference solution. To solve the problem, the primary field in the corresponding homogeneous half-space was used, whereas the secondary field due to the layer was estimated by finite-difference. Several source configurations (Figure IV.1) were investigated:

❏ the case of a horizontal electric dipole in the axe and oriented perpendicularly to the reception profile direction ($HED^{\perp}$). This configuration is also known as *broadside*.

❏ the case of a horizontal electric dipole in the axe and oriented parallel to the reception profile direction ($HED^{//}$). This configuration is also known as *in-line* .

❏ the case of a vertical magnetic dipole VMD.
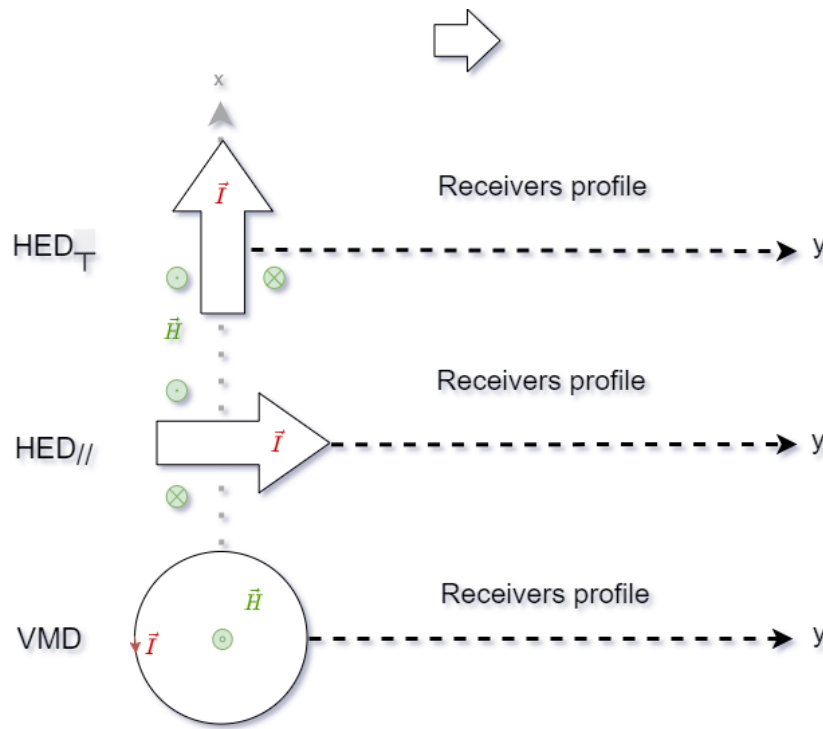
Figure IV.1: *Sketch of the different types of sources considered. $HED^{\perp}$, $HED^{//}$ are broadside and in-line horizontal electrical dipole. VMD is a vertical magnetic dipole, i.e. representing a horizontal loop of current.*

Validation of the 1DSA solution

The solutions of the electric and magnetic fields measured at the surface of an homogeneous half-space are found in Zonge and Hughes (1991) and were derived from Wait (1961) and Bannister (1966) for a grounded horizontal electrical dipole :

$$E_r = \frac{p\,cos(\Phi)}{2\pi\sigma r^3}[1 + e^{-ikr}(1 + ikr)] \tag{IV.4}$$

$$E_\Phi = \frac{p\,sin(\Phi)}{2\pi\sigma r^3}[2 - e^{-ikr}(1 + ikr)] \tag{IV.5}$$

$$H_r = \frac{p\,sin(\Phi)}{2\pi r^2}\left(3\mathcal{I}_1\left(\frac{ikr}{2}\right)\mathcal{K}_1\left(\frac{ikr}{2}\right)\right.$$
$$\left. + \frac{ikr}{2}\left[\mathcal{I}_1\left(\frac{ikr}{2}\right)\mathcal{K}_0\left(\frac{ikr}{2}\right) - \mathcal{I}_0\left(\frac{ikr}{2}\right)\mathcal{K}_1\left(\frac{ikr}{2}\right)\right]\right) \tag{IV.6}$$

$$H_\Phi = -\frac{p\,cos(\Phi)}{2\pi r^2}\left(\mathcal{I}_1\left(\frac{ikr}{2}\right)\mathcal{K}_1\left(\frac{ikr}{2}\right)\right) \tag{IV.7}$$

$$H_z = -\frac{3p\,sin(\Phi)}{2\pi k^2 r^4}[1 - e^{-ikr}(1 + ikr - \frac{1}{3}k^2 r^2)] \tag{IV.8}$$

(r, Φ, z) are the cylindrical coordinates (z positive downward) centered at the transmitter position which is oriented towards $\Phi = 0$ direction. p is the moment of the electric dipole obtained by multiplying the injected current (I) and the length of the cable (ℓ) $p = I\ell$. $\mathcal{I}_n, \mathcal{K}_n$ are the modified Bessel functions of the nth order.

Another common source in EM geophysical application concerns vertical magnetic dipole composed by a horizontal loop with no coupling to the ground. The solutions for the VMD source are given by (Wait, 1951) and Bannister (1966):

$$E_\Phi = \frac{3im\mu\omega}{2\pi k^2 r^4} \cdot \left[1 - \left(1 + ikr - \frac{1}{3}k^2 r^2\right)e^{-ikr}\right] \tag{IV.9}$$

$$H_r = \frac{mk^2}{4\pi r^3}\left[\mathcal{I}_1\left(\frac{ikr}{2}\right)\mathcal{K}_1\left(\frac{ikr}{2}\right) - \mathcal{I}_2\left(\frac{ikr}{2}\right)\mathcal{I}_2\left(\frac{ikr}{2}\right)\right] \tag{IV.10}$$

$$H_z = \frac{9m}{2\pi k^2 r^5} \cdot \left[1 - \left(1 + ikr - \frac{4}{9}k^2 r^2 - \frac{1}{9}ik^3 r^3\right)e^{-ikr}\right], \tag{IV.11}$$

$$\tag{IV.12}$$

m is the magnetic moment of the dipole in equations above and is obtained by the product of the current intensity circulating in the loop (I), the surface area of the loop (S) and the number of spires (n) giving $m = ISn$.

In the following images, the 1DSA solutions are compared to the analytical solutions for several cases according to figure IV.1 with a reception profile considered in the Y direction. These cases are :

❏ the electric field of a $HED_\perp$ source which is oriented cross-line to the reception profile according to equations (IV.4) and (IV.5), as the radial component vanishes perpendicularly to the source axis.

❏ the electric field of a $HED^{//}$ source which is thus oriented in-line to the reception profile as the orthoradial component controlled by the sine of the orientation vanishes.

❏ the electric field of a VMD source which curls around the source and has thus an orientation cross-line to the reception profile.

❏ the vertical magnetic field of the VMD source.

The choice to present here the electric field was made in agreement with the following work which will focus more on electric field. As the vertical magnetic dipole is more frequently used to study the magnetic response of the ground, its magnetic response was presented.

Figures IV.2 to IV.5 show the in-phase and the quadrature phase fields for both solution in these different cases. They show the relative error (in percent) between the real or imaginary part of the component considered $\mathcal{F}(F)$ ($\mathcal{F}$ being the real or imaginary part function) relative to the analytic solution or relative to the total amplitude of the component. The second option allows to discriminate errors that occurs when a component vanishes compared to the other, which is thus not significant.

$$\Delta_{\mathcal{F}(F)} = \left| \frac{\mathcal{F}(F_{SA}) - \mathcal{F}(F_{AN})}{\mathcal{F}(F_{AN})} \right| \tag{IV.13}$$

$$\Delta_{|F|} = \left| \frac{\mathcal{F}(F_{SA}) - \mathcal{F}(F_{AN})}{|F_{AN}|} \right| \tag{IV.14}$$

The results are displayed from 0.01 Hz to 10 kHz and for a receiver with at an offset of 1 skin depth in the background at 100 Hz ($r \simeq \delta_{skin} \simeq 503$ m) to investigate the response from the near field at low frequencies to the edge of the far field at high frequencies ($\frac{\delta_{skin}}{10} \geq \delta_{skin}(f) \simeq 10\delta_{skin}$).
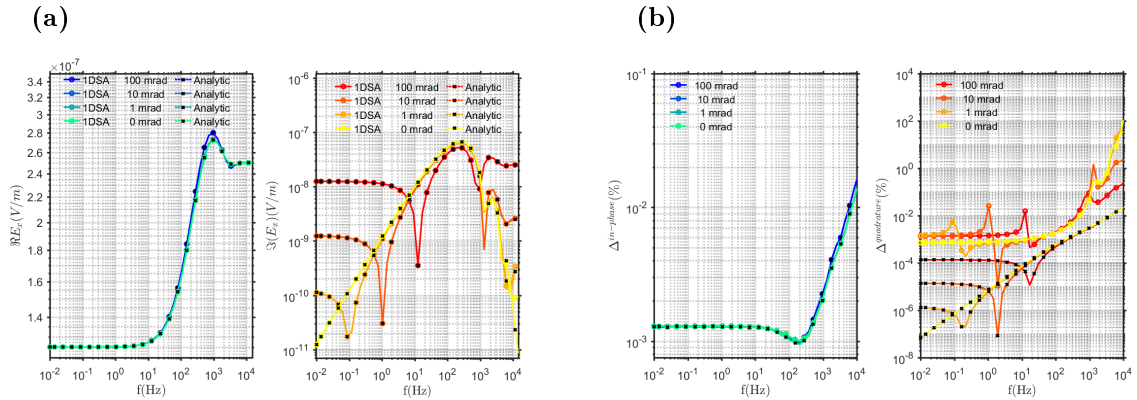

Figure IV.2: *Comparison between the 1DSA and the analytic electric field solution (Zonge and Hughes, 1991) for a $HED_\perp$ source over a homogeneous halfspace of 100 Ω.m and several CR phase values. a) In-phase and out-of-phase fields are presented on the left and b) the relative errors are presented on the right. Relative errors were computed with respect to the corresponding part of the field (Colored dot) or with respect to the total amplitude (black cross)*
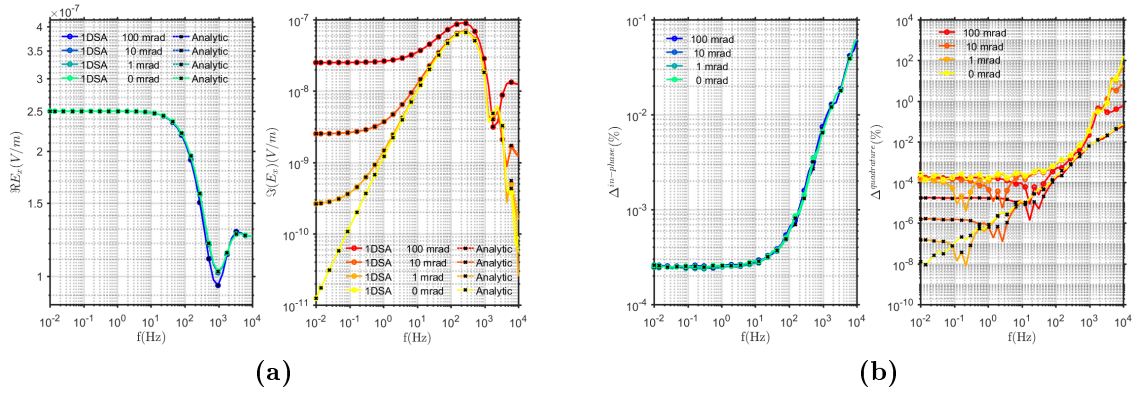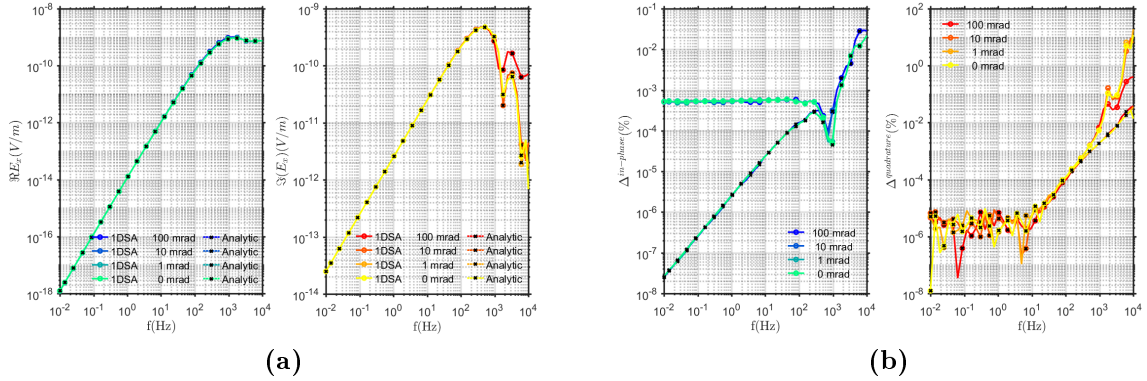
Figure IV.3: *Comparison between the 1DSA and the analytic electric field solution ([Zonge and Hughes](), [1991]()) for a $HED_{//}$ source over a homogeneous halfspace of $100\,\Omega.m$ and several CR phase values. a) In-phase and out-of-phase fields are presented on the left and b) the relative errors are presented on the right. Relative errors were computed with respect to the corresponding part of the field (Colored dot) or with respect to the total amplitude (black cross)*
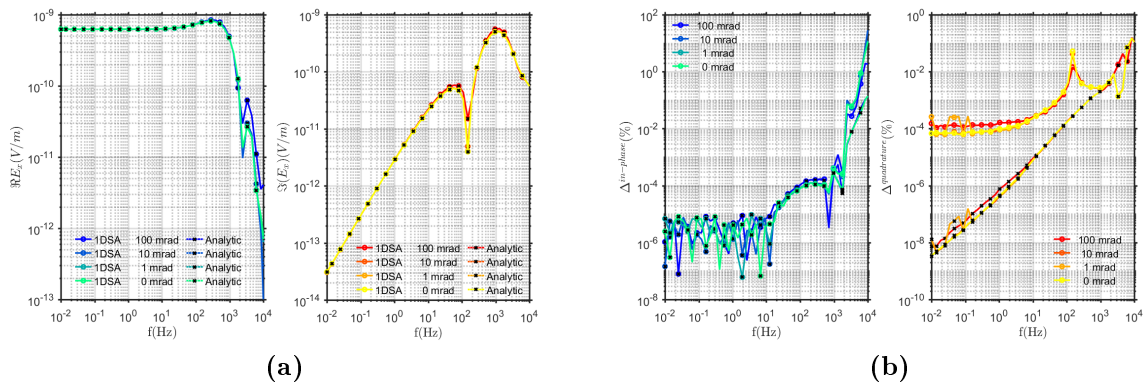

Figure IV.4: *Comparison between the 1DSA and the analytic electric field solution ([Zonge and Hughes](), [1991]()) for a VMD source over a homogeneous halfspace of $100\,\Omega.m$ and several CR phase values. a) In-phase and out-of-phase fields are presented on the left and b) the relative errors are presented on the right. Relative errors were computed with respect to the corresponding part of the field (Colored dot) or with respect to the total amplitude (black cross)*

Figure IV.5: *Comparison between the 1DSA and the analytic vertical magnetic field solution (*Zonge and Hughes*, *1991*) for a VMD source over a homogeneous halfspace of 100 Ω.m and several CR phase values. a) In-phase and out-of-phase fields are presented on the left and b) the relative errors are presented on the right. Relative errors were computed with respect to the corresponding part of the field (Colored dot) or with respect to the total amplitude (black cross)*

It is shown in each *a)* figure that the 1DSA solutions are in very good agreement with the analytic solutions, each 1DSA curve being superimposed to the analytic solution. Looking closer to the relative errors in *b)* figures, the error is limited for each case below 0.1% for frequencies below 1 kHz. The error increases at higher frequencies and can exceed 1 % relatively to the corresponding component. It happens for the electric field in quadrature. Nevertheless in these cases the field is vanishing compared to the in-phase part. Indeed, the relative error with respect to the amplitude of the horizontal electric field is constrained below 0.1%. Same characteristics can be observed for the vertical magnetic field of the VMD source.

Validation of the 3D secondary field solution

Figure IV.7 presents a comparison between the 1DSA response of an infinite polarizable layer of 100 Ω.m with -100 *mrad*, 100 meters thick and a top at 100 meters depth within a homogeneous background of 1000 Ω.m, to the 3D finite difference (3DFD) solution of a 3D anomaly of similar thickness with lateral extension towards the edges of the grid. The primary field solution used to calculate the 3DFD E^s solution is the response for the homogeneous background. The grid uses a 20x20x10 meters (x,y,z direction) mesh grid in the area of the acquisition at the center of the grid, whereas it is refined vertically at the interfaces (5 meters cells) and are expanding towards the edges of the grid. **Large-scale modelling and inversion performed during this thesis were essentially performed using the CINES (Centre Informatique National de l'Enseignement Supérieur) supercomputer *OCCIGEN*.** The model has a total of 615384 cells (74x99x84) and was solved using a supercomputer on 256 cores and took around 1 minute per frequency. As the minimal skin depth in the medium is about 50 meters, the grid ensures a discretization smaller than 4 cells per skin depth vertically and

is a bit coarser horizontally to avoid increasing the size of the problem too drastically. Figure IV.6 presents the core of the 3D model used for the validation in the acquisition area, whereas cell sizes expand outside this domain. Solutions of the electric field are displayed for the three sources at an offset of 1000 meters. Magnetic field solutions are not shown as the forward problem is solved using an electric field formulation of Maxwell equations. The magnetic field obtained by applying a curl operator on the FD grid is less accurate, especially in symmetric position, where the electric field have a null component. Due to its fast variation around these positions, a very fine grid should be used to estimate the magnetic field with accuracy.
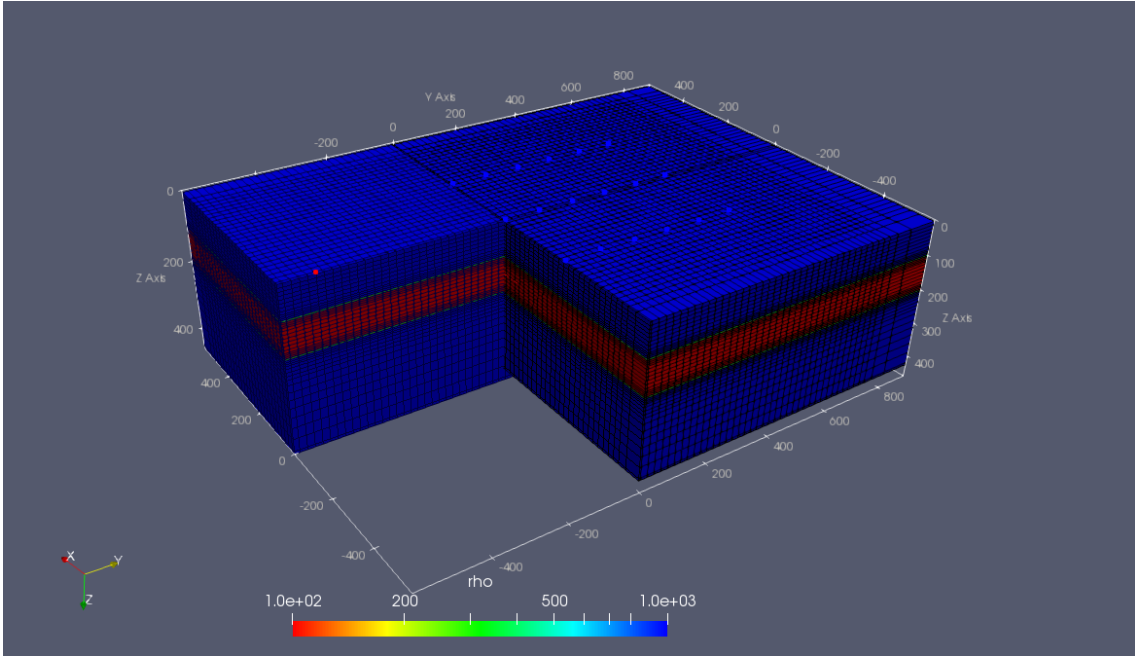
Figure IV.6: *Representation of the 3D model of the conductive layer used for the finite-difference computation of the layer response. Primary fields are calculated on the grid for the homogeneous half-space.*

The results in figure IV.7 show a very good fit on the real and imaginary parts of the electric field. The accuracy decreases slightly with frequency as the cell becomes slightly larger compared to the skin depth, which decreases with frequency. Nevertheless, a good accuracy around 1% is obtained for most of the spectrum with a slight increase to 2 % above 1000 Hz. The spikes in relative errors for the $HED_{//}$ and VMD source, correspond to the area where a field reversal is expected, where the offset from the source corresponds approximately to a wavelength $\lambda/2 = \pi\delta$ in the background. The largest relative error observed on the quadrature component for the $HED_{//}$ source corresponds to a sign reversal at the surface.
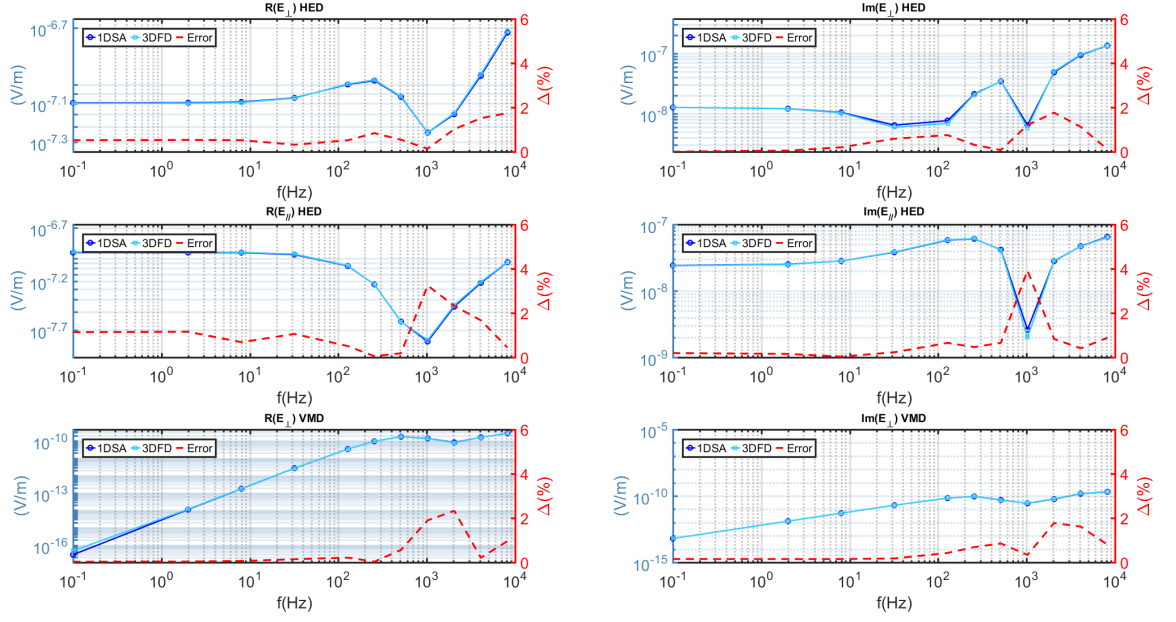
Figure IV.7: *Comparison between the 1DSA and the 3D finite-difference solution for a layer of 100 $\Omega.m$ and -100 mrad in a homogeneous halfspace of 1000 $\Omega.m$, for the three types of source considered at an offset of 1000 m.*

Accuracy of the 1DSA solution is then very satisfactory as well as the accuracy of the 3DFD code solution for a complex resistivity medium. The errors observed for the 1DSA solution are mostly below 0.1 %. Considering the 3DFD solution, it is clear that numerical errors are more important, around 1%, with locally some slightly larger values and will depend on the mesh designed to solve the FD forward problem.

IV.2   CSEM Sensitivity study to CR

In this section, I present an evaluation of the sensitivity of CSEM data to IP effects in order to better understand their impacts on CSEM measurements and thus, which information could be inverted in the next stage of the work. 1D modelling was carried out to study the effect of an imaginary part of the resistivity in CSEM data for several source configurations to gather an exhaustive view of the problem. The degree of complexity of the following examples gradually increases to identify at each step the impact of the IP anomaly. At first, a homogeneous half-space with a constant CR is studied for the three source configurations discussed previously, the $HED^{\perp}$, the $HED^{//}$ and the VMD transmitters for a relatively complete overview. Secondly, the frequency dependence of the CR is studied according to a classic Cole-Cole resistivity model. Thirdly, a buried target is considered for a conductive and polarizable layer in a homogeneous background. Finally, IP effects due to a 3D polarizable target in the medium are presented. This approach is the first step in order to elaborate an efficient strategy for CR inversion.

To quantify IP impact in CSEM data, the term IP effect Δ_{ip} is introduced similarly to Qi et al. (2019). Considering the electric response, it measures the relative variation

between a response $F(E_{\rho^*(\omega)})$ of a model taking into account a CR that can be frequency-dependent, to the electric response $F(E_{\rho^0})$ of a real and constant resistivity as used for an ERT or CSEM survey. The operator $F()$ represents a mean of representation of the electric response as the real and imaginary parts or its amplitude and phase. The response difference is normalized by the amplitude of the electric field for the given component to avoid giving importance to IP effect where the given component and IP effect are very weak. In the case of IP effect shown for the electric phase, the absolute difference will be kept instead of a relative IP effect. Frequency-dependent CR medium is studied using the response of a medium following a Cole-Cole relaxation CR model and is compared to the medium "without IP". Medium without IP for frequency-dependent CR case, is defined as the medium for a constant and real resistivity ρ_0, corresponding to the resistivity in the static case (ρ_0 = first Cole-Cole parameter). IP effect is thus given by the relation :

$$\Delta_{ip}(\omega) = \left| \frac{F(E_{\rho^*}) - F(E_{\rho^0})}{|E_{\rho^0}|} \right| \tag{IV.15}$$

Note that, according to the frequency dependence of the CR, IP effect as defined here is obviously dependent on the choice of resistivity of the reference model. Indeed, an effect due purely to the presence of the imaginary part is expected, but also a frequency effect compared to a real and constant resistivity approximation. I made the choice of using the real DC resistivity model as reference as it corresponds to an IP parameter of several models describing CR variations as for the Cole-Cole model.

IV.2.1   Constant CR Half-space

Starting with the simplest case of a homogeneous half-space of constant resistivity in which a CR phase of -100 $mrad$ was introduced ($\rho^q = \frac{\rho^r}{10}$), I compare in following images (figure IV.8 and IV.9) the EM fields with and without IP effect for the three sources considered. The EM fields are represented as their in-phase/out-of-phase decomposition or as amplitude and phase as a matter of completeness. Furthermore, the results are represented to generalize the response independently to the resistivity of the medium considered. Indeed, SIP method assumes to work in the static case, whereas CSEM method uses electromagnetic induction to sound the ground at several frequencies by varying then the skin depth and the volume in which the wave is sensitive. The static case is respected when the offset r from the source is largely smaller than the skin depth $r \ll \delta$, corresponding to the "near field", which is in opposition to the "far field" with $r \gg \delta$ and corresponding to the plane wave zone used in magnetotelluric method. Following responses are then represented according to the ratio of the offset over the skin depth r/δ with a normalization. This particular representation allows the visualization of the EM response of an homogeneous medium from the near field (DC approximation) ($r/\delta \ll 1$) to the far field ($r/\delta \gg 1$), independently of the resistivity norm of the half space. Normalized EM fields for a homogeneous half space with respect to the r/δ ratio, follows thus a proportionality relationship between the increase of in offset and the increase in frequency, as skin depth is proportional to the reciprocal of the square root of the frequency. EM fields are normalized by their total amplitude in the static case for a real resistivity,

except for the electric field of the VMD case. As electric field of inductive sources vanishes towards the static limit due to Faraday's law, the normalization is made for its value at 10 r/δ instead of its DC value.

Figure IV.8 presents the electric field responses for a homogeneous half-space of constant resistivity with and without a CR phase of -100 $mrad$. This CR phase value can be considered as a large IP response that can be found for some disseminated metallic particles. The non-zero components for a y-directed profile are presented (see figure IV.1), excluding the vertical electric field of the $HED_\perp$ case, as the vertical electric field is generally not measured due to technical difficulties.

Electric Field
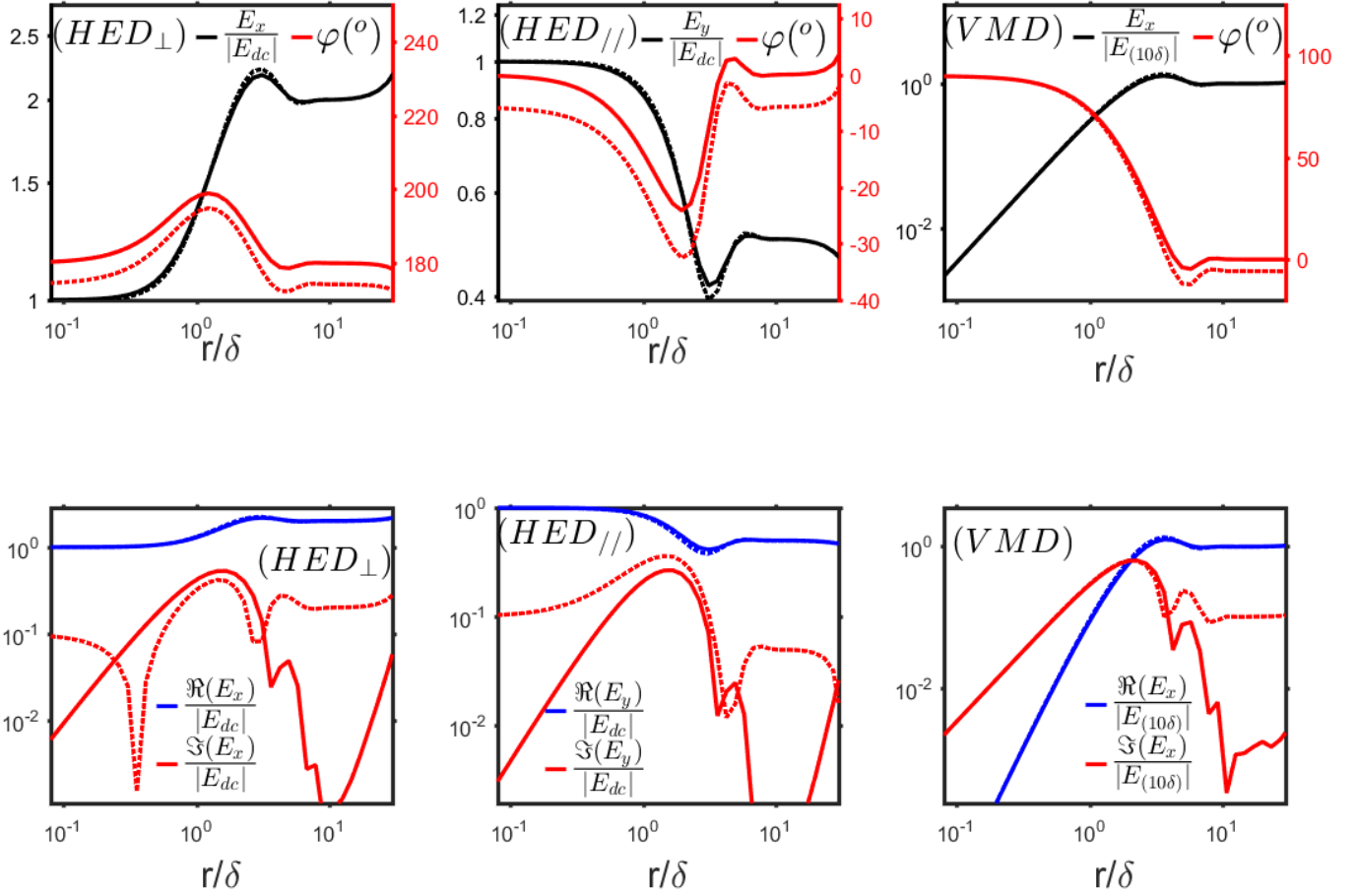
Figure IV.8: *Normalized amplitude and phase (top) and normalized in-phase and out-of-phase (bottom) electric responses with respect to the offset over skin depth ratio, for the three kind of sources considering a 100 $\Omega.m$ model with (dashed) and without (solid) $-100mrad$ of CR phase delay. Dotted lines represent the CR model response whereas solid lines represent the real resistivity response (without IP effect).*

In figure IV.8, it is shown that the inclusion of a significant imaginary part in the resistivity has little effect on the measured amplitude of the electric field for the three sources. Only a slight perturbation can be noticed in the transition zone around 3 r/δ. As in a homogeneous half-space amplitude reflects mainly the variation of the in-phase part of the electric field due to a low quadrature response. The same observation can be made for the real part of the electric field. On the contrary, a large difference is observed on the measured phase, as the presence of the imaginary part of the resistivity induces an additional phase delay in the data. The observed phase delay is linked to a large variation of the quadrature phase component due to the IP relaxation currents and medium chargeability. Note that these effects are missing in the near-field of the inductive source as the electric current vanishes in static limit, whereas galvanic sources show these effects on the complete spectrum. IP currents are opposed to the primary electric field. It results that IP effect enhances the electric response in quadrature phase for the $HED_{//}$ and VMD cases as their quadrature response are also opposed to it on the domain considered. On the contrary, for the $HED_{\perp}$ the quadrature response is oriented in the same direction as the in-phase response for the receivers profile considered. Then the IP quadrature phase effect is opposed to them and a sign reversal can be observed.

Considering galvanic sources, low frequency phase delay is entirely caused by IP phenomena in the near-field domain as there is no induction in the medium. CR phase can then linearly be deduced from the electric phase using a geometric coefficient as for the SIP method. Nevertheless, when r/δ becomes greater than $\frac{1}{10}$, the phase delay caused by EM induction in the half-space gradually adds up to the electric response as the quadrature currents increase. In these cases, DC hypothesis does not hold anymore to interpret SIP data and it becomes crucial to take EM induction into account by modelling the full EM response to access to IP information. Figures IV.10a and IV.10b show IP effects observed on the electric field response of the homogeneous half-space. It confirms that the electric field amplitude and its real part are weakly perturbed by IP effects with a small anomaly limited below 6% on the amplitude for a limited frequency window. VMD case is the most impacted whereas $HED_{\perp}$ is less impacted with an IP effect around 2% of the total field. In-phase IP-effects present similar patterns but are relatively more impacted (around 2 to 3% more) than the total amplitude due to the small compensation that happens between real and imaginary components resulting in an amplitude with less variations. On the contrary, the quadrature electric field and its phase are relatively more impacted by the presence of the imaginary part of the resistivity. Galvanic sources present around 6° of additional phase delay representing on the quadrature phase electric field around 10 % of the total amplitude. These effects are present over the complete spectrum with an oscillation in the intermediate area due to variations of the in-phase-field. Complex effects due to an additional direct coupling between EM induction and IP effects in the medium are present.
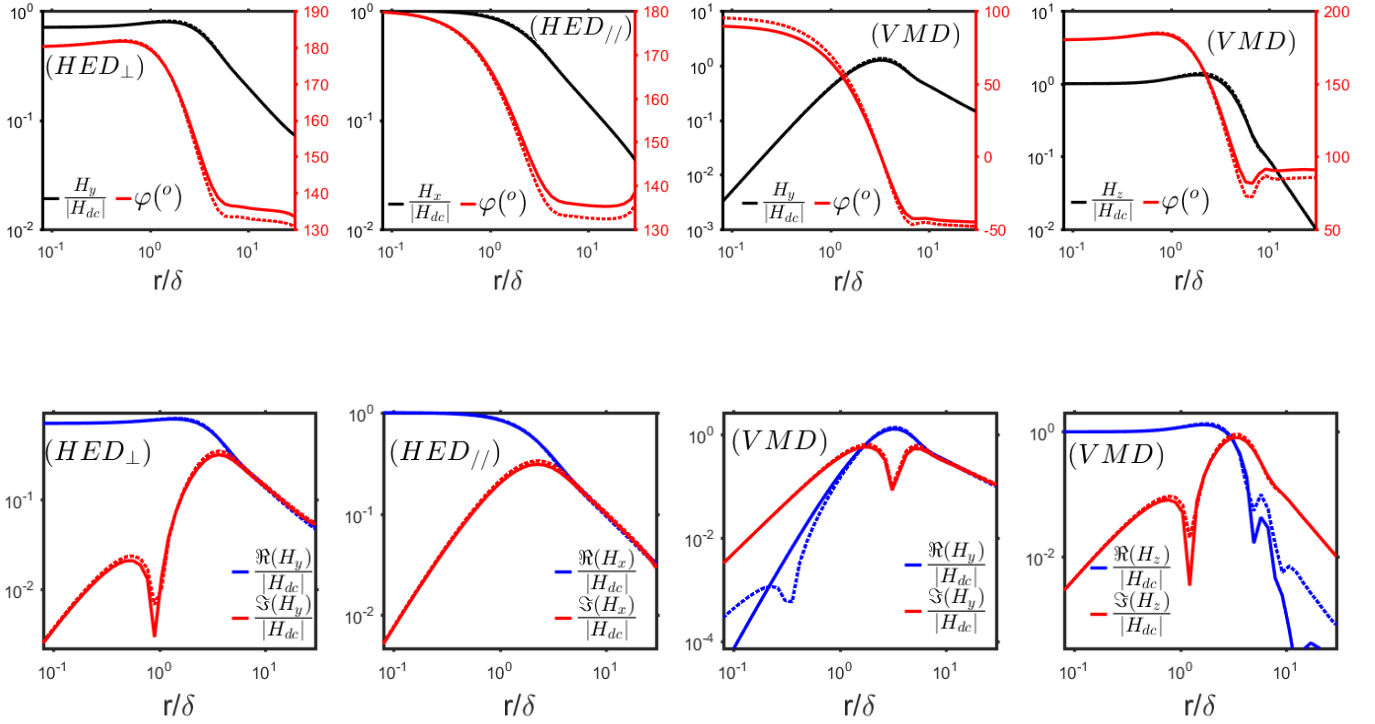
Magnetic Field

Figure IV.9: *Normalized amplitude and phase (top) and normalized in-phase and out-of-phase (bottom) magnetic responses with respect to the offset over skin depth ratio, for the three kind of sources considering a 100 Ω.m model with (dashed) and without (solid) −100mrad of CR phase delay. Dotted lines represent the CR model response whereas solid lines represent the real resistivity response (without IP effect).*

Figure IV.9 shows the magnetic responses of the homogeneous half-space with and without IP effect similarly to the previous images for the electric field responses. At first, we note that by taking the limit towards the near-field from the analytic equation of the magnetic field for a HED (eq. (IV.6),(IV.7) and (IV.8), see Zonge and Hughes (1991) for their limits), the magnetic field is not sensitive to the medium resistivity or to the frequency. Magnetic field is said to be "*saturated*" in the near field for galvanic sources. Similar reasoning can be done for the magnetic field of the VMD source and it can be noted that its vertical component is "*saturated*" as well in the near field limit. The radial component shows nevertheless a dependence to the medium resistivity and to the frequency used, but the horizontal magnetic field vanishes towards the DC limit. These behaviours can be clearly observed throughout figure IV.9. In the near field, thus towards low frequencies, the magnetic field will not help the imaging.

Considering these limitations, IP effects still can be observed on the magnetic field. Observed effects on the amplitude of the magnetic field are again relatively weak. Responses with and without IP are hard to differentiate on the amplitude of the magnetic field. Figures IV.10c and IV.10d show that the maximal IP effect is about 6% at a resonance frequency for the horizontal magnetic field of the *VMD* source. A similar IP effect

can be observed for its vertical component. The IP effects for the amplitude of the mag-
netic field response associated to galvanic sources are weaker, around 2 to 3%. IP effects
are again mainly observed on the magnetic field phase in the intermediate and the far
field area with a large phase delay. The high frequency (intermediate to far field) phase
delay associated to IP effects and observed on the magnetic field is due to a decrease of
the in-phase field and to the increase of the quadrature phase for the horizontal magnetic
components. The vertical magnetic field phase of the VMD source is impacted by IP ef-
fects in the intermediate range due to an increase of the quadrature phase part, whereas
towards the far-field a large effect on the in-phase part is observed. IP effect on each in-
phase and quadrature phase components are presenting a peak at a resonance frequency,
representing around 6 to 7% of the total magnetic field for the VMD source components
and a bit lower around 4 to 5% for the galvanic sources. IP effects for the horizontal
magnetic components, in-phase and out-of-phase, tend to a constant value toward the
far-field. On the contrary, what seemed to be a large IP effect towards the far-field on the
in-phase part of the vertical magnetic field of the VMD source, is in fact decreasing and
becomes less significant relatively to the total amplitude. This is also the case of the IP
effects over the horizontal magnetic fields in the near-field. The large IP effect observed
on the phase and due to the real part of the magnetic field is not significant. Indeed, the
in-phase magnetic response becomes vertical approaching to the loop at short r/δ, and
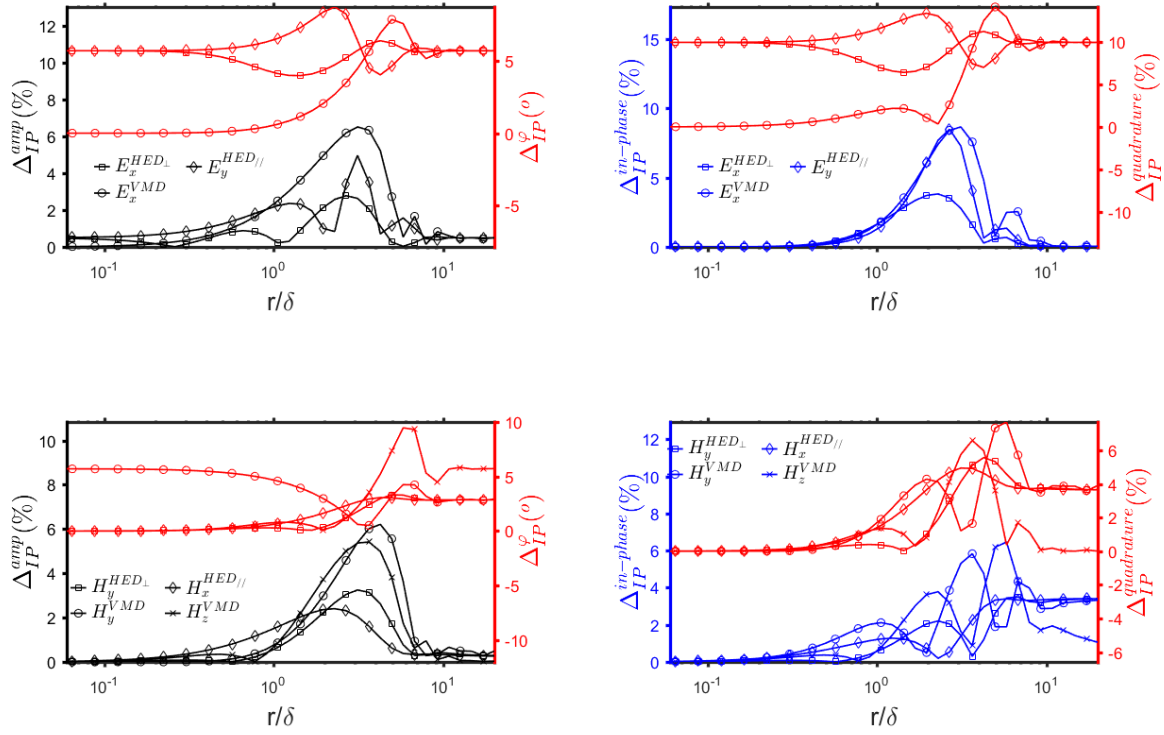the observed IP effect represents less than 1 % of the total magnetic field.

Figure IV.10: *IP effect over EM responses with respect to the offset over skin depth ratio, for each type of source. Top: electric field responses; bottom: magnetic responses; amplitude and phase representation (left); in-phase and quadrature phase representation (right)*

Resistivity Phase effect

In previous section the effect of an imaginary part ρ^q through a phase delay of -100 $mrad$ by keeping constant ρ^r was presented. Figure IV.11, compares the effect of the resistivity phase variations for a half-space and the $HED_{//}$ case at constant $|\rho^*|$ or at constant ρ^r on electric fields. For each component, a proportionality can be observed with the phase increase. A proportionality between the CR phase delay and electrical response is observed, involving that a -10 $mrad$ halfspace produces around 10 times less IP effect than a -100 $mrad$ halfspace. As CR phase delay decreases, IP effect is thus weakening, passing below 1% relative anomaly for -10 $mrad$ of CR phase delay, which is generally considered as a noise threshold, whether it is an anthropogenic, geometric or numerical accuracy limit.

A fundamental difference can be observed between the amplitude and the real part between $|\rho^*|$ constant or ρ^r constant cases. Indeed, towards DC limit, the curves become distinct. In the case of $|\rho^*|$ constant, increasing the phase has weak impact at low frequencies on the electric field amplitude, whereas keeping ρ^r constant when increasing the phase has a slightly higher impact at low frequencies with IP effects tending to an asymptote. This observation can also be made for the real/imaginary parts, unless that it will be the $|\rho^*|$ constant case that is more impacted at low frequencies by varying the CR

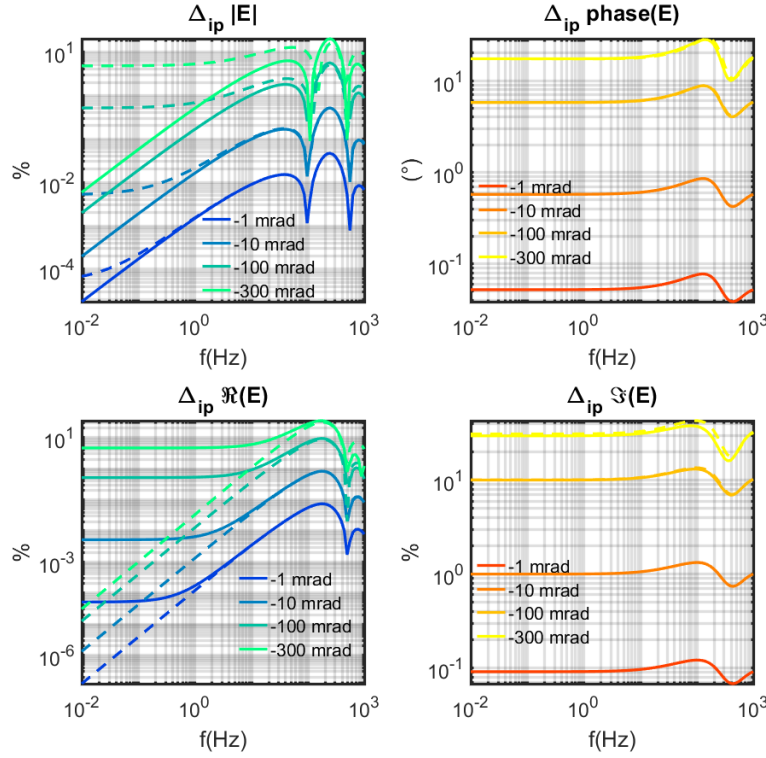phase. At higher frequencies, IP/EM coupling intervenes and explains the larger effects.

Figure IV.11: *IP effect observed over the electric field amplitude and phase (top left and right) and over the in-phase and out-of-phase electrical response (bottom left and right) for increasing CR phase introduced in the medium by keeping the CR norm $|\rho^*|$* **constant (solid lines)** *or keeping the real part $\rho^{\mathbf{r}}$* **constant (dashed lines)**

Looking closer to the radial static response E_r of an inline HED source over a homogeneous half-space for the DC limit :

$$E_r = \frac{2I\rho^*}{2\pi r^3} \tag{IV.16}$$

It is straightforward that the real part of the electric field is directly proportional to ρ^r and the imaginary part to ρ^q in the static limit, whereas if looking for the amplitude and the electric phase φ_E responses, we have:

$$|E| = \frac{2I}{2\pi r^3}\sqrt{(\rho^{r2} + \rho^{q2})} = \frac{2I|\rho^*|}{2\pi r^3} \tag{IV.17}$$

$$\varphi_E = atan(-\frac{\rho^q}{\rho^r}) \approx \Phi_{cpx} \tag{IV.18}$$

It highlights that when looking at the amplitudes and phases of the electric responses, evaluating the IP effect by comparing model at $|\rho^*|$ constant should be preferred instead of ρ^r constant and the opposite when looking at real/imaginary parts of the electric field. Reformulated in a more practical way considering the following argumentation on

observables used for inversion, it highlights that varying the CR phase by keeping the norm constant, perturbs less the electric amplitude and reciprocally for the real/imaginary part.

Intermediate conclusion for the constant CR Half-space

This section shows that a considerable IP effect caused only by a constant imaginary part of the resistivity can be observed in CSEM data. In this case, IP effects amplitudes are controlled by the CR phase Φ_{cpx}, the ratio between the imaginary and the real part. The presence of an imaginary resistivity ρ^q impacts mainly the phase of the data and has a weak effect over the amplitude of the EM responses, that have significant IP effects only within a limited bandwidth in the transition area for one frequency. Within this frequency band, an additionals weak IP/EM coupling occurs. Electric field is more sensitive to IP effect than magnetic field with stronger relative IP effect over the quadrature phase component. Galvanic sources show IP effects over the complete spectrum for the homogeneous half-space electric response. On the contrary, the VMD electric response vanishes in the near field, resulting in less recoverable information over the spectrum. Furthermore, the low frequency spectrum is free of EM induction, which is the part exploited in DCIP methods and allows the complete separation of the IP effects from EM induction. IP effects over the magnetic field have always a strong induction coupling. Even if the aim of this work is to separate both effects, it is obvious that there will be easier to investigate both effects using the electric field response as the EM/IP coupling will increase gradually with frequency, letting a part of the IP information totally or at least partially free of induction.

IV.2.2 Half-space frequency-dependent CR

Now that the influence of the presence of a constant imaginary part of the resistivity in an homogeneous medium was studied for several source configurations, more complexity can be added to better understand IP effects due to polarization phenomena. It is known that the complex resistivity of the medium can be frequency-dependent and in the following part, the frequency variation of the resistivity and its implication in CSEM data are presented. In this part, the response of an homogeneous half-space following a classic Cole-Cole resistivity model is studied. Only the case of the $HED^{//}$ is presented in this part, as following conclusions can be extrapolated to other sources and other relaxation models for the CR frequency dependence.
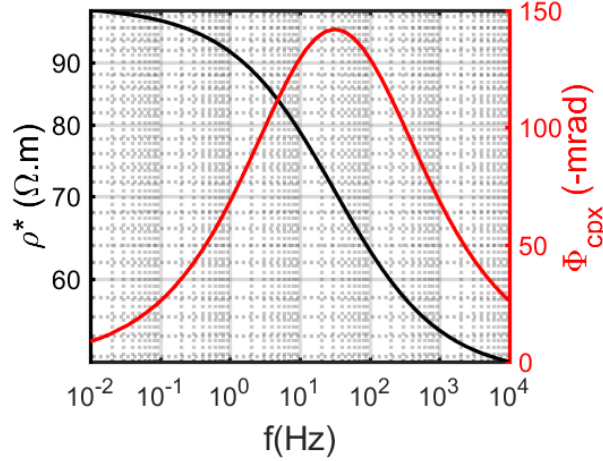
Figure IV.12: *Cole-Cole resistivity model used for the homogeneous half-space modelling with the CC parameters : $\rho_0 = 100\Omega.m, m = 0.5, \tau = 0.01s, c = 0.5$). The chargeability of 0.5 gives a high-frequency asymptote for $\rho_\infty = 50\Omega.m$. CR is presented as its norm (black curve) and phase (red curve)*

Figure IV.12 presents the Cole-Cole resistivity model introduced into the homogeneous half-space using the following parameters $\rho_0 = 100\Omega.m, m = 0.5, \tau = 0.01s, c = 0.5$. A relatively short relaxation time was chosen in order to appreciate IP/EM coupling domain.

HED Electric Field

Figure IV.13 presents the electric response for the HED case. As it was shown previously that the CR phase has little impact over the amplitude/real part of the electric field, the effect of the variation of the resistivity norm is clearly seen on the amplitude/real part of the electric field. The behaviour of the electric field varies gradually with frequencies, between the responses of the corresponding real resistivity model of each Cole-Cole asymptote (ρ_0 to ρ_∞) at low and high frequency. Considering the CC resistivity model shown in figure IV.12 and taking the DC resistivity half-space as reference, the IP effect over the in-phase electric field increases from around 1% at low frequencies to reach approximately 50% at higher frequencies with a maximum in the transition area (Figure IV.12). This observation of large IP effect on the electric amplitude is a major difference with the constant case and highlights the necessity to look globally over a wide frequency range. As EM induction in a simple half-space is weak, the electric amplitude reflects essentially the real part of the electric response variation as in previous examples for the galvanic sources. This gradual change is less obvious concerning the quadrature phase response. Indeed, the variation of $|\rho^*|$ has an effect over the EM induction, that is mixing up with the extra phase delay due to the frequency-dependent CR phase Φ_{cpx} variations. A slight shift between 200 to 500 Hz is observed due to the variation of the CR norm, whereas an observed additional phase delay is proportional (at first order) to the CR phase variations. IP effects on the electric field phase and quadrature phase, shown in figure IV.15, shows an IP anomaly up to 14° with a peak that coincides approximately to the maximal CR phase. Additional phase delay due to the variation of the resistivity

norm and its associated EM coupling in the data are distorting the IP effect due to the CR phase and a direct reading of the phase delay should be avoided. For comparison, the phase delay IP anomaly peak of 14° observed in the data represents -244 mrad. An important difference with the homogeneous case concerning the CR phase effect is that for target responding according to a CC like model, CR phase will not be significant over the complete frequency range.
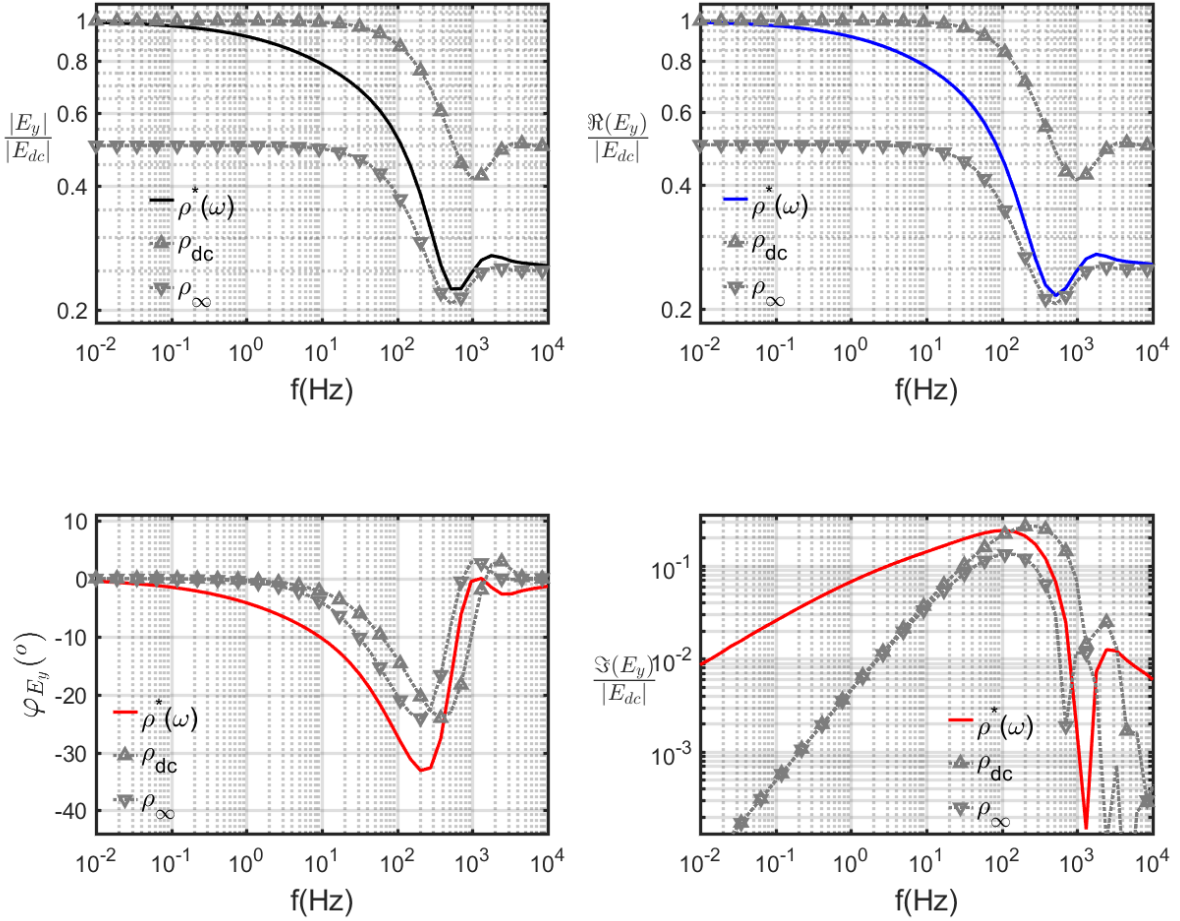

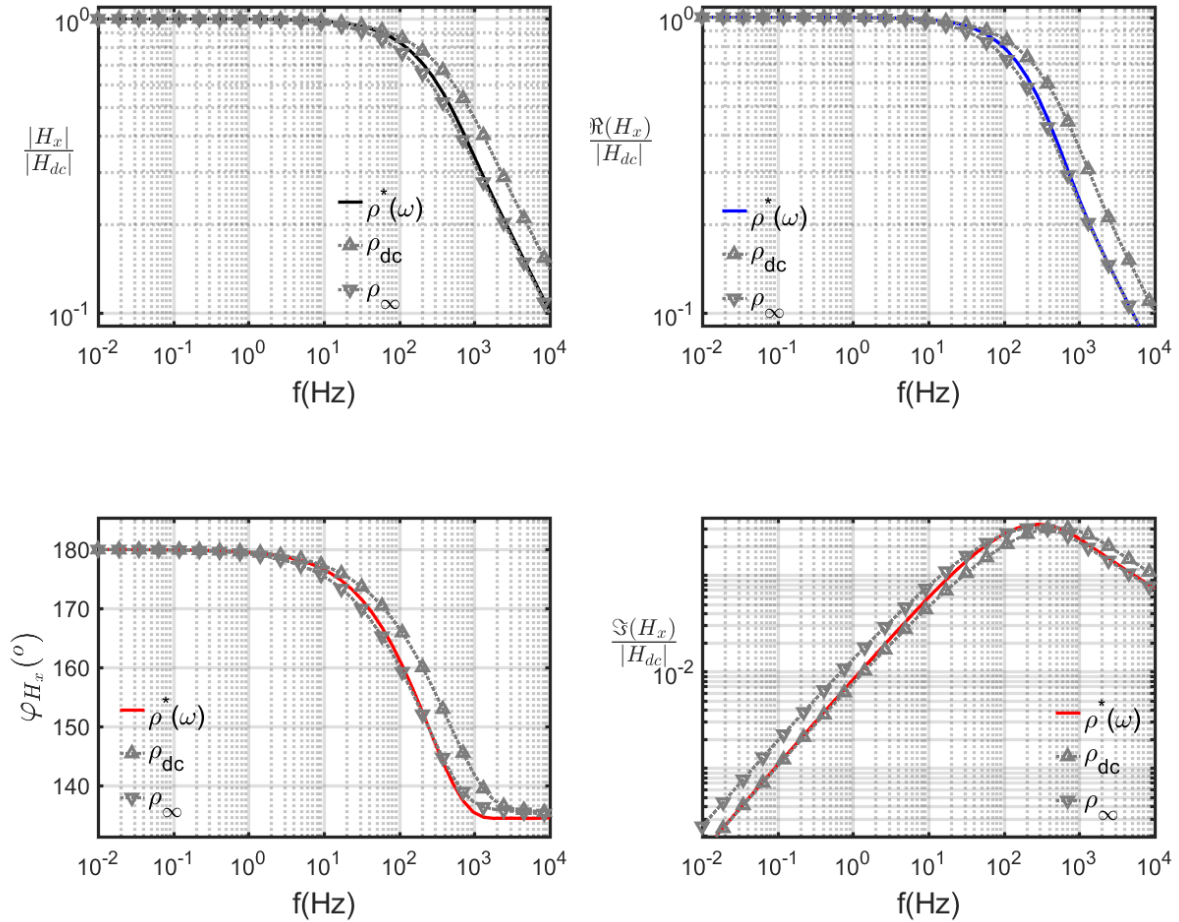**Figure IV.13:** *Normalised amplitude and phase (left) and normalised in-phase and out-of-phase (right) electric response with respect to the frequency, for the $HED^{//}$ source considering a C-C polarizable halfspace ($\rho_0 = 100\,\Omega.m, \rho_\infty = 50\,\Omega.m, m = 0.5, \tau = 0.01\,s, c = 0.5$). Normalisation is made using the electric amplitude in the static case (for the ρ_{dc} model). Solid lines represent the CR model response whereas grey dotted lines represent the real resistivity response for ρ_{dc} and ρ_∞ of the Cole-Cole model asymptotes.*

The influence of IP effect over the horizontal magnetic field is briefly depicted in figure IV.14. Observations made for the electric field can be extended to the magnetic field with some basic differences linked to previous observation when it deals with magnetic field. In these images, it is shown once more that the magnetic field is not sensitive to the medium resistivity at low frequencies, thus no variation of the amplitude or the phase of

the magnetic field is observed due to IP effect, whereas in this frequency range the CR shape could be clearly appreciated on the variations of the electric field. The gradual change of the magnetic field amplitude can be observed at higher frequencies, but to a lesser extent than for the electric field as it represents a maximum around 25 % of the amplitude (IV.15). The frequency for which the IP effect becomes significant on the magnetic field amplitude, is way higher ($\Delta_{IP}^{amp} > 1\% \equiv f > 30\,Hz$) compared to the electric field response. Separation of the effect of the CR norm and phase is less clear on the real/imaginary magnetic field components, as both are impacted by the CR phase variation and its norm.

Figure IV.14: *Normalized amplitude and phase (left) and normalised in-phase and out-of-phase (right) magnetic responses with respect to the offset over skin depth ratio, for the $HED^{\perp}$ source considering a C-C polarizable halfspace ($\rho_0 = 100\,\Omega.m, \rho_{\infty} = 50\,\Omega.m, m = 0.5, \tau = 0.01\,s, c = 0.5$). Dotted lines represent the CR model response whereas solid lines represent the real resistivity response for ρ_{dc} and ρ_{∞} of the Cole-Cole model asymptotes.*

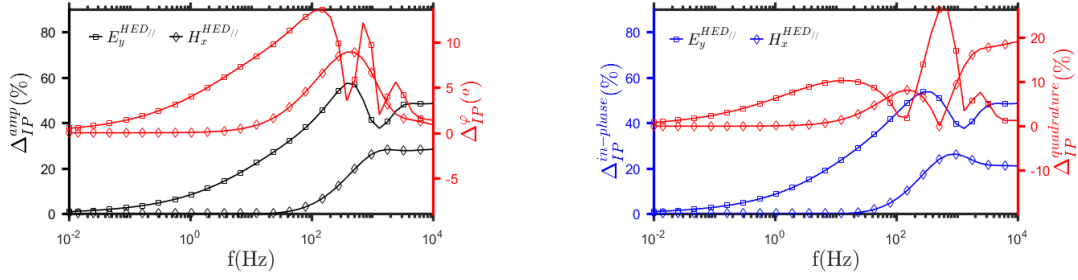**IP effect for a frequency-dependent CR**

Figure IV.15: *IP effect for a C-C polarizable halfspace ($\rho_0 = 100\,\Omega.m, \rho_\infty = 50\,\Omega.m, m = 0.5, \tau = 0.01\,s, c = 0.5$). Left: amplitude and phase representation ; right: in-phase and quadrature phase representation*

In this part it was shown that CSEM/IP electric field data will be more sensitive to the CR norm or its real part variations compared to the effect of the CR imaginary part or phase that induces a weaker IP effect over the electric quadrature field. Magnetic field shows similar observation to a lesser extent, particularly as the frequency range investigated on which the CR variations are sensitive is more limited. Considering then the frequency dependence of the CR, a broad spectrum is necessary to characterize the complex resistivity variations. If the investigated frequencies does not hold in the frequency range where ρ^* and its variation is sensitive, important IP information can easily be missed. These observations highlight the necessity to choose carefully the frequencies used relative to the target and the subsequent difficulties linked to the fact that in a real survey only a partial information will be accessible as it will be of increasing significance for buried targets as presented in the following section.

IV.2.3 Layered model

The understanding of the perturbation of the IP effects in CSEM data for the simplest case of an homogeneous half-space was presented in previous sections for several source configurations and investigating the electric and the magnetic field responses. The IP effect due to the presence of an imaginary part in the resistivity was first considered, then the frequency effect of the CR for a common relaxation model was studied to highlights some limitations but also some advantages when it comes to retrieve the CR and its variations from a medium. The Earth is composed most of the time of very heterogeneous materials with large geological variations. In order to pursue the approach involving an increasing complexity in the modelling step by step, the IP effects of a buried target will be investigated through 1D model. The IP effects due to a conductive and polarizable layer in an homogeneous background is presented in the next section. Again a constant CR ($10\Omega.m$ and $-100mrad$) and then a frequency-dependent CR using a similar CC resistivity model (using $\rho_{dc} = 10\Omega.m$), are considered for the layered resistivity model.

Sensitivity to IP effect will depend on several factors in the case of a buried target. They are linked to the two fundamental differences between geometric and frequency

sounding concepts. DC method uses geometrical sounding to control investigation depth by varying Tx-Rx offset, whereas CSEM method uses frequency sounding, or generally, a complex mix of both, to control investigation depth with frequency and offset variation. Sensitivity to the buried body depends then on the offset and the frequency used. EM data will lose their sensitivity to the target at too short offsets, depending on the survey geometry, or at skin depths smaller than the target depth.

Figure IV.16 shows the electric field response of the constant CR layer case, a 100 meter thick conductive layer, embedded at 100 meters in a homogeneous half-space of $100\Omega.m$. The real part of the conductive layer was chosen with a $1 : 10$ ratio with the background, resulting to $\rho^r = 10\,\Omega.m$, and its imaginary part ρ^q corresponds to $\phi_{cpx} = -100\,mrad$. As the sensitivity to the target is varying with offset, I choose to present here a mean offset corresponding approximately to 5 times the depth of the target, keeping a δ separation (in the background) at 100 Hz. This choice ensures a sufficient offset for geometric investigation and for studying EM induction coupling. A shorter offset would result in data respecting a near field case over most of the frequency range or to an insufficient investigation depth, whereas larger offsets show weak amplitudes.

The figure IV.16 compares the in-phase and quadrature parts of the electric field for the real resistivity case E^r and for the constant CR case E^*. Furthermore, electric field response of the background E^{bg} is plotted with the IP response component. IP response is separated here analogously to the primary/secondary field separation $E_s^r = E^r - E^{bg}$, commonly used in CSEM and corresponding to $E_{\Delta ip} = E^* - E^r$. Similar observations as for the half-space case can be made: there are weak to negligible effects of ρ^q component over the in-phase electric field with only a 7% maximum IP effect on a limited frequency range around $100Hz$, whereas an effect around 8% can be observed over the quadrature electric field under $100Hz$ (Figure IV.18a). For frequencies higher than 2.5 kHz, the response of the layer slowly tends toward the response of the homogeneous background as the skin depth is decreasing below the depth of the target with increasing frequencies. A major difference with the half-space case is the strong EM induction response of the layer, corresponding to the out-of-phase secondary field $\Im(E_s^r)$ much larger than for the homogeneous case. It results in a competition between IP effect and EM induction at higher frequencies. For this particular case, EM induction becomes greater than $E_{\Delta ip}$ over the quadrature of the electric field around 10 Hz. This case illustrates that where EM induction is too large compared to IP effect, IP information due to ρ^q would not, or hardly, be recoverable. It implies that where IP effect due to ρ^q and EM induction are distinguishable will depends of the amplitude of both effect and of the offsets where EM induction arises. Furthermore, the sensitivity to the target to the skin depth variation is also to take into account and will hinder investigation of the target for high frequencies. Study of the CR behaviour at higher frequencies will then be helped by as short offsets as possible according to geometrical investigation depth, in order to avoid as possible the frequency range where EM induction is largely dominant.
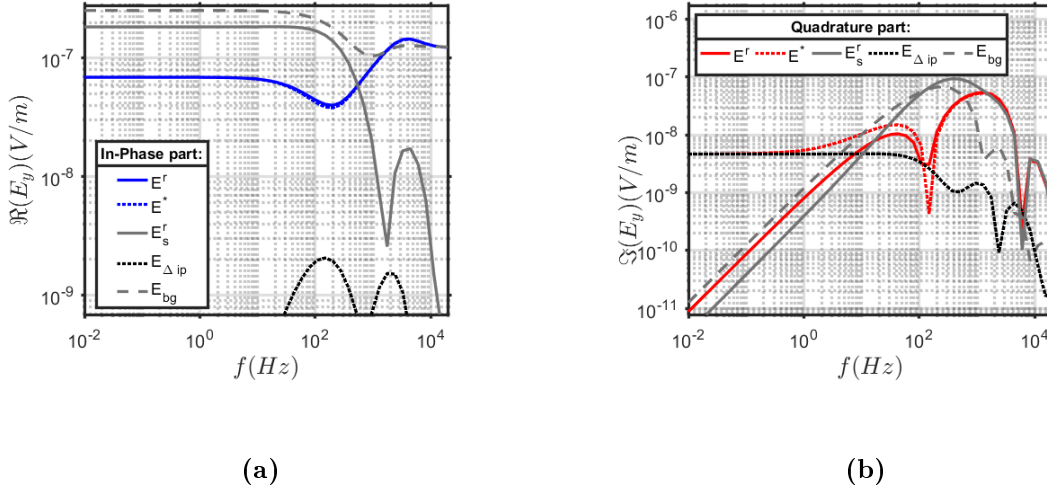
(a)   (b)

Figure IV.16: *In-phase (top-left) and out-of-phase (top-right) electric field responses of a constant 10 $\Omega.m$ layer without (E^r) and with (E^*) a -100 mrad CR phase, in a 100 $\Omega.m$ background at an offset equal to the skin depth in the background. Responses were decomposed into the primary field (E_{bg}), the real resistivity model secondary field (E_s^r) and the IP contribution $E_{\Delta ip} = E^* - E^r$.*

Figure IV.17 shows results of the modelling in the same condition as previously except that resistivity of the layer follows the CC model presented earlier with $\rho_0 = 10\Omega.m$. Observed IP effects in this case can be straightforwardly deduced from previous observations made on the constant homogeneous half-space model, the corresponding frequency-dependent model and the constant CR layer. **A large IP effect due to the CR norm variation can be seen on the real part of the electric field**. The quadrature electric field presents mixed effects due to the CR norm and phase variations. As depicted in the constant case, the sensitivity to the layer is slightly lost at higher frequencies due to the skin depth effect. Due to the CR norm variation and the slight shift associated in the quadrature phase spectrum, an IP effect can be observed above 100 Hz (Figure IV.18a).
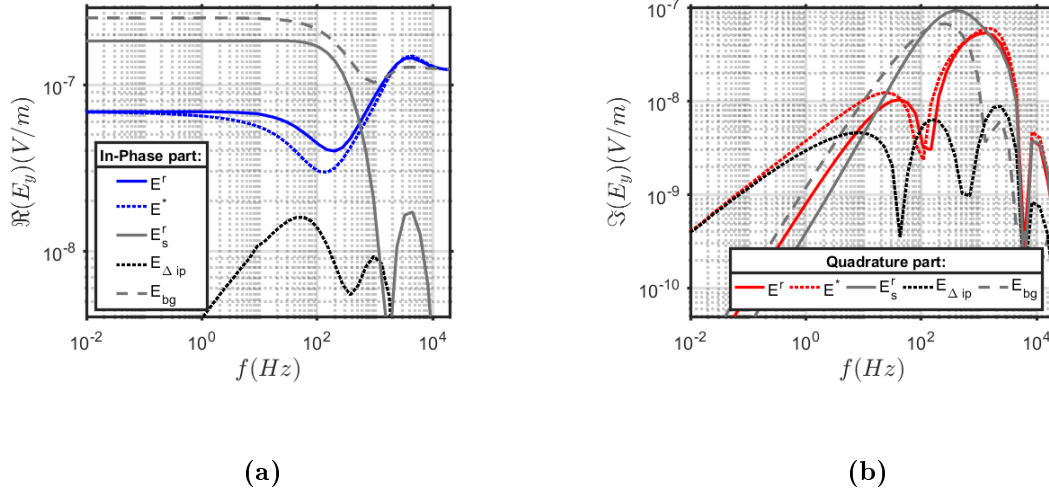
(a)   (b)

Figure IV.17: *In-phase (top-left) and out-of-phase (top-right) electric responses of a constant 10 $\Omega.m$ layer (E^r) or a frequency-dependent CR layer model based on the previous CC model ($\rho_0 = 10\,\Omega.m, \rho_\infty = 50\,\Omega.m, m = 0.5, \tau = 0.01\,s, c = 0.5$ (E^*), in a 100 $\Omega.m$ background at an offset equal to a skin depth at 100 Hz in the background ($\delta_{100Hz} = 503\,m$) . Responses were decomposed into the primary field (E_{bg}), the real resistivity model secondary field (E_s^r) and the IP contribution $E_{\Delta ip} = E^* - E^r$.*

(a)
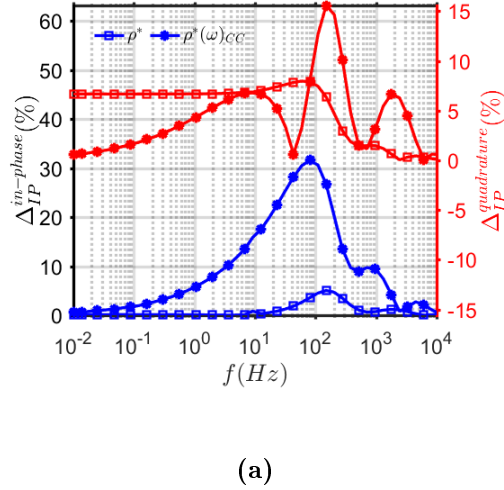
Figure IV.18: *IP effect observed for the In-phase (blue) and out-of-phase (red) electric responses of the constant CR layer model and the frequency-dependent CR layer model based on the previous CC model with a 1/10 factor ($\rho_0 = 10\,\Omega.m, \rho_\infty = 50\,\Omega.m, m = 0.5, \tau = 0.01\,s, c = 0.5$)*

IV.2.4   3D cube

Here, 3D example is presented for the completeness of the study, considering a buried conductive anomaly with a CR into a homogeneous real background. EM responses of the buried targets have very complex behaviours depending on the size compared to the depth of the anomaly and on the geometry of the acquisition. Furthermore as 3D anomalies have lateral boundaries compared to the 1D case, a more complex EM response pattern is expected, as lateral boundaries will present strong charge concentrations depending on the illumination given by the source and an induction number that will highly depends on the anomaly shape. The following examples are not presented to provide an exhaustive overview of 3D target responses as it would be highly case-specific. I stick to a simple and general case of a constant and a frequency-dependent conductive cube anomaly to highlight the differences and similarities with the previous observations made on 1D modelling. It will be shown that the behaviour of IP effect of the three-dimensional target could be extrapolated to 3D cases from previous observation made on 1D modelling and considering the illumination given by the EM source.

Only the electric field response of the $HED_{//}$ case is presented. Dimension of the cubic anomaly are 200x200x150 meters with its top placed at a depth of 100 meters and centered at an offset of 500 meters from the source. The cube resistivity is set as 10 $\Omega.m$ with -100 mrad of CR phase for the constant CR case, whereas the background resistivity is set at 100 $\Omega.m$. The frequency-dependent CR cube case has the same CC properties as the layer presented in previous section ($\rho_0 = 10\,\Omega.m, \rho_\infty = 50\,\Omega.m, m = 0.5, \tau = 0.01\,s, c = 0.5$).

Constant CR cube

Figure IV.19 shows a representation of the electric field for a vertical and horizontal slices of the real resistivity cube model and crossing the cube (x=0 m, y=150m) at 0.1 Hz. The conductive cube results in a weakening of the amplitude on the total electric field. This is due to current channelling into the conductive body and to the charge concentration at the interfaces of the cube. The characteristic illumination of the $HED_{//}$ can also be better understood. At the position of the cube the primary electric field is mainly Y-directed resulting in a better illumination of the cube faces perpendicular to it. Figure IV.20 presents the secondary electric field associated to the cube response of the two slices considered. On this image a well known galvanic effect is observed: the cube acts as a secondary source in the half-space. As the cube is conductive compared to the background, the secondary source has the same orientation as the primary electric field that illuminates its perpendicular interface. Consequences are a secondary field opposed to the primary field inside the cube and at the surface above the cube. Quadrature phase field is weak and not significant at this frequency for a real resistivity case.

Figure IV.21 presents the IP effect (relative to the total amplitude in percent) due to the constant CR cube. Similar patterns are observed. In this case, the in-phase IP effect at this frequency is not relevant: the IP effect over the phase is weak and tends to vanish at low frequencies as seen previously. On the contrary, a large IP effect over the quadrature is expected and observed. IP effects over the quadrature follow a similar

pattern as the in-phase secondary field as they are (in the static case) proportional to them, but in opposition of phase. The IP effect due to the cube, can then be considered as a secondary source in quadrature phase of same orientation into the medium. These slices give a brief overview of the importance of the illumination of the source according to the geometry of the target and are a classic problem in CSEM method sensitivity study. In order to maximize the IP effect of a constant CR target, the problem will be similar to maximizing the response of the real resistivity target.
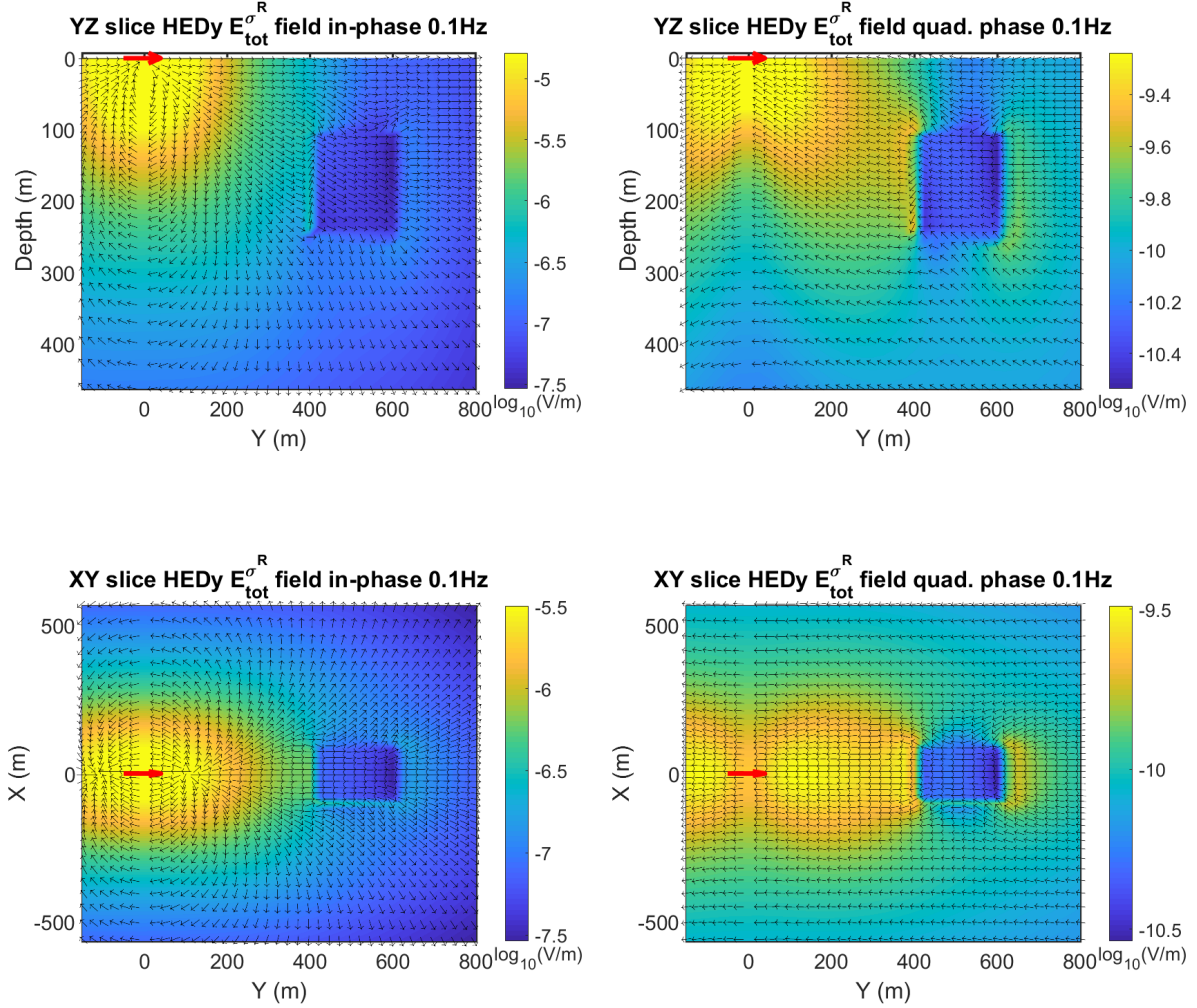
Figure IV.19: *Representation of the total electric field E^p at 0.1 Hz for a vertical Y-directed slice in-line (x=0 m) with the HED source orientation (top) and for a horizontal slice at z=150m (bottom)* **_for the cube model with a constant and real resistivity_** *. Left images represent the in-phase electric field, whereas right images the out-of-phase component. The amplitudes are represented by the color scale (Caution to the range of scales that are not kept constant for a better visualization of the anomaly) and the arrows represent the orientation of the field in the slice.*
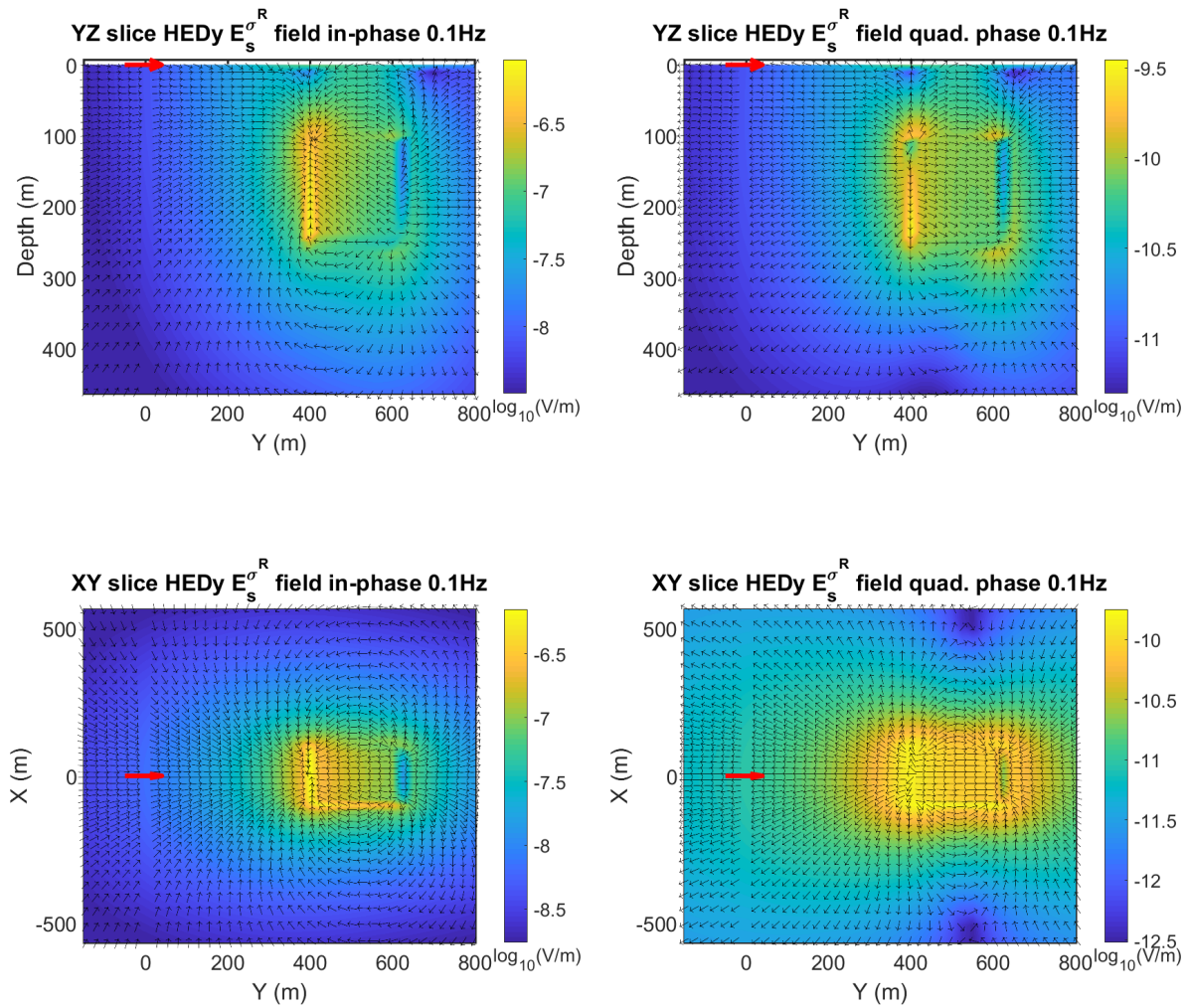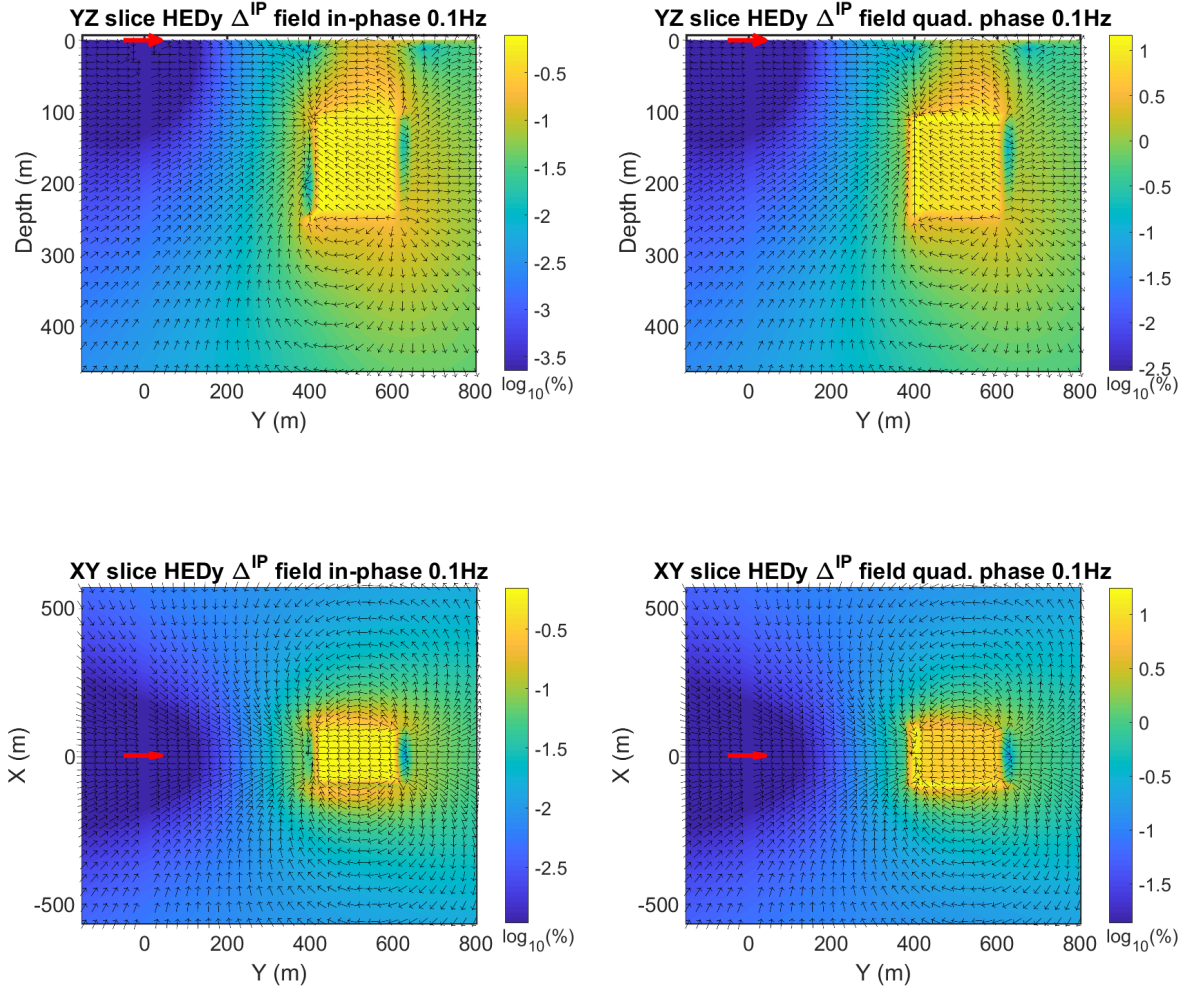
Figure IV.20: *Representation of the secondary electric field E^s at 0.1 Hz for a vertical Y-directed slice in-line (x=0 m) with the HED source orientation (top) and for a horizontal slice at z=150m (bottom)* **_for the cube model with a constant and real resistivity_** *. Left images represent the in-phase electric field, whereas right images the out-of-phase component. The amplitudes are represented by the color scale (Caution to the range of scales that are not kept constant for a better visualization of the anomaly) and the arrows represent the orientation of the field in the slice.*

Figure IV.21: *Induced polarization effect on the electric field at 0.1 Hz (similar decomposition as in figure IV.16, but expressed relative to the total electric field (ρ^r medium) in percent, $\Delta ip = 100 \times (E^* - E^r)./|E^r|$ for a vertical Y-directed slice in-line (x=0 m) with the HED source orientation (top) and for a horizontal slice at z=150m (bottom)* __for the CR cube model of 10 $\Omega.m$ and -100 mrad__ *Left images represent the in-phase IP effect, whereas right images the out-of-phase component. The amplitudes are represented by the color scale*

Looking closer to the surface response, figure IV.22 presents the in-line electric response spectrum and the IP effect for the constant CR cube model. The spectrum is similar to what was observed previously for the layered CR case. IP effect on the in-phase part is merely observed, and does not exceed 0.7 %. On the other hand, an effect over the quadrature part is observed at low frequencies and vanishes at the highest frequencies due to the skin effect, the increase of the induction response and the decrease of the in-phase field jointly. Compared to the laterally boundless layer case, the low frequency IP effect on the quadrature of the electric field is significantly lower around 1.7%
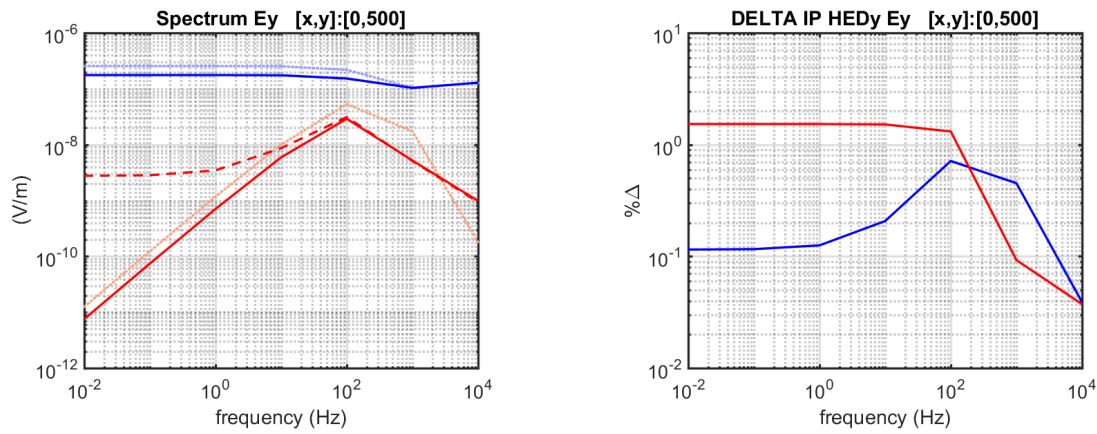
Figure IV.22: *Left: measured electric field spectrum at the point directly above the cube center (x=0m, y=500m, z=0). Blue shaded curves represent in-phase field, whereas red shaded curves the quadrature phase. Solid lines represent the response for a real resistivity cube (10 Ω.m; 0 mrad), dashed lines represent the response for a CR cube (10 Ω.m; -100 mrad) and light dotted lines the responses in the homogeneous (100 Ω.m) background. Right: corresponding IP effect for the in-phase and quadrature part in blue and red lines respectively*

Figure IV.23 presents the spatial variation of the electric field and the IP effect associated on two profiles of interest at 0.1 Hz . In-line field (Y-directed) is presented for the in-line profile and a cross-line profile (X-directed) passing both by the point at the surface directly above the center of the cube. Conductive anomaly decreases the observed electric field above it, compared to an homogeneous half-space response due to galvanic effect occurring at the cube interfaces. The figure shows that IP effect is larger above the cube for the in-line component (Ey) and decreases away from it. Cross-line electric field is zero on the axis of the in-line profile due to symmetry of the source pattern. Its IP effect is maximal above the edges of the cube but is not significant for a target at this depth (0.3% on the quadrature field).
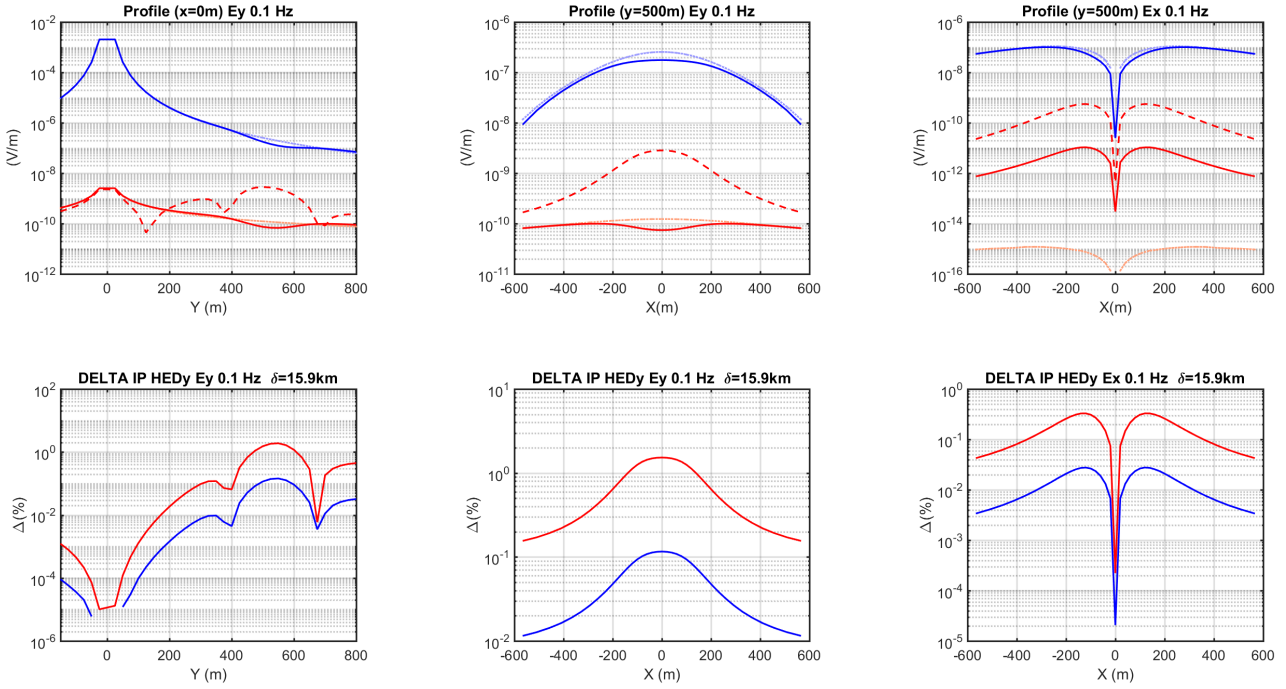
Figure IV.23: *Top: measured electric field at the surface at 0.1 Hz represented for the crossing Y and X-profile (cube between y =∈ [400, 600] and x =∈ [−100, 100]). Blue shaded curves represent in-phase field, whereas red shaded curves the quadrature phase. Solid lines represent the response for a real resistivity cube (10 Ω.m; 0 mrad), dashed lines represent the response for a CR cube (10 Ω.m; -100 mrad) and light dotted lines the response in the homogeneous (100 Ω.m) background. Bottom: corresponding IP effect over the profile considered for the in-phase and quadrature part in blue and red lines respectively*

Frequency-dependent CR cube spectrum

The electric field spectrum and IP effect obtained for the frequency-dependent CR cube according to a Cole-Cole model are presented in figure IV.24. Again what could be observed for the layer case remains true for the cube model with smaller IP effect. A slight variation of the in-phase electric field can be detected due to the variation of the real part of the CR with frequency with a maximum of 6% at 100 Hz. The quadrature phase IP effect depends on both parts of CR variation with a lower effect towards low frequencies due to the CR phase that decreases according to the characteristic relaxation time of the CC model. A slight shift in frequency can also be noticed and interpreted as an effect of the variation of the real part of the CR. IP effect on the quadrature phase is then slightly higher with a maximal 2.4% anomaly.
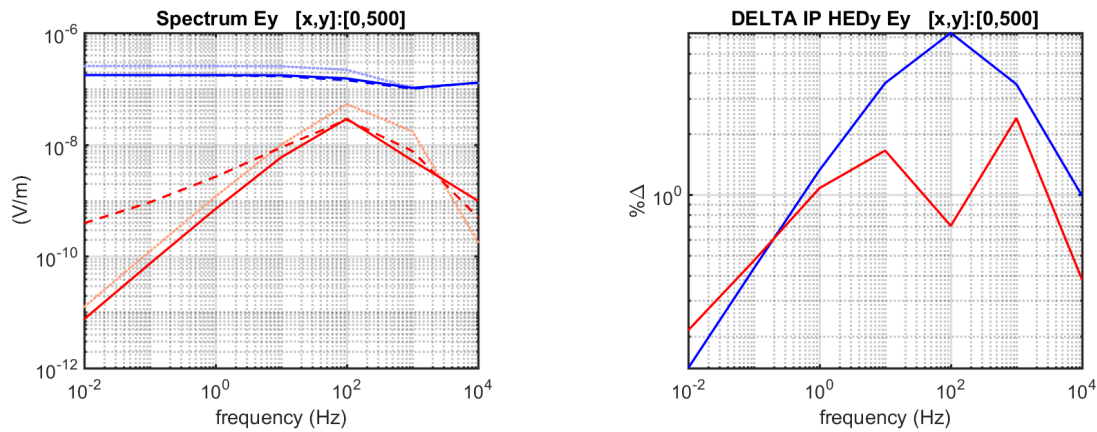
Figure IV.24: *Left: measured electric field spectrum at the point directly above the cube center (x=0m, y=500m, z=0). Blue shaded curves represent in-phase field, whereas red shaded curves the quadrature phase. Solid lines represent the response for a real resistivity cube (10 Ω.m; 0 mrad), dashed lines represent the response for a frequency-dependent CR cube ($\rho_0 = 10\,\Omega.m, \rho_\infty = 50\,\Omega.m, m = 0.5, \tau = 0.01\,s, c = 0.5$) and light dotted lines the response in the homogeneous (100 Ω.m) background. Right: corresponding IP effect for the in-phase and quadrature part in blue and red lines respectively*

Sensitivity conclusion

Through these models, I demonstrated that even if the full EM response is accounted for in a CSEM/IP survey and before considering signal to noise ratio, there are strong limitations on which information would be recoverable from a CSEM/IP survey depending to the target and acquisition geometries:

❏ The EM fields due to a VMD source or magnetic field due to a galvanic source present a limited bandwidth on which the IP information is accessible as the field responses are vanishing towards near field or are "*saturated*" and not sensitive to resistivity. Study of the electric field from galvanic sources should be preferred to access low-frequency information.

❏ A Medium without ρ^r frequency dependence would be harder to characterize as its variation with frequency induces large effects on the amplitude of the field.

❏ IP effect over the quadrature electric field due to ρ^q becomes negligible compared to EM induction arising from medium anomalies at the highest frequencies and largest offset.

❏ Sensitivity to an anomalous body is function of the offset and frequency compared to its depth and size, which will limit the frequency range where the resistivity spectrum of the target is recoverable.

Accessing to IP information is a challenge for several reasons. Even in a perfect case, it will often leads to recover only an incomplete information, limited by EM induction in the medium, depth of the target, survey design or shape of the resistivity relaxation out of the range of the frequency band investigated. Figure IV.25 presents a sketch of a simplified recoverable IP information domain, resuming the survey limitations according to the frequency and geometric sounding capacities, the domain where data are defined sensitive to CR assuming the simplest case of a half-space, the domain where IP is saturated by EM induction and the domain where the skin depth becomes shorter than the position of the target and where the target effect is not measurable at the surface for the highest frequencies.
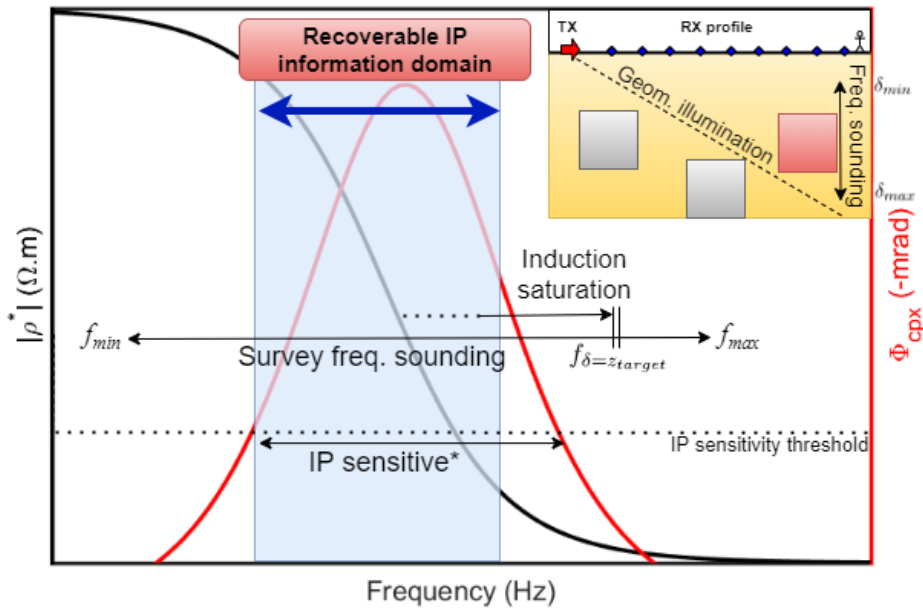

Figure IV.25: *Sketch of the expected recoverable IP domain for a buried target according to frequency limitation (survey frequency limit, skin depth limits), induction saturation and IP sensitivity threshold (*, defined as the domain where frequency variations or resistivity phase of the target is sufficiently large to be measured in a half-space). In addition, geometrical illumination should be consistent with the depth of the target. In the top-right sketch the grey targets are too close to the source compared to their depth and are not illuminated by the source contrary to the red target.*

Nevertheless, CSEM data are sensitive to IP effects. A sensitivity study over a constant CR half-space showed that CSEM data are sensitive to induced polarization according to the CR phase in the medium and to the variation of the CR norm. Even if IP effects due to Φ_{cpx} are relatively weak and can be drowned in EM induction effect at high frequencies, taking into account the full-EM response allows the extension of the range of application of the IP method as a large frequency range is sensitive to both effects simultaneously. IP also impacts resistivity with a frequency dependence of the

CR norm, which could have a large impact in CSEM data if not taken into account for multi-frequency survey, even in the EM induction domain if the CR norm variation is significant.

From this sensitivity study, in addition to the estimation of the magnitude of IP effects in CSEM data, two major observations were made concerning IP effect in CSEM data and will impact the way that I chose to tackle the problem of the CR multi-parameter inversion: for galvanic sources the CR phase has weak effect on the amplitude of the electric field, whereas it impacts mostly the phase of the electric field with an additional delay. This is especially true for buried targets as data sensitivity tends to decrease with the depth of the target. These observations imply that strategies similar to DCIP prospecting can be considered. Indeed, data inversion in electrical method processes the CR norm and CR phase separately. EM induction arising in CSEM data prevents a complete separation, but using this sensitivity difference as a gauge to constrain efficiently the multi-parameter inversion will be the subject of the next chapter dealing about the CR inversion.

Complex resistivity inversion

Chapter V deals with the inversion of EM data for a constant and for a frequency-dependent CR. At first the inverse problem is undertaken though a 1D inversion module that was developed and implemented in the main code 3D code and based on the fast 1DSA solution. A multiparameter inversion strategy is developed and evaluated through synthetic examples. In the second part, the developments are transposed to the large and computationally expensive 3D problem.

V.1   1D inversion of CR

V.1.1   Constant complex resistivity ρ^*

Method and multi-stage workflow

There are several purposes to the implementation of a 1D inversion module. First, throughout this thesis, it shown to be a good way to master the architecture of the POLYEM3D code and to develop a strategy of implementation of the multi-parameter problem, as originally the code take only the real resistivity (constant) as an inversion parameter. Second, the 3D problem is large and involves a very high computational cost with an inverse problem hard to constrain. Implementing a 1D inversion module allows to develop and test an inversion for the CR at low computational cost. Furthermore, the problem can be easily controlled considering the small number of parameters and their effects in the data. Third, a 1D inversion module integrated to POLYEM3D that can take the same inputs to solve a 1D medium prior to a 3D inversion can be practical in many situations. Especially when looking to invert a large dataset and for an evaluation of the information that is contained in the data during the first stages of the inversion process.

   As presented in chapter III, solving the local inverse problem consists to seek a model minimizing an objective function χ (V.1), with a data associated function χ_d and a model regularisation term χ_m.

$$\chi = \chi_d + \lambda \chi_m \tag{V.1}$$

   The data minimization term consists in the norm of the data vector residuals between the calculated and the observed data (d^{cal} and d^{obs} respectively), weighted by a diagonal matrix W_d composed by the reciprocal of the data standard deviation. Data vectors are of the size N_d depending on the number of frequencies, transmitters, receivers and

components of the fields considered. In the following the L2 norm is used but other norms implemented in the original POLYEM3D are available. The model regularisation term uses a function imposing some constraints on the model parameters with λ a Lagrange multiplier controlling the trade-off between data fit and model regularization.

As presented in chapter III the inverse problem is solved iteratively with a deterministic linearised descent method. The optimisation algorithm is a preconditioned gradient-based descent implemented through a reverse communication algorithm, combined with a line search based on a bracketing strategy (Métivier and Brossier, 2016; Nocedal and Wright, 2006). It requires at each iteration the computation of the cost function and its gradient $\partial_m \chi$. Determination of the gradient is a critical task in local optimization problem: local optimization using gradient-based methods solves iteratively the problem (eq. (V.3)) at the iteration k and starts from a model m_0 with a defined step Δm in the descent direction. m is the vector of model parameters of size N_m and depending on the inversion domain size and parametrization. Usually a smaller grid is used with some variable transformation compared to the forward grid medium definition. The descent direction, therefore the model perturbation, is determined by the reverse gradient of the cost function:

$$m_{k+1} = m_k + \Delta m_k \tag{V.2}$$

$$m_{k+1} = m_k - \alpha \partial_m \chi \tag{V.3}$$

Partial derivatives with respect to a variable are noted with a compact notation. The partial derivative m is then noted $\partial_m = \frac{\partial}{\partial m}$. The optimal descent step α is determined using a line-search technique respecting the Wolf conditions and ensuring that the objective function decreases of a sufficient amount using the curvature condition. The gradient of the data cost function for an L2 norm needs estimation of the sensitivity matrix J and the data residuals δ_d and is expressed as :

$$\partial_m \chi_d = \Re(J^\dagger \delta_d) \qquad \text{with } \begin{array}{l} J_{i,j} = \frac{\partial d_i}{\partial m_j} \quad \text{with i=1,...,}N_d \text{ and j=1,...,}N_m \\ \delta_d = d^{cal} - d^{obs} \end{array} \tag{V.4}$$

† denotes the transposed conjugate operator.

On the other hand, the Gauss-Newton method was also implemented in the 1D module and takes advantage of the approximate Hessian $\boldsymbol{H}$ (eq.(V.5)) to solve the model step and neglecting second-order terms compared to full Newton method.

$$\boldsymbol{H} = \frac{\partial^2 \chi}{\partial m^2} \simeq \Re(J^\dagger J) \tag{V.5}$$

The Hessian helps to counter-balance the sensitivity gap between parameters. Considering a linear problem and taking the second-order derivative of the Taylor expansion of the data misfit function, it was presented earlier that a solution for Δm_k solves equation (V.6).

$$\boldsymbol{H} \Delta m_k = -\partial_m \chi_d \tag{V.6}$$

For small problems as for the 1D case, the approximate Hessian can directly be inverted to find the optimal step size. In order to take into account the non-linearity of the problem, a line-search should still be applied to obtain the next iteration as :

$$m_{k+1} = m_k - \alpha \boldsymbol{H}^{-1} \partial_m \chi_d \tag{V.7}$$

Gradient based or Gauss-Newton optimization need both the calculation of the Jacobian in order to obtain the gradient (eq. (V.4)) and the Hessian of the optimization problem (eq. (V.5)).
The calculation of the Jacobian in the 1D module was implemented explicitly using the perturbation method with central point difference. A slight perturbation δ_m is applied to each parameter separately in both directions and partial derivatives are computed for each terms of the Jacobian.

$$
\begin{aligned}
J_{i,j} &= \frac{\partial d_i}{\partial m_j} \\
&= \lim_{\delta_m \to 0} \frac{\mathcal{F}(m_j + \delta_m) - \mathcal{F}(m_j - \delta_m)}{(m_j + \delta_m) - (m_j - \delta_m)} \\
&= \lim_{\delta_m \to 0} \frac{\mathcal{F}(m_j + \delta_m) - \mathcal{F}(m_j - \delta_m)}{2\delta_m},
\end{aligned}
\tag{V.8}
$$

$\mathcal{F}$ being the forward operator.

Perturbation was chosen as 1% of the resistivity to ensure a slight variation in the data and account for linear approximation. The approximate Hessian can then be obtained using equation (V.5). The Hessian matrix is inverted through a LU decomposition using routines of the SCALAPACK library in order to use a Gauss-Newton optimization.

Example of a 1D inversion for a simple real and constant resistivity
A 4-layer model is presented as a demonstration in figure V.2 of the 1D inversion code dealing with a real and constant resistivity medium. This is the case of a classic CSEM inversion without IP in the data. Layered medium properties (Thickness h and ρ^r) are given in (table V.1). Observed data was generated with the same 1DSA code. Synthetic survey geometry is a 500 meter profile of 21 receivers and an inline HED source, oriented in the profile direction with a minimal offset of 50 meters to ensure a good geometric coverage (Figure V.1). Logarithm of the in-line electric field (*i.e.* the logarithmic amplitude and the phase of the electric field) data were used with 13 frequencies logarithmically spaced from 10^{-2} to 10^4 Hz. The layered inversion grid uses 21 layers of increasing thickness (10% increase factor) starting from a first layer below air interface of 20 meters. In this way, the inversion grid does not match perfectly the interfaces of the true model as it would be for a real data inversion work-flow.

Layer #	h (m)	$\rho^r (\Omega.m)$
1	50	1000
2	100	100
3	100	500
4	∞	10

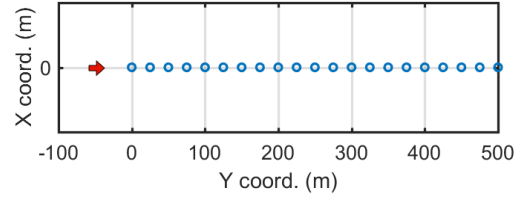Table V.1:   Properties of the four-layer model, with h the thickness of the layer.

Figure V.1: *CSEM synthetic survey geometry using a 500 meters profile of 21 receivers (blue circles) and a HED source oriented in-line, in the Y direction (red arrow)*
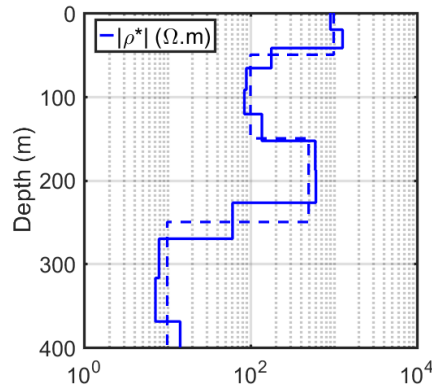
Figure V.2: *Resistivity model result for a 1D inversion considering a classical synthetic CSEM survey taking into account a constant and real resistivity medium; solid line represents the inverted resistivity model and dashed line the true model. rms = 1.02%*

The starting model was chosen as an homogeneous half-space with $\rho^r = 50\Omega.m$. Data residuals were weighted by a 1% relative error in the covariance matrix (see annexe A.1 for covariance and rms estimations). No noise was added in the modelled data. A maximum smoothness regularization was used in following 1D examples with a parameter λ equal to 1. The Gauss-Newton optimization was used. The resistivity model is well retrieved and the rms is satisfactory and reaches 1%.

CR resistivity parameterization

Considering at first a constant CR, the number of parameters is doubled compared to the real resistivity case: in the simplest case of a constant CR, the model parameter vector m contains $2N_{inv}$ real parameters, with N_{inv} the number of inverted cells in the medium. m contains the CR of the medium separated into a parameter associated to the real part $(\rho^r, \sigma^r, \log(\rho^r, ...))$ responsible of conduction current and a parameter associated to the imaginary part $(\rho^q, \sigma^q, \log(\rho^q, ...))$ linked to induced polarisation phenomena in the medium. This separation can also take the form of the resistivity norm $|\rho^*|$ with the CR phase Φ_{cpx}. $|\rho^*|$ can be associated to a real part as $\rho^r \gg \rho^q$. On the other hand,

Φ_{cpx} can be associated to the imaginary part, as it reflects its ratio with the real part, with induced polarisation effect being significant only when this ratio is high enough, as presented in section IV.2.1.

In the following and considering the previous sensitivity study, the choice of parametrization will be focus on the $|\rho^*|$ and Φ_{cpx} resistivity description. Indeed, this choice of parametrization was preferred as IP effect linked to the presence of an imaginary part of the resistivity, depends on the value of the real part in the medium and is therefore proportional to the CR phase. Using this parametrization facilitates the management of the boundaries during the inverse problem, as the parameter will have to be limited according to the CR phase value.

Furthermore, the logarithm of these parameters will be mainly investigated here as it imposes the positiveness of the solution. In order to respect the parametrization choice, some change of variables should be carefully applied to the Jacobian depending of the original formulation. As for the mono-parameter case the perturbation method is used to obtain the Jacobian, the respective parameters can be straightforwardly perturbed to obtain the gradient from equation V.4. Otherwise changes of variables for the gradient can be achieved using the chain rule (as it is necessary for the 3D problem) following:

$$\partial_\rho \chi = \frac{\partial \chi}{\partial \rho} \tag{V.9}$$

$$\partial_m \chi = \frac{\partial \rho}{\partial m} \frac{\partial \chi}{\partial \rho} \tag{V.10}$$

Considering at first m as the vector containing the CR norm and the CR phase, one after the other :

$$m_{|\rho^*|,\Phi_{cpx}} = \begin{pmatrix} |\rho^*| \\ \Phi_{cpx} \end{pmatrix} \tag{V.11}$$

The gradient (or the Jacobian) is calculated first according to the forward formulation with respect to ρ^r and ρ^q separately :

$$\frac{\partial \chi}{\partial m_{\rho_r,\rho_q}} = \begin{pmatrix} \frac{\partial \chi}{\partial \rho_r} \\ \frac{\partial \chi}{\partial \rho_q} \end{pmatrix} \tag{V.12}$$

As the cost function depends on both variables for the CR case the perturbation of the gradient can be noted :

$$d\chi = \frac{\partial \chi}{\partial \rho_r} d\rho_r + \frac{\partial \chi}{\partial \rho_q} d\rho_q \tag{V.13}$$

Both parts of the gradient of the cost function with respect to the norm and the phase of the CR can then be expressed for each cell according to their gradient with respect to the real and imaginary parts of the resistivity :

$$\frac{\partial \chi}{\partial m_{|\rho^*|}} = \frac{\partial \rho_r}{\partial |\rho^*|}\frac{\partial \chi}{\partial \rho_r} + \frac{\partial \rho_q}{\partial |\rho^*|}\frac{\partial \chi}{\partial \rho_q}$$
$$\frac{\partial \chi}{\partial m_{\Phi_{cpx}}} = \frac{\partial \rho_r}{\partial \Phi_{cpx}}\frac{\partial \chi}{\partial \rho_r} + \frac{\partial \rho_q}{\partial \Phi_{cpx}}\frac{\partial \chi}{\partial \rho_q}$$

(V.14)

Using the real and imaginary part in its cosine/sine formulation, we can differentiate each terms with respect to amplitude/phase of CR into the following matrix:

$$\begin{pmatrix} \frac{\partial \rho_r}{\partial |\rho^*|} & \frac{\partial \rho_q}{\partial |\rho^*|} \\ \frac{\partial \rho_r}{\partial \Phi_{cpx}} & \frac{\partial \rho_q}{\partial \Phi_{cpx}} \end{pmatrix} = \begin{pmatrix} \frac{\partial |\rho^*|cos(\Phi_{cpx})}{\partial |\rho^*|} & \frac{\partial |\rho^*|sin(\Phi_{cpx})}{\partial |\rho^*|} \\ \frac{\partial |\rho^*|cos(\Phi_{cpx})}{\partial \Phi_{cpx}} & \frac{\partial |\rho^*|sin(\Phi_{cpx})}{\partial \Phi_{cpx}} \end{pmatrix} = \begin{pmatrix} cos(\Phi_{cpx}) & sin(\Phi_{cpx}) \\ -|\rho^*|sin(\Phi_{cpx}) & |\rho^*|cos(\Phi_{cpx}) \end{pmatrix}$$

(V.15)

Gradient with respect to amplitude and phase of the resistivity is finally obtained from real/imaginary gradient using the following change of variables:

$$\frac{\partial \chi}{\partial m_{|\rho^*|,\Phi_{cpx}}} = \begin{pmatrix} cos(\Phi_{cpx}) & sin(\Phi_{cpx}) \\ -|\rho^*|sin(\Phi_{cpx}) & |\rho^*|cos(\Phi_{cpx}) \end{pmatrix} \begin{pmatrix} \frac{\partial \chi}{\partial \rho_r} \\ \frac{\partial \chi}{\partial \rho_q} \end{pmatrix}$$

(V.16)

To obtain its equivalent for the logarithm of the amplitude and phase, the corresponding chain rule differentiation is applied.

Multi-staged workflow

Taking into account CR increases the need to manage large number of parameters which implies non-uniqueness of the solution and parameters with different sensitivities. It will be particularly critical for a frequency-dependent CR, as more unknowns are added to an already undetermined problem. Developing a strategy allowing the stabilization of the inversion is of crucial importance. The main idea developed here to constrain optimization, is to take advantage of the difference in IP effect caused by a variation of the CR norm and of the phase of CR in the CSEM data. From the sensitivity study it was demonstrated that the impact of Φ_{cpx} over the amplitude of the electric field is weak considering a constant $|\rho^*|$. To take advantage of this particularity, a multi-stage approach is presented allowing to manage the CR parameters independently in each stage, similarly to what can be done for DCIP methods.

❏ A first stage (1) consists in inverting the amplitude of the electric field to obtain the amplitude of the CR $|\rho^*|$.

❏ A second stage (2) inverts the residuals remaining on the electric field phase to solve the CR phase Φ_{cpx} of the model.

The amplitude/phase parameterization of the electric field was preferred over the separation of real/imaginary parts as amplitude comprises a mix of both galvanic and induction information contained in the data, contrary to the real part of the electric field which is mainly associated to galvanic effects.

This is the fundamental concept of the multi-stage framework that will be used to constrain the multi-parameter problem. During the first stage, despite the fact that the CR phase impacts particularly the electric phase data, the EM induction phase delay increases to become dominant in the data. A part of this information is contained in amplitude data, but a part of the information as the sign, is totally omitted and not perturbed enough by IP to be discarded. This is why, one could penalize appropriately the covariance of phase data during stage (1): it allows to take into account only EM induction effects that are larger to a threshold determined by the maximal phase delay that is expected due to IP. This is similar to considering the IP as a noise over the phase data during the first stage. During stage (2), the main idea relies on the inversion of phase data as they are the most affected by the CR phase, but the complete data can be considered as well. However, amplitude of the electric field must be correctly fitted after stage (1), otherwise artefacts could appear during the CR phase inversion.

ρ^* layered model inversion

Inversion of a 3-layer model is presented here to study a constant CR layer model. The Gauss-Newton method is used. The model is composed of a conductive middle layer of 10 $\Omega.m$ and a resistivity phase of -100 $mrad$ into a more resistive, purely real, background (table V.2).

Layer #	h (m)	$\|\rho^*\|(\Omega.m)$	$-\Phi_{cpx}(mrad)$
1	100	100	0
2	100	10	100
3	∞	40	0

Table V.2: Properties of the three layers CR model, with h the thickness of the layer.

Acquisition geometry and the layered grid are similar to those of the previous example but are recall here. Survey geometry is a 500 meters profile of 21 receivers recording the field due to an inline HED source (Figure V.1). Logarithm of the in-line electric field data are used with 13 frequencies logarithmically spaced from 10^{-2} to 10^4 Hz. The layered inversion grid uses 21 layers of increasing thickness starting from a first layer below air interface of 20 meters. Starting model was chosen as an homogeneous half-space with $\rho^r = 50\,\Omega.m$. When a CR is considered in the following a low imaginary part is considered in the starting model taking $\rho^q = -0.05\,\Omega.m$ to obtain a starting model of $\Phi_{cpx} = -1\,mrad$. Data residuals were weighted by a 1% relative error and no noise was considered as well. A maximum smoothness regularization was used in following 1D examples with a Thikhonov parameters λ equal to 1.

In the figures V.3a and V.3b, results of inversions of the real part of the resistivity are presented, for synthetic data generated without and with IP in order to estimate the impact on the inversion. Then, inversions of CR models are presented searching for the CR norm and phase simultaneously during the process in a multi-parameter inversion and then separately through the multi-stage strategy proposed in the previous paragraph

(Figures V.3c and V.3d). The latter inversion uses only electric field amplitude data during the first stage, then the second stage deals with the electric field phase data only. Figures V.4a and V.4b present the inversion results for a second order gradient based method (l-BFGS).
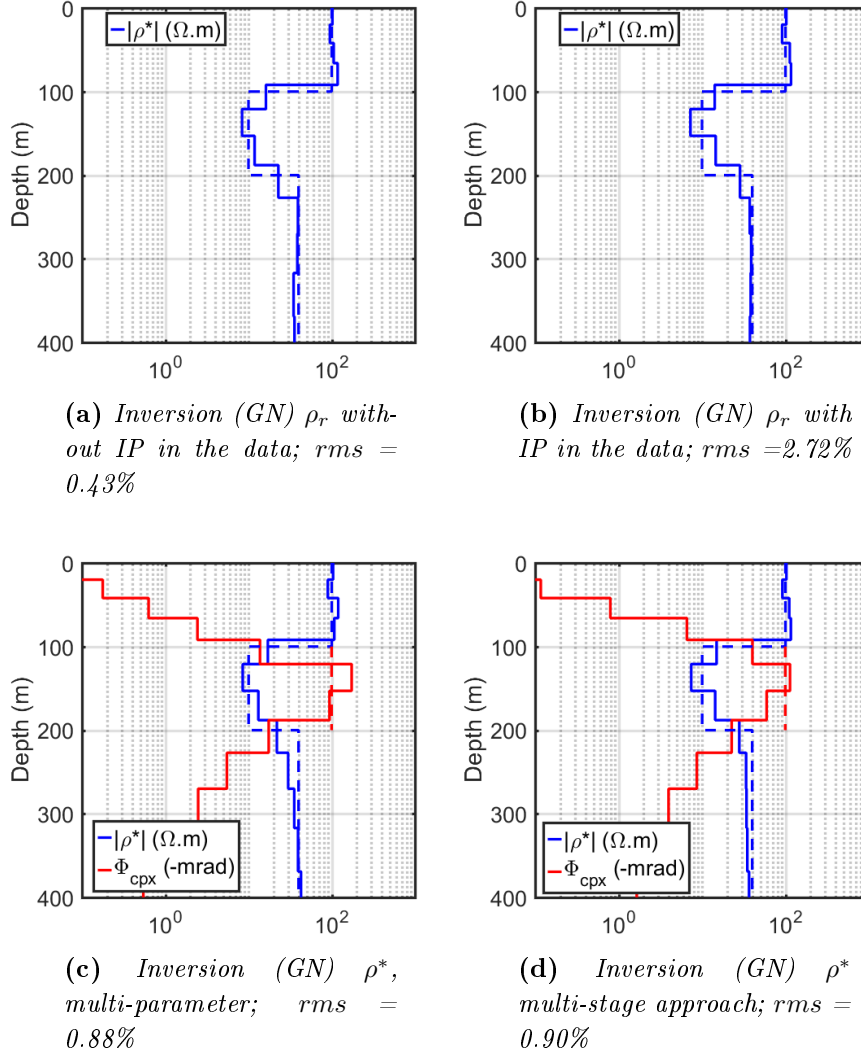

(a) *Inversion (GN) ρ_r without IP in the data; rms = 0.43%*

(b) *Inversion (GN) ρ_r with IP in the data; rms =2.72%*

(c) *Inversion (GN) ρ^*, multi-parameter; rms = 0.88%*

(d) *Inversion (GN) ρ^* multi-stage approach; rms = 0.90%*

Figure V.3: *1D results for the different inversions considering a real resistivity medium with and without IP, or a CR medium using a multi-parameter or a multi-stage inversion. (a) and (b),(c), (d) was inverted with a GN optimization*

The first inversion result (figure V.3a) that seeks a real and constant resistivity model without IP in the data is well resolved with smooth variations with a data *rms* equal to 0.43 %. The second inversion result (figure V.3b) includes IP effects in the data but does not take into account a CR during the inversion. The model is well resolved, nevertheless data *rms* stayed stuck at 2.72 %. The residuals are due to the phase of the data that is not well fitted due to the IP effects which is not taken into account here. A multi-parameter inversion of the CR resolving simultaneously its amplitude and phase of the CR is shown in figure V.3c: data are well fitted with a *rms* below 1 % and a model close to the true

model. The fourth inversion was performed through the multi-stage workflow (figure V.3d): results are very similar to the multi-parameter inversion, but the complexity of managing parameters of different classes with different sensitivity was avoided. After the first stage, *rms* on the data was around 2.7 %, similarly to the second inversion. At the end of the 2nd stage, a satisfactory *rms* was reached as well with *rms*=0.90 % and demonstrates the efficiency of the multi-stage work-flow. Improvement of the data fit during the procedure is presented in the following examples for a frequency-dependent CR layer inversion.

(a) *Inversion (l-BFGS) ρ^*, multi-parameter without scaling; rms = 2.70%*

(b) *Inversion (l-BFGS) ρ^*, multi-parameter with a preconditioning of Φ_{cpx} ($m_\Phi = (1/10)\Phi_{cpx}$); rms = 0.40%*
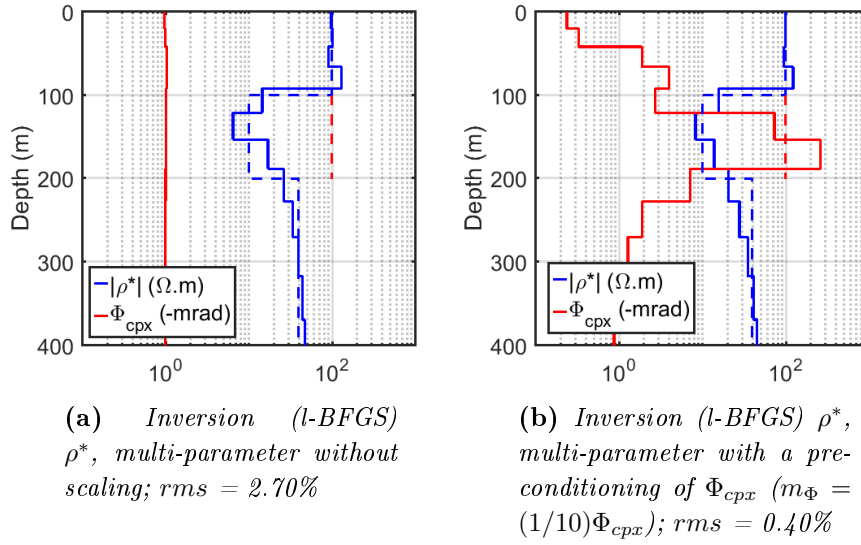
Figure V.4: *1D inversion results considering a CR medium using a multi-parameter inversion with a gradient based optimization (l-BFGS), with and without a scaling of Φ_{cpx} to correct the sensitivity disparity between both parameter class*

Figure V.4, presents a comparison with ℓ-BFGS optimization results, that preconditions the descent direction with an estimation oh the inverse Hessian from the gradient calculated at previous iterations. The convergence and the account of non-linearity and sensitivity disparity are improved compared to STD method. Despite using, a second-order gradient-based method, the multiparameter inversion presented in figure V.4a failed to solve the CR phase. Figure V.4b shows that in this case a scaling of the parameter was necessary to correct for the sensitivity difference between the CR norm and phase. It illustrates that decomposing the problem through a multi-stage framework is a practical strategy to facilitate the inversion without adding supplementary tuning parameter, as in cases where the Hessian information are not sufficient to correct for non-linearity and sensitivity disparity, or when computationally cheaper optimization methods are used.

V.1.2   Frequency-dependent $\rho^*(\omega)$

Polynomial parametrization

Inverting a frequency-dependent resistivity $\rho^*(w)$ is a challenge because each frequency multiplies the total number of model parameters. To decrease the total number of parameters, one can impose a parametrization based on a specific relaxation model, for instance a 4-parameter Cole-Cole model (Cole and Cole, 1941; Pelton et al., 1978). Nevertheless, this parameterization make the assumption that the resistivity model follows strictly a Cole-Cole relaxation. Consider a Cole-Cole model: ρ_0 fix the DC resistivity, m the amplitude of the drop from ρ_0 to ρ_∞ at high frequency and the phase peak amplitude, τ the inflexion point and the frequency exponent c control the shape. The sensitivity to IP effect is reasonably small compared to EM effects as seen previously and a part of the IP information will not be accessible due to depth sounding and frequency limitations. Then only a small portion of the residual contains information on the shape of the CR model.

I choose a 2nd order polynomial support to describe the CR spectrum adapted to a multi-staged strategy: two independent polynomials are obtained to describe the medium, each having a different sensitivity to electrical data.

As CSEM data are more sensitive to the CR norm variation than to the CR phase, using a CC model a CR phase spectrum will be retrieved even if data do not contain significant IP information due to a non-null CR phase, which could be seen as an advantage or misleading in cases with low information on the medium. Looking for two independent polynomials allows to cross check results between CR norm and phase and to focus on what is reliable in the data. In most cases, 2nd order polynomials are expected to be sufficient to describe CR model with an acceptable accuracy according to resolution limitation with depth and expected noise. It results in 6 parameters per cell: 3 for each polynomial, p^n and q^n describing respectively $|\rho^*|$ and ϕ_{cpx}. Nevertheless, using the multi-staged strategy, only 3 parameters are managed at once, the coefficient of degree zero dealing with a mean constant resistivity and the two coefficients of higher degree managing the frequency dependence shape as a slope and the second degree curvature of the CR spectrum. As seen earlier, IP effects in galvanic CSEM data are controlled by the variation of amplitude and phase of the CR, the logarithm of these parameters was chosen. Furthermore, as resistivity variation with frequency is often following a power law with frequency, logarithm of the frequency was chosen for the polynomial description. Polynomial coefficients used to support CR spectrum are then defined by equations (V.17) and (V.18):

$$log(|\rho^*|) = \sum_{j=0}^{n=2} p_j * log_{10}(f)^j \tag{V.17}$$

$$log(\Phi_{cpx}) = \sum_{j=0}^{n=2} q_j * log_{10}(f)^j \tag{V.18}$$

Model vector becomes then:

$$m = \begin{pmatrix} p^0 \\ p^1 \\ p^2 \\ q^0 \\ q^1 \\ q^2 \end{pmatrix} \tag{V.19}$$

Using logarithm of the frequency the zero order term corresponds naturally to the value at 1 Hz. To keep this value over the investigated frequency range, a translation of this "pivot" frequency was undertaken to obtain a pivot frequency in the middle of the spectrum investigated.

Change of Variable (CoV)

In the case of the frequency-dependent CR, the gradient can be obtained by directly perturbing each polynomial coefficient or by using a change of variable from discrete $|\rho^*|(\omega)$ and $\Phi_{cpx}(\omega)$ gradient. The change of variable allows a considerable improvement using 2 calls to forward modelling per data and per layers as for the constant resistivity case, whereas perturbing directly the polynomial coefficients needs $2(N_p + 1)$ forward calls per data and layer. Gradient is obtained by CoV as follow, considering $|\rho^*|(\omega)|$ polynomial part:

$$\left(\frac{\partial \chi}{\partial p_n} \right) = \left(\frac{\partial log(|\rho^*|(\omega))}{\partial p_n} \frac{\partial \chi}{\partial log(|\rho^*|(\omega))} \right) \tag{V.20}$$

It results in sum notation in :

$$\left(\frac{\partial \chi}{\partial p_n} \right) = \sum_{i=1}^{N_{freq}} log_{10}(f_i)^n \frac{\partial \chi}{\partial log(|\rho^*|(f_i))} \tag{V.21}$$

Φ_{cpx} polynomial part gradient and Jacobian are obtained with the same method.

Preconditioning of p^n for $n > 0$

Furthermore, to constrain the inversion, a preconditioning of the inverse problem is applied by rescaling the polynomial coefficients of degrees higher than zero. These coefficients are related to the slope and the 2nd order "curvature" of the spectrum which are ruling the data in a second order compared to the constant component of the resistivity. Figure V.5 presents the effect of the preconditioning on the inversion of the CR for a homogeneous half-space considering a gradient-based optimization[b]. In figures V.5a and V.5b the polynomial parameters describing the CR are not scaled during the inversion and the parameter of higher degree is varying abruptly at firsts iterations. This behaviour should be avoided as it does not reflect the natural data sensitivity by introducing a large

---

[b]As the non-linearity of the problem is very weak for such simple model, the Hessian correct completely the scaling and a regularization should be used instead of a scaling if the Gauss-Newton method is used

frequency dependence when a mean constant resistivity is not yet correctly solved. It can lead the inversion in a wrong direction and a model with more complexity and consequently stuck in a local minimum. On the contrary, figures V.5c and V.5d presents the preconditioned case using a scaling coefficient of 10 for first and second-degree coefficients. The final result are equivalent for the CR spectrum reconstruction, but the paths taken by the optimization are significantly different. Priority is given to the constant coefficient at first, then an acceptable slope and/or the 2nd order curvature.
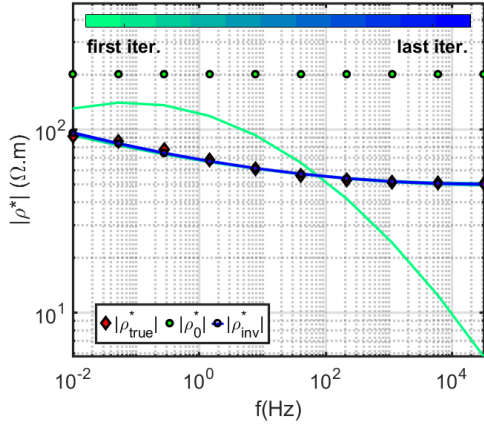
(a) *Resistivity amplitude* $|\rho^*|$ *results for inversion of* p^n *not scaled*
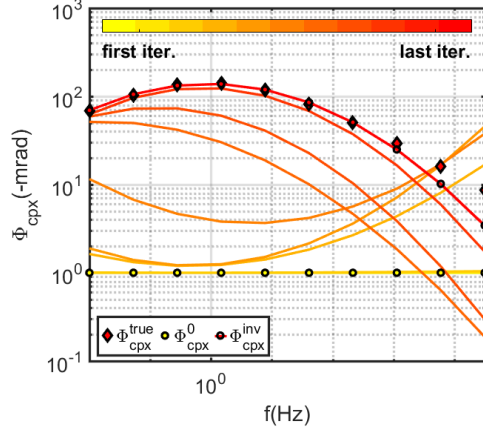
(b) *Resistivity phase* $-\Phi_{cpx}$ *results for inversion of* q^n *not scaled*
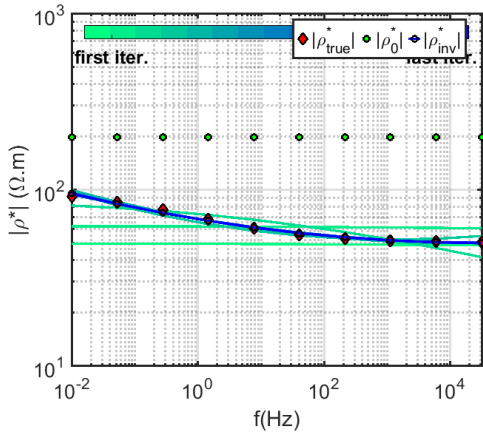
(c) *Resistivity amplitude* $|\rho^*|$ *results for inversion of* p^n *preconditioned* $(n > 0)$
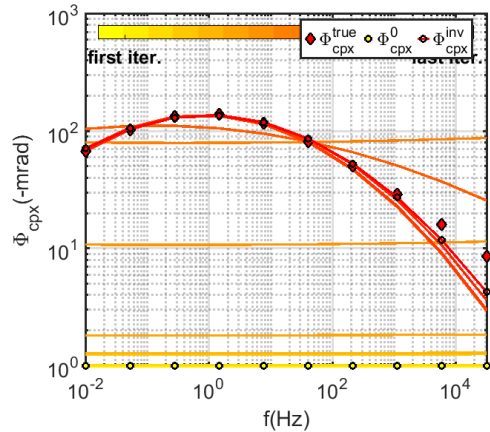
(d) *Resistivity phase* $-\Phi_{cpx}$ *results for inversion of* q^n *preconditioned* $(n > 0)$

Figure V.5: *Inversion of a unique cell model with a true resistivity based on a C-C model, without and with a scaling of* p^n *and* q^n *coefficients for* $n > 0$; *Scaling used is a* $\frac{1}{10}$ *factor*

Scaling by a constant p^n_{sc} is used as a trade-off between parameters, preconditioning in a sense the priority order of each parameter. An optimal way to lead the inversion to the true resistivity starting from an homogeneous medium is to use a parameterization giving

an appropriate weight to polynomial coefficient, solving the main constant component first as it controls the data at first order, then an acceptable slope and/or the 2nd degree coefficient, which control the data at second order.

$\rho^*(\omega)$ layered model inversion

Synthetic inversions of a frequency-dependent CR 1D model are presented to illustrate the multi-parameter and multi-stage inversion results. Synthetic survey and model geometry used for the constant CR model inversion were re-used with a frequency-dependent CR conducting layer based on two different Cole-Cole models presented in figure V.6. A polynomial is fitted on each curve to illustrate an idea of the resolution capabilities of 2nd order polynomials considering CR of a CC model. The chosen CC models are similar with $\rho_0 = 10\Omega.m$, $m = 0.5$, and $c = 0.5$ ensuring a sufficient response with a maximum CR phase above $-100mrad$, whereas two different relaxation times were chosen, to play with the inductive coupling response with $\tau_1 = 0.1s$ presenting low to medium EM/IP coupling and $\tau_2 = 0.001s$ presenting a high coupling between IP and induction responses.

(a) *Cole-Cole resistivity model introduced in the conductive layer in the low frequency IP case;* $\rho_0 = 10\Omega.m$ $m = 0.5$ $\tau = 0.1s$ $c = 0.5$

(b) *Cole-Cole resistivity model introduced in the conductive layer in the high frequency IP case;* $\rho_0 = 10\Omega.m$ $m = 0.5$ $\tau = 0.001s$ $c = 0.5$
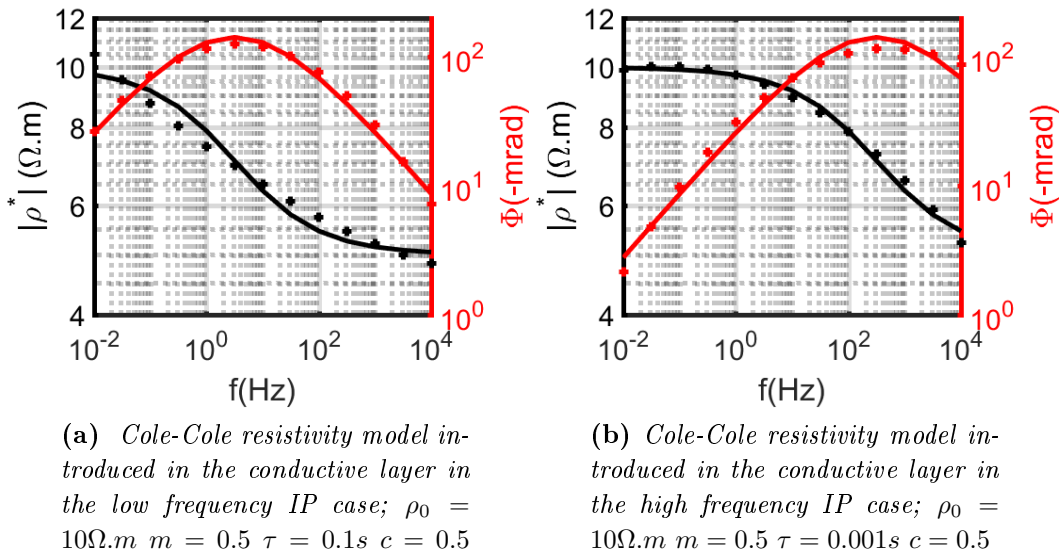
Figure V.6: *Cole-cole resistivity models introduced in the conductive layer of the true model; solid lines represent the true model whereas cross markers represent the best polynomial fit using a second order polynomial.*

Synthetic data were calculated using a 1D SA code for the exact 3-layer model with corresponding CC model. Inversions were performed using the polynomial support as described previously on a grid of 21 layers. GN optimization was used. Regularization was a maximum smoothness constraint with the previous iteration as reference in order to ensure smooth variations. Furthermore, minimum L2-norm deviation from the previous iteration was added in order to regularize large model updates between iterations. Additional regularization with the minimum norm allows to stabilize the multi-parameter problem: it better stabilizes the large step of one parameter compared to the others as

GN methods re-equilibrate sensitivity of parameter beyond the application of the pre-conditioning which was used on the contrary to slow down higher degree polynomial coefficient. The starting model is as previously a 50 $\Omega.m$ half-space with -1 $mrad$. Results of the multi-staged inversion are shown in figures V.7a and V.7b for the late τ_1 and the short time constant τ_2 models. Amplitude of the resistivity was solved in a first stage 1), whereas the resistivity phase was solved in a second stage using final inversion model obtained in 1). In these examples a scaling, p_{sc}^1 and p_{sc}^2 of 0.1 and 0.025 was used in order to help the trade-off between polynomial parameters of degree zero and $n > 0$ and to avoid giving too much weight to these higher degree parameters as they rule the data to a second order only.

(a) τ_1 *CC layer model*   (b) τ_2 *CC layer model*
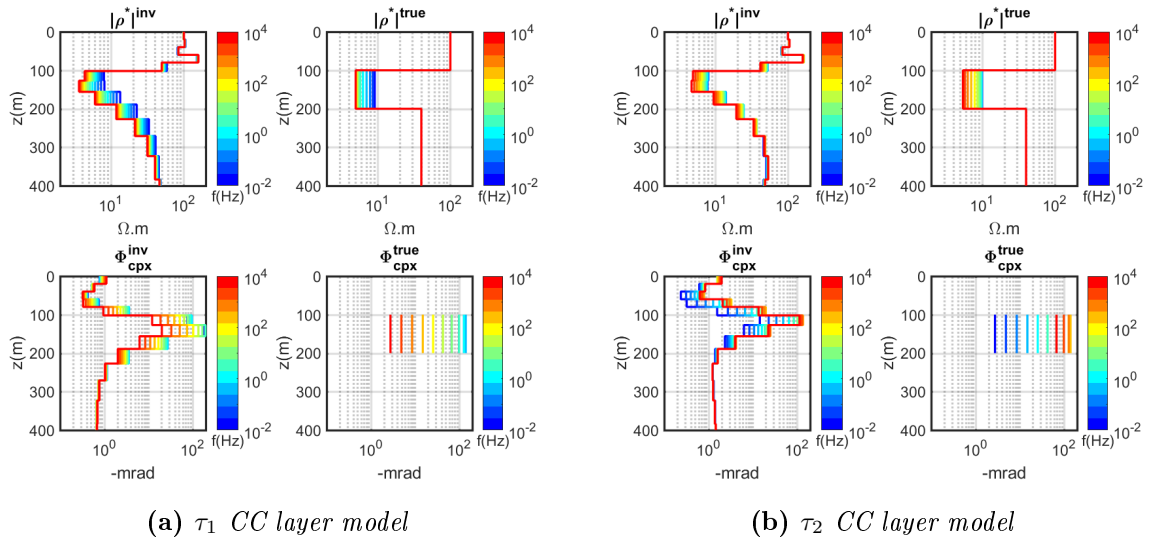
Figure V.7: *Inversion results for the τ_1 and τ_2 CC layer model with respectively a low and a high EM/IP coupling using a 500 meters profile of 21 receivers and an inline HED source as described in figure V.1*

CR norm images correspond to the result of the first stage of the inversion procedure with an unmodified constant and negligible CR phase set to $-1mrad$, whereas CR phase images correspond to the result of the second stage starting from the result of the first stage model. τ_1 model had a starting *rms* of 70.4 %, was improved to 2.70 % during stage (1) and a final *rms* of 0.97 % was reached after stage (2). Considering the τ_2 model starting *rms* was around 64% and was improved in (1) to 1.45 % and in (2) to 0.84 %. *rms* are lower for the short relaxation time layer model, as IP effects are competing with EM induction and the loss of sensitivity to the buried layer towards high frequencies due to skin depth effect. Figure V.8 presents an example of the data fit improvement during the multi-stage procedure for a receiver at the center of the acquisition profile and for τ_1 and τ_2 layer model. Amplitude and phase data of the electric field are very well fitted. Notice that at the end of stage (1), amplitude data are perfectly fitted whereas a relatively large residual is remaining on the phase. This phase residual is inverted with success during the stage (2) of the inversion workflow.
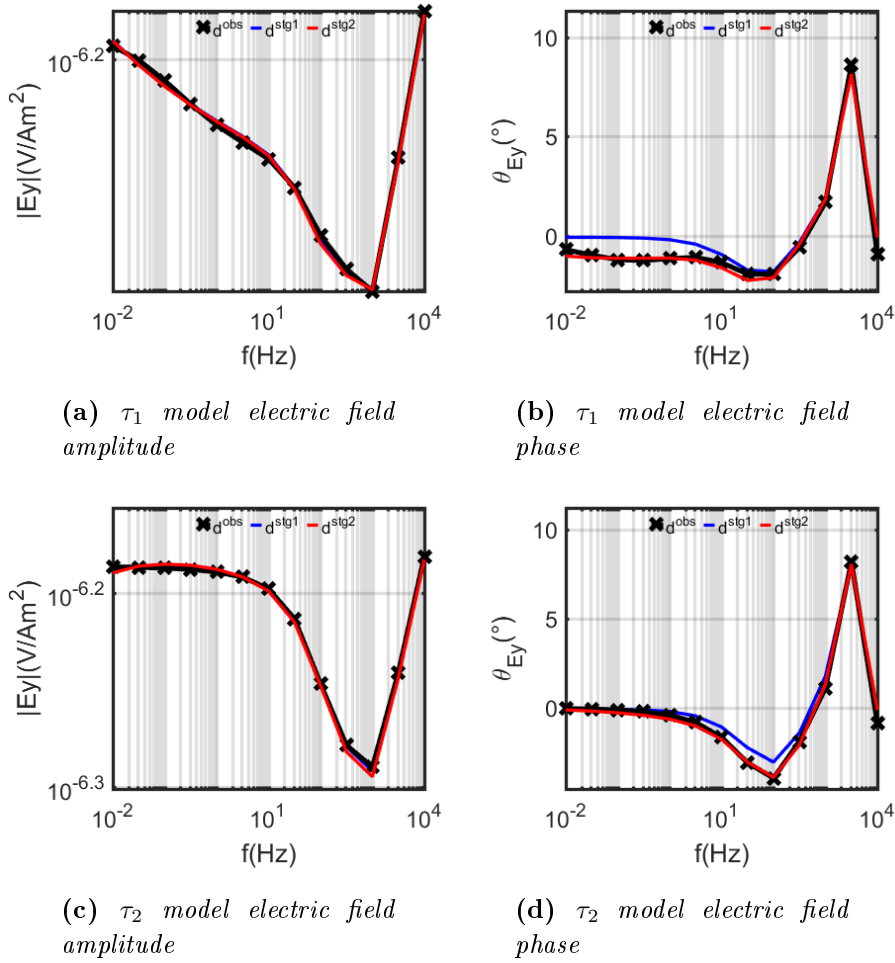
(a) τ_1 *model electric field amplitude*

(b) τ_1 *model electric field phase*

(c) τ_2 *model electric field amplitude*

(d) τ_2 *model electric field phase*

Figure V.8: *Data fit on the in-line electric field amplitude and its phase at each stage of the multi-stage inversion for the τ_1 and τ_2 CC layer model for the receiver at the center (offset = 300m) of the profile of 21 receivers (Figure V.1). Black crossed lines are the observed data d^{obs}, blue lines are the data at the end of stage (1) d^{stg1} and red lines are the data at the end of stage (2) d^{stg2}*

During the first stage, geometry of the true medium is correctly solved for both relaxation times inverting the electrical amplitude of the data and the frequency dependence of the CR norm is also resolved. The top of the polarizable layer is well imaged whereas the bottom limit of the conductive layer shows a smoother transition as bottoms of conductive layer sare harder to solve due to classical loss of sensitivity in this configuration. Resulting soundings show that a correct trend is obtained for both CC relaxation time constants. Figure V.9 shows CR spectra in the polarizable layer for the true, the starting and the inverted model. The second stage allows a good evaluation of the CR phase by inverting the electrical phase data only. The polarizable layer geometry is well resolved. The shapes of the phase spectrum are in good agreement with the CC phase shape. However, the shape is not well constrained for lower CR phase. Indeed, low frequency variations can be seen above the layer but with low CR phase value. Furthermore, for the CR phase spectrum image in figure V.9b and V.9d, phase maxima are relatively well retrieved, but bell shapes are not well constrained on its extrema where phase values

decrease steeply. This is due to the low sensitivity of IP effect, especially for the lower phase values as presented in figure IV.11 for a homogeneous half-space.
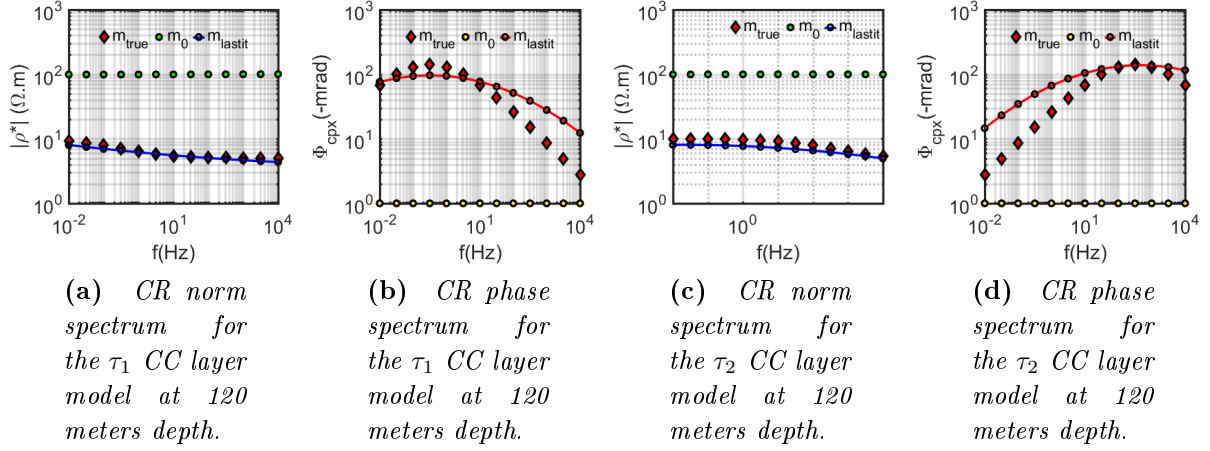

(a) CR norm spectrum for the τ_1 CC layer model at 120 meters depth.

(b) CR phase spectrum for the τ_1 CC layer model at 120 meters depth.

(c) CR norm spectrum for the τ_2 CC layer model at 120 meters depth.

(d) CR phase spectrum for the τ_2 CC layer model at 120 meters depth.

Figure V.9: *Inversion results for the τ_1 and τ_2 CC layer model with respectively a low and a high EM/IP coupling using a 500 meters profile of 21 receivers and an inline HED source as described in figure V.1*

In this part, it was shown that this approach is capable of retrieving at the same time the geometry of the layer and the shape oh the CR spectrum for the norm and the CR phase separately. The bell shape of the CR phase spectrum is damped, where Φ_{cpx} is low despite the good fit. This is due to an IP effect that decreases for lower CR phase IV.11, thus data are less sensitive to these variations. Note that residuals to fit on electrical phase data are already low after stage 1 inversion.

Frequency vs geometric sounding

(a) *Inversion result with a lack of geometrical information. rms = 2.43*

(b) *Inversion result with an optimal geometrical illumination. rms = 1.66*

(c) *True model*
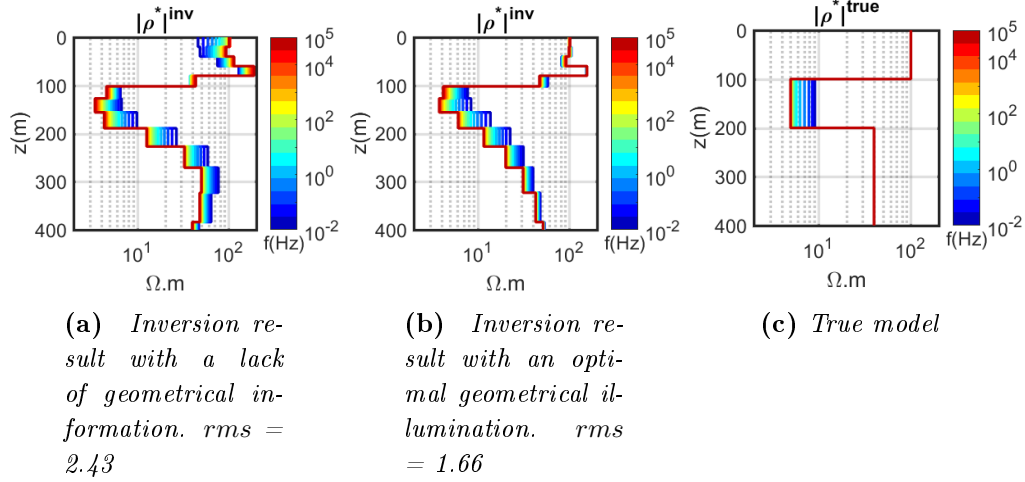
Figure V.10: *Comparison of the capacity to solve the frequency variation of the CR using an optimal frequency sounding acquisition (15 frequencies from 0.01 Hz to 10^5 Hz) and an optimal acquisition geometry (figure V.1), or using a farther source (x=0 m, y=-500 m) with a lack of geometric information at short offset*

The previous case was based on data with good acquisition geometry and investigation frequency window considering the targeted chargeable layer dimension and depth. In CSEM surveys, a part of geometrical information needed in DC method can be obtained with frequency soundings by scanning the medium with the variation of the skin depth and lowering the number of source needed to obtain a correct image. Figure V.10 presents the result of stage (1) for two cases with different geometric coverages and shows the importance of conserving the maximum of geometrical information to obtain a reliable frequency-dependent CR model. To ensure a perfect frequency sounding even for the shallowest layers of the inverted model, 15 frequencies logarithmically spaced from 10^{-2} to 10^5 Hz are used, giving a minimal skin depth of 15 meters for 100 $\Omega.m$. Figure V.10b presents the result for the same acquisition geometry as previous examples (figure V.1) for an optimal coverage. On the other hand, figure V.10a presents the inversion result for a farther source with a minimal offset of 500 meters. In this way there is a lack of geometrical information. Without a sufficient geometric information, inversion is unable to relocate frequency variations in the correct layer. Contrary to classic CSEM where resistivity is considered constant with frequency, which allows to constrain depth of investigation, there are more degrees of freedom and equivalences issues. A sufficient geometric information is thus essential to correctly locate the frequency varying CR.

V.1.3 One-dimensional conclusion

In the previous sections, an overview of the IP effect in frequency-domain CSEM data was carried out in order to better understand how they impact the data according to the variation of the CR and its frequency dependence. This work helped to separate effects associated to IP in CSEM data and a particular attention was given to IP effect

on electric field response from a galvanic source:

❏ the CR phase is responsible for a relatively large phase delay on the electric field due to relaxation. Its effect over the electric field amplitude was considered negligible in a first approximation considering data at the field scale. This assumption was confirmed by 1D inversions of IP contaminated data that retrieve almost similar mediums whether taking into account a CR or not.

❏ the presence of a medium with a significant CR norm variation with frequency is considered as a large source of IP effect, which prevails compared to the CR phase effect on CSEM data.

❏ the CR norm variation impacts electric field phase data as well.

Following these observations, a multi-stage inversion framework of the CR was designed and tested on 1D synthetic model using a second order polynomial parameterization in order to describe the spectral signature of CR :

❏ Stage (1) is based on the inversion of the amplitude of the electric field (and correctly weighted phase) to obtain the amplitude of the CR $|\rho^*|$.

❏ Stage (2) seeks to invert mainly the residuals on the electric field phase to solve the CR phase Φ_{cpx} of the medium.

It was demonstrated that the multi-stage work-flow helps to constrain the multi-parameter inversion and that satisfactory results were obtained using the polynomial parametrization of the CR. Polynomial parametrization prevents the use of a specific IP model with the norm and the phase of the resistivity hardly correlated. Consequently, the inversion framework of CR in several stages and based on a second order polynomial parameterization, was adapted to the 3D case.

V.2 3D inversion of CR

In this section, the implementation of the CR and the polynomial parametrization into the main part of POLYEM3D is briefly discussed. Inversions of exhaustive synthetic models are presented to demonstrate the efficiency of the designed inversion framework and its polynomial parameterization to image deep 3D CR targets that are frequency-dependent.

V.2.1 Gradient and Frechet modification

Following 1D development, the inversion framework of CR in several stages and based on a second-order polynomial parameterization, was adapted to the 3D case. Forward problem was adapted to CR. The gradient calculation with respect to the real conductivity of the medium is based on the adjoint state method (Plessix, 2006; Plessix and Mulder, 2008) described in chapter III. For the CR case, the gradient is computed for the real $\partial_{\sigma^r}\chi_d$ and the imaginary part $\partial_{\sigma^q}\chi_d$ of the complex conductivity independently at each calculated frequency without more forward problem calculation by using equations (III.44). Indeed, the matrix A and the adjoint field λ_e are similar to the real resistivity case. The difference relies thus only on the differentiation of the system of finite-difference equations A with respect to σ in equation (III.38), which contains a term $i\omega\mu$ dependent of σ^*. The difference between the real and imaginary term is thus a factor by the imaginary number i and the differentiations with respect to σ_r and σ_q becomes :

$$\partial_{\sigma^r}(A(\sigma^r)E^S - b^*)^* = (i\omega\mu)^*(E^{S*} + E^{P*}) \tag{V.22}$$

$$\partial_{\sigma^q}(A(\sigma^q)E^S - b^*)^* = (-\omega\mu)^*(E^{S*} + E^{P*}) \tag{V.23}$$

The gradient for the polynomial parameterization is then built up from $\partial_{\sigma^r}\chi_d$ and $\partial_{\sigma^q}\chi_d$ using change of variable following the chain rule as presented previously.

Validation of the gradient

The gradient obtained using the adjoint state method was validated using the perturbation method on a restricted inversion domain of a 3D model for a constant CR phase. Each cell of the inversion domain was perturbed in one direction to calculate the resulting perturbation in the data and build the Jacobian matrix. As the problem is 3D, the number of perturbations needed is very large and becomes prohibitive as the domain considered increases. Hence, the gradient was calculated only on a vertical profile for a coarse grid and only for a low frequency (10 mHz) using two far sources ($x = 0m$ and $y = +/-4000m$) to limit numerical issues. The gradient was calculated from an homogeneous half-space with a true model containing an anomaly of CR phase of dimension 600x600x250m centered in x=0m, y=0m and with the top of the cube at z=100m.

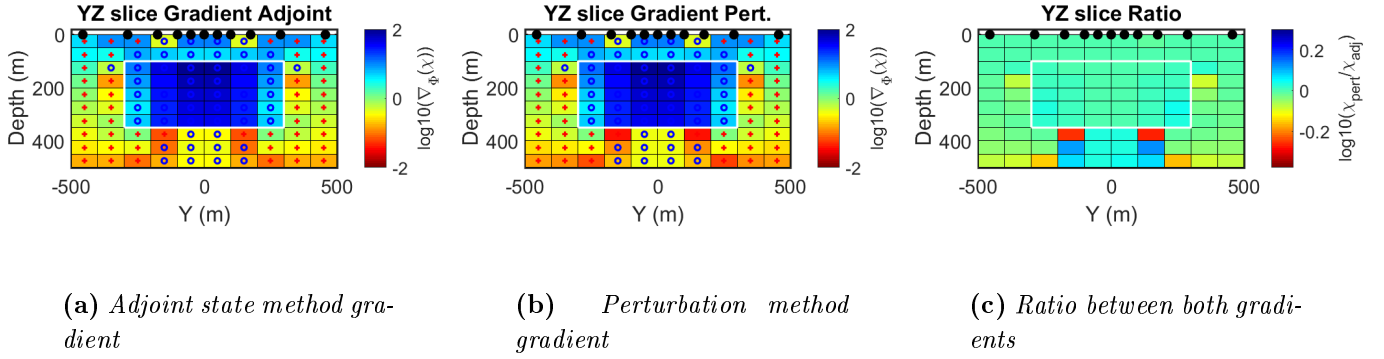**(a)** *Adjoint state method gra-dient*

(b) *Perturbation method gradient*

(c) *Ratio between both gradi-ents*

Figure V.11: *Comparison of the CR phase gradient $\nabla_{\Phi_{cpx}}\chi$. Red crosses repre-sent the positives values, blue circles the negatives values. White line represents the position of the CR phase anomaly.*

Figure V.11 shows that the gradient $\nabla_{\Phi_{cpx}}\chi$ obtained using the adjoint method and the gradient obtained by perturbation are very close. The same pattern is observed on both images, with a large negative value in the center of the image. This negative value pattern is due to the presence of the anomaly of CR phase in the true model, which is absent in the homogeneous half-space of low CR phase used as starting model. Consequently, as the gradient points towards the descent direction, the optimization will update the starting model with a positive perturbation ($m^{k+1} = m^k - \alpha\partial_m\chi$, eq. (V.3)) in order to increase the CR phase. The ratio between both gradient is close to 1 on the domain considered, which confirms a very good coherence between them. The ratio is less good where the gradient is weaker, probably due to a lower accuracy of the perturbation method gradient. The validity of the gradient on a coarse grid was thus evaluated positively for the next step on finer grid inversion.

V.2.2   "Two cubes" model inversion

"Two cubes" model description   To demonstrate and discuss the performance of the inversion approach for a 3D case considering a frequency-dependent CR with a second-order polynomial parameterization, synthetic examples are presented for two 3D targets with different spectral resistivity characteristics. Two cubes of 200 meters with different CC properties embedded in a 100 $\Omega.m$ homogeneous half-space are investigated. Cube dimensions and depths are close to the anomaly investigated by Zhdanov et al. (2018). The first cube ($\sharp 1$) is a polarizable conductive cube with CC parameters $\rho_0 = 10\Omega.m$ $m = 0.5$ $\tau = 1s$ $c = 0.5$, which can be close to an ore body anomaly presenting an IP response. The cube 1 is centered at $x = 100m$, $y = -100m$ and $z = 200m$. The second cube ($\sharp 2$) centered at $x = -100m$, $y = 100m$ and $z = 200m$ was defined with CC parameters as $\rho_0 = 100\Omega.m$, similar to the background, $m = 0.5$, $\tau = 0.01s$, $c = 0.5$ (figures V.12) to evaluate the capacity to image a target with low resistivity contrast with the background using IP effects mainly. Two different relaxation times were used with a short and a long τ parameter. At first, each cube model is inverted separately

in the homogeneous medium. Models will be referred as *"cube 1"* model and *"cube 2"* model respectively. A third, inversion is then presented that includes both cubes simultaneously in the half-space to add complexity and to evaluate interactions between both cube responses during the inversion. Acquisition geometry uses a 700x700 meters regular receiver grid at the surface measuring the electric field in two perpendicular horizontal directions with a 50 m separation in X and Y direction. Five HED transmitters are used. Transmitters were positioned 700 meters to the right and left of the center of the survey with X-directed and Y-directed polarization to enhance sensitivity to each vertical faces of the cubes with orthogonal current lines, whereas a fifth HED transmitter Y-oriented was positioned at the center of the grid to ensure a minimal geometric constrain. Considering the central source, data from receivers with offset shorter than 100 meters from it were excluded from the inversion.
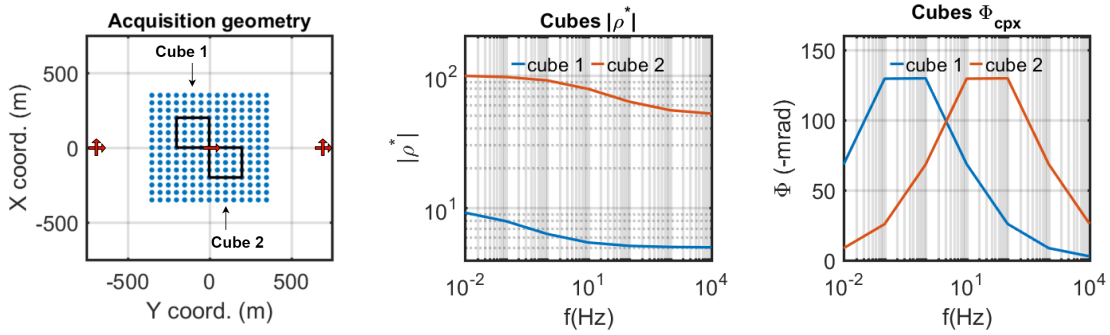
Figure V.12: *Acquisition geometry (left) using a surface 50x50 meters reception grid (blue dots) above the cubes (surface projection represented by black lines) and 5 HED sources (red arrow) and CR spectrum (center and right) of the Cole-Cole model of cube 1 ($\rho_0 = 10\Omega.m$ $m = 0.5$ $\tau = 1s$ $c = 0.5$) and cube 2 ($\rho_0 = 100\Omega.m$ $m = 0.5$ $\tau = 0.01s$ $c = 0.5$)*

Grid description   As 3D forward problem results in much higher computational costs than the 1D case, only 7 frequencies from 10^{-2} to 10^4 Hz were used in these examples. The forward grid used by the inversion is composed by cells of 12.5x12.5 meters horizontally in the core area, from 750 meters in both direction in the Y-direction and 400 meters in the X-direction as no source is present along this axis. Outside this domain, cells expand progressively to 50x50 meters until 1000 meters and 750 meters respectively. It allows to maintain sufficiently small cell sizes in the neighbourhood of the acquisition, but reduce the total number of cells as no variation is expected outside the acquisition area for the synthetic examples. Vertically, the cells are 3 meters thick at the air-ground interface and expand by 10% with depth until 500 meters. Outside this domain, cells expand more abruptly until a far limit to ensure Dirichlet boundary condition. The forward grid is thus composed of 59x112x76 cells (respectively in the z, y, x-direction) for a total size of 552 km in the z direction (including 500 km for the air layer) and 80 km in the horizontal directions. Furthermore, a different grid was used for the inversion. Indeed, the number of parameter for a classic CSEM inversion is already large and hardly manageable, which

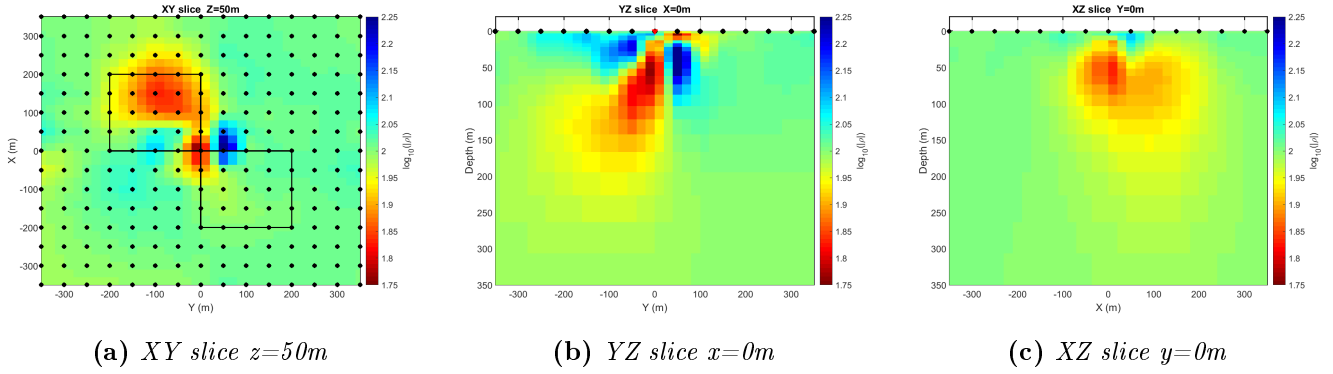(a) *XY slice z=50m* (b) *YZ slice x=0m* (c) *XZ slice y=0m*

Figure V.13: *Results of the inversion after 5 iterations for XY, YZ and XZ slices and for the inversion that do not correct for the geometrical disparity of sensitivity; Black lines and points indicates the position of the cubes and the position of the receivers (projected from the surface).* $rms_{iter.(5)} = 7\%$
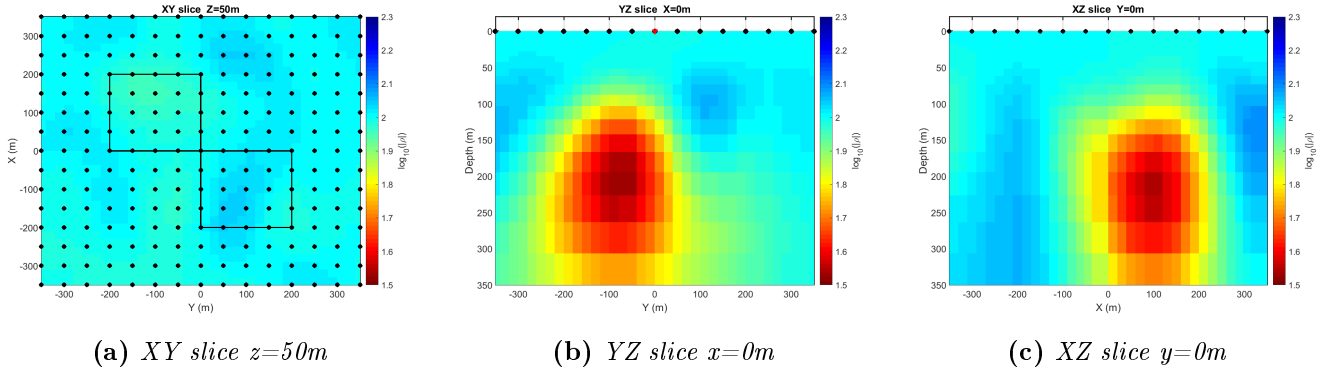

(a) *XY slice z=50m* (b) *YZ slice x=0m* (c) *XZ slice y=0m*

Figure V.14: *Results of the inversion after 5 iterations for XY, YZ and XZ slices and for the inversion with a preconditioning by $\boldsymbol{P_{J_m}}$; Black lines and points indicates the position of the cubes and the position of the receivers (projected from the surface). This inversion correspond to the iteration 5 of the model presented in the following in figure V.16c.* $rms_{iter.(5)} = 3.2\%$

Figure V.13 presents the results of the inversion after 5 iterations for the two cubes model considering a real resistivity, without supplementary correction of the geometrical sensitivity disparity due to the acquisition layout. If no care is taken, the inversion tends to introduce anomalies in surface, directly below the receivers and in particular under the source. Indeed, the results present many artefacts near the surface where the majority of the anomalies concentrates compared to the inversion scaled by $\boldsymbol{P_{J_m}}$ presented in figure V.14.

A representation of the reciprocal of the Jacobian scaling $1/\boldsymbol{P_{J_m}}$ is presented in figure V.15. This representation is close to a representation of the sensitivity in the shallow part. The footprint of the acquisition can be noted with very high values, especially at the central source position where the sensitivity is therefore maximal. A slight asymmetry can be observed as only one illumination orientation is considered for the central source.

Due to the threshold value γ, the scaling values do not decrease much below 230 meters, otherwise the dynamic would be much more important towards with depth because of the loss of sensitivity. It ensures the stability of the scaling.
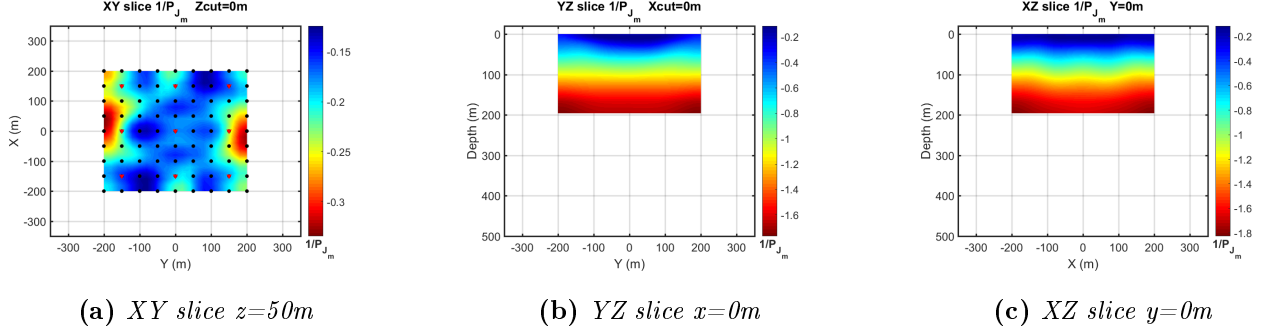

(a) *XY slice z=50m*   (b) *YZ slice x=0m*   (c) *XZ slice y=0m*

Figure V.15: *Representation of the reciprocal of the Jacobian scaling $1/\boldsymbol{P_{J_m}}$ calculated for the lowest frequency considered and for the homogeneous half-space model used as starting model for XY, YZ and XZ slices (z=0 m, x=0m and, y=0m respectively). Black lines and points indicates the position of the cubes and the position of the receivers. Acquisition geometry is presented in figure V.12a with source positions.*

Stage Zero

Synthetic CSEM data were inverted with a GN algorithm using LSQR method to evaluate the model perturbation Δm at each iteration. Maximum smoothness regularization was used with a Tikhonov parameter that can be estimated using an Lcurve. Considering that 3D problems are more complicated than 1D and that IP effects are usually small, a stage "zero" prior to the stage (1), was performed to help the local optimization. In order to get closer to the true medium resistivity before inverting for frequency dependence retrieval, stage (0) inverts data for p^0, thus a constant resistivity norm medium as for a classic CSEM survey. Figure V.16 presents the results of this stage (0) for the cube-cube model and the cube 1 model. No stage (0) inversion was performed for the cube 2 model as there is a low contrast between background and cube 2, the starting model data and synthetic observed data are already very close. An additional image presents the inversion result of the IP contaminated data of the two-cube model considering a real and constant resistivity and is referred as a "classical" CSEM inversion. In this case, no special care on IP contamination was taken. Inversions iterations were stopped when acceptable *rms* were reached with a convergence rate considered too low. In a real case survey, a user with an experienced eye is needed to understand EM and IP contribution in CSEM data in order to manage these stages by detecting the low IP effect in EM data and having a better picture of the ability to fit the data set.
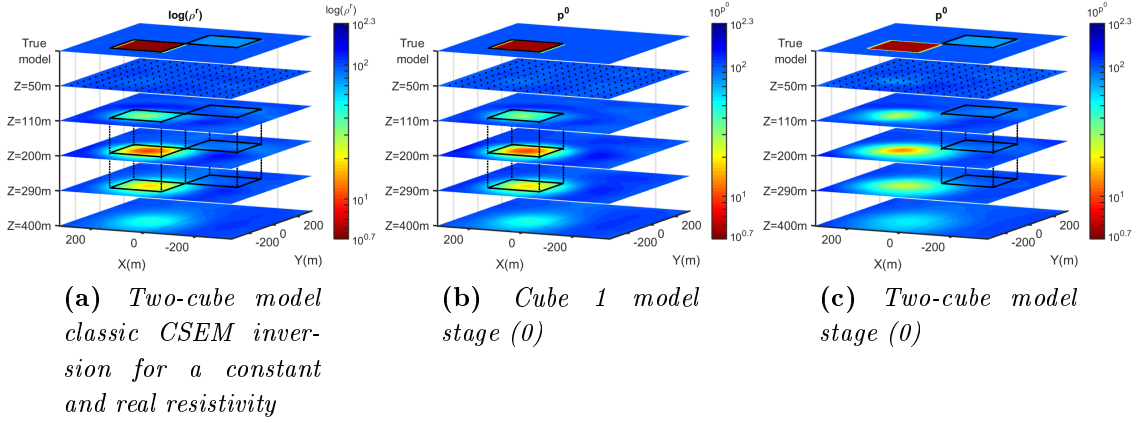
(a) *Two-cube model classic CSEM inversion for a constant and real resistivity*

(b) *Cube 1 model stage (0)*

(c) *Two-cube model stage (0)*

Figure V.16: *Inversion results for a classic CSEM and stage 0 of cube-cube and cube 1 model. Each plot represent constant ρ^r (left) or the p^0 polynomial parameter at several horizontal slices through the 3D inverted model for depth Z=50, 110, 200, 290 and 400 meters. The first slice (top) represent the corresponding image for the true ρ^r or p^0 model within the cubes (from 100 to 300 meters depth). Surface receivers are represented as black dots and projected on the shallower slice, whereas contour of the cubes are represented as black lines*

The starting rms for the cube 1 model is 20% , whereas the rms of the cube 2 model, with low contrast anomaly is 2 % only. The two cube model is about 22%. Each images are close to the true model considering CSEM imaging capacity (Diffusion domain). Cube 1 resistivity is slightly underestimated but well located, with a cube around 10 $\Omega.m$ in its center. Cube 2 can not be separated clearly from the background at this stage in figure V.16a and V.16c. Classic CSEM inversion is not severely perturbed by IP effect, nevertheless the data are not perfectly fit with a remaining rms of 1.33 % on amplitude, 0.75 % on phase data and a total rms of 1.53 %. The remaining rms is already acceptable even without considering IP effects for target at this depth, which highlight the necessity of a very low noise dataset in order to look for CR spectrum. In the next steps, I applied the stage (1) of the inversion worklflow. It starts from the model obtained at stage (0) in order to retrieve the frequency dependence expected in the cubes inverting p^n polynomial coefficients before the consideration of the stage (2).

Cube 1 model

In stage (1), the coefficients of the polynomial describing the norm of the resistivity $|\rho^*|$ are retrieved from the slight variation remaining on electric field amplitude data and the weighted phase data. The stage (2) starts then from the model obtained with a 1% covariance on phase data to fit the phase residual due to the imaginary part of the CR. Stage (2) was directly inverted for the three polynomial coefficients q^n without passing by an intermediate stage solving at first a constant parameter q^0 model.

A Tikhonov parameter equal to 1 was used for stage (1), whereas a values of 0.1 gave better results during stage 2 as the problem had some difficulties to converge. Figure V.17 from V.17a to V.17c, shows the p^n polynomial coefficients obtained at the end of

stage 1 for the cube 1 model starting from the constant resistivity model from stage (0) presented in figure V.16b with a starting phase of -1 $mrad$. At the end of stage 1 for this model and the followings, data rms is already below 1. As the rms are still locally slightly above 1, in area above the cube, I thus allowed an over-fitting using a covariance with 0.25% of relative error in order to enhance area with lower fit with the quadratic norm. Following figures from V.17d to V.17f present results of the second stage for the q^n polynomial coefficients with a final $rms = 0.67\%$.
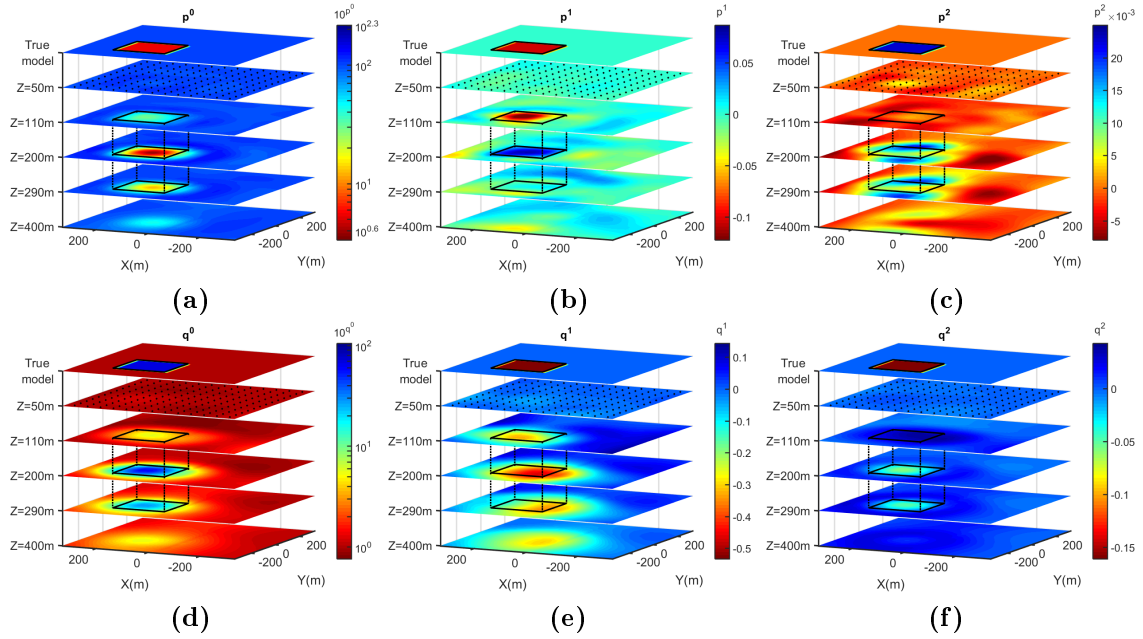

Figure V.17: *Inversion results for the conductive cube 1 model. Each sub-plot represent a p^n (top) or q^n (bottom) from the zeroth to the second degree (left to right) polynomial parameter as several horizontal slices through the 3D inverted model for depth Z=50, 110, 200, 290 and 400 meters. The first slice (top) represent the corresponding image for the true model within the cubes (from 100 to 300 meters depth). Surface receivers are represented as black dots and projected on the shallower slice, whereas contour of the cubes are represented as black lines*

Looking at model results at the end of stage 1, it can be noticed that the inversion procedure failed to retrieve correctly the frequency dependence of the CR norm of the cube 1 with a perturbed geometry. Indeed, several artefacts are seen in the area of cube 1, with a slope p^1 tending to a correct value at the top of the cube but going in the wrong direction below but at lesser extents. Similar observation can be made on p^2 value, which tends towards the real value on the edge of the cube only. Stage 2 results presents the q^n polynomial coefficients and shows that even with a very low residual remaning to fit, the inversion workflow was able to retrieve the CR phase and a part of the spectral signature of cube 1. The constant CR phase image obtained for the parameter q^0 is very well resolved. A negative slope of the CR phase was retrieved from q^1 image for the cube 1. Geometry of the cube is slightly less well resolved as it extends more in depth and slightly overflow its interface at $x = 0m$ limit. The second order coefficient q^2 present a slight

anomaly at the cube position in the right direction but its value is largely underestimated and is barely significant.

Cube 2 model

Similar inversion was undertaken for the cube 2 model, which presents a low contrast with the background medium, but a strong IP response (figure V.12). This cube has weak variation of the CR norm below 1 Hz due to the short relaxation time used. IP properties would thus be harder to resolve with a static approximation used in DCIP method, as most of the information is at higher frequencies with an increasing EM coupling. Figure V.18 from V.18a to V.18c, shows p^n polynomial coefficients obtained during the first inversion stage for the cube 2 model and from V.18d to V.18f the results of stage (2) with a final $rms = 0.41\%$. The p^n polynomial describing the CR norm of the cube 2 model is well resolved. The geometry of the anomaly fit the dimension of the 3D cube. p^0 and p^1 values at the center of the cube are in agreement with the true values but slightly underestimated. p^2 value presents an anomaly reflecting the cube dimension but its value is largely underestimated. Considering q^n polynomial describing the CR phase of the medium the constant parameter is well resolved and image the position of the cube. The spectral behaviour is less well resolved, a large and overestimated, positive slope is obtained at the cube position and no q^2 parameter is imaged.
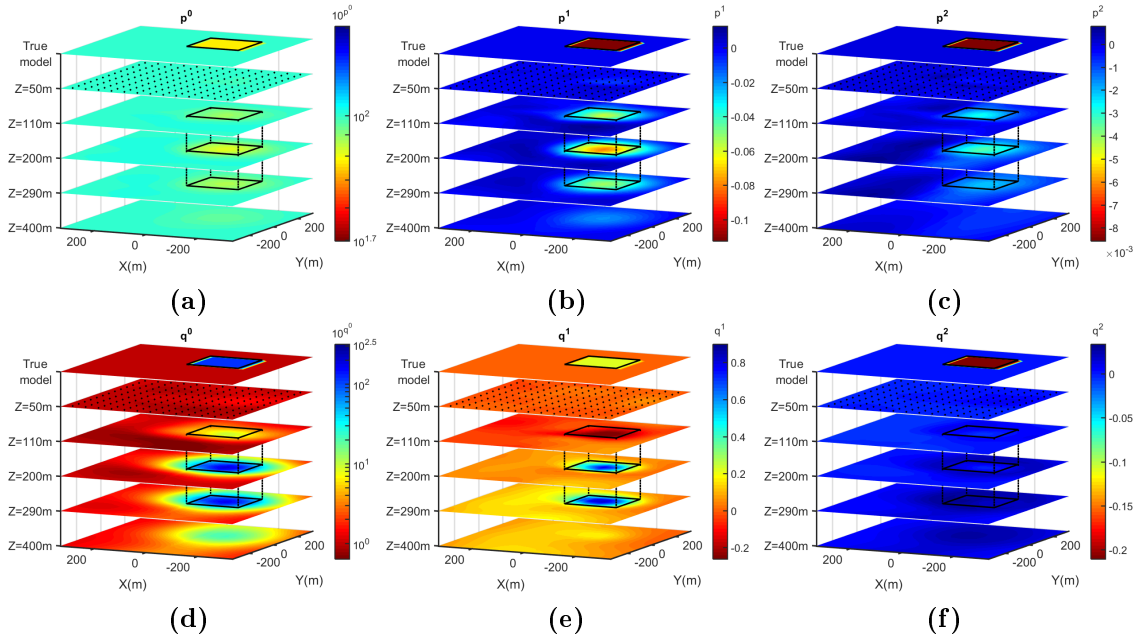

Figure V.18: *Inversion results for the cube model with low contrast with the background. Each sub-plot represent a p^n (top) or q^n (bottom) from the zeroth to the second degree (left to right) polynomial parameter as several horizontal slices through the 3D inverted model for depth Z=50, 110, 200, 290 and 400 meters. The first slice (top) represent the corresponding image for the true model within the cubes (from 100 to 300 meters depth). Surface receivers are represented as black dots and projected on the shallower slice, whereas contour of the cubes are represented as black lines*

Two-cube model

In a third inversion, both cubes are inserted into the homogeneous half-space to increase the complexity and to determine if previous observations are impacted by interactions between them during the inversion process. Figure V.19 presents both polynomial co-efficients results describing the CR of the medium and following the same layout as for figures V.17 and V.18. The final *rms* at the end of the inversion workflow is 0.9%.
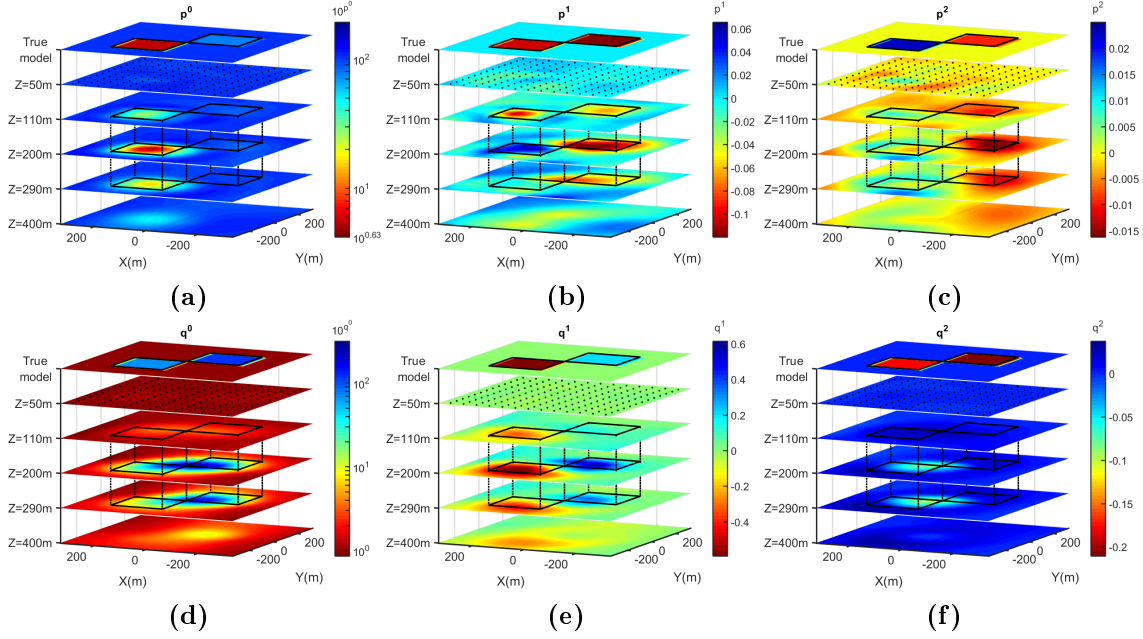

Figure V.19: *Inversion results for the "two cube" model. Each sub-plot represent a p^n (top) or q^n (bottom) from the zeroth to the second degree (left to right) polynomial parameter as several horizontal slices through the 3D inverted model for depth Z=50, 110, 200, 290 and 400 meters. The first slice (top) represent the corresponding image for the true model within the cubes (from 100 to 300 meters depth). Surface receivers are represented as black dots and projected on the shallower slice, whereas contour of the cubes are represented as black lines*

Looking at model results at the end of stage 1, the inversion failed to retrieve correctly the spectral signature (p^1 and p^2) of cube 1. Similar artefacts are observed. Cube 2 polynomial p^n is correctly retrieved. However, notice that with the larger resistivity contrast of the two-cube model compared to that of the cube 2 model, the cube 2 is not differentiated from the background on the constant p^0 parameter. On the contrary, the parameters describing the CR norm spectral shape are well retrieved and allows to clearly dissociate the cube from the background. Indeed, p^1 and p^2 signs and magnitude are in agreement with the true values presented in the upper slices. p^1 is geometrically well resolved, whereas p^2 is spreading out of the cube bounds. Stage 2 results presents the q^n polynomial coefficient where both cubes are imaged by a unique constant CR phase anomaly. Indeed, cubes are seen as a smooth and elongated q^0 anomaly oriented in the cubes diagonal. However, the CR phase slope q^1 clearly differentiates both cubes from the background and more importantly between themselves, with two slopes in opposite

direction. Considering, the last parameter q^2, a slight negative variation can be observed but is not really significant.
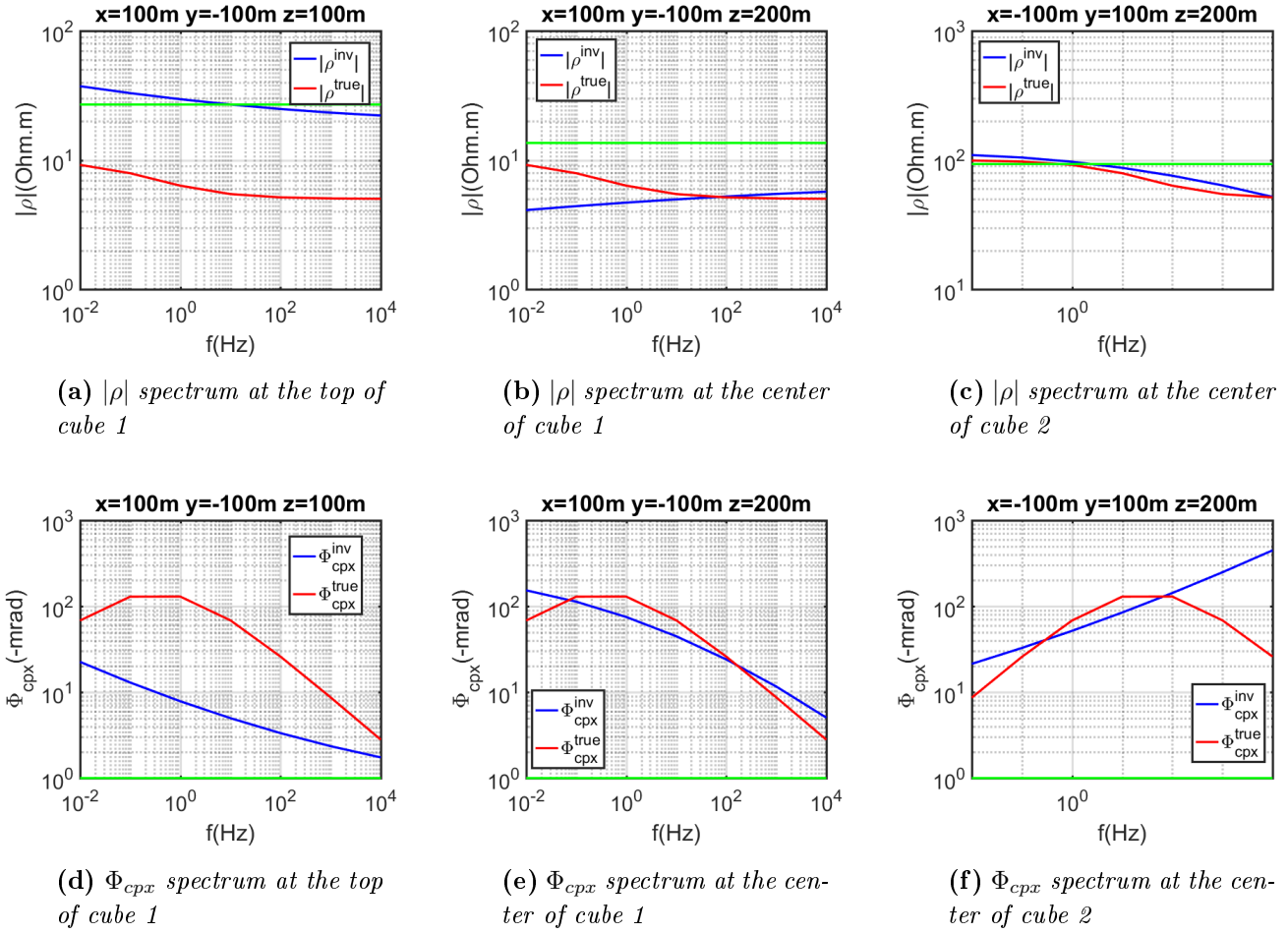

(a) $|\rho|$ *spectrum at the top of cube 1*

(b) $|\rho|$ *spectrum at the center of cube 1*

(c) $|\rho|$ *spectrum at the center of cube 2*

(d) Φ_{cpx} *spectrum at the top of cube 1*

(e) Φ_{cpx} *spectrum at the center of cube 1*

(f) Φ_{cpx} *spectrum at the center of cube 2*

Figure V.20: *CR spectra at the center of the cubes and at the top-center of cube 1 for the Cube-Cube model. Green curves are the spectrum at the end of previous inversion stage (stage 0 for $|\rho|$ and stage 1 for Φ_{cpx}*

Figure V.20 resumes the results of the polynomial coefficients under the form of CR spectra at the center of the cubes positions. The spectra at the top of cube 1 are also displayed as its geometry was not well retrieved. It shows that the cube 1 anomaly at the top-center of the cube could reflects a coherent CR norm spectral variation in spite of the anomaly retrieved below, at the center of the cube 1. CR norm spectra of cube 2 is in very good agreement with the true model. Considering CR phase spectra both are in good agreement with the major trends of the true CR phase spectral shapes. The CR phase of cube 2 is largely overestimated at high frequencies which can be explained by the loss of sensitivity due to skin effect.

V.2.3   Two-cube model discussion

A multi-stage workflow and a polynomial parameterization workflow were developed and used to constrain the multi-parameter inverse problem associated to a CR medium taking into account its spectral signature. The method is based on the decomposition of the linked effects between amplitude of the electric field and the CR norm and between the electric phase IP delay associated to a CR phase. The proposed strategy solves the CR norm and phase separately during the inversion based thus uniquely on data sensitivity to these parameters. Indeed, both parts describing the CR are not coupled by a specific model. 1D synthetics demonstrated the efficiency of the method and parameterization allowing the evaluation of a good spectrum shape for the norm and the phase of a buried layer. Nevertheless, even for cases using a 1D approximation, IP sensitivity was already challenging for a buried target.

Considering 3D synthetics, the inverse problem is much larger and the IP sensitivity of CSEM data to buried and limited polarizable body is decreasing. Some encouraging results can nevertheless be highlighted here. Cube 2 CR spectrum trend was relatively well retrieved in both synthetic models on the norm and the phase. Cube 1 model failed to retrieve the correct CR norm spectrum shape due to equivalence problem. Nevertheless, the constant parameter and the main trend of CR phase spectral variation was correctly retrieved and well located during the second stage for the q^1 parameter. Excepting for the cube 2 CR norm (Figure V.19c) matching relatively well the true p^2 value, the second order polynomial coefficient was not well imaged in the 3D case for a target at this depth. In addition to the low sensitivity of IP effect, the limited resolution of the CR spectral shape can be explained partially by the depth of the buried target and the gradual loss of sensitivity of EM data at increasing frequencies, as the skin depth decreases. The spectrum shape is thus less well constrained at high frequencies and no more sensitive to these depths. Through these 3D models, it was demonstrated that both cubes could be discriminated from the background in several ways when looking for IP effects. Cube 1 is easily dissociated from the background due to its high conductivity, but also with his constant CR phase parameter q^0. Even though it failed to obtain a correct norm spectrum for this anomaly, a correct CR phase trend, which decreases due to the long characteristic time, could be retrieved from the electric field phase residual. On the contrary, cube 2 anomaly presents a short characteristic time and is very hard to dissociate from the background using a simple constant CR norm, whereas large EM induction perturbations are expected due to depth of the target and frequency needed to investigate such short time relaxation. Cube 2 results highlight thus the advantages of taking into account IP effect in CSEM data, where the CR norm variation was successfully retrieved from the constant background. Considering the CR phase, the constant parameter q^0 allows the dissociation of the second cube from the background as well, but also its spectral variation parameters that retrieved its main variation. Finally, the spectral behaviour of both cubes could also be differentiated between themselves using the opposed slope q^1 observed on the CR phase. Resulting slopes on the CR phase let us differentiate between the late and the short relaxation time anomalies.

3D buried targets at significant depths, even with large CR frequency variations (high

chargeability, CR phase peak above -100 mrad) as in our examples, present low IP effects in surface CSEM data, which are close to numerical accuracy. Signal to noise ratio can be generally improved with a larger transmitter, nevertheless considering geometrical or numerical errors, data and forward problem solver of very high quality are essential in order to expect to retrieve CR spectrum shapes as well as taking EM effects into account. It was shown that by using an appropriate parametrization and a pragmatic workflow, I was able to retrieve a significant part of the IP information for a deep target as well as taking EM induction into account.

On the other hand, during the process a close constant and real resistivity model of the 3D buried targets were retrieved without artefacts due to IP effect, even considering relatively large IP anomalies of the target. This is due to the weak IP effect compared to EM response, especially for targets at these depths. Considering shallower targets, larger IP effect on the data are expected and the choice of the method should thus be cautiously considered. Indeed, the need of a numerically expensive CSEMIP inversion, instead of DCIP should be carefully evaluated according to the EM information contained in the data. Indeed, as targets are shallower, shorter offsets can be used for the imaging problem, thus data are gradually less subject to EM contamination, but contains also less EM information for the reconstruction of the medium. While ERT method can offer a considerably better resolution in surface due to a large TX/RX configuration with easier numerical resolution afterwards, it requires a much larger logistics as information is geometrical only. To the contrary, using frequency sounding information can reduce efforts on the field with a certain complementarity. Indeed, the cubes are imaged relatively well with only 5 transmitters in these examples by taking into account EM effects simultaneously during the inversion. Furthermore, if frequency sounding used in EM survey can lighten the acquisition, the problem still requires a sufficient geometrical constrain to solve the CR spectral behaviour due to the undetermined inverse problem. Otherwise, some artefacts can appears as in the reconstruction of the cube 1 polynomial p^n, which points out that a few supplementary sources could be preferred. IP effect is not sensitive enough at these offsets and target depths to be really quantitative, but allows the discrimination of the target responses with significantly different spectral signatures.

Conclusion

In this chapter, I presented the implementation of a frequency-dependent CR into a 3D CSEM inversion code. It was presented in previous chapter that the presence of a CR phase has a weak effect on the amplitude of the electric field, whereas it impacts mostly the phase of the electric field with an additional delay. Following these observations, the multi-parameter inverse problem was decomposed in two main stages based on electric field sensitivity to the norm and phase of the CR and using a second order polynomial parametrization. This approach does not rely on a particular IP model. The method was developed and tested on 1D synthetic problems, before an application on a complete 3D synthetic example with two different deep targets showing interest, a conductive and polarizable cube and a polarizable cube with no to low resistivity contrast with the background. Recovered spectral shapes are imperfect due to the low sensitivity to IP effects

of deep buried targets. Some equivalence and non-linearity issues intervening for the CR norm variation for one of the targets points out the complexity of the problem despite a good data fit. The multi-stage workflow, coupled to a polynomial parametrization of the CR, allowed to retrieve an important part of the CR spectral trends of the 3D anomalies considered. CSEMIP method shows a great potential to discriminate between deep polarizable bodies and to take into account EM induction for the imaging. The spectral behaviour should be sufficiently contrasted for a discrimination of deep target spectral signatures. The CSEMIP problem would require a dataset of high quality (accurate positioning, good signal over noise ratio, good frequency and geometric coverage) to access to weak IP effect contained in EM data and implies the use of forward problem solvers of sufficient accuracy.

Application of the CSEMIP code

Introduction

In this final chapter, I present the application of the methodology developed during this Thesis to real CSEM datasets. This work tests the multi-stage method as well as the polynomial parametrization in real conditions with data that can contain various unknown sources of noise. Difficulties can arise on the field and the actual acquisition geometry can thus appear to be not optimal for logistic reasons or if the geology turns out to be more complex than the one expected.

At first, I present the work performed on a 2D CSEM survey carried out near Schleiz in Germany (namely the Schleiz survey in the following), which presents evidences of large IP contamination. These data were kindly shared by the Institute of Geophysics and Meteorology (IGM) of the University of Cologne. A first subset of the data was shared to test the 1D code, whereas promising results lead to a sharing of the complete dataset for more investigations.

Later, a 3D survey carried out during this thesis is presented. This survey was carried out (in late December 2020) on a former mining site presenting large recognized IP effects and due to large mineral deposits, at La Porte-Aux-Moines, Côtes-d'Armor in western France. The complex geology of La Porte-Aux-Moines precludes any 1D interpretation and justifies a 3D survey.

VI.1   Schleiz survey (Germany)

The Schleiz survey was performed within the framework of the Deep Electromagnetic Soundings for Mineral Exploration (DESMEX) project in 2016 and 2017 in a former antimony mining area near Schleiz in the eastern Thuringia Slate mountains, in Germany. The location was chosen as a validation site for a semi-airborne method (Smirnova et al., 2019), where land based acquisition was performed in parallel. The site presents a highly conductive target composed of massive alum (graptolite) shales in a resistive host rock (Mörbe et al., 2020; Smirnova et al., 2019) providing thus an ideal target for imaging demonstrator. The survey is composed of several transmitter (TX) positions along an 8.5 km long profile of 52 receiver (RX) positions, where the electric field was recorded. The transmitters are long grounded wires (around 1000 meters each) perpendicular to the profile line and centered on it. Therefore, the electric field perpendicular to the profile was recorded. Indeed, considering simple media, there should be pure broadside for this geometry. Details on the survey, as well as the inversion results of the data in frequency

and in time-domain are presented by Mörbe et al. (2020).

A presentation of the survey geometry as well as the geological context is presented in figure VI.1. Geological structures are at first order well suited for a 2D approximation. The dataset consists of recorded signals from 0.23 Hz to 25 kHz for a square wave (50% duty cycle) TX signal and its harmonics, providing slightly more than 5 complete decades of frequencies. They were processed using a robust processing tool based on Egbert and Booker (1986). Data show a very good quality up to 1 kHz.
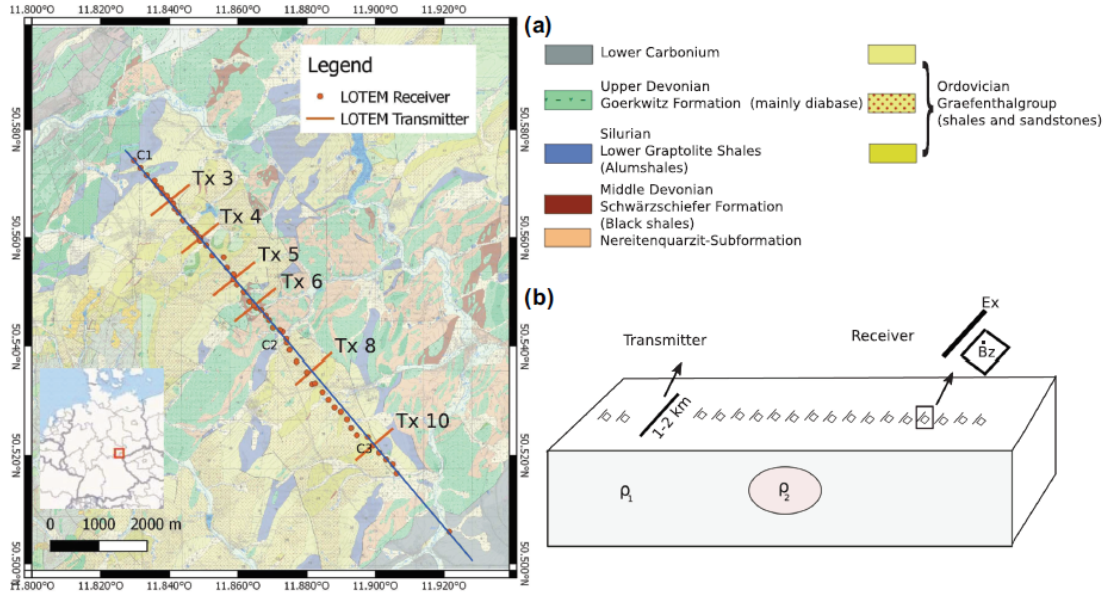

Figure VI.1: *Presentation of the geological context and the acquisition geometry of the Schleiz survey. The profile of receivers recording the cross-line electric field from 6 transmitters composed of grounded wires perpendicular to the profile is presented in a) superposed over the geological map. b) Sketch of a broadside survey layout (from Mörbe et al., 2020)*

Mörbe et al. (2020) identified a part of the signal in their data that they were unable to fit to IP effects. Indeed, a previous IP survey in the area confirms the presence of a strong IP response of the graptolite shales following a study conducted by Martin et al. (2018), with chargeabilities up to M=250 mV/V. Mörbe et al. (2020) performed some modelling based on their results to evaluate and compare the IP effect on their data (see VI.2). They showed that they were able to fit manually some of the residuals in the real resistivity model. Considering these findings and as the results were already published by the IGM, it was the opportunity for a collaboration and sharing the dataset. It gave me the opportunity for a first trial of the developed inversion workflow in real conditions using the 1D inversion code.
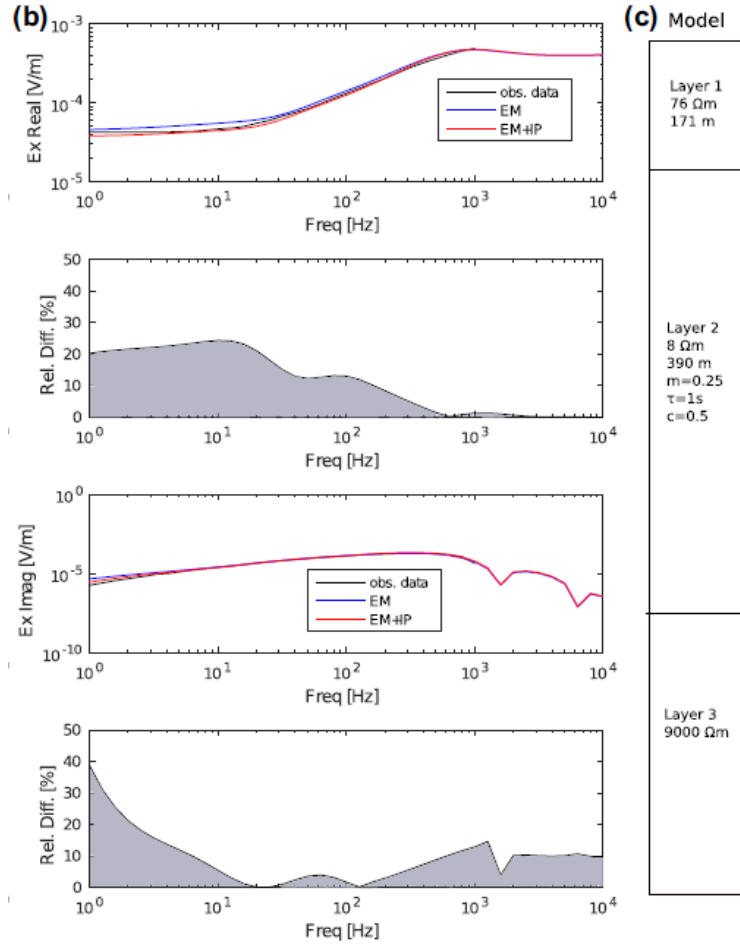
Figure VI.2: *Presentation of the IP forward modelling undertook by Mörbe et al. (2020) for a receiver at around 1000 meters offset from the TX8. Electric field in-phase and quadrature phase are presented for the observed data, the modelled data without IP (EM blue curves, m=0) and for the modelled data with IP considering a thick 2nd layer with a CC like CR spectrum (EM+IP red curves). The 1D model is presented on the right. The relative difference between the EM and EM+IP curves are plotted in the grey plot*

VI.1.1 Data presentation

The IGM team shared a first subset of the Schleiz dataset of 6 receivers with the records of the electric field perpendicular to the profile. The 6 receivers could be divided in two packs illuminated by two different sources. The first pack was composed of stations 4, 7 and 8 coupled to the transmitter number 4 (Figure VI.1). These stations are located in an area with low to no IP expected. The second pack is located over the large and very conductive anomaly C2 (in figure VI.1), which showed evidences of IP effects[a]. These stations (RX18, 22 and 928) are coupled with the TX8 located on the west of the C2 anomaly. The electric field spectra at each station is presented in figure VI.3. In the following, the first pack of stations (North-west (NW) of the profile) will be straightforwardly referred as package 1,

---

[a]Figure VI.2 presents a station from this area.

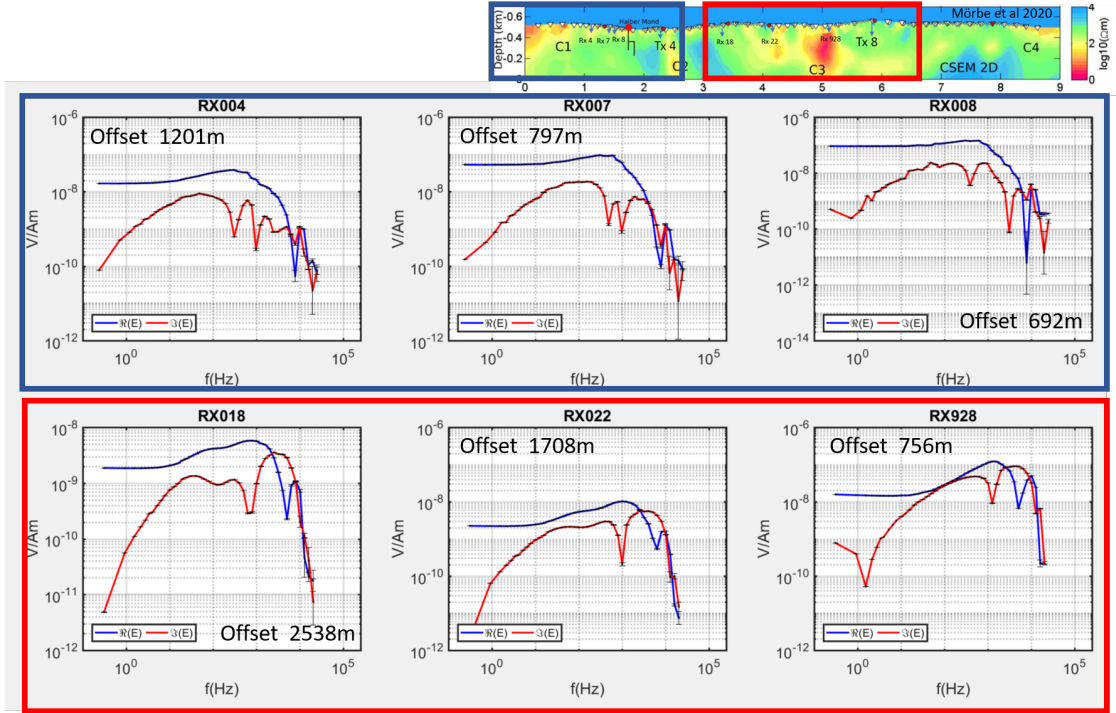and the second, as package 2 (South-east (SE) of the profile).

Figure VI.3: *Electric field responses of the subset of the Schleiz survey shared by the IGM of Cologne university. The location of each data pack are highlighted in the upper-right corner resistivity image from (Mörbe et al., 2020)*

The real and imaginary parts of the electric field at each station are represented from 0.23 the 25 kHz approximately. As noted in their publication, the data are of good quality, at least up to 1 kHz where some oscillations can be noted in the first pack of receivers. It can be hard to see at first glance evidence of IP effect. However, RX928 is of special interest. Indeed, the electric field out-of-phase presents a sign reversal towards the low frequencies as depicted in earlier 1D modelling for $HED_\perp$ dipole (figure IV.8d). This sign reversal is characteristic of IP effect in this configuration, as the IP response is opposed to the quadrature response of the real resistivity model. This observation is linked to a considerable phase delay at low frequencies (not shown here). Furthermore, a correlation with an increase of the in-phase electric field towards the DC limit can be made, which can indicate a frequency effect of the resistivity. Such observations can be suspected for RX 18 and 22, but not in a conclusive manner without a proper inversion or modelling comparison.

VI.1.2   1D inversion of the CR

In order to evaluate the dataset, I carried out data inversion for each reception position individually accounting for a constant and real conductivity. Following a multi-stage strategy as data may contain IP effects, first only the amplitude of the data was inverted (Stage 0). A similar range of frequency was used from 0.23 Hz to 1 or 3 kHz approximately, with 33 or 36 frequencies logarithmically spaced for package 1 and 2 respectively. The

model used 50 meter layers at the surface with an increment factor with depth. These inversion results are displayed in figure VI.4 and compared to the 2.5D resistivity image obtained by Mörbe et al. (2020) using the Mare2dem inversion code (Key, 2016). Inversion results are in close agreement, especially for the receivers of package 2, considering that 1D and 2.5D problems are constrained differently. Obviously, 1D inversion are more limited in depth due to the available offsets compared to the 2.5D inversion results that benefit from the complete data set (and farther sources combination). The discrepancies between both models can be explained partially by the imprint of the source in the data. Indeed, concerning package 1, the 2.5D inversion result shows a shallow resistive structure that becomes thinner toward the north-west, which is the trend observed in the 1D results. Therefore, even if 2.5D image shows a dipping conductor from the surface at TX3 location letting place to a thick resistive structure towards NW under RX4 (not observed in 1D result), these results can be explained and correlated considering the source illumination. Such illumination effect explains also the presence of the conductive body under RX22, whereas RX928 is too close to the source to be sensitive to the second large conductive anomaly below 1000 meters depth. The *rms* considering only the data amplitude is around 4 % for the package 1 and around 3 % for the package 2. It can be noted here, that inversion with several couple of RX (of the same pack) simultaneously were carried out, nevertheless due to the 2D (or 3D) geological structure, 1D inversions were not successful.
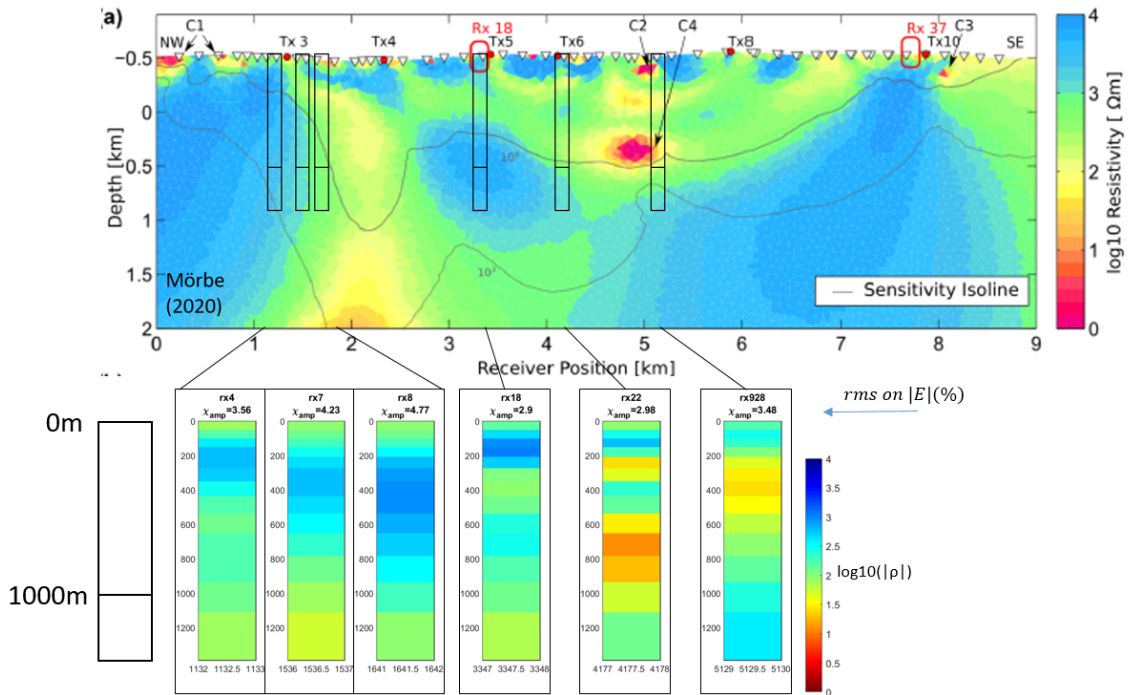

Figure VI.4: *Results of the 1D inversion of each station independently (bottom soundings) for a real and constant resistivity compared to the 2.5D inversion result (top) of Mörbe et al. (2020). Black columns are superposed at the reception position over the 2.5D slice for scale purposes.*

Data of package 1 are less well fitted due to a larger noise content. Amplitudes of the

electric field were well fitted with no further IP evidence (Figure VI.5). On the other hand, the phase (not inverted), was not fitted perfectly, however the phase residual, could not be attributed to IP effect as the observed data phase is higher than the inverted phase. In addition, no negative phase is observed at the lowest frequencies, thus no further investigation of this package will be presented here, as the residual was interpreted as 2D or 3D effects[b].

---

[b]Amplitude and phase inversion were also tested to verify, if the phase could be fitted, with no more significant results.
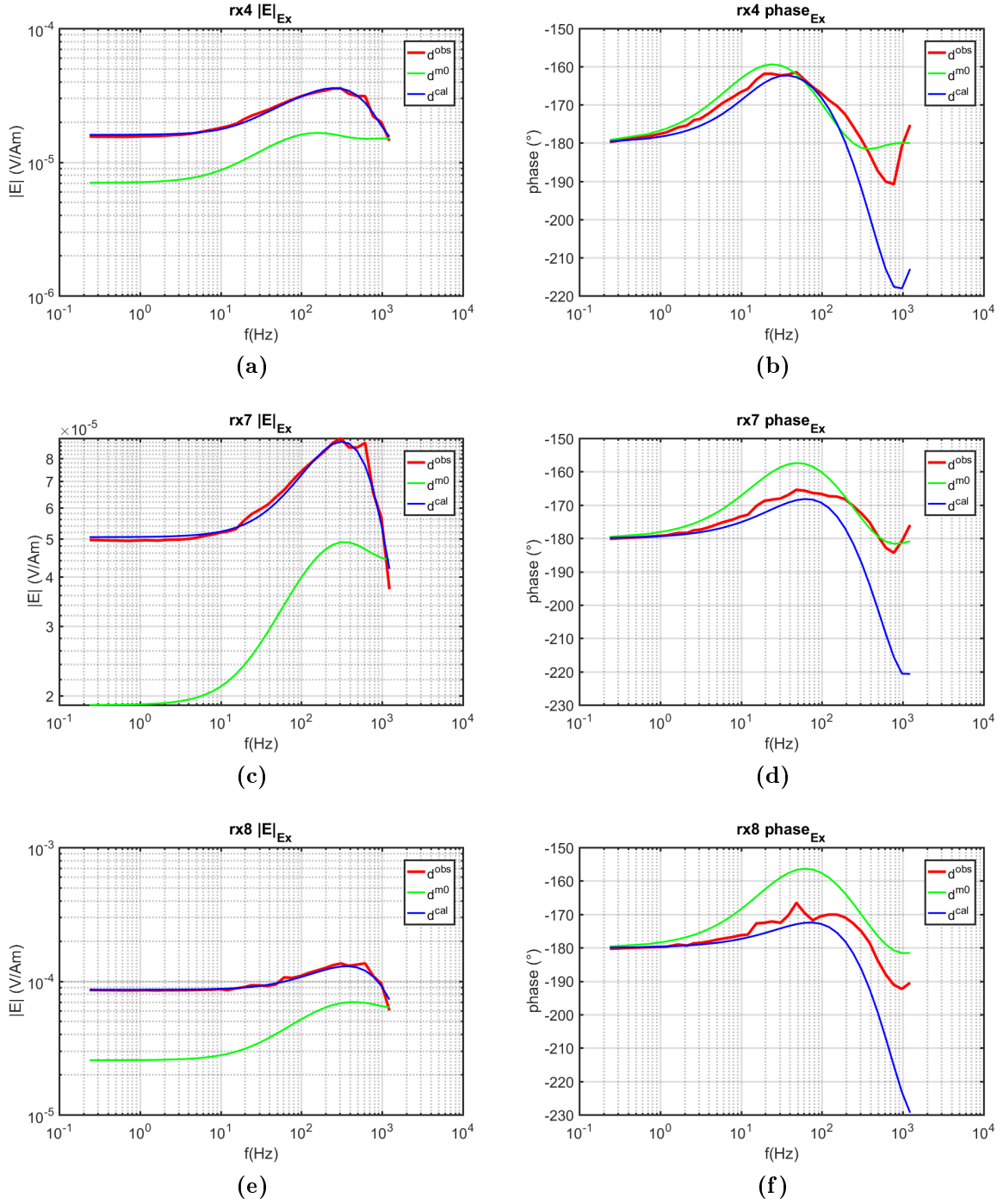
Figure VI.5: *Data fits of the 1D inversion results for a constant resistivity of the first RX package from the subset of Schleiz survey presented in figures VI.4 and VI.4. Observed electric field responses d^{obs} are presented with the responses of the starting model d^{m0} and with the inverted data d^{cal}.*

The fit of the second package is presented in figure VI.6. In these cases, amplitudes of the electric field are well fitted as well, however the 1D inversions are unable to fit the low frequency part. The phase data are in good agreement without being inverted, except for frequencies higher than 1 kHz and at the low frequencies part not fitted over the amplitude. The observed residuals are in agreement with IP effect evidences and can

be correlated to a CR that decreases with frequency (decreasing therefore the amplitude of the electric field, where a DC asymptote should be observed), whereas a phase delay is observed indicating a target with a significant CR phase. The case of the RX928 is of great interest as it shows the largest IP evidences, as well as a negative low frequency phase between 0.3 Hz and 2 Hz. These observations are critical for the interpretation of IP presence and the 1D inversion of a frequency-dependent CR was carried out on package 2.
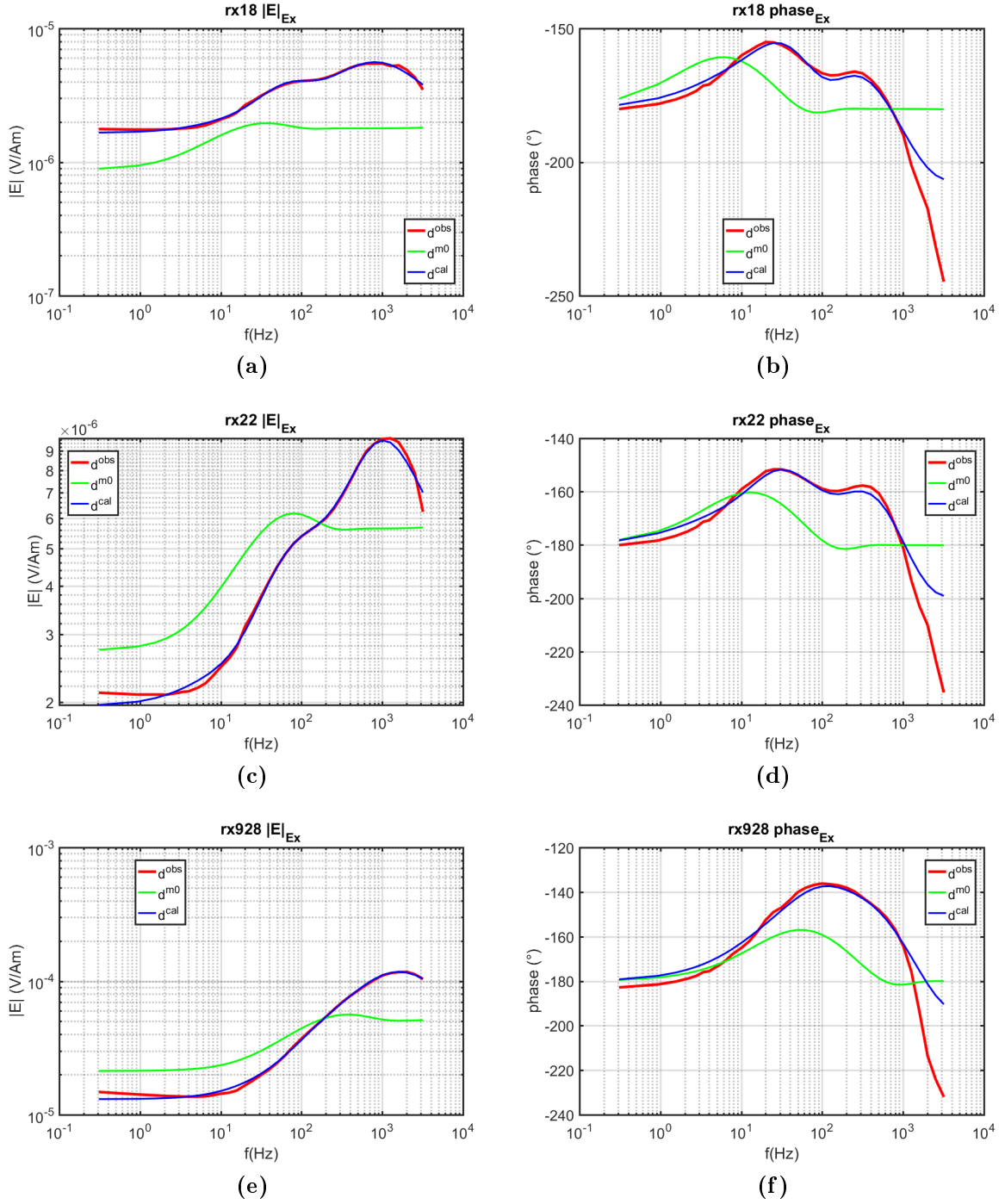
Figure VI.6: *Data fits of the 1D inversion results for a constant resistivity of the second RX package over the C2 anomaly from the subset of Schleiz survey presented in figures VI.1 and VI.4. Observed electric field responses d^{obs} are presented with the responses of the starting model d^{m0} and of the inverted model d^{cal}.*

RX928 considering a frequency dependent CR

Following previous results assimilated to stage 0, the inversion of a frequency-dependent

CR was carried out through the multi-stage procedure, starting thus with the stage 1 inverting amplitude data to solve a CR norm model and its frequency dependence. As phase data were harder to fit, some of the highest frequencies were removed in stage 2[c]. Note that a depth scaling (see appendices A.3) was used in order to compensate the loss of sensitivity with depth, but mainly to constrain the low geometrical information as only one offset can be inverted (see previous chapter figure V.10). That is each layer are scaled similarly to the Jacobian scaling P_J used in the synthetic model. Results of both stages for RX928 are presented below in figure VI.7. Two inversion results are highlighted, the first one in figures VI.7a and VI.7b starting from the constant resistivity model obtained previously, and the second one in figure VI.7c and VI.7d starting directly from an homogeneous half-space. Both models explain very well the data and the residual that remained previously is correctly fitted. The fits at the end of both stages are presented in figure VI.8.
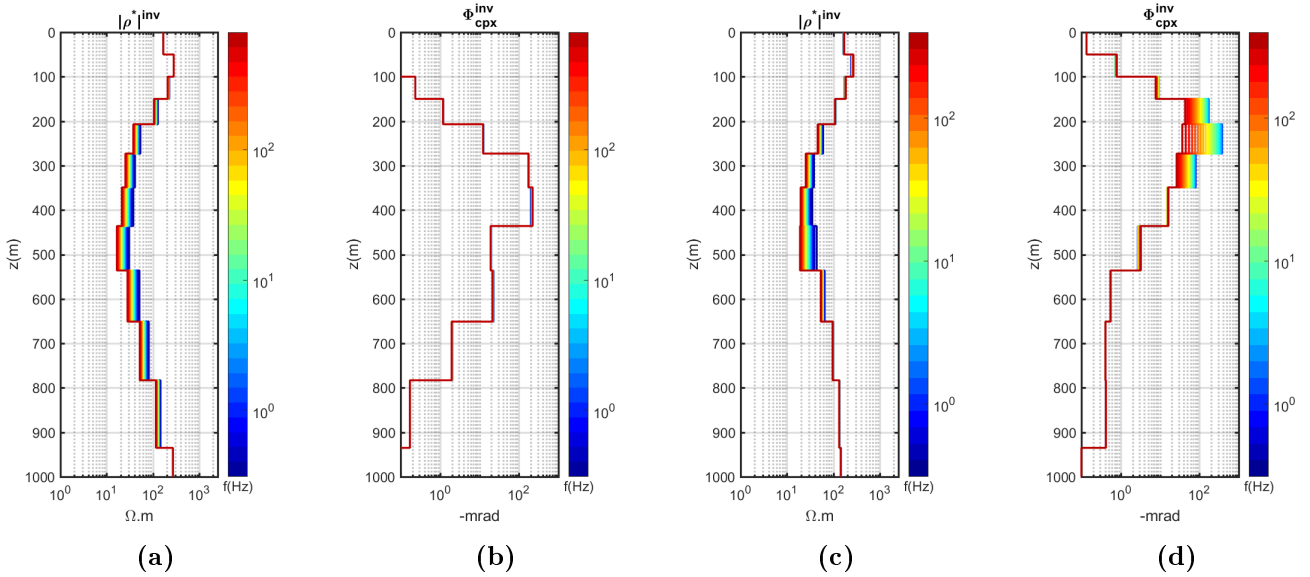

Figure VI.7: *Inversion results for the multi-staged inversion of RX928 data. (a) and (b) present the inversion starting with the constant resistivity model obtained previously, whereas (c) and (d) correspond to an inversion restarted from a homogeneous half-space.*

---

[c]As inversion were not carried out at the same moment, it appears that a few additional frequencies were filtered for the second example, to be coherent with another model at that time
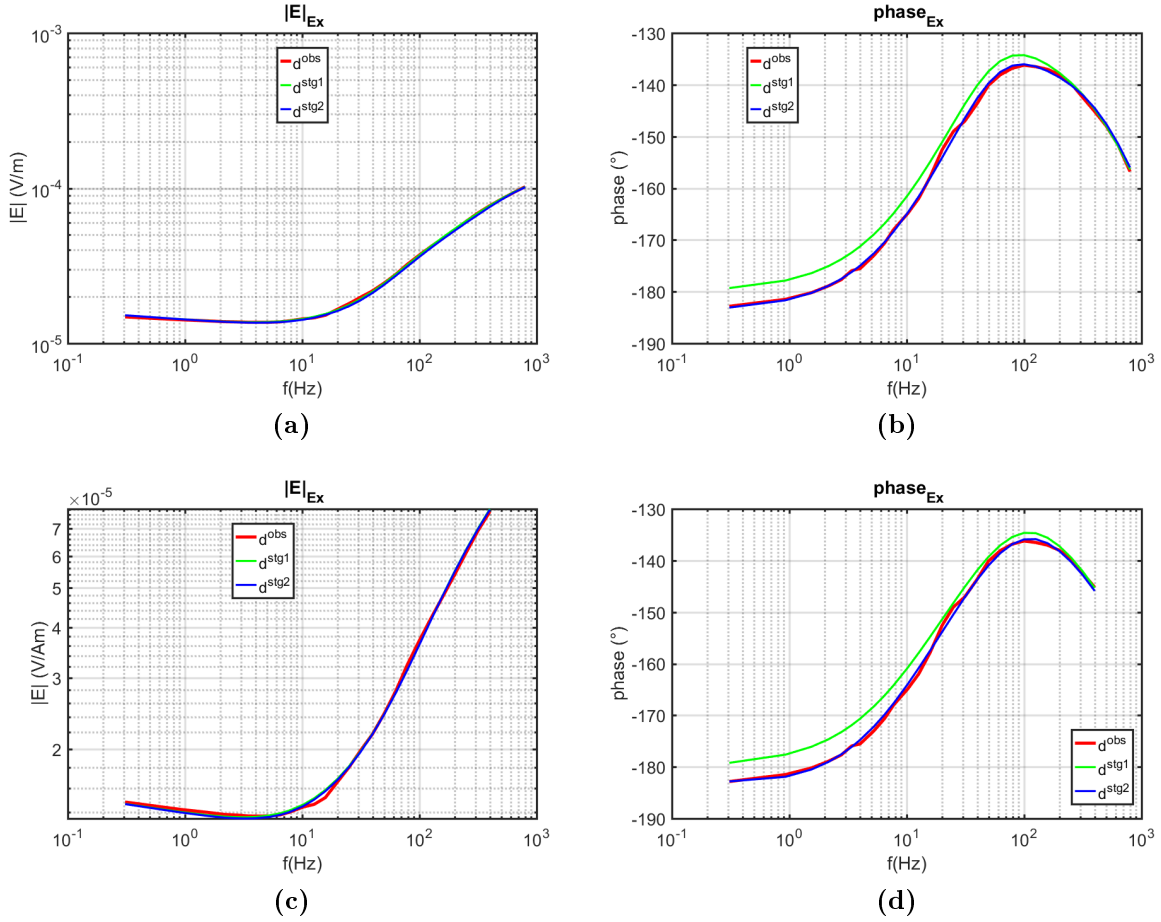
Figure VI.8: *Data fit results for the multi-staged inversion of RX928 data. Top images concerns the inversion following the constant resistivity model obtained previously, whereas bottom images correspond to an inversion restarting from a homogeneous half-space without a-priori. Fit at each stages are represented.*

Both inversion had to introduce a decrease of the CR norm with increasing frequency in the model during stage 1. The inversion starting from the homogeneous half-space model presents a sharper anomaly, from 200 m to 500 m, than the other models where the frequency dependence spreads from 200 m to 800 m. The maximum of frequency variation of the resistivity is thus less important in the latter. For both models only a linear slope was retrieved and was sufficient to explain the amplitude data. The largest difference between both models occurs during stage 2, when the phase residual is inverted as shown in figure VI.8d. Indeed, in the first case no frequency variation was introduced and a constant CR phase with a maximum between 300 and 400 meters was sufficient to explain the data. On the other hand, in the second case, a CR phase with a significant frequency variation was introduced during inversion at a shallower depth.
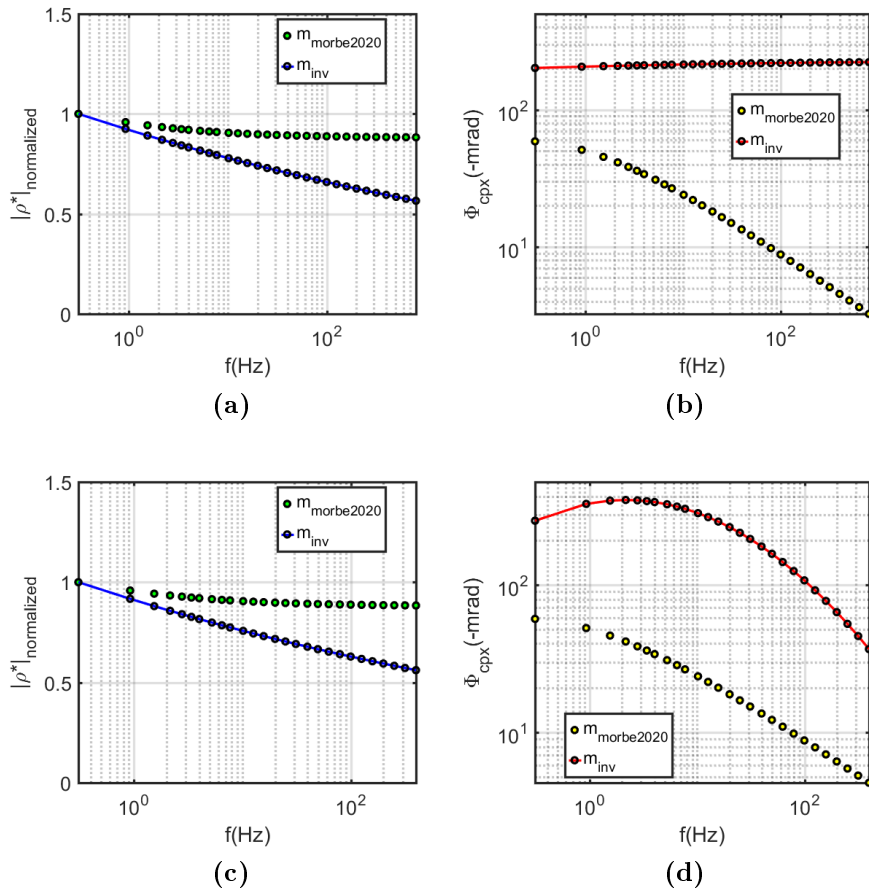
Figure VI.9: *CR spectrum extracted in the layer at 400 meters (or 250 m for the CR phase of the second inversion in figure VI.8d), for comparison with the CC model used in the modelling made by Mörbe et al. (2020) in figure VI.2. For comparison purposes, the resistivity norm is normalized by its value at the lowest frequency*

CR spectra results are presented in figure VI.9 and are compared to the CR spectra used for the IP modelling made by VI.2 and based on a Cole-Cole model determined from shallow IP measurements from (Martin et al., 2018). In both cases, the frequency effect on the CR norm is larger than for the CC model introduced in their forward modelling. A large decreasing trend was retrieved from the CR norm. Note that the sensitivity is decreasing at depth due to the skin effect, thus values at higher frequencies are not significant[d]. From surface to 400 meters depth (the depth of the CR spectra plotted above), CR norm variation for both inversions are similar. It is probable that the shallower upper-layers with a lower CR variation plays a more significant role in the data fit. A larger CR phase was nevertheless also retrieved in both cases. In the second inversion, the CR phase shape presents some similarities with the modelling results. Both models explain equally the data and it is not possible to evaluate which model is closer to the true medium, pointing out the equivalences issues for quantitative analyses. But it is

---

[d]as an indication skin depths in a 10 $\Omega.m$ half-space are $delta_{skin}(f = 100Hz) = 160m$ and $delta_{skin}(f = 10Hz) = 503m$.

unlikely that the frequency variations of the CR phase retrieved in the second inversion are really significant even if both models explain the data equivalently.

RX22

RX928 was the receiver with the largest IP evidences. To compare the results obtained for this site, inversion of the data of RX22 is briefly presented in figure VI.10 and VI.11. Similar observations were made on the results of the RX18 and only the case of RX22 is briefly presented below. The constant resistivity 1D model obtained in stage 0 revealed two conductive layers. One around 200 meters with a thickness of 100 meters and a deeper one between 600 meters and 1000 meters depth. Application of the multi-stage workflow and inverting for a frequency-dependent CR lead to introduce a CR norm variation, as well as a deep constant CR phase anomaly below 300 meters.
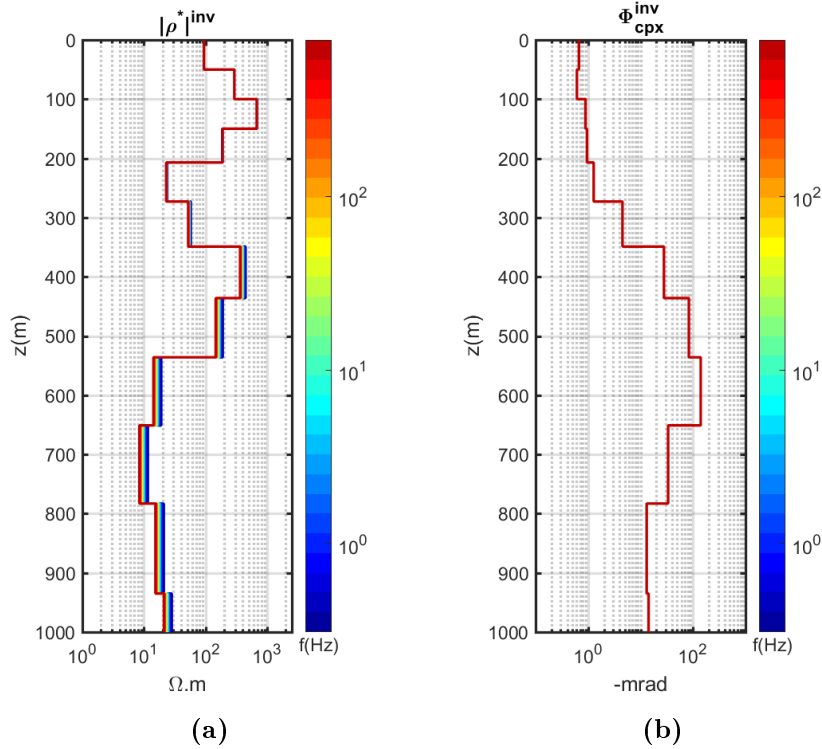

Figure VI.10: *Inversion results for the multi-staged inversion of RX22 data. Stage 1 starts from the constant resistivity model obtained previously*
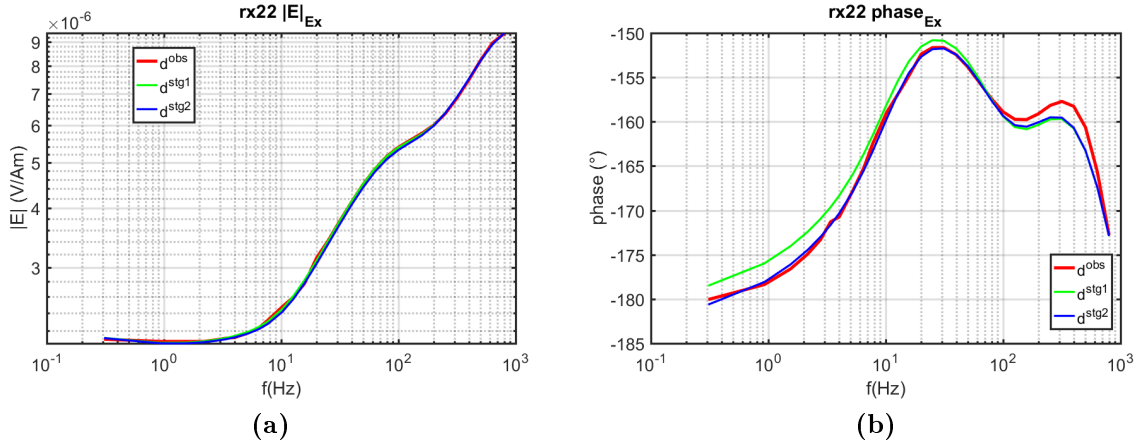
Figure VI.11: *Data fit results for the multi-staged inversion of RX22 data. Fit at each stages are represented.*

The low frequencies residuals on the amplitude of the electric field (Figure VI.6d) are well fitted by the introduction of a CR norm variation in depth, even if it seems to be weak variation. Nevertheless, the fit of the phase data is not as good as for the RX928 (figure VI.8). The station is further from the source and can thus be more impacted by 2D/3D effects. Phase data kept relatively high unexplained residuals at high frequencies, which are more probably due to 2D/3D effects instead of IP. The low frequency phase delay is nonetheless well fitted during stage 2. This case is maybe less promising than for RX928 as the location of the CR norm variation can be questionable as we expect the conductive bodies to be at the origin of the IP, whereas here CR norm variation is also located in the resistant around 400 meters. In an attempt, the CR phase anomaly could be correlated with the top of the deepest conductive anomaly, nevertheless it would imply that the shallower anomaly in figure VI.10a could be of different kind as no polarization was retrieved for this layer. However, the CR norm variation is also introduced below the first conductive layer and is correlated approximately with the CR phase anomaly. The RX22 deep anomaly is relatively similar to the RX928 anomaly with similar CR phases ($\approx -150mrad$) and a decrease, slightly lower, of the CR norm with frequency. Therefore, it could suggest a similar origin of both anomalies. Figure VI.12 present the CR spectrum in the deep conductive layer compared to the modelling made by Mörbe et al. (2020).
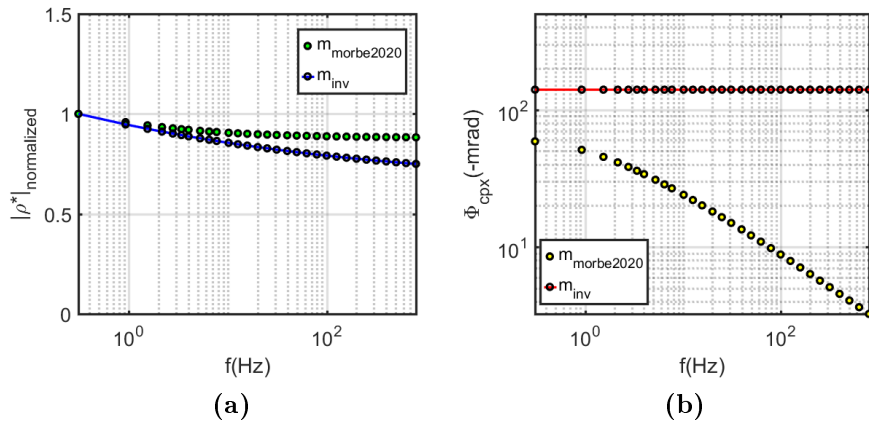
Figure VI.12: *CR spectrum extracted in the layer at 600 meters, for comparison with the CC model used in the modelling made by Mörbe et al. (2020) in figure VI.2. For comparison purposes, the resistivity norm is normalized by its value at the lowest frequency*

Obviously such interpretations are far from being straightforward as the constrains with depth of these inversions are very questionable, as only one component and offset were used and considering equivalence issues as for RX928. All attempts to couple these RX were unfortunately not successful in 1D. However, some observations were encouraging, especially concerning RX928: even if the depth of the anomalies are not well constrained, the CR norm variation introduced is coherent with what is expected. Its existence is however well-constrained by the data as it improves considerably the fit. Furthermore, an inversion starting from a real resistivity model and one starting from an homogeneous medium lead to similar results. Concerning the CR phase, several anomalies were retrieved but their frequency variations, if any, appear to be not robust due to a low sensitivity.

VI.1.3   Supplementary work and Schleiz outlook

These encouraging results lead to a second shipment of the Schleiz data. The complete land-CSEM E-field dataset was shared by the IGM team at the end of March 2021. The purpose was to find a RX or TX combination which could be coupled with the RX928 (or another combination) to add supplementary constrains compatible with a 1D approximation. Furthermore, another purpose was to go further by testing the 3D part of the code through a 2.5D inversion, based therefore on a 3D forward problem. Concerning the 1D work, RX and TX in the area of the pack 2 were evaluated for a combined inversion, however as for the subset data combination, these trials were not conclusive and no supplementary findings were obtained due mainly to 2D/3D effects. This is why I concentrated for a time my work on a 2.5D CSEMIP inversion attempt. Between 10 to 15 stations were selected in the conductive anomaly area using 2 or 3 combinations of sources with 6 frequencies logarithmically spaced between 0.3 and 1 kHz. A dense 3D grid was built according to the selected survey dimension for the 3D forward problem resolution,

whereas a coarser 2D grid was used for the inversion. Inversion grid parameters were thus extended in the third dimension towards the 3D forward grid boundaries.
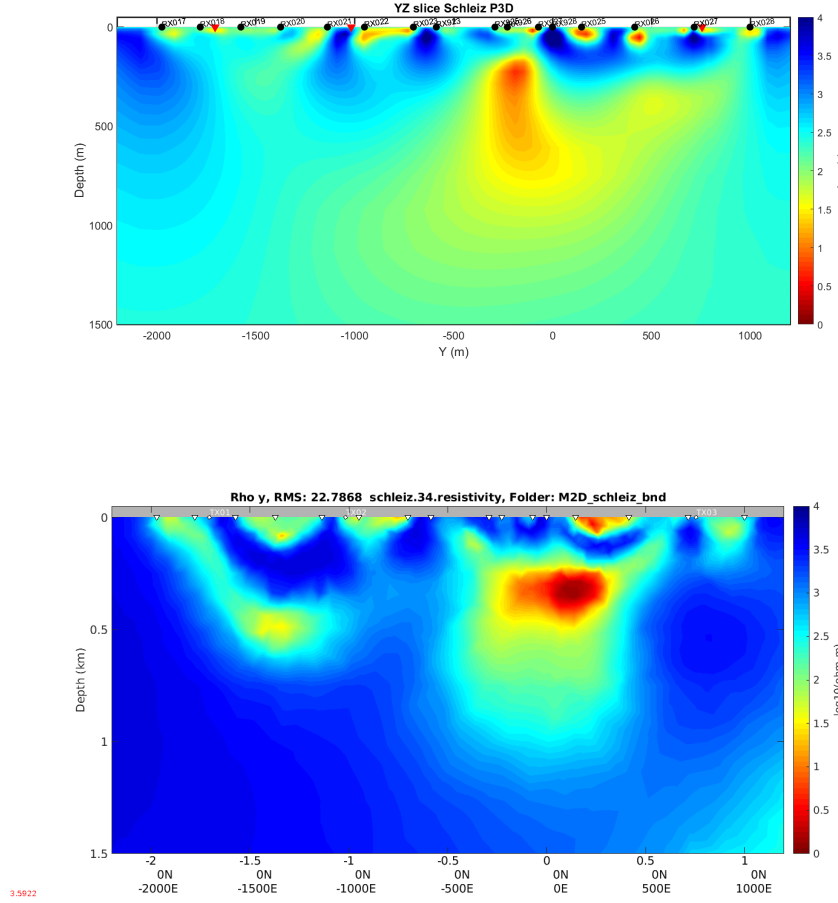

Figure VI.13: *Inversion examples of a selected subset of the Schleiz 2D survey centered in the area of the conductive anomaly presenting a large IP response (i.e. between 3 to 6 km position approximately in figure VI.4). Top: 2.5D inversion result obtained with POLYEM3D stopped at rms = 37% due to slow convergence and calculation cost consideration. Bottom: 2.5D inversion of the same data subset using Mare2dem code. Inversion results are relatively different but present similar structures*

However, after several trials with different selected data, I was not able to fit sufficiently the data with a constant resistivity model. Indeed, convergence of my inversion attempts abruptly decreased after few iterations and the inversions were thus manually stopped. It did not ensures completely that the fit would not have decrease further with more time, but one needs to take into account computational costs. I decided to stop the inversion as I had few explanations on the origin of this slow convergence. For comparison and to try to understand why the inversion seems to be stuck around 37% *rms*, I re-used the same dataset for a real 2.5D inversion with Mare2dem (Key, 2016) as done by Mörbe et al. (2020) for the complete dataset. Mare2dem reached in its case a 22 %

rms. An example of Polyem3D and Mare2dem inversion results are presented in figure VI.13. Mare2dem fit seems to encourage to restart the inversion and letting it to converge slowly. However, its *rms* is still relatively high as well to consider IP. A supplementary sorting of the data should be considered among other consideration, as the presence of some static artefacts that seems to be present in Polyem3D inversion under receivers, or adding more frequencies. I will not go into further details for this work, which is unfortunately not finalized and requires additional work. The choice to stop at this point 2.5D investigation of Schleiz data was motivated to focus my work on a 3D CSEMIP survey that was acquired during this thesis.

VI.2 La Porte-Aux-Moines (Côte-d'Armor) survey

In the framework of this thesis and the ANR *EXCITING* program, a 3D CSEM survey was planned in order to demonstrate the 3D inversion code capabilities. The former mining site of La-Porte-Aux-Moines (PAM) shows large IP anomalies according to a series of former BRGM geophysical surveys of the 70's/80's. La Porte-Aux-Moines is a small village of *Côte-d'Armor* in west of France where a massive sulphides ore was discovered during the 70's and gained a lot of interest during these years among many other sites of this area, with several coring boreholes and about 1000 meters of galleries dug down to 150 meters depth approximately. Lately, the site was subject of some controversy following the grant of an *"exclusive mining research permit"* (PERM) in the area of PAM accorded to *Variscan Mine* in 2013. It is familiarly known in France as the PERM of Merléac, which suffered from a strong local opposition and which partially lead to its abandon a few years later. However, it was therefore an opportunity for us to take advantage of such a known shallow ore body with strong polarization effects. A 3D CSEM survey was thus carried out in December 2020 to apply the developments of this thesis work on a real dataset.

VI.2.1 Geological settings

The PAM mining target was discovered around 1970, following a strategic geochemical investigation at the scale of the Armorican massif. It followed several geophysical surveys in order to localize and characterize the target of interest. Cored wells in the area were carried out during this period and crossed many sulphide mineralization areas which supported more investigations. The PAM anomaly is related to a topographic structure called "La Butte Saint-Michel" (*i.e.* The Saint-Michel Hill) with a summit at 321 meters results of several geological phase of deformation. The mineralization is concentrated at the bottom of the hill and is related to a succession of volcanic events and sedimentary deposits in shallow-water environments (Aye, 1983a). The anomaly is a poly-metallic sulphides ore with concentration of Zn, Cu, Pb, Ag and pyrite. The mineral content is estimated to 1.86 Mt with major components proportion of 7,83% Zn, 1,60% Pb, 0,76% Cu and 96,6 g/t of Ag elements (Aye, 1983b) representing around 14 500 t Zn, 31 000 t Pb , 14 100 t Cu and 179 t Ag. A geological interpretation of the PAM area is presented in figure VI.14 which reveals at this scale vertical structures oriented E-W.
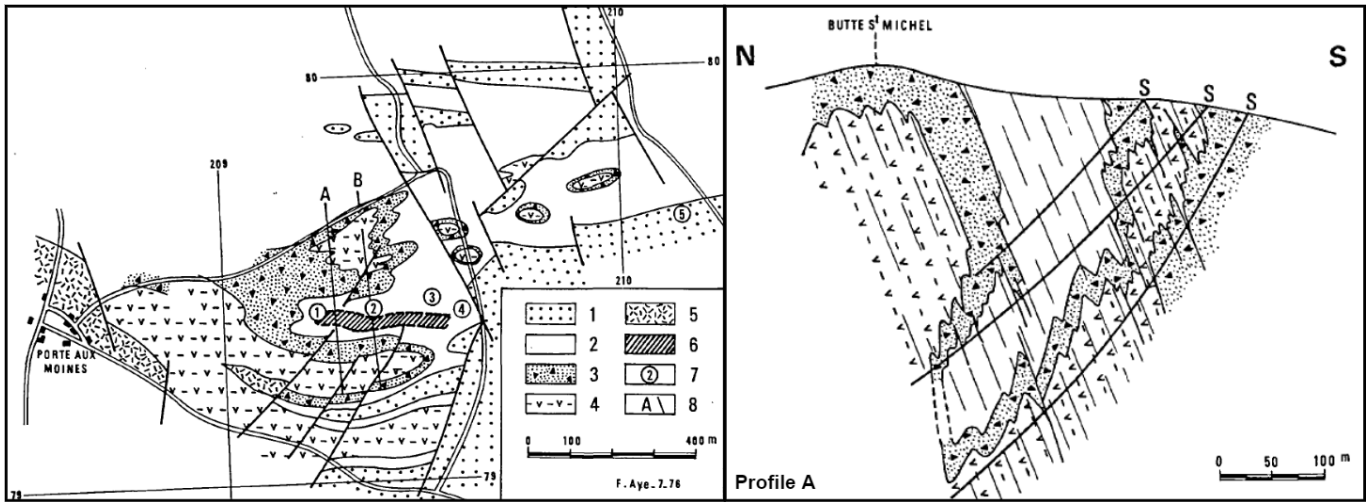
Figure VI.14: *Geological map and geological cross-section representation of PAM area from* Aye (1978). *1) Sandstones (Quartzite) containing some disseminated mineral of pyrite, galena and graphite. 2) Black sandstone and black shale formation bearing the sulphides mineralization. 3) Acid volcano-sedimentary rock formation composed of lave, tuffs and tuffs-sandstone. 4) Basic volcano-sedimentary rock formation composed of lave, tuffs and interbedded tuffites in a black sandstone and shale alternation - disseminated mineralization in stockwerck. 5) Dolerite. 6) Approximated projection of the massive sulphides ore body to the surface.*

In-situ measurements of resistivity were conducted in the galleries of the former mine and give an idea of the resistivity contrast that can be expected:

Rock type	$\rho(\Omega.m)$	IP (%) (T=5s)
Massive mineral	0.01	35 - 40
Black shales	400-900	24
Sandstone and shales	2000-4000	22.5
Acid tuff	500-1300	25
Chloritizised rock	190-230	26

Table VI.1: In-situ mean resistivity and IP(%) at $T = 5\,s$ measured in the PAM gallery (Le Masne et al., 1980)

The geology of the site appears to be relatively complex after figure VI.14 and (very) large resistivity contrasts are expected from measurements presented in table VI.1 with a variation over 6 decades and large IP effects. However, the authors of these measurements point out that these IP values should be taken with caution due to noisy data, which could explain the low differences between each measurement. Note that values in table VI.1 are not integrating a large volume of rock and it can therefore be expected a smaller range for surveyed data[e], according to surface electrical measurements. Therefore, a resistive

---

[e]especially concerning lower conductivity measurements made directly on the mineral ore

background of several thousands ohm.meters is expected with very conductive anomalies within 0.01 to 10 $\Omega.m$ range.

In figure VI.15 a summary representation of the geophysical surveys carried out before 1978 at PAM is presented. Many methods were tested on the site, among them, gravimetry, VLF, SP, magnetism and several ERT profiles including DCIP time domain method. The sulphides ore can be located approximately in the colored area of the map, the area where large frequency effects were measured. This anomaly is well correlated with other methods. It crosses the conductive and IP anomalies of profile S4 and S1. VLF method revealed a conductive axe. A strong SP signal is measured. The gravimetric anomaly is slightly shifted towards the north. Furthermore, a second conductive IP anomaly was detected toward the SE and was interpreted as graphites. This zone will be referred as the graphite area in the following. To the west of the area a magnetic anomaly is present and is related to the presence of *green rocks* and corresponds to the dolerite formation (5). Considering IP anomalies that interest us, high apparent CR phase values up to 70 mrad were measured at the indicated zone presented in figure VI.15 but large phases were measured along all the profile S4 with value around 30 mrad to the south and 50 mrad in the northern resistive area of the profile. These anomalies present a similar apparent resistivity around 50-100 $\Omega.m$
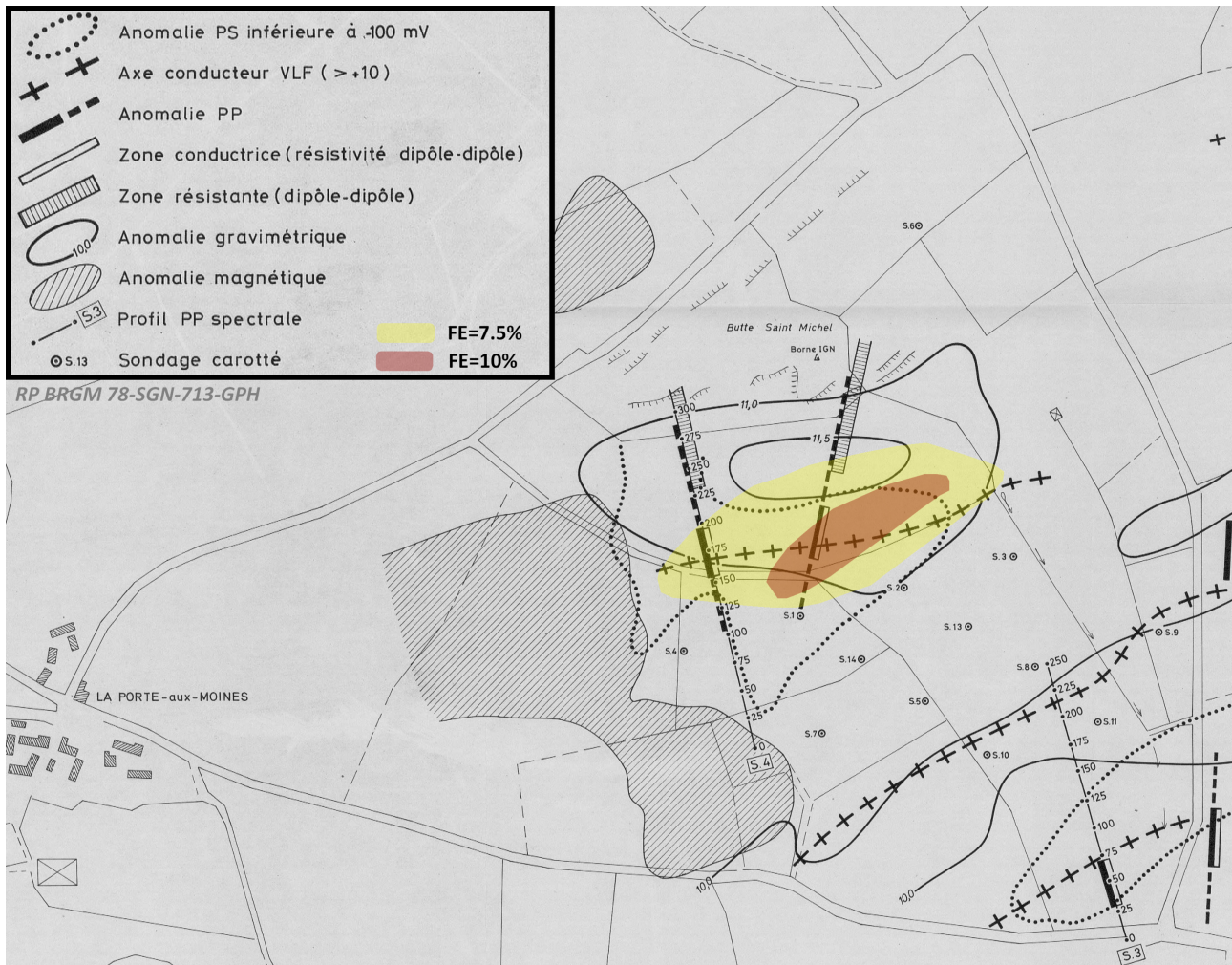
Figure VI.15: *Summary of geophysical investigations carried out at PAM mining site, modified from* Vaillant (1978).

PAM has several features of interest for the test of the developed inversion procedure:

❏ large apparent CR phase values.

❏ large frequency effect over the massive sulphide anomaly.

❏ Two potential distinct IP targets: the massive sulphide main target and the presence of graphite to the SE of the area was interpreted.

The latter is of primary concern as in some conditions massive sulphides and graphites could be discriminate using spectral IP method (Figure VI.16, Hallof and Klein (1983); Pelton et al. (1978)). Former measurements conducted on the site were not able to discriminate between both anomaly responses, although they were limited by the instrumentation at that time (Vaillant, 1978). Therefore, the possibility to discriminate both mineralizations was considered of high interest and the survey was designed according to these needs.
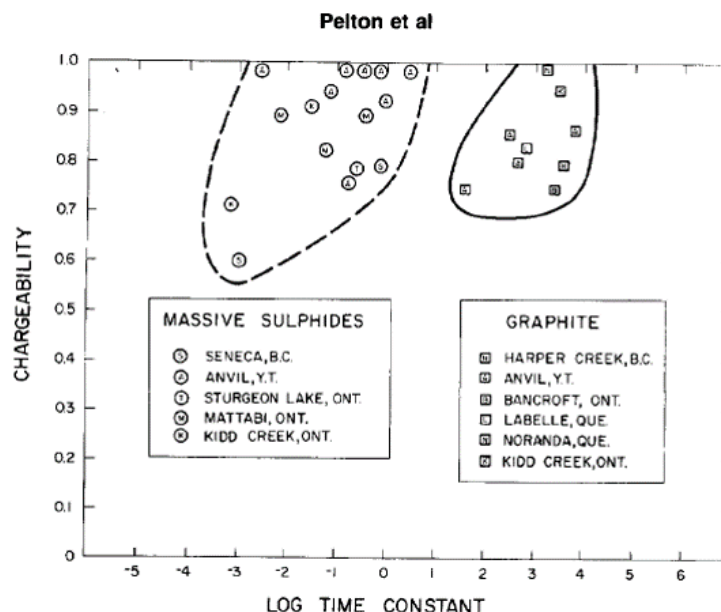
Figure VI.16: *Characterization of the time-constant and chargeability according to the type of mineralization, graphite of sulphides, from (Pelton et al., 1978)*

VI.2.2 CSEM survey presentation

The survey was designed to image mainly the central massive sulphide ore and a second target to the SE towards the graphites area. The survey design had to consider logistical limitations (Time, equipment, personnel, etc...). The survey was acquired on a week from 14 to 19 December 2020. The personnel was composed of 2 researchers, 2 PhD students and a technician affiliated to the BRGM and/or Strasbourg university/ITES. The available material was composed by the high voltage (6kW, 3000V) TIP 6000 transmitter developed by IRIS instruments (actually, the first deployed prototype own by ITES) associated to its generator, approximately 1500 meters of wires for transmitters, a set of 22 receptions stations with unpolarizable electrodes, 2 current recorder devices and a differential GPS. The reception stations were composed of two monocomponent RAU devices from Sercel, which are small recording devices for cable free seismic acquisition. A homemade (BRGM) impedance adaptor (ZA, *i.e.* Z =impedance) was added. These recording units are running at a sample frequency up to 2000 Hz, limiting the usable recordings to a maximum of 800 Hz (Nyquist and anti-aliasing filter). In addition, two complete sets of MT stations (ADU-07 and ADU-08 from Metronix) were deployed for additional constrains purpose near sources. RAU devices present large advantages despite a limited sampling frequency (ADU can record up to 64 kHz), as they are lighter and easier to install compared to ADU. Indeed, they are programmed in advance to start automatically at given time with a large battery life. Taking all these information into account a survey was designed based on three rotations of the RX position to cover up the area.

Several source positions were considered to obtain the best illumination possible, however it depends on the frequency sequences considered. High frequency measurements are

not time consuming, on the contrary, low frequencies / long periods are time consuming especially to reach a sufficient number of stacks. If graphites could be discriminated from sulphides, low-frequency records are required, as they exhibit long relaxation times (Figure VI.16). Considering that frequency above 1000 Hz would not be reachable due to Nyquist and that periods below 100 seconds are pretty unrealistic according to the schedule of the survey. Figure VI.17 presents the optimal frequency window that has been targeted compared to Cole-Cole model with time constant expected for graphites and sulphides.
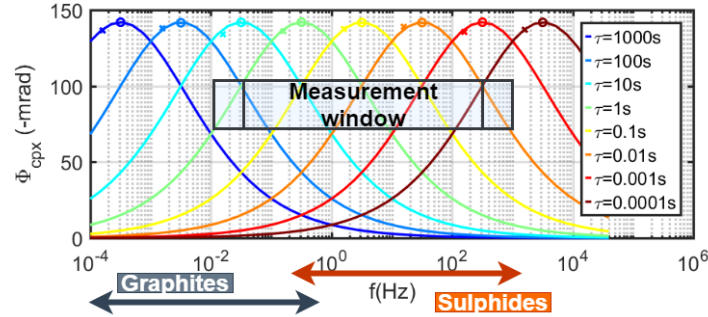

Figure VI.17: *Representation of Cole-Cole model with various relaxation time τ. The frequency window of possible measurements at PAM are represented, higher and lower limits are defined by instrumentation limits considering the planned material. Frequency window containing the CR phase peak of graphite and massive sulphides is indicated for comparison according to Hallof and Klein (1983) laboratory measurements*

These considerations lead to optimize the injection frequencies with 5 injection sequences from periods of 128 seconds to frequency of 2 Hz with a minimum number of stacks of 10 periods (Figure VI.18[f]). It results in a spectral spacing approximatively logarithmic and a total record time around **1 hour and 10 minutes per source position** which allows our team to record 4 complete transmitter positions for each of the 3 RX spreads.

Seq. #	T0 (s)	f0 (Hz)	Time (mn)	Nstack
1	128	0.0078	25	10
2	40	0.025	15	20
3	10	0.1	20	100
4	2	0.5	5	150
5	0.5	2	5	600

Figure VI.18: *Fundamental injection sequences used at the PAM survey ranging from 128 seconds to 2 Hz. Injection sequences are based on a square wave signal (or 50 % duty cycle) was used for sequences.*

---

[f]see appendices A.4 for a more complete description of the injection sequences

Survey summary:

The CSEM survey was composed of 5 injection sequences presented in figure VI.18, recorded at 66 receivers for 4 transmitter positions. Transmitters were composed of 3 grounded wires of 200 meters, two on the west of the survey with perpendicular orientation (1.1 and 1.2 TX) and one to the east (TX 2.1, oriented EW). A so-called *"gradient"* source (TX3) was also measured with a pole common to the TX1.1 and the other pole common to TX2.1. A fifth TX (TX2.2) was originally planned but due to time considerations was not maintained. One MT station was left recording above the main anomaly during the week and the second MT station recorded some points near the sources for additional constraints. The receivers grid was thus deployed in three rotations, recording the NS and EW components with electrodes of around 10 meters separation installed in "L" configuration. All electrodes positions were taken accurately by DGPS, as well as the grounded wires position which is modelled during the inversion. A simplified schedule of the mission is presented in appendix figure A.1 and the final map layout is presented in figure VI.19.
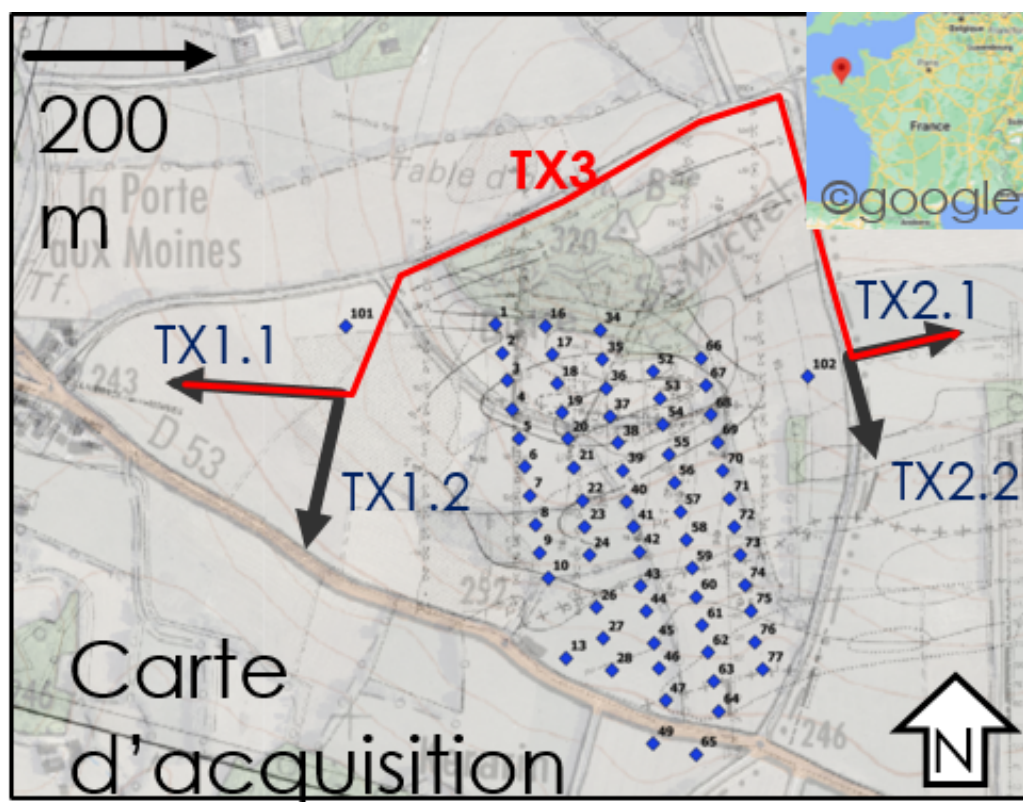

Figure VI.19: *Acquisition map of the CSEM/IP survey of La Porte-Aux-Moines realized in December 2021. 5 grounded wires are represented by black arrows and red line, whereas blue dots represent the receivers of the survey.*

Figure VI.20 presents some pictures of the PAM CSEM survey.

(a) *Picture of a part of a receivers line*

(b) *Picture of the RAU re-ceivers*

(c) *Picture of the TIP trans-mitter*

(d) *Picture of one of the TX pole*

Figure VI.20

Data processing

The data were processed using the PROCATS Matlab code developed at BRGM. It estimates $\mathcal{T}$ the electromagnetic transfer function $E = \mathcal{T}.I$ of each receivers and for each transmitter. The transfer functions can be calculated using robust processing (Egbert and Booker, 1986), however the data were of extremely good quality, thanks to the use of a stable transmitter and a large number of stacks and did not require a more processing as we injected several amperes at limited offsets of few hundred meters. The mains disturbance factors are nevertheless present due to instrumentation problems and the *"cows factor"*[g]. An example of the processing of PROCATS is presented in figure VI.21. The injected current and the measured voltage are presented in the upper image for a small part of the recorded signal. Passing in the spectral domain by Fourier transform the spectra of the signals are displayed in left images. The fundamental frequency of the injection signal is accurately determined and used to calculate the exact ray pointing on

---

[g]I refer here to the taste of the cows to eat wires or mistake the white nodes with salt blocks, which lead to lose a few wires and data

each harmonics of the square signal. In most of the cases the signal was good enough to look up to several hundred harmonics.

That is, the limited frequency of 2 Hz available by the TIP transmitter was not restrictive, indeed harmonics of the 2 Hz signal allowed to reach the highest frequencies that could be recorded (1000 Hz) with the RAU devices. To obtain the transfer function on the right, the ratios between the peeks of the measured voltage and the injected current are calculated with a normalization by the reception electrodes separation length obtained accurately from the GPS coordinates.
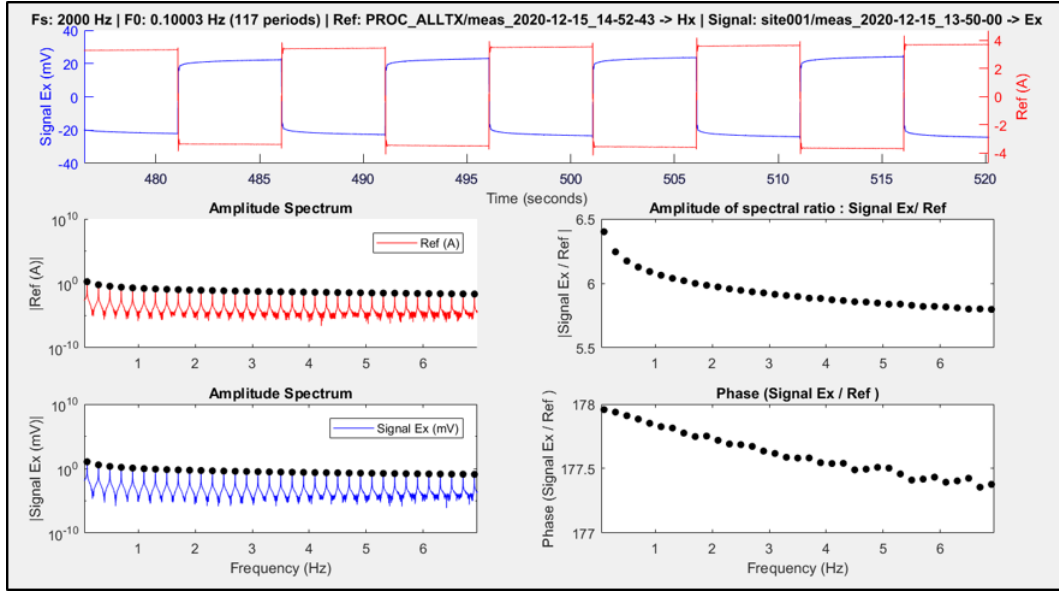

Figure VI.21: *Illustration of the data processing for a component of the electric field recorded at site 001 and for an injection frequency $f_0 \approx 0.1 Hz$ using PRO-CATS treatment; The time series are presented in the top plot with the record of the injected current (red) and the recorded voltage at the reception position. Left plot, middle and bottom are the spectrum for both time series with the injected fundamental and firsts (≈ 30) harmonic frequencies represented by a black marker. The ratio is used to obtain the transfer function corrected by the length of reception electrode separation.*

Thanks to the large current that was injected with the TIP transmitter and the long wires that were used to increase moment of the sources, the signal to noise ratio is not a concern for the vast majority of the stations. Nevertheless, some instrumental problems occurred and a part of the data were lost or left unusable. Finally, after a rigorous data quality control stage (verifying the time series and the spectra smoothness, comparison with modelling, removing outliers data,etc...), approximately 68% of the recorded data were remaining.

Induced polarization evidence

The processed data were mostly of very high quality and as presented in figure VI.21 it was possible to see the square wave modulation of the measured voltage directly on the

time series. Therefore, IP responses could be observed easily on time series and present very large responses. Figure VI.22 presents an example of time series for a period of 40 seconds near the massive sulphide ore body, showing a large IP response with the charge and discharge phases of the ground.
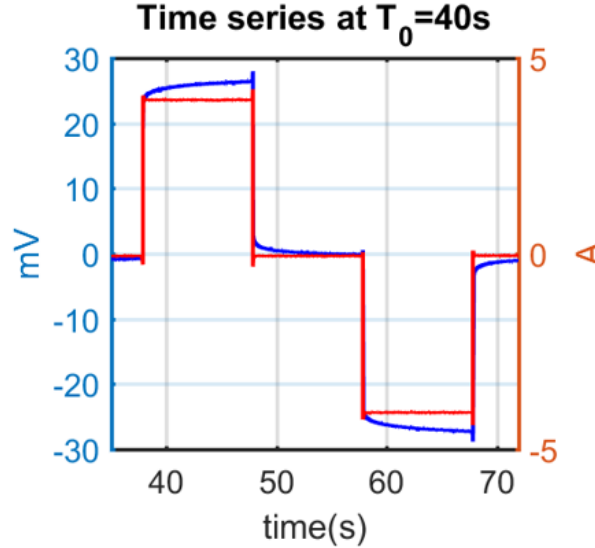

Figure VI.22: *Time series focused on a square signals presenting large evidence of IP with a charge and a discharge phase of the ground. Blue curve: measured voltage; red curve, injected current $T_0 = 40s$*

An example of processed data is presented in figure VI.23. It presents the electric field spectrum (Amplitude, phase and in-phase, out-of-phase) oriented EW for the station RX1 at the extreme NW of the reception grid. Each fundamental injection frequencies and its associated harmonics are presented with a different color curve. The perfect continuation and superposition of each curves is an indication of the high quality of the data. Several IP evidences can be noted as previously for the Schleiz case. Indeed, at low frequency, where the DC plateau is expected when there is no IP, a large variation of the electric field can be observed on the in-phase part and amplitude. The phase presents a large phase delay at low frequency, which is reflected by a large magnitude of the quadrature part. Even considering one of the closest RX from the transmitter, it can be noted that EM effects appears clearly from 10 Hz.
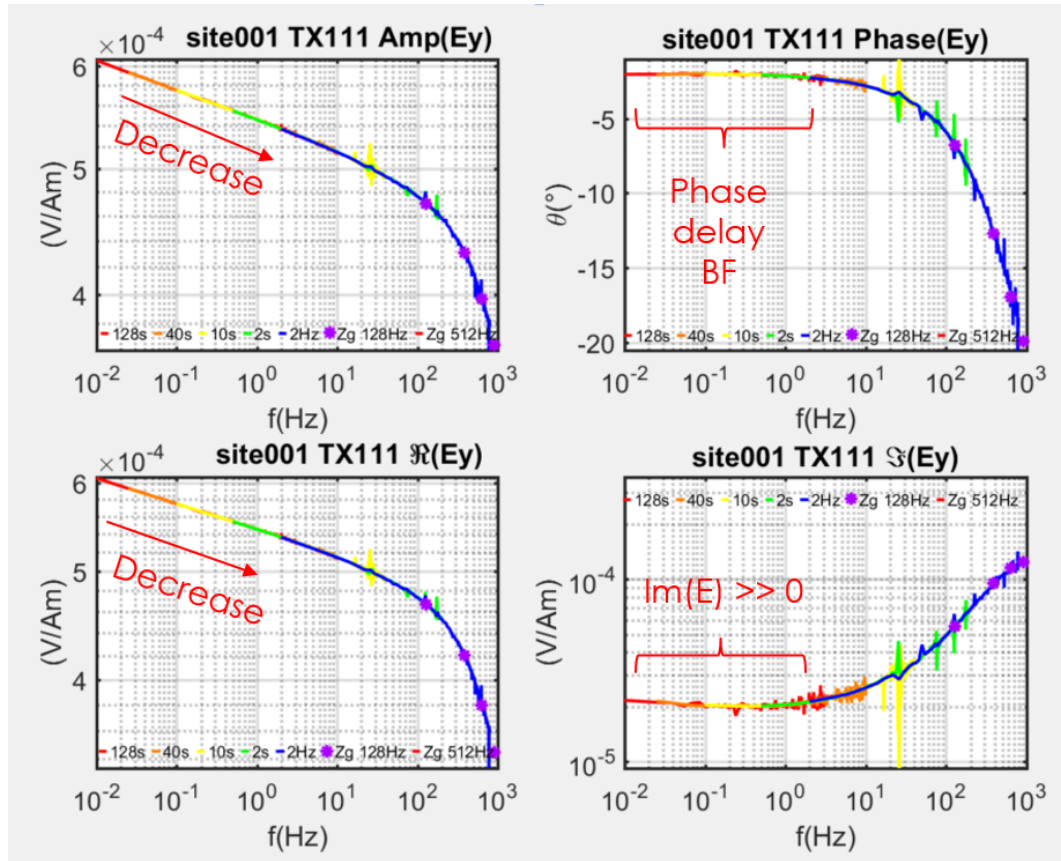
Figure VI.23: *Presentation of the harmonic superposition on the electric field transfer functions acquired at each injection sequences for an example site with IP clues. Each fundamental injection frequency and its associated harmonics are presented with a different color curve*

Electric field orientation and modelling comparisons

Data quality control processes went though some simple modelling comparison in order to detect outliers and instrumental issues. In-phase electric field maps of each sources at 2 Hz are represented below in figure VI.24. They are plotted against the corresponding synthetic field modelled for a homogeneous half-space of 1000 $\Omega.m$.
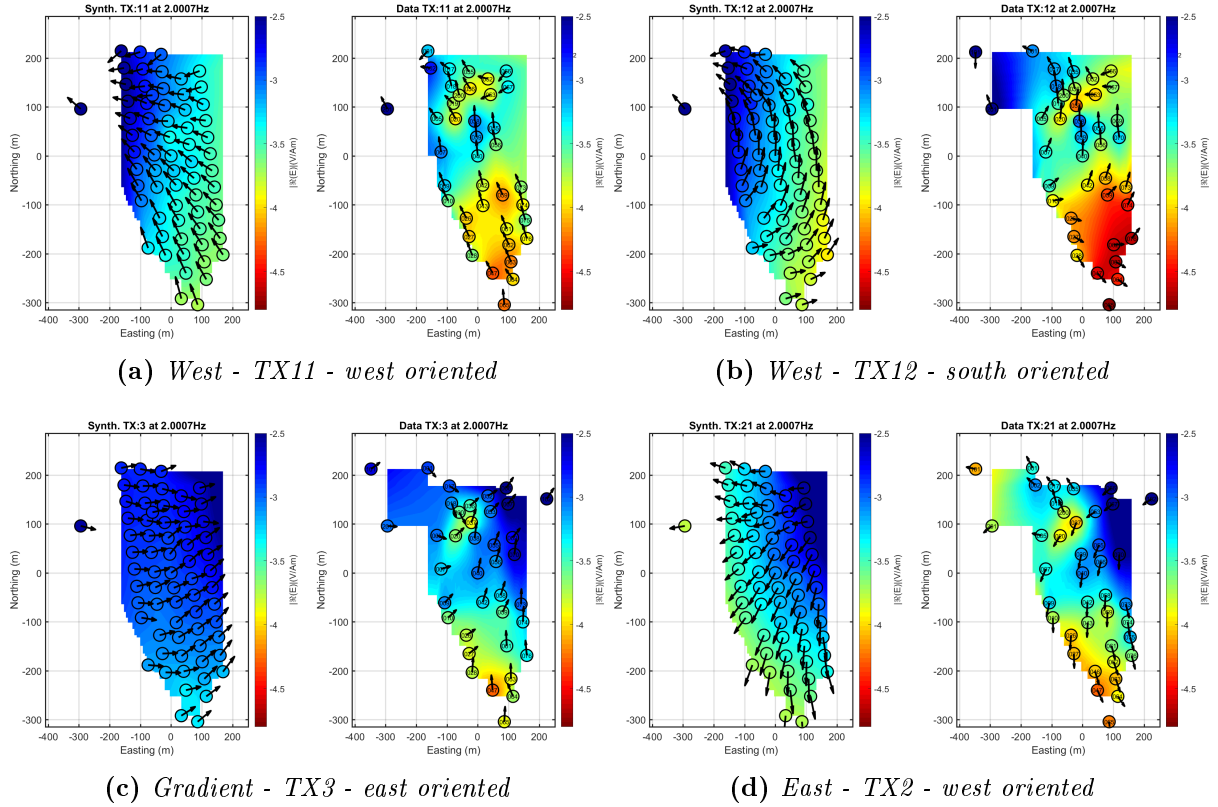
(a) *West - TX11 - west oriented*

(b) *West - TX12 - south oriented*

(c) *Gradient - TX3 - east oriented*

(d) *East - TX2 - west oriented*

Figure VI.24: *Electric field (real-part) map of the PAM survey for modelled data over a homogeneous half-space of 1000 Ω.m (left of the subplots) and the measured data (right of the subplots). Each source is represented at a frequency of 2 Hz. Patch of color represents a station and is not plotted if data was sorted out or if a component is missing (right image only).*

At the survey scale, the modelled field amplitudes are relatively in good agreement with the field data. However, the 3D geological complexity can be noticed at first sight with large decreases of the electric field amplitudes, which indicate a medium with larger apparent conductivity. It concerns, especially the south of the survey in the *"graphite area"* and the area of the massive sulphides, where a drop of the electric field is very well correlated for each sources illuminations.

The orientations of the in-phase electric field are also in very good agreement with TX12 and TX21, however this is not the case for TX11 and TX3 (gradient configuration). Indeed, TX1 on west side of the survey is oriented in the EW direction, whereas the TX3 is a very long wire grounded at farthest poles of TX11 and TX21. Both fields should have a predominant EW orientation (in the northern part of the survey at least) in the case of a 1D medium. This is especially the case for the gradient configuration, which is designed to optimize sub-parallel current lines. This is clearly not the case. The electric fields for these transmitters are predominantly oriented NS. It indicates the presence of very large contrast anomalies (inside but also outside the survey reception area) that reorients abruptly the electric field orientation and which could be of concerns for the inversion stability.

Note on 1D inversion trials:

Several stations were considered for 1D inversions (independently, 1 RX/TX couple) in an attempt to obtain more information. All attempts of 1D inversion were not successful which can easily be understood by previous modelling in figure VI.24 indicating a very complex 3D geological setting. I concluded that 1D approximation was not compatible with the data for transmitter at these offsets, which are closer compared to Schleiz dataset (Offset$_{Schleiz}$ ≈ 1000 meters and Offset$_{PAM}$ ≈ 400 meters, except that there was only one component available for Schleiz). Next step, was to considered thus 3D inversions.

VI.2.3   3D inversion of the PAM dataset

3D inversion of the PAM dataset was undertaken following the same scheme as for the synthetic two-cube model presented in chapter V, starting therefore with the inversion of the logarithm of the amplitude of the data considering a constant resistivity (stage 0). The phase data were also considered with an appropriate weighting to avoid to fit the IP effect. In this particular case, I considered important to introduce the phase information to take into account the polarity informations, as electric field orientations shows spatial variation due to the complex geology. Several inversions were carried out by varying the inversion grid to evaluate progressively potential perturbation remaining in the data or due to the grid. It helps to appreciate progressively the information content of the data. Inversion grid based on linear splines was used for the inversion of PAM survey. The inversion that I present in the following are based on the built grid presented in figure VI.25, which results in 12480 splines basis to invert, instead of ≈ 360 000 cells for the grid used for forward modelling over a similar domain (The total grid size, including cells expanding towards grid boundaries is about 1 million cells). The outer transmitter poles were kept in the inversion grid, as previous modelling suggested the presence of large anomalies outside the reception grid, which was confirmed by first inversions results. Indeed, it will be shown further that a very large resistant structure was inserted near the west sources and was necessary to explain the NS orientation of the electric field from TX1.1 and TX3. Spline basis separations progressively expand outside the reception grid for constrain purposes as (almost) no information is available.

A smoothing constrain was used to regularize the inversion. To scale the sensitivity, the Jacobian scaling was not used in this case. I used some features of POLYEM3D original code, indeed two scaling of model parameters were applied, called depth scaling (DS) (used in 1D inversion of Schleiz) and module scaling (MS). They allow compensating the loss of sensitivity with depth and to compensate for the sensitivity of the source position (See annexe A.3 for more details). Depth scaling was set mainly to reduce the first layer sensitivity and avoid large variation in the cells close to receivers. It improves the numerical stability and the inversion convergence.
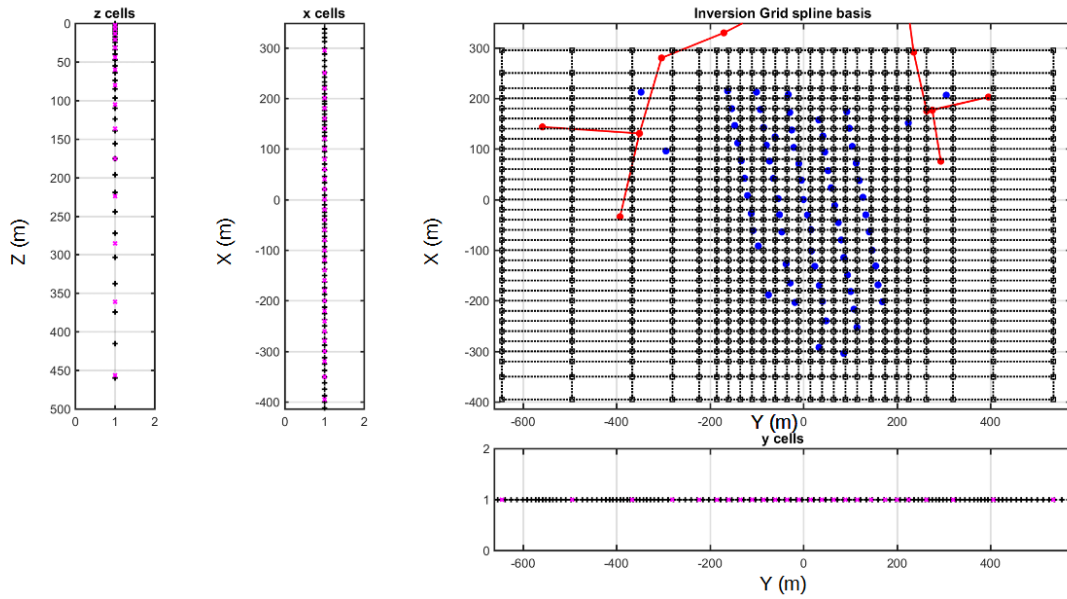
Figure VI.25: *Inversion grid based on linear spline, used for the inversion of PAM survey. z, y and x cells plot present the cells limits (black crosses) and the position of the basis of spline (magenta crosses). The big plot (top-right) represent the resulting inversion "grid" in black, with the position of the grounded wires (red) and receivers (blue dot). It results in 12 480 spline basis to invert, instead of $\approx$ 360 000 cells to invert on the forward grid for a similar domain.*

Constant resistivity inversion

The geology of PAM is very complex and data inversion turned out obviously to be very complex, without even considering IP effect. Many inversions were carried out with several phases of data suppression or grid adjustment. I will stick to the presentation of the most advanced work on the dataset for two cases. Four frequencies were selected (2 Hz, 42 Hz, 206 Hz, and 798 Hz) for these inversions. Lowest frequencies were avoided as they contains only IP supplementary information, which is not required nor wanted during this stage. A larger number of frequencies did not provide better results, so this choice was made to limit computation times. Figure VI.26 and figure VI.27 present inversion of the sorted data for all sources (INV1) and for only two source positions (INV2). The second inversion better fit the data, however it contains also less data as only two source are considered. If phase data are omitted in the *rms* calculation, INV1 model fits the amplitude data with an *rms* of 30% starting from 70%, whereas INV2 result present a *rms* of 12.45 % and started from 64 %.
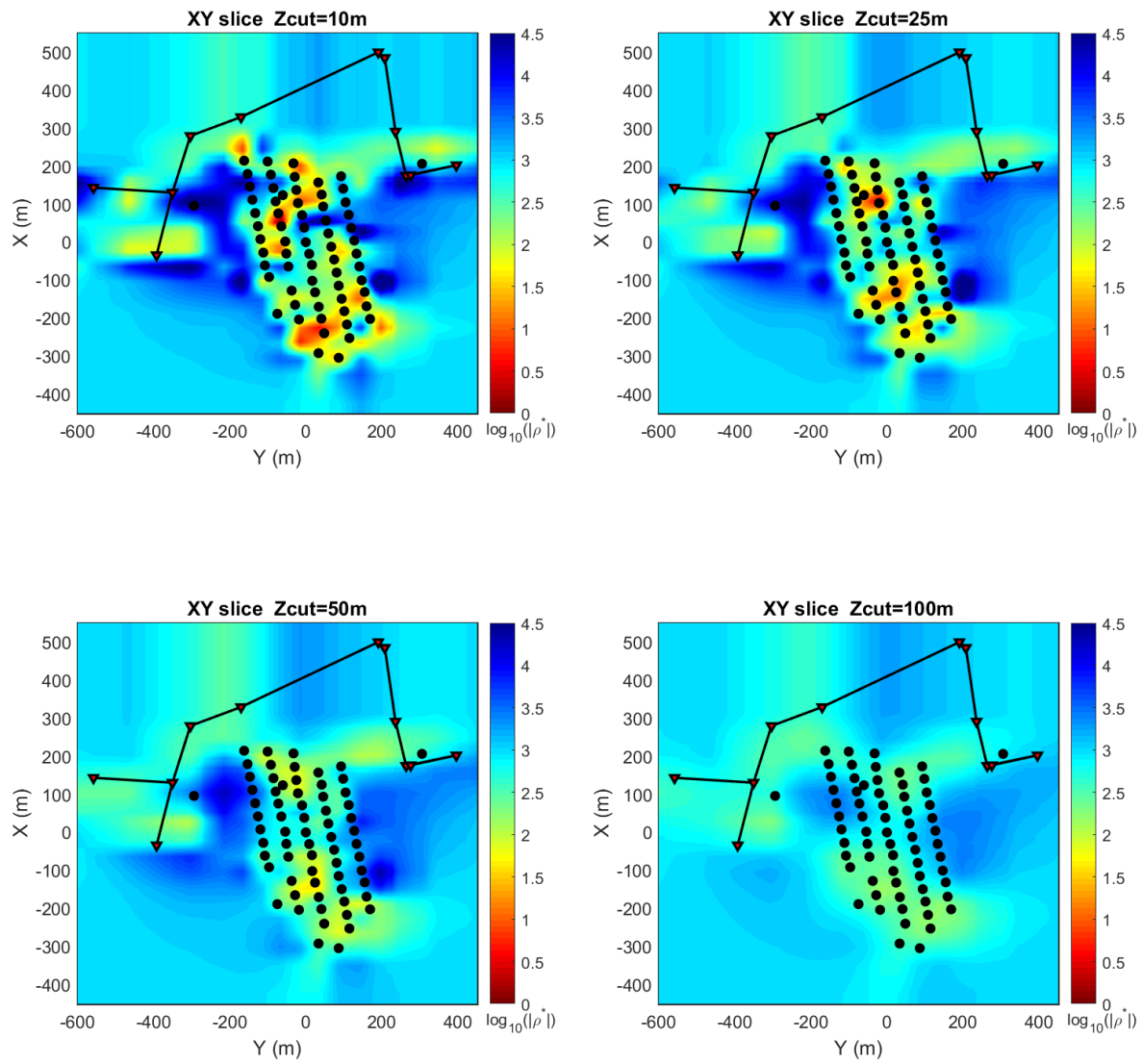
Figure VI.26: *Inversion result of INV1 data, considering all the sources and a constant resistivity for horizontal slices at different depths*
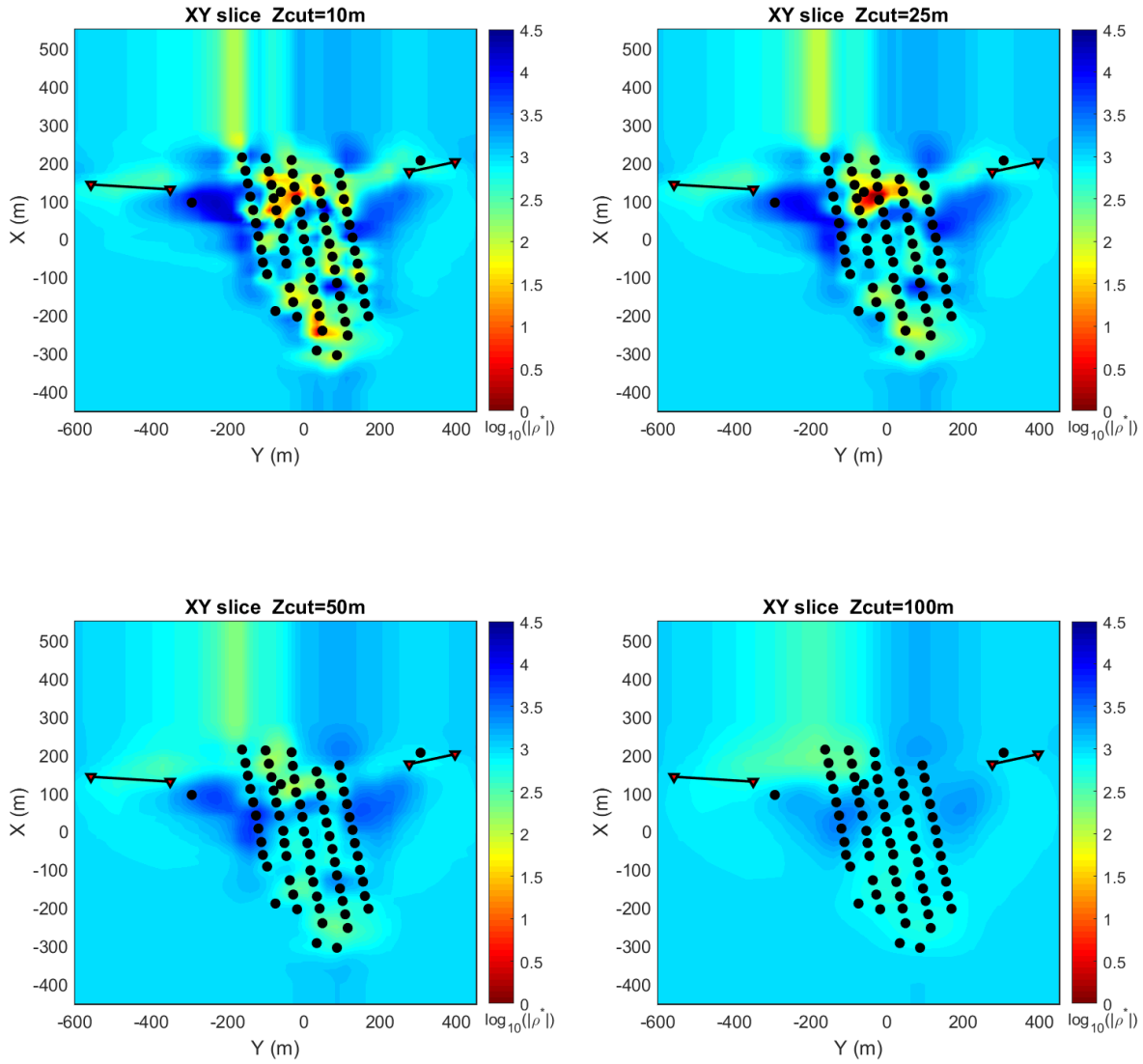
Figure VI.27: *Inversion result of INV2 data, considering only TX1.1 and TX2.1 and a constant resistivity for horizontal slices at different depths*

The results are presented as horizontal slices in the resistivity model at 10, 25, 50 and 100 meters depth. Both models present similar patterns. The range of resistivity is really broad and covers values from 3-10 $\Omega.m$ to 10-50 $k\Omega.m$. Inversion INV1 taking into account all the sources has slightly higher resistivities. It can be noted the presence of a large resistive bodies that extend along the west side of the reception grid and along the east side. Conductive body around the sources are also present but with lower resistivity contrasts. These structures are necessary to explain the electric field orientation for TX1 and TX3 data. The resistive body to the West can be linked to the magnetic anomaly that was mapped in the past by geophysical investigations presented in figure VI.15. It was interpreted as a dolerite formation. The massive sulphides area (around x=100m and y=0m) is very conductive and shows a large resistivity contrast.

Other conductive bodies are located more south of the survey. It can be noted on figure VI.26 for INV1 result that the conductive anomalies appear to be elongated in a NEE direction. It is less clear on INV2 result. However, an attempt to correlated these structures to the geological structures oriented EW in figure VI.14 can be made, but it is highly hypothetical especially concerning INV1 which presents a larger *rms*. As INV2 includes fewer source positions, the medium is less well *illuminated* and can explain the shape difference of southern conductive anomalies, but it can also be explained by the different receivers used. A test with a larger regularization was carried out, but similar structures are appearing, but slightly larger due to a bigger smoothing constrain. In both inversions, no anomaly was introduced at depth. The anomalies are limited to shallow surface and vanished faster toward depth. Unfortunately, this is probably due to a lack of high frequencies to better constrain the depth and geometry of shallow anomalies (with shorter skin depth) combined to a lack of deep information due to the relatively short offsets and the large shallow contrasts hiding deeper anomalies. Therefore, it seems that inversion is limited due to a lack of vertical resolution at this point.
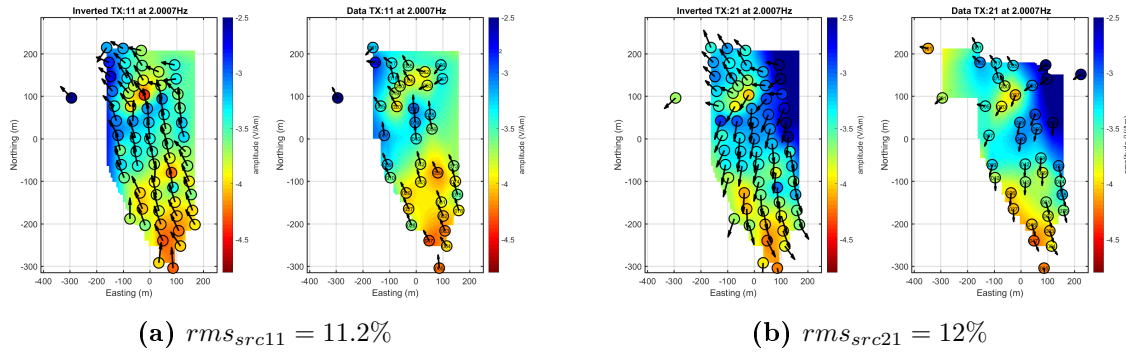

(a) $rms_{src11} = 11.2\%$ (b) $rms_{src21} = 12\%$

Figure VI.28: *Electric field (real-part) map of the PAM survey for inverted data from INV2 result (left of the subplot) and the observed data (right of the subplot). Each source is represented (left: TX1.1 and right: TX2.1) at a frequency of 2 Hz. Patches of color represent a station and is not plotted if a data was sorted out or if a component is missing (right image only).*

The resulting fields for INV2 (the inverted model with the best fit), is presented in figure VI.28. If the anomalies are hard to interpret, except for the conductor horizontal position, after inversion, the in-phase amplitude of the inverted electric field is in relatively good agreement with the data. Orientations are also mainly coherent. This work illustrates perfectly the complexity of 3D EM imaging of a CR medium, as reaching a sufficient fit can already be a challenge. Reaching 12 % of *rms* with INV2 model, a frequency-dependent inversion of the CR norm was considered, inverting thus p^n polynomial.

CR norm frequency dependence

A late attempt of inverting the CR norm frequency variation was carried out from INV2 model and the results are presented in figure VI.29. In this case, low frequencies were

added resulting in 6 frequencies (Period of 128 s and 8 s were added). Unfortunately the results are at this stage limited due to a fit that is not satisfactory and requires additional work. Indeed, the decrease of rms from 12.5 % to 10.64 % is abruptly stopped after 3 iterations. It can be explained by the large anomaly introduced at the source TX2.1 position on p^1 polynomial. Indeed, the rms drop is asymmetric between both source and mainly concern TX 2.1. However, some encouraging results can be highlighted for the pursuit of the work. A frequency dependence is mainly detected as a negative slope p^1 of the resistivity frequency variation if introduced. The area of the massive sulphide ore body is the most impacted by a frequency decrease if the eastern source artefacts are nevertheless omitted. This anomaly is also the one that goes the deeper. The south of the survey is also impacted, however other anomalies can be observed at the center of the acquisition.
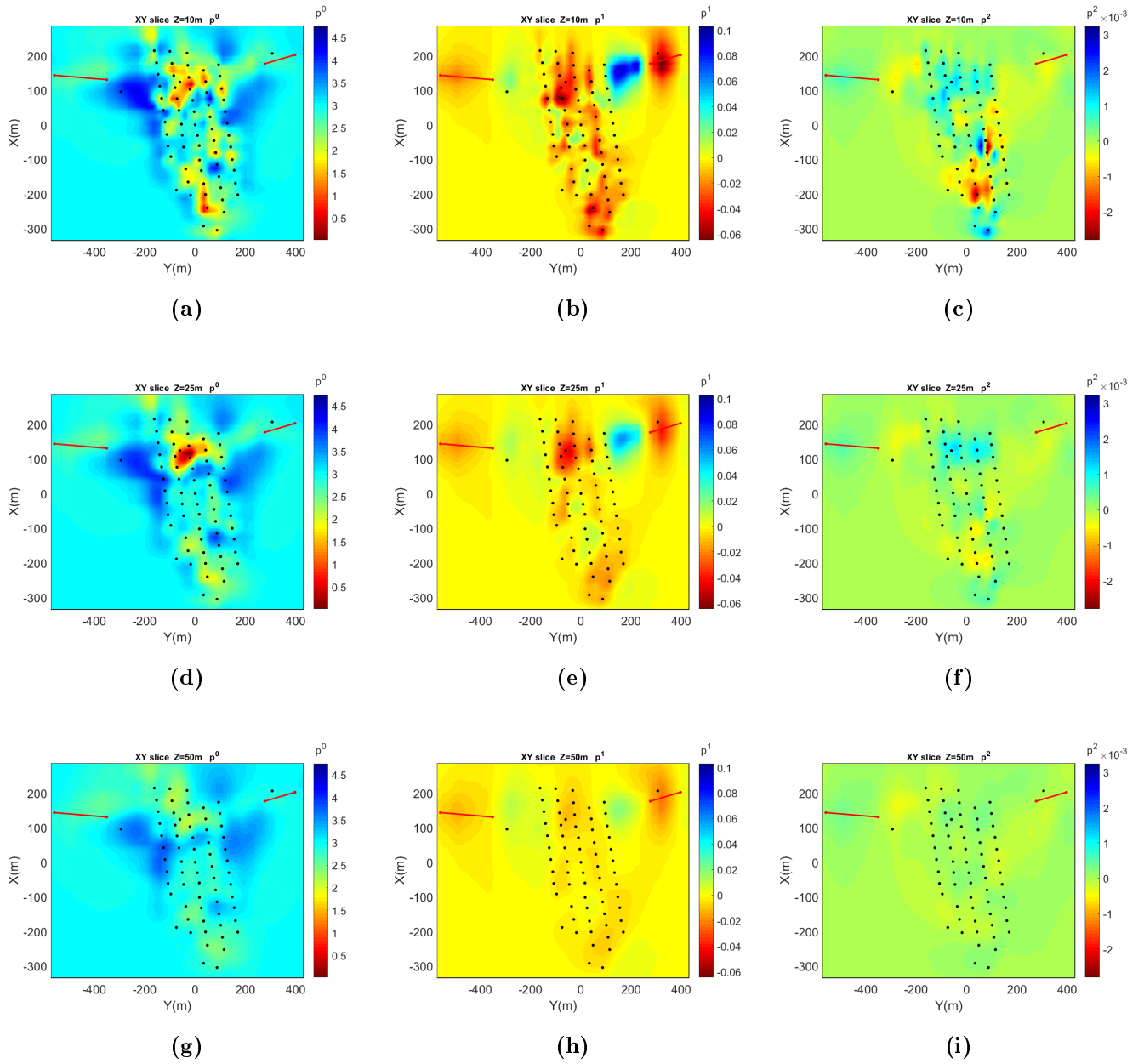
Figure VI.29: *Representation of p^n polynomial coefficients after several iterations for horizontal slices at three different depths.*

Figure VI.30 presents four CR norm spectra extracted for representatives anomalies observed on p^1 and p^2 coefficients. The CR norm spectra for the massive sulphides ore body position is presented, for the position of the large south-west p^2 anomaly, for the southern position of the formerly interpreted area of the "graphites" and for one of the p^1 anomaly near the center of the acquisition. It shows the decrease with frequency of the CR in each position. The p^2 anomaly is not significant compared to the frequency variation due to p^1 anomaly as observed in figure VI.30d.

(a) *Massive sulphides location*

(b) *Center anomaly*

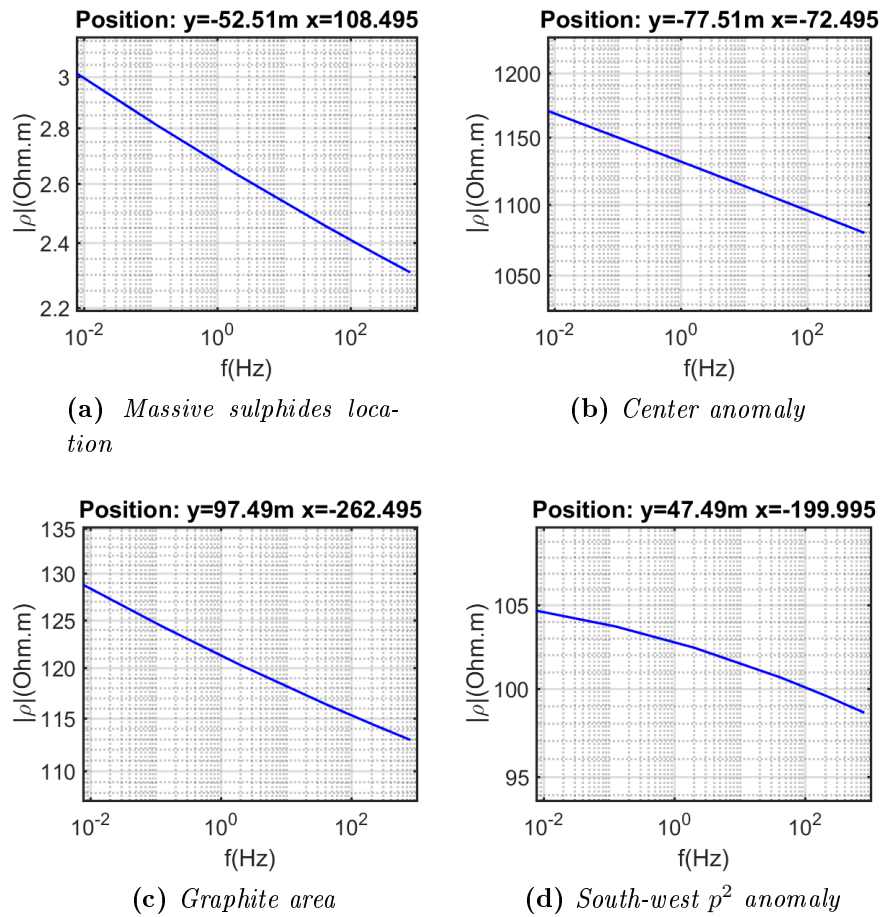(c) *Graphite area*

(d) *South-west p^2 anomaly*

Figure VI.30: *CR norm spectra at different point of interest at 15 meters depth*

A representation under the form of the percent frequency effect $(\rho_0 - \rho_\infty)/\rho_\infty$ (taking higher and lower frequency relativities) at a shallow depth of 10m is also shown in figure VI.31.
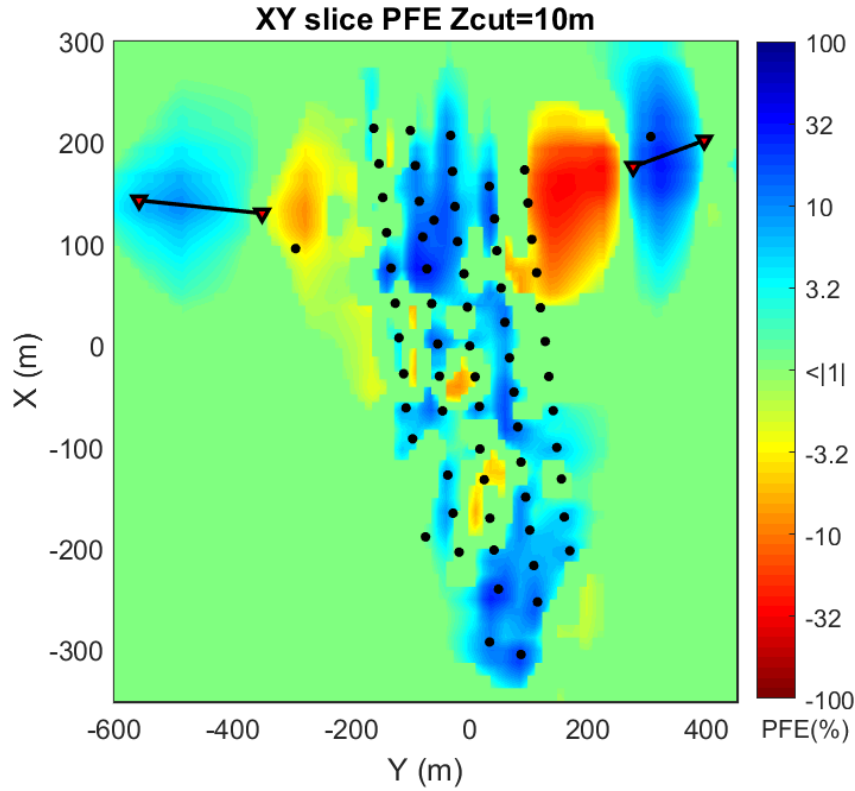
Figure VI.31: *Percentage frequency effect (PFE) obtained from inversion presented in figure VI.29. As some artefacts appear during the inversion, negative PFE anomalies can be observed mainly in area with no constrains close to the transmitters.*

It follows obviously the variation observed on p^1, as p^2 coefficient is weak and is not representative of the frequency variation introduced.

Limitations and discussion

Data fit:
Figures VI.32 and VI.33 present some examples of the fit of the data at the end of stage 1 for 6 receivers trying to be representative of the data set. Site 1 and 73 present the fit for stations where no frequency variation was introduced closed to the surface, site 37 is above the sulphide anomaly, site 40 is in the center of the grid, site 47 is in the graphite southern area and site 67 is a station located along the northern large source artefact with negative PFE.

Figure VI.32: *Examples of electric field amplitudes fits at the end of stage 1 for RX01, RX37 and RX40. m0 refers to the starting model data at stage 1, i.e the fit at the end of stage 0*

The data fits shows that the introduction of the frequency variation, mainly through a decreasing slope, improved slightly the fit. It can be more clearly noted for RX37 and 47. TX21 data are presenting a larger variation of the fit, whereas TX11 data are

less impacted. This is partially due to the illumination difference, but more probably to the large source effects due to the anomalies inserted below the TX21. Indeed, it can be supposed from RX01 and RX73, which are located in area with no anomaly of p_1 coefficient, however a low frequency variation of the electric field amplitude (decreasing) is still observed on inverted data.
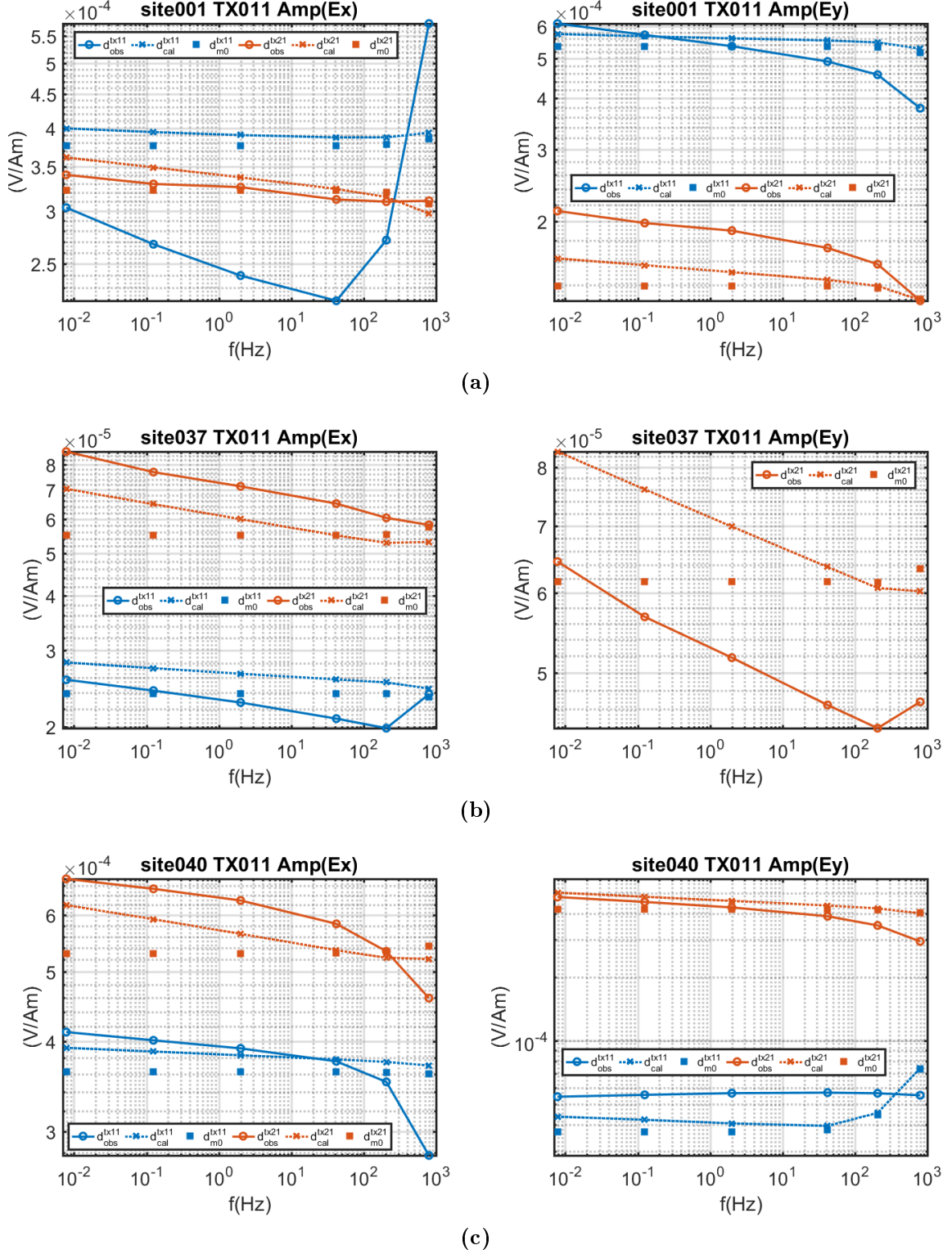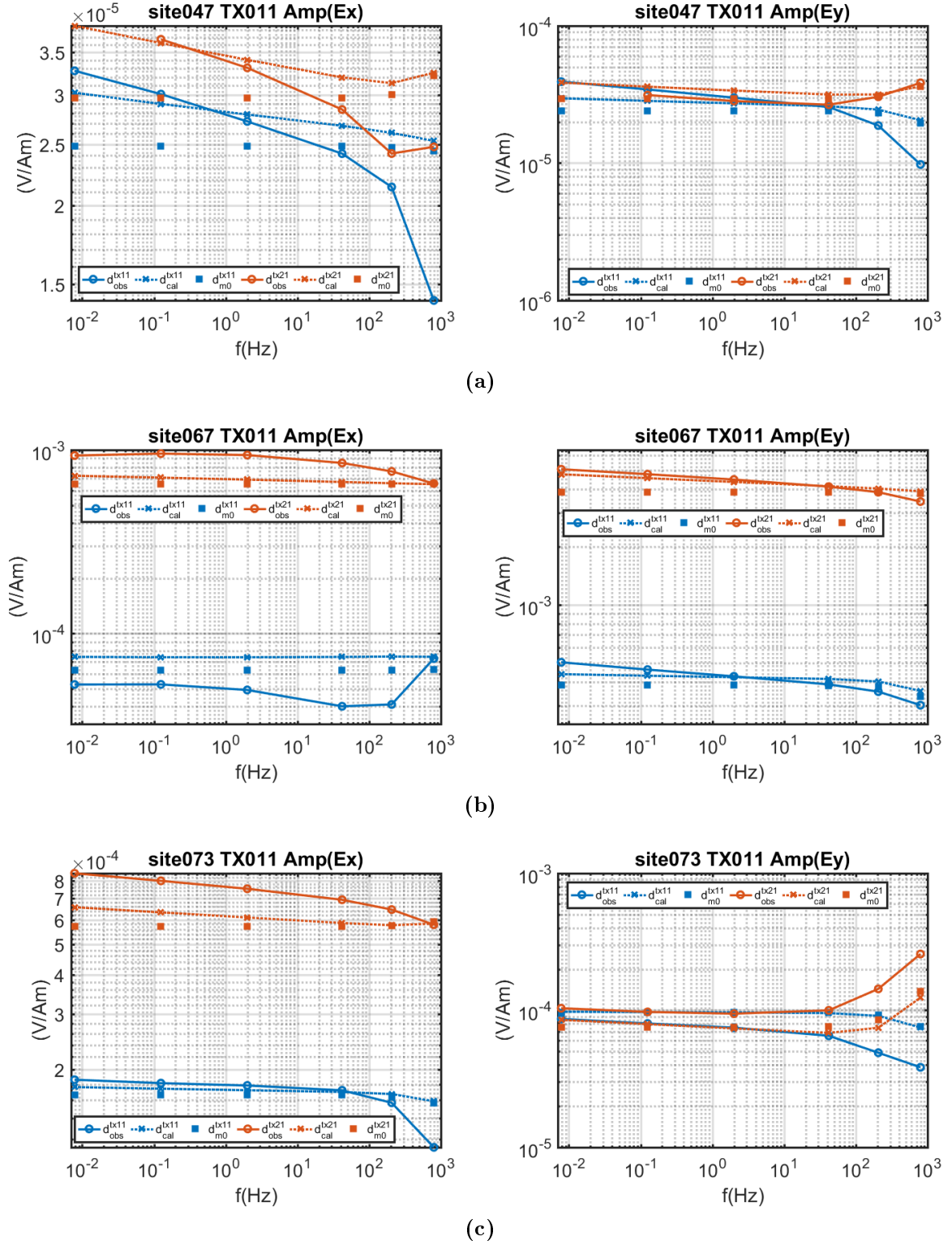
Figure VI.33: *Examples of electric field amplitudes fits at the end of stage 1 for RX47, RX67 and RX73. m0 refers to the starting model data at stage 1, i.e the fit at the end of stage 0*

These figures illustrate that the data are not completely fitted at the end of stage 1. IP effects are one of the main reasons of these discrepancies, but also due to EM effects that are not fitted at high frequencies when the variation of the field increases above

≈ 100 Hz. The fit of the phase data are presented in appendices figures A.4 and A.5. However, the phase data are generally badly fitted, even if some examples could be fitted by adding a CR phase in the medium (*i.e.*. RX01/TX21). Inversion of the CR phase from phase data makes therefore little sense. An attempt to inverse a constant CR phase for 3 of the lowest frequencies was carried out, however the inversion did not converge.

Limitations

According to previous observations, inversion results of the PAM dataset are a bit disappointing at this stage. Indeed, a large portion of the amplitude data still need to be fit, whereas the electric phase data are poorly fitted. The residual can be largely attributed to the large IP effects of PAM area, however a consequent portion at high frequency ($> 100\,Hz$) is attributed to EM effect that are hardly fitted, which can be confirmed by the large phase residuals (larger than what IP effect could realistically produce). Therefore, considering the disappointing fits, some supplementary work is necessary, especially to better explain the high frequency part of the data containing EM induction information.These informations are critical to improve the vertical resolution, which are nevertheless lacking of sensitivity due to too short offsets and low frequencies. A way to better penalize these parts of the data should be considered and would lead most likely to restart an inversion from scratch. As very conductive anomalies with sharp interfaces are retrieved some numerical issues can also be partially suspected.

A new approach should be considered in order to better constrain the inversion which was stuck during stage 1 around a 10 % *rms*. In order to improve the convergence of the inverse problem, the source singularities should be better constrained for higher degree of polynomial coefficients in order to attenuate the large p^1 artefacts under the source locations. Other sources should also be reconsidered more closely to better understand the reasons which lead the convergence to fail, in spite of several unsuccessful trials with more sources combined.

On the other hand, despite these limitation due to considerable difficulties linked to a very complex geological setting with large resistivity contrasts, the multiparameter inversion seems to tend towards a good direction for IP/EM consideration. Again, the usefulness of a multi-stage approach is highlighted.

Conclusion

In conclusion, in this final thesis chapter I focused on firsts applications of the CSEM(IP) inversion using the proposed multistage workflow and a polynomial parametrization, for the inversion of real datasets. At first, the 1D application was presented on a 2D CSEM dataset acquired in the framework of the DESMEX project on a former mining area near Schleiz, by the IGM of the University of Cologne, which kindly agreed to share the data for my thesis work. The dataset contained some evidences of large IP effects in the viscinity of a large conductive body and noticed formerly by the IGM team. I applied the method and the 1D multiparameter inversion code developed during this thesis on separated RX sites containing IP information and retrieved a coherent CR norm frequency variation as

well as a CR phase. However the sensitivity of the CR phase did not allowed to retrieve its frequency variation, if any (the medium can follow a constant phase model).

On the other hand, a 3D CSEM survey was acquired in December 2020 on a former mining site, at La Porte-Aux-Moines in west of France. The recorded data are of high quality and present large IP effects due to the presence of a massive sulphides ore body and potentially some graphites. The 3D survey was at a smaller scale with very shallow anomalies compared to the Schleiz dataset. Several inversions were carried out, nevertheless the complex geology with large resistivity contrasts was making the task very difficult, especially outside the receivers grid and under the sources, with convergence issues arising, even to retrieve a coherent constant resistivity. The stage 1 inversion for a CR norm frequency-dependent was carried out and leads to promising results, however more work is necessary to better constrain the problem. It is probable that in the case of PAM survey, the lack of higher frequencies and larger TX-RX offsets to improve the vertical resolution would remain a major issue. On the other hand, the work on the 2.5D complete dataset of Schleiz have some potential in order to retrieve IP signal at depth.

Conclusion & Outlook

Spectral induced polarization method has been used extensively to access indirectly the medium properties as IP effects are closely linked to the textural characteristics of the medium, with originally many applications for mining exploration, but also for hydrological studies, clay characterization and more recently in the expanding domain of the biogeophysics. This thesis work was motivated to improve the inversion procedure of IP parameters of the ground, as classical method uses an extension of electrical resistivity tomography with a direct current hypothesis, that generally does not take into account the presence of EM effects. EM induction arises at increasing frequencies, offsets, conductivities and wire coupling limiting thus the accessible CR spectrum not affected. On the other hand, EM data content is rich of information for the reconstruction of the medium. IP effects are translated as a complex resistivity into the Maxwell's equations, however 3D codes with the capabilities to invert both parameters are rare, or do not take into account explicitly the frequency variation of the CR. Consequently, this work was focused on the implementation of a frequency-dependent CR into a 3D CSEM modelling and inversion code.

Following conclusion of a sensitivity study of CSEM data to IP effects, a multistage workflow was proposed in order to constrain the multiparameter inversion. At first, a stage focused on the inversion of the amplitude data of the electric field is proposed as they are controlled mainly by the CR norm variation and neglecting the weak effect due to the presence of a CR phase. Synthetic inversion examples are demonstrating that this assumption is fully valid at the scale of the field. The second stage of the workflow consists in the inversion of the electric field phase residual remaining in the data, which concentrates the IP effect due to the CR phase. It was shown that using this multistage strategy, the complexity of the inversion was reduced by separating a part of the parameters only and associated to the CR norm or to the CR phase.

A polynomial parametrization of the CR was proposed in order to describe any spectral behaviour and reduce the number of parameters with the increase of frequency considered. Both norm and phase of the CR are described by the coefficients of two independent polynomials. Therefore, no particular model of the CR is assumed in the inversion, which usually hardly link the CR norm variations to the CR phase, as for the popular Cole-Cole or Constant Phase Angle model. In this work 2nd order polynomials were used leading to 3 coefficients to invert per stage. 2nd order polynomials are considered sufficient to describe the CR medium at a field scale considering the many limitations arising, as generally only a limited range of frequencies is available in the field, and/or sensitive to the target of interest considering its depth or CR spectrum[h]. Furthermore, IP effects

---

[h]see figure IV.25 for an attempt to summarize the limitation of the reconstruction of the CR spectrum

are naturally weak compared to EM induction generally reaching barely a few percent of relative error.

A novel CSEM(IP) inversion workflow and parametrization was therefore proposed and applied to various 1D and 3D synthetic dataset. However, IP effects are very small compared to EM effects when considering deeply buried targets. IP effects in CSEM data for anomaly with limited boundaries as the 3D cubes models that were presented are especially weak and close to the numerical accuracy limit. Therefore, there is no place for noisy data, which should be of exceptional quality, with a good processing. Nevertheless, the resulting 3D synthetic inversions allowed the extraction of enough information to discriminate each of the considered targets from the background and through their different spectral behaviours.

At last, applications on real datasets were undertaken with the large 2D CSEM dataset near Schleiz (Germany) shared by the IGM of the University of Cologne and a small scale 3D survey carried out during this thesis work at the former mining site of La Porte-Aux-Moines (Côte-d'Armor). In this part of the work, successful 1D inversions were presented for the Schleiz dataset. Coherent IP anomalies and CR shapes were retrieved. However the 2D geological complexity lead to mono-receiver 1D inversions badly constrained vertically. A 2.5D inversion work based on the 3D code has begun, nevertheless no definitive conclusion was reached in the time frame of the PhD. The PAM survey gathers a dense reception grid over a massive sulphides ore body with 4 illuminations of source. The dataset is of very good quality and presents very large IP evidences. However, some difficulties were encountered, among them the complexity of the geological setting as well as very large resistivity contrasts badly constrained outside the receivers grid (especially under the sources) and a lack of vertical resolution that prevented the inversion to converge correctly to a resistivity model solution explaining correctly the data. An attempt to retrieve the CR norm variation was carried out and lead to promising results. However, the work should be continued to better constrain the source and better weight high frequency data that are relatively poorly fitted. These applications highlight the complexity of the inversion of a CR medium taking EM induction into account as well as IP effects.

This PhD work on 3D CR imaging will finally help to retrieve the spectral behaviour of deeply buried target with a frequency-dependent CR that requires therefore to take into account EM induction to investigate larger offsets. For shallower targets, for which the DC approximation fits usually well, it would help to investigate the CR variations at the highest end of the CSEM frequency window where EM induction arises even at short offset. The developments made during this thesis will contribute to establish a better inversion strategy of EM data to invert EM information as well as IP information, which contains critical information on the medium.

For buried targets, retrieving quantitative information about CR are challenging due to the weak magnitude of IP effects. Nevertheless, the data can be sensitive enough to IP for critical discrimination between different spectral CR behaviours, even at large depths as demonstrated on the cube-cube synthetic model.

For shallow targets, or targets close to the receivers (*i.e.* cross-well measurements), a proper comparison with EM removal techniques should be carried out for performance and

results comparison, as EM induction is less sensitive at short offsets and would contain few additional information of the surrounding medium.

Among outlooks, it can be mentioned that the work can be continued on implementing other parametrization of the CR for comparison purposes and/or to be used when enough constrains are known[i]. Furthermore, the link between field measurements inversion integrating a large volume with partial information and medium properties at smaller scale should be evaluated more closely through downscaling procedures.

Obviously the promising (and challenging) work on the PAM dataset should be continued as well as the work on the 2.5D Schleiz complete dataset which was obtained relatively late during the PhD. Considering the large IP responses observed in the PAM dataset, the acquisition of a second CSEM/ERT survey to complete some data gaps could be justified and considered for a better constrain of the inversion.

The implementation of an iterative solver to reduce the computational requirements for 3D inversions compared to direct solver would be of interest, despite they will reduce the speed of convergence. Indeed, with a direct solver, each inversion required the use of large supercomputers, which can limit the availability of such methods because of the costs of calculation within a project.

Throughout this work the sensitivity limits of CSEM data to IP effects were overviewed on synthetic and field data inversions. In spite of encouraging results, the feasibility of this kind of work should be put in perspective with other common issues encountered in the field with similar or higher sensitivities, as topographic effects, resistivity anisotropy, the presence of conducting pipes, etc...

Indeed, I worked here with isotropic resistivity, however many geological media are anisotropic due to sedimentary beddings and deformation processes, which would have an impact on the data as well as IP. The perspective to mix both in the code formulation in a next step is of high interest, but would make even more complex an inversion procedure.

---

[i]A Cole-Cole parametrization was started to be implemented, but requires a few more developments and testing to be used.

Bibliography

Amestoy, P., Buttari, A., L'Excellent, J.-Y., and Mary, T. (2019). Performance and Scalability of the Block Low-Rank Multifrontal Factorization on Multicore Architectures. *ACM Transactions on Mathematical Software*, 45:2:1–2:26.

Amestoy, P., Duff, I. S., Koster, J., and L'Excellent, J.-Y. (2001). A fully asynchronous multifrontal solver using distributed dynamic scheduling. *SIAM Journal on Matrix Analysis and Applications*, 23(1):15–41.

Archie, G. E. (1942). The electrical resistivity log as an aid in determining some reservoir characteristics. *Transactions of the AIME*, 146(01):54–62.

Armijo, L. (1966). Minimization of functions having lipschitz continuous first partial derivatives. *Pacific Journal of mathematics*, 16(1):1–3.

Atekwana, E. A. and Slater, L. D. (2009). Biogeophysics: A new frontier in earth science research. *Reviews of Geophysics*, 47(4).

Aye, F. (1978). Les gisements à zinc-plomb-cuivre-arget de bodennec et portes-aux-moines. *Chroniques de la Recherche Minières*, (n° 445):1–69.

Aye, F. (1983a). *Contrôles géologiques des gîtes stratiformes de Pb, Zn, Cu, Ag de la bordure du bassin de Châteaulin: Massif armoricain, France: trois exemples types, La Porte aux Moines, Bodennec-Yeun Dong, Menez Albot*, volume 120. Editions du BRGM.

Aye, F. (1983b). Département gites minéraux note n° 954 les gites volcano-sedimentaires du massif armoricain (france). *Département gîtes minéraux*, (Note n° 954):1–42.

Baker, G. S., Jordan, T. E., Pardy, J., et al. (2007). An introduction to ground penetrating radar (gpr). *Special Papers-Geological Society of America*, 432:1.

Bannister, P. R. (1966). Quasi-static fields of dipole antennas at the earth's surface. *Radio science*, 1(11):1321–1332.

Beyer, J. (1977). Telluric and dc resistivity techniques applied to the geophysical investigation of basin and range geothermal systems, part ii: a numberical model study of the dipole-dipole and schlumberger resistivity methods. Technical report.

Binley, A., Slater, L. D., Fukes, M., and Cassiani, G. (2005). Relationship between spectral induced polarization and hydraulic properties of saturated and unsaturated sandstone. *Water Resources Research*, 41(12).

Bleil, D. F. (1953). Induced polarization: A method of geophysical prospecting. *Geophysics*, 18(3):636–661.

Bonnans, J.-F., Gilbert, J. C., Lemaréchal, C., and Sagastizábal, C. A. (2006). *Numerical optimization: theoretical and practical aspects*. Springer Science & Business Media.

Börner, F. (1991). *Investigation of the complex electrical conductivity between 1 mHz and 10 kHz*. PhD thesis, Ph. D. dissertation, Freiberg Mining Academy.

Börner, F., Gruhne, M., and Schön, J. (1993). Contamination indications derived from electrical properties in the low frequency range1. *Geophysical Prospecting*, 41(1):83–98.

Borner, F. D. and Schon, J. H. (1991). A relation between the quadrature component of electrical conductivity and the specific surface area of sedimentary rocks. *The Log Analyst*, 32(05).

Busch, S., van der Kruk, J., Bikowski, J., and Vereecken, H. (2012). Quantitative conductivity and permittivity estimation using full-waveform inversion of on-ground gpr data. *Geophysics*, 77(6):H79–H91.

Börner, F. D., Schopper, J. R., and Weller, A. (1996). Evaluation of transport and storage properties in the soil and groundwater zone from induced polarization measurements1. *Geophysical Prospecting*, 44(4):583–601.

Cagniard, L. (1953). Basic theory of the magneto-telluric method of geophysical prospecting. *Geophysics*, 18(3):605–635.

Chelidze, T. and Gueguen, Y. (1999). Electrical spectroscopy of porous rocks: a review—i. theoretical models. *Geophysical Journal International*, 137(1):1–15.

Clark, D. and Emerson, D. (1991). Notes on rock magnetization characteristics in applied geophysical studies. *Exploration Geophysics*, 22(3):547–555.

Cole, K. S. and Cole, R. H. (1941). Dispersion and Absorption in Dielectrics I. Alternating Current Characteristics. *The Journal of Chemical Physics*, 9(4):341–351.

Commer, M. and Newman, G. A. (2008). New advances in three-dimensional controlled-source electromagnetic inversion. *Geophysical Journal International*, 172(2):513–535.

Commer, M., Newman, G. A., Carazzone, J. J., Dickens, T. A., Green, K. E., Wahrmund, L. A., Willen, D. E., and Shiu, J. (2008). Massively parallel electrical-conductivity imaging of hydrocarbons using the ibm blue gene/l supercomputer. *IBM Journal of Research and Development*, 52(1.2):93–103.

Commer, M., Newman, G. A., Williams, K. H., and Hubbard, S. S. (2011). 3d induced-polarization data inversion for complex resistivity. *Geophysics*, 76(3):F157–F171.

Constable, S. (2010). Ten years of marine CSEM for hydrocarbon exploration. *GEOPHYSICS*, 75(5):75A67–75A81.

Constable, S. C., Parker, R. L., and Constable, C. G. (1987). Occam's inversion: A practical algorithm for generating smooth models from electromagnetic sounding data. *Geophysics*, 52(3):289–300.

Dai, Y.-H. (2002). On the nonmonotone line search. *Journal of Optimization Theory and Applications*, 112(2):315–330.

Davidson, D. W. and Cole, R. H. (1951). Dielectric relaxation in glycerol, propylene glycol, and n-propanol. *The Journal of Chemical Physics*, 19(12):1484–1490.

De Boor, C. and De Boor, C. (1978). *A practical guide to splines*, volume 27. springer-verlag New York.

Debye, P. (1929). Polar molecules, the chemical catalog company. *Inc., New York*, pages 77–108.

Dias, C. A. (1968). *A NON-GROUNDED METHOD FOR MEASURING ELECTRI-CALLY INDUCED POLARIZATION ANDCONDUCTIVITY*. PhD thesis, University of California, Berkeley.

Dias, C. A. (1972). Analytical model for a polarizable medium at radio and lower frequencies. *Journal of Geophysical Research*, 77(26):4945–4956.

Dias, C. A. (2000). Developments in a model to describe low-frequency electrical polarization of rocks. *Geophysics*, 65(2):437–451.

Egbert, G. D. and Booker, J. R. (1986). Robust estimation of geomagnetic transfer functions. *Geophysical Journal International*, 87(1):173–194.

Fiandaca, G., Madsen, L. M., and Maurya, P. K. (2018). Re-parameterisations of the cole–cole model for improved spectral inversion of induced polarization data. *Near Surface Geophysics*, 16(4):385–399.

Ghorbani, A. (2007). *Contribution au développement de la résistivité complexe et à ses applications en environnement*. PhD thesis, Université Pierre-et-Marie-Curie, Paris (France).

Ghorbani, A., Cosenza, P., Revil, A., Zamora, M., Schmutz, M., Florsch, N., and Jougnot, D. (2009). Non-invasive monitoring of water content and textural changes in clay-rocks using spectral induced polarization: A laboratory investigation. *Applied Clay Science*, 43(3-4):493–502.

Grayver, A. V., Streich, R., and Ritter, O. (2013). Three-dimensional parallel distributed inversion of CSEM data using a direct forward solver. *Geophysical Journal International*, 193(3):1432–1446.

Gupta, A. (2000). Wsmp: Watson sparse matrix package (part-i: direct solution of symmetric sparse systems). *IBM TJ Watson Research Center, Yorktown Heights, NY, Tech. Rep. RC*, 21886.

Haber, E., Ascher, U., Aruliah, D., and Oldenburg, D. (2000). Fast simulation of 3d electromagnetic problems using potentials. *Journal of Computational Physics*, 163(1):150–171.

Hallof, P. and Klein, J. (1983). Characterization of electrical properties of metallic mineral deposits. *Ontario Geological Survey Open File Report*, 5468.

Hördt, A., Blaschek, R., Kemna, A., and Zisser, N. (2007). Hydraulic conductivity estimation from induced polarisation data at the field scale—the krauthausen case history. *Journal of Applied Geophysics*, 62(1):33–46.

Ingeman-Nielsen, T. and Baumgartner, F. (2006). Numerical modelling of complex resistivity effects on a homogeneous half-space at low frequencies. *Geophysical Prospecting*, 54(3):261–271.

Iwamoto, M. and Bhushan, B. (2012). Maxwell–wagner effect. *Encyclopedia of nanotechnology*, pages 1–276.

Jiracek, G. R. (1990). Near-surface and topographic distortions in electromagnetic induction. *Surveys in Geophysics*, 11(2):163–203.

Jonscher, A. K. (1977). The 'universal'dielectric response. *nature*, 267(5613):673–679.

Kang, S. and Oldenburg, D. (2017). Tem-ip: extracting more induced polarisation information from grounded source time domain electromagnetic data. *Geophysical Prospecting*.

Keller, G. (1959). Analysis of some electrical transient measurements on igneous, sedimentary and metamorphic rocks. *Overvoltage research and geophysical applications*.

Kemna, A. (2000). *Tomographic inversion of complex resistivity*. PhD thesis, Ruhr-Universität Bochum.

Kemna, A., Binley, A., Cassiani, G., Niederleithinger, E., Revil, A., Slater, L., Williams, K. H., Orozco, A. F., Haegel, F.-H., Hördt, A., et al. (2012). An overview of the spectral induced polarization method for near-surface applications. *Near Surface Geophysics*, 10(6):453–468.

Kemna, A., Binley, A., and Slater, L. (2004). Crosshole ip imaging for engineering and environmental applications. *Geophysics*, 69(1):97–107.

Kessouri, P., Furman, A., Huisman, J. A., Martin, T., Mellage, A., Ntarlagiannis, D., Bücker, M., Ehosioke, S., Fernandez, P., Flores-Orozco, A., Kemna, A., Nguyen, F., Pilawski, T., Saneiyan, S., Schmutz, M., Schwartz, N., Weigand, M., Wu, Y., Zhang, C., and Placencia-Gomez, E. (2019). Induced polarization applied to biogeophysics: recent advances and future prospects. *Near Surface Geophysics*, 17(6):595–621.

Key, K. (2016). MARE2DEM: a 2-D inversion code for controlled-source electromagnetic and magnetotelluric data. *Geophysical Journal International*, 207(1):571–588.

Kim, H. J., Song, Y., and Lee, K. H. (1997). High-frequency electromagnetic inversion for a dispersive layered earth. *Journal of geomagnetism and geoelectricity*, 49(11-12):1439–1450.

Kruschwitz, S., Binley, A., Lesmes, D., and Elshenawy, A. (2010). Textural controls on low-frequency electrical spectra of porous media. *Geophysics*, 75(4):WA113–WA123.

Lavoué, F., Brossier, R., Métivier, L., Garambois, S., and Virieux, J. (2014). Two-dimensional permittivity and conductivity imaging by full waveform inversion of multioffset gpr data: A frequency-domain quasi-newton approach. *Geophysical Journal International*, 197(1):248–268.

Le Masne, D., Lesage, P., and Millon, R. (1980). Expérimentation par la méthode de polarisation provoquéespectrale sur le prospect de la-porte-aux-moines (cotes-du-nord). Technical report, BRGM80–SGN–740–GPH.

Lee, K. H., Jang, H., Jang, H., and Kim, H. J. (2011). Sensitivity analysis of marine controlled-source electromagnetic methods to a shallow gas-hydrate layer with 1d forward modeling. *Geosciences Journal*, 15(3):297–303.

Lelièvre, P. G. (2003). *Forward modelling and inversion of geophysical magnetic data.* PhD thesis, University of British Columbia.

Leroy, P. and Revil, A. (2009). A mechanistic model for the spectral induced polarization of clay materials. *Journal of Geophysical Research: Solid Earth*, 114(B10).

Leroy, P., Revil, A., Kemna, A., Cosenza, P., and Ghorbani, A. (2008). Complex conductivity of water-saturated packs of glass beads. *Journal of Colloid and Interface Science*, 321(1):103–117.

Lesmes, D. P. and Frye, K. M. (2001). Influence of pore fluid chemistry on the complex conductivity and induced polarization responses of berea sandstone. *Journal of Geophysical Research: Solid Earth*, 106(B3):4079–4090.

Lesmes, D. P. and Morgan, F. D. (2001). Dielectric spectroscopy of sedimentary rocks. *Journal of Geophysical Research: Solid Earth*, 106(B7):13329–13346.

Liu, M., Yang, J., Feng, J., Wang, T., and Zhang, H. (2016). A discussion on the performance of seven existing models proposed to describe induced polarizationIP models and analog computation. *Geophysics*, 81(6):E459–E469.

MacLennan, K., Karaoulis, M., and Revil, A. (2014). Complex conductivity tomography using low-frequency crosswell electromagnetic data. *Geophysics*, 79(1):E23–E38.

Madden, T. R. and Cantwell, T. (1967). Part d. induced polarization, a review. In *Mining Geophysics, Volume II, Theory*, pages 373–400. Society of Exploration Geophysicists.

Marshall, D. J. and Madden, T. R. (1959). Induced polarization, a study of its causes. *Geophysics*, 24(4):790–816.

Martin, T., Orozco, A. F., Günther, T., and Dahlin, T. (2018). Comparison of tdip and sip measurements in the field scale. In *5th International Workshop on Induced Polarization*.

Maurya, P., Fiandaca, G., Christiansen, A., and Auken, E. (2018a). Field-scale comparison of frequency-and time-domain spectral induced polarization. *Geophysical Journal International*, 214(2):1441–1466.

Maurya, P. K., Balbarini, N., Møller, I., Rønde, V., Christiansen, A., Bjerg, P. L., Auken, E., and Fiandaca, G. (2018b). Subsurface imaging of water electrical conductivity, hydraulic permeability and lithology at contaminated sites by induced polarization. *Geophysical Journal International*, 213(2):770–785.

Menke, W. (1984). 3 - solution of the linear, gaussian inverse problem, viewpoint 1: The length method. In Menke, W., editor, *Geophysical Data Analysis: Discrete Inverse Theory*, pages 35–60. Academic Press.

Métivier, L. and Brossier, R. (2016). The seiscope optimization toolbox: A large-scale nonlinear optimization library based on reverse communicationthe seiscope optimization toolbox. *Geophysics*, 81(2):F1–F15.

Mörbe, W., Yogeshwar, P., Tezkan, B., and Hanstein, T. (2020). Deep exploration using long-offset transient electromagnetics: interpretation of field data in time and frequency domain. *Geophysical Prospecting*, 68(6):1980–1998.

Nabighian, M. N. (1988). *Electromagnetic Methods in Applied Geophysics: Voume 1, Theory*. Society of Exploration Geophysicists.

Newman, G. A. and Alumbaugh, D. L. (1995). Frequency-domain modelling of airborne electromagnetic responses using staggered finite differences1. *Geophysical Prospecting*, 43(8):1021–1042.

Nocedal, J. and Wright, S. (2006). *Numerical optimization*. Springer Science & Business Media.

Okay, G. (2011). Caractérisation des hétérogénéités texturales et hydriques des géomatériaux argileux par la méthode de polarisation provoquée: application à l'edz de la station expérimentale de tournemire. *Ph.D. Thesis*.

Okay, G., Leroy, P., Ghorbani, A., Cosenza, P., Camerlynck, C., Cabrera, J., Florsch, N., and Revil, A. (2014). Spectral induced polarization of clay-sand mixtures: Experiments and modeling. *Geophysics*, 79(6):E353–E375.

Olhoeft, G. (1985). Low-frequency electrical properties. *Geophysics*, 50(12):2492–2503.

Operto, S., Gholami, Y., Prieux, V., Ribodetti, A., Brossier, R., Metivier, L., and Virieux, J. (2013). A guided tour of multiparameter full-waveform inversion with multicomponent data: From theory to practice. *The leading edge*, 32(9):1040–1054.

Paige, C. C. and Saunders, M. A. (1982). Algorithm 583: Lsqr: Sparse linear equations and least squares problems. *ACM Transactions on Mathematical Software (TOMS)*, 8(2):195–209.

Palacky, G. (1988). Resistivity characteristics of geologic targets. *Electromagnetic methods in applied geophysics*, 1:53–129.

Pelton, W. (1983). Interpretation of complex resistivity and dielectric data: Part i. *Geophys. trans.*, 29:297–330.

Pelton, W. H., Ward, S. H., Hallof, P. G., Sill, W. R., and Nelson, P. H. (1978). Mineral discrimination and removal of inductive coupling with multifrequency IP. *Geophysics*, 43(3):588–609.

Plessix, R.-E. (2006). A review of the adjoint-state method for computing the gradient of a functional with geophysical applications. *Geophysical Journal International*, 167(2):495–503.

Plessix, R.-E., Darnet, M., and Mulder, W. (2007). An approach for 3d multisource, multifrequency csem modeling. *Geophysics*, 72(5):SM177–SM184.

Plessix, R.-E. and Mulder, W. (2008). Resistivity imaging with controlled-source electromagnetic data: depth and data weighting. *Inverse problems*, 24(3):034012.

Pratt, R. G., Shin, C., and Hick, G. (1998). Gauss–newton and full newton methods in frequency–space seismic waveform inversion. *Geophysical journal international*, 133(2):341–362.

Qi, Y., El-Kaliouby, H., Revil, A., Soueid Ahmed, A., Ghorbani, A., and Li, J. (2019). Three-dimensional modeling of frequency-and time-domain electromagnetic methods with induced polarization effects. *Computers & geosciences*.

Revil, A. (2012). Spectral induced polarization of shaly sands: Influence of the electrical double layer. *Water Resources Research*, 48(2).

Revil, A. (2013). Effective conductivity and permittivity of unsaturated porous materials in the frequency range 1 mhz–1ghz. *Water resources research*, 49(1):306–327.

Revil, A. and Cosenza, P. (2010). Comment on "generalized effective-medium theory of induced polarization". *Geophysics*, 75(2):X7–X9.

Revil, A. and Florsch, N. (2010). Determination of permeability from spectral induced polarization in granular media. *Geophysical Journal International*, 181(3):1480–1498.

Revil, A., Florsch, N., and Mao, D. (2015). Induced polarization response of porous media with metallic particles—part 1: A theory for disseminated semiconductors. *Geophysics*, 80(5):D525–D538.

Revil, A., Qi, Y., Ghorbani, A., Coperey, A., Ahmed, A. S., Finizola, A., and Ricci, T. (2019). Induced polarization of volcanic rocks. 3. imaging clay cap properties in geothermal fields. *Geophysical Journal International*, 218(2):1398–1427.

Routh, P. S. and Oldenburg, D. W. (2001). Electromagnetic coupling in frequency-domain induced polarization data: A method for removal. *Geophysical Journal International*, 145(1):59–76.

Samouëlian, A., Cousin, I., Tabbagh, A., Bruand, A., and Richard, G. (2005). Electrical resistivity survey in soil science: a review. *Soil and Tillage research*, 83(2):173–193.

Schlumberger, C. (1920). *Etude sur la prospection electrique du sous-sol.* Gauthier-Villars.

Schwarz, G. (1962). A theory of the low-frequency dielectric dispersion of colloidal particles in electrolyte solution1, 2. *The Journal of Physical Chemistry*, 66(12):2636–2642.

Seidel, K. and Lange, G. (2007). Direct current resistivity methods. In *Environmental geology*, pages 205–237. Springer.

Seigel, H., Nabighian, M., Parasnis, D. S., and Vozoff, K. (2007). The early history of the induced polarization method. *The Leading Edge*, 26(3):312–321.

Seigel, H. O. (1949). *Theoretical and experimental investigation into the application of the phenomenon of overvoltage to geophysical prospecting.* PhD thesis, University of Toronto.

Seigel, H. O. (1959). MATHEMATICAL FORMULATION AND TYPE CURVES FOR INDUCED POLARIZATION. *GEOPHYSICS*, 24(3):547–565.

Shantsev, D. V. and Maaø, F. A. (2015). Rigorous interpolation near tilted interfaces in 3-d finite-difference em modelling. *Geophysical Journal International*, 200(2):745–757.

Slater, L. D. and Lesmes, D. (2002). Ip interpretation in environmental investigations. *Geophysics*, 67(1):77–88.

Smirnova, M. V., Becken, M., Nittinger, C., Yogeshwar, P., Mörbe, W., Rochlitz, R., Steuer, A., Costabel, S., Smirnov, M. Y., and Group, D. W. (2019). A novel semiairborne frequency-domain controlled-source electromagnetic system: Three-dimensional inversion of semiairborne data from the flight experiment over an ancient mining area near schleiz, germany. *Geophysics*, 84(5):E281–E292.

Song, Y., Kim, H. J., and Lee, K. H. (2002). An integral equation representation of wide-band electromagnetic scattering by thin sheets. *Geophysics*, 67(3):746–754.

Sternberg, B. K. (1991). A review of some experience with the induced-polarization/resistivity method for hydrocarbon surveys: Successes and limitations. *Geophysics*, 56(10):1522–1532.

Streich, R. (2009). 3d finite-difference frequency-domain modeling of controlled-source electromagnetic data: Direct solution and optimization for high accuracy. *Geophysics*, 74(5):F95–F105.

Sumner, J. S. (1984). *Principles of induced polarization for geophysical exploration*. Elsevier.

Tarantola, A. (2005). *Inverse problem theory and methods for model parameter estimation*. SIAM.

Tarantola, A. and Valette, B. (1982). Generalized nonlinear inverse problems solved using the least squares criterion. *Reviews of Geophysics*, 20(2):219–232.

Tarasov, A. and Titov, K. (2013). On the use of the cole–cole equations in spectral induced polarization. *Geophysical Journal International*, 195(1):352–356.

Vacquier, V., Holmes, C. R., Kintzinger, P. R., and Lavergne, M. (1957). Prospecting for ground water by induced electrical polarization. *Geophysics*, 22(3):660–687.

Vaillant, F. (1978). Expérimentation par la méthode de polarisation provoquéespectrale sur le prospect de la-porte-aux-moines (cotes-du-nord). Technical report, BRGM78–SGN–713–GPH.

Vanhala, H. (1997). Mapping Oil-Contaminated Sand and Till with the Spectral Induced Polarization (sip) Method. *Geophysical Prospecting*, 45(2):303–326.

Vinegar, H. and Waxman, M. (1984). Induced polarization of shaly sands. *Geophysics*, 49(8):1267–1287.

Virieux, J. and Operto, S. (2009). An overview of full-waveform inversion in exploration geophysics. *Geophysics*, 74(6):WCC1–WCC26.

Wait, J. R. (1951). The magnetic dipole over the horizontally stratified earth. *Canadian Journal of Physics*, 29(6):577–592.

Wait, J. R. (1959). *Overvoltage Research and Geophysical Applications: International Series of Monographs on Earth Sciences*. Pergamon Press.

Wait, J. R. (1961). The electromagnetic fields of a horizontal dipole in the presence of a conducting half-space. *Canadian Journal of Physics*, 39(7):1017–1028.

Ward, S. and Fraser, D. (1967). Part b—conduction of electricity in rocks. In *Mining Geophysics, Volume II, Theory*, pages 197–223. Society of Exploration Geophysicists.

Ward, S. H. (1988). The resistivity and induced polarization methods. In *1st EEGS Symposium on the Application of Geophysics to Engineering and Environmental Problems*, pages cp–214. European Association of Geoscientists & Engineers.

Waxman, M. H. and Smits, L. (1968). Electrical conductivities in oil-bearing shaly sands. *Society of Petroleum Engineers Journal*, 8(02):107–122.

Weiss, C. J. and Constable, S. (2006). Mapping thin resistors and hydrocarbons with marine em methods, part ii—modeling and analysis in 3d. *Geophysics*, 71(6):G321–G332.

Weller, A., Seichter, M., and Kampke, A. (1996). Induced-polarization modelling using complex electrical conductivities. *Geophysical Journal International*, 127(2):387–398.

Weller, A., Slater, L., Binley, A., Nordsiek, S., and Xu, S. (2015). Permeability prediction based on induced polarization: Insights from measurements on sandstone and unconsolidated samples spanning a wide permeability range. *Geophysics*, 80(2):D161–D173.

Wolfe, P. (1969). Convergence conditions for ascent methods. *SIAM review*, 11(2):226–235.

Wong, J. (1979). An electrochemical model of the induced-polarization phenomenon in disseminated sulfide ores. *Geophysics*, 44(7):1245–1265.

Yee, K. (1966). Numerical solution of initial boundary value problems involving maxwell's equations in isotropic media. *IEEE Transactions on antennas and propagation*, 14(3):302–307.

Zhdanov, M. (2008). Generalized effective-medium theory of induced polarization. *Geophysics*, 73(5):F197–F211.

Zhdanov, M., Endo, M., Cox, L., and Sunwall, D. (2018). Effective-medium inversion of induced polarization data for mineral exploration and mineral discrimination: Case study for the copper deposit in Mongolia. *Minerals*, 8(2):68.

Zhdanov, M. S. (2009). New advances in regularized inversion of gravity and electromagnetic data. *Geophysical Prospecting*, 57(4):463–478.

Zhengwei Xu and Zhdanov, M. S. (2015). Three-Dimensional Cole-Cole Model Inversion of Induced Polarization Data Based on Regularized Conjugate Gradient Method. *IEEE Geoscience and Remote Sensing Letters*, 12(6):1180–1184.

Zonge, K. L. and Hughes, L. J. (1991). Controlled source audio-frequency magnetotellurics. In *Electromagnetic Methods in Applied Geophysics: Volume 2, Application, Parts A and B*, pages 713–810.

Appendices

Appendix A

A.1 Error estimation

Error estimation on the result of the inversion was calculated using a weighted root mean square deviation:

$$rms = \sqrt{\frac{(\delta_d W_d)^\dagger W_d \delta_d}{N_d}} \tag{A.1}$$

vector W_d is defined as the inverse of the data standard deviation. For synthetic data, standard deviation is defined according to a relative error r :

$$W_d^{linear} = 1/\sigma \qquad \text{with } \sigma \text{ the standard deviation} \tag{A.2}$$

$$W_d^{linear} = \frac{1}{|d_{obs}|r} \qquad \text{with r the relative error} \tag{A.3}$$

As we are using the logarithm of the data (logarithm of the amplitude of the considered EM field and its phase) the standard deviation had to be converted to its log equivalent. The variance and standard deviation of an observed data in logarithm can be written according to its relative error as :

$$
\begin{aligned}
\sigma_{log}^2 &= (log(d_{obs} + rd_{obs}) - log(d_{obs}))^2 \\
\sigma_{log}^2 &= log\left(\frac{d_{obs} + rd_{obs}}{d_{obs}}\right)^2 \\
\sigma_{log} &= log(1 + r)
\end{aligned}
\tag{A.4}
$$

A relation independent of the magnitude of the data is obtained. The covariance matrix for logarithmic data is thus written as :

$$W_d^{log} = \frac{1}{log(1 + r)} \simeq \frac{1}{r} \qquad \text{for small variation} \tag{A.5}$$

By using a relative error representing 1% of the total field amplitude for rms calculation, the weighted rms can be seen as a percentage of variation of the data fit. Relative errors are thus estimated for a component of the field E^k (k, being the X or Y component of the field) in comparison to the total field E^{tot} then $r_{1\%} = \frac{0.01|E^{tot}|}{|E^k|}$. $r_{1\%}$ is then the value used in equation (A.4) for covariance calculation.

A.2   PAM CSEM schedule

	Lundi		Mardi	Mercredi	Jeudi	Vendredi	Samedi
	TEAM IPGS	BRGM	*	*	*	*	
08:00	Déplacement Strasbourg -> Saint-Brieuc	Déplacement Orléans -> PAM	inst. RAU #1 / inst. TX11, TX12	Inj. TX12	Dépl. RAU#1 --> RAU#2	Dépl. RAU#2 --> RAU#3	Retour BRGM / Strasbourg
09:00							
10:00							
11:00				Inj. TX3			
12:00							
13:00			Tests TIP	Inj. TX21	Inj. TX11, TX12, TX3, TX21	Inj. TX11, TX12, TX3, TX21	
14:00			Inj. TX11 / inst. TX3, TX21				
15:00		Repérage / implantation		Dépl. RAU#1 --> RAU#2			
16:00						Démobilisation	
17:00			Test Zonge GGT3 (RIP)		Dépl. RAU#2 --> RAU#3		
18:00							

Figure A.1: *Approximated schedule of the PAM mission*

A.3   Depth Scaling (MS) and Module Scaling (MS)

Depth scaling:
The depth scaling is a preconditioner of the inverse problem that compensates for the loss of sensitivity with depth of EM inversion. It is a linear operator associated to a change of variable using a diagonal matrix W_{DS} with scaling coefficients. The change of variable is applied as follow:

$$m_{scaled} = W_{DS}^{-1}m, \tag{A.6}$$

It is thus is applied to each line of the Fréchet derivatives or to the gradient of the misfit function with:

$$F_{scaled}(m) = W_{DS}F(m), \tag{A.7}$$

The depth scaling function is:

$$W_{DS}(z) = \frac{1}{((z-z_0)^\gamma e^{-\beta\frac{z-z_0}{\delta}} + \epsilon)} + \epsilon \tag{A.8}$$

δ controls the power of the exponential scaling. It should be chosen of the order of magnitude of the average skin depth to compensate the exponential decrease of sensitivity with depth. Because such a function would amplify the effect of noise for larger depth, a depth window is add by multiplying the depth scaling function A.8 by two cosine taper functions controlled by 4 depths.

Module scaling:
In a similar way as the depth scaling, a scaling of the model and the sensitivity can be applied according to an arbitrary external function. The idea is to use for this scaling a function based on the module of the electric field computed for a reference model at an average frequency. The function is damped to avoid increasing too much the sensitivity far from the source or at large depth. The scaling function is thus:

$$W_{MS}(z) = \frac{1}{|E_0| + \epsilon} \tag{A.9}$$

with $|E_0|$ the module and $\epsilon = 0.01 \max |E_0|$.

Because of the high value of ϵ, this scaling function has mostly an effect on reducing sensitivity close to the transmitter, so it can be combined with the depth scaling.

A.4 Sequences Waveforms PAM

Seq. #	Square (s)	Waveform	T0 (s)	f0 (Hz)	Record time (mn)	Nstack
1	4	"Sqx32"	128	0.0078	25	10
2	10	Sq. 50% Duty cycle	40	0.025	15	20
3	5	Sq	10	0.1	20	100
4	1	Sq	2	0.5	5	150
5	0.25	Sq	0.5	2	5	600

Figure A.2: *Fundamental injection sequences used at the PAM survey ranging from 128 seconds to 2 Hz. A square wave (Sq) was used for sequences 3 to 5; a 50 % duty cycle square wave was used for sequence 2 and the lowest frequency was reached using an atypical wave composed of 8 positive squares with zero passages followed by 8 negative squares with a square of 4 seconds. This waveform was called "Sqx32" as the square duration is multiplied by 32 to obtain the fundamental period $T_{square} \times [8\,squares \times 2\,polarities(+/-) \times 2\,(50\%DC)]$.*

Note that higher injection frequencies at PAM survey were not possible due to the TIP transmitter limitation floored to a 2 Hz signal. However, square signals are used (or with a 50% duty cycle) allowing to take advantages of each odd harmonics of the square wave spectral content. Furthermore, the TIP is also limited at low frequency to 10 seconds square signals (here it refers to the duration of a positive square $T_{square} = 10s = T_0/2$ and thus a half period, T_0 being the fundamental period). For the second injection sequence, this period limit was increased using a conventional 50% duty cycle square signal reaching thus a period of 40 seconds. In order to improve even more this limit and reach a 100 seconds period as ideally planned, a functionality of the TIP was tested and adopted on the field, allowing a waveform with a 16 "bits" $(+/-)$ pattern. This waveform is thus composed of "bits" of positive and negative *"units"* of signal. Therefore, based on a square signal with 50% duty cycle, a signal based on 8 consecutive positive bits followed by 8 negatives bits was set. It has the effect of creating a signal with a fundamental period of 32 times the square duration. This waveform is presented in figure A.3. Using this waveform pattern, the TIP limitation could be pushed up to a period of 320 seconds. In our case, we limited the lowest period to 128 seconds with $T_{square} = 4\,s$.
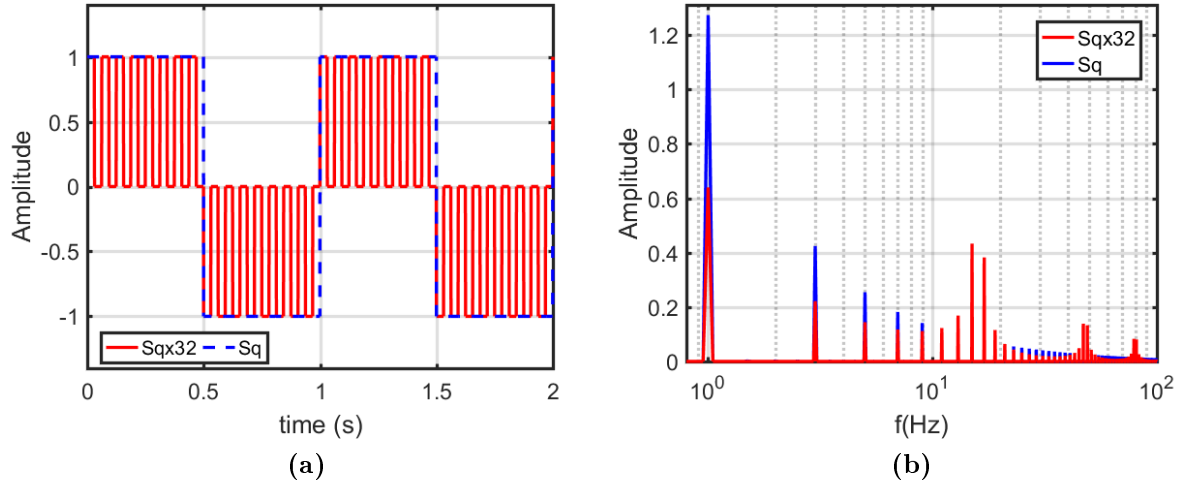
(a)   (b)

Figure A.3: *Presentation of the "Sqx32" waveform designed to reach the lowest frequencies with the TIP transmitter limited to 10 seconds square signal. Left: time series of the "Sqx32" waveform (red) build from a square of duration $T_{square} = \frac{1}{32}s$ plotted beside a 1 Hz square wave; right: corresponding spectrum after Fourier transform. Such an atypical wave has for effect to distribute the energy of firsts harmonics on higher harmonics concentrated around $n(2/T_{square})\,Hz$ (n being an odd positive number).*

A.5   Phase Data fit PAM

(a)

(b)

(c)
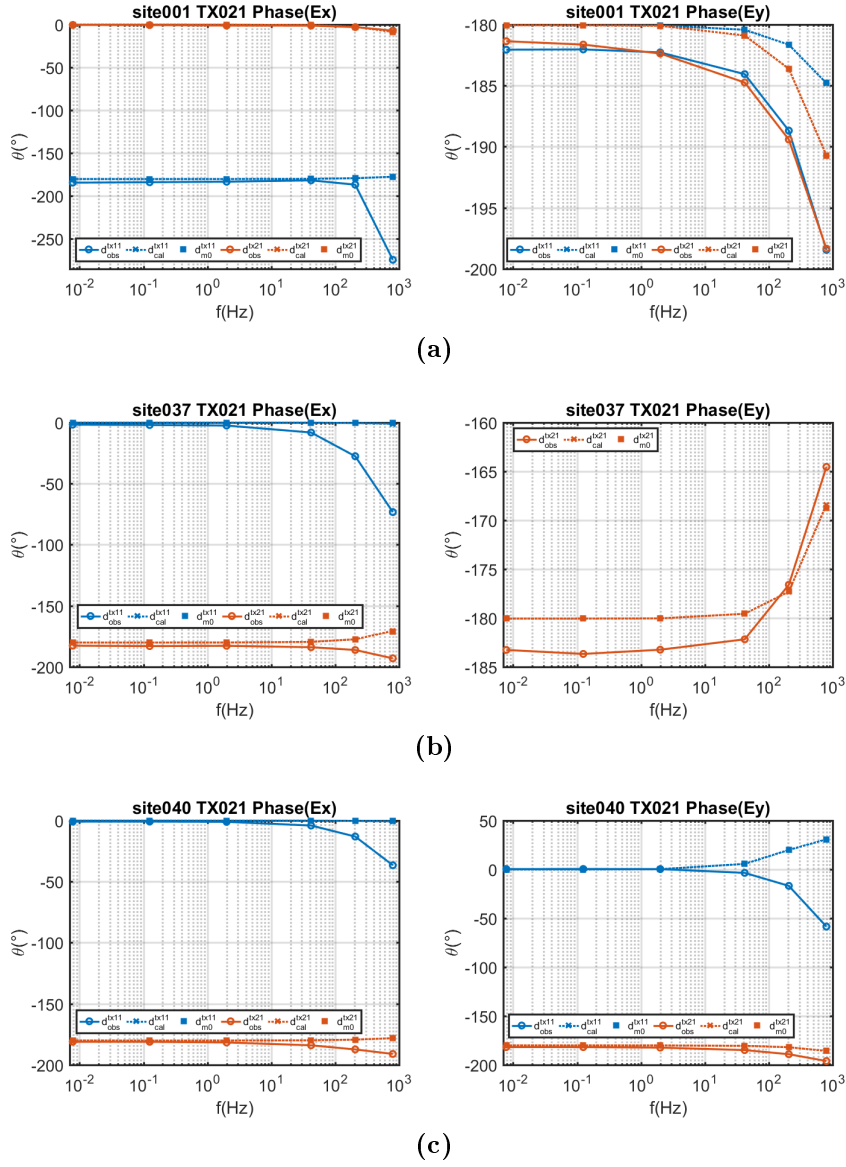
Figure A.4: *Examples of electric field phase fits at the end of stage 1 for RX01, RX37 and RX40. m0 refers to the starting model data at stage 1, i.e the fit at the end of stage 0*
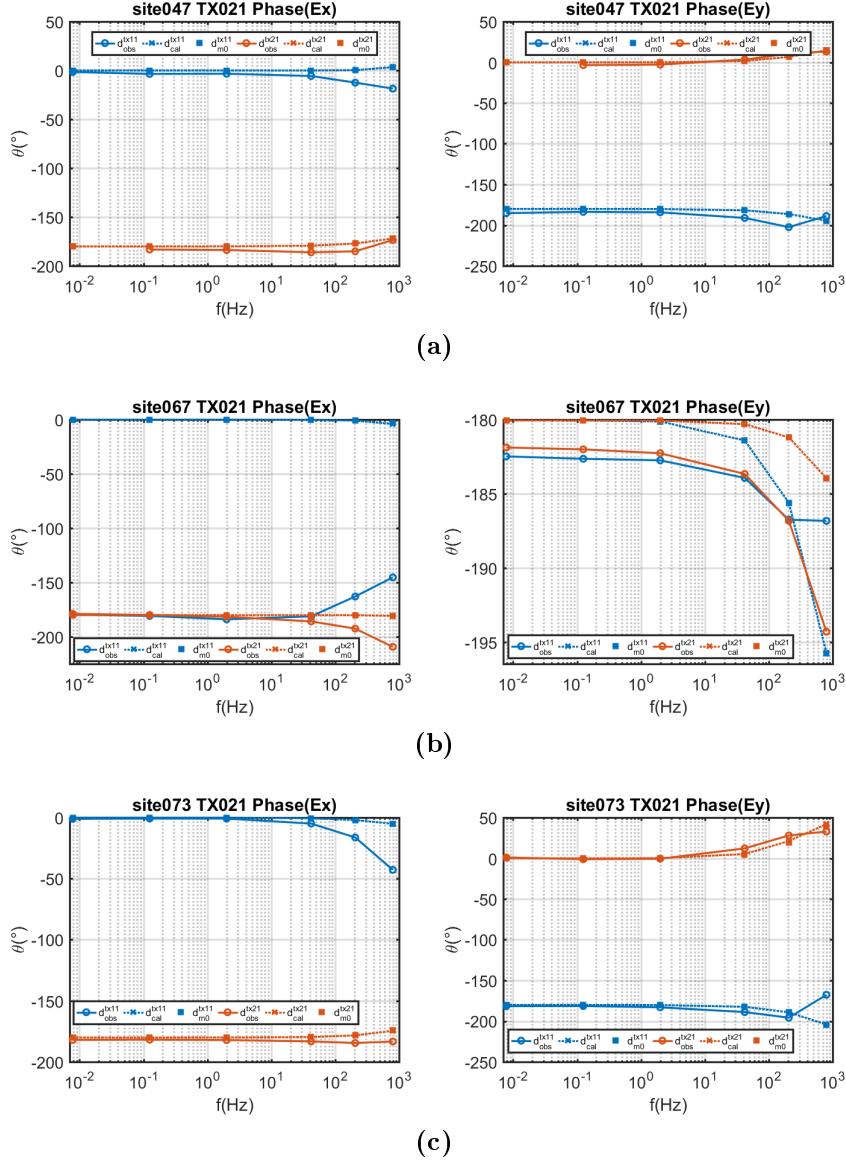
(a)

(b)

(c)

Figure A.5: *Examples of electric field phase fits at the end of stage 1 for RX47, RX67 and RX73. m0 refers to the starting model data at stage 1, i.e the fit at the end of stage 0*

Appendix B

<div align="right">

APPENDIX B

</div>

Appendix B: Ringlebach article

B.1 Ringlebach article

A supplementary work during the early stages of this thesis was to continue my work related to a CSEM survey data inversion within the framework of the ANR *CANTARE* project, that I carried out during my former master degree internship at BRGM. The project dealt with a multi-scale and multi-disciplinary approach to increase our knowledge of the deep transition zone between the sedimentary cover and the basement of sedimentary basin as the Rhine graben, which is of high interest for the exploitation of high temperatures geothermal resources as demonstrated by some pilot geothermal plants in Alsace (Soultz-Sous-Forêts, Ritthershoffen). However accessing to this area remains challenging because of the very deep context around 4 to 5 km, with a crucial need to estimate the high fluid content and permeable zones of the medium for a successful geothermal exploitation. Therefore, a good characterization of such targets coupled to reliable geophysical methods able to detect permeable areas with high fluid content are necessary.

Within this framework, a geophysical study was performed on an analogue of the transition zone at the Ringelbach catchment basin area (Soultzeren village), on the flank of the Rhine graben in the Vosges Mountain. Several geophysical methods were carried out to characterize electrical and seismic properties of the transition zone, including a CSEM survey which was originally the subject of my MSc in geophysics engineering internship. I participated to the CSEM survey in July 2017 and in the following seismic and MT survey of 2018. I processed and inverted the CSEM data in 2.5D using Mare2dem (Key, 2016) and participated to the 3D inversions using Polyem3D code. I participated to the general interpretations as well as the discussions about the results.

These works lead to a general publication in which I am co-author and that was recently accepted in *Geothermics* journal (02/09/21) with minor corrections. The preprint of this article is presented in the following appendix as it is related to resistivity imaging and CSEM method.

Geophysical signature of the transition zone between the sedimentary cover and the basement from an analogue of the Rhine Graben

F. Bretaudeau[a], M. Darnet[a], J. Porté[a,b], C. Lerouge[a], S. Neeb[a], J.F. Girard[b], J.M. Baltassat[a], N. Coppo[a], Y. Lucas[c], C. Dezayes[a]

[a]*BRGM, Orléans, FRANCE*
[b]*EOST-IPGS, Strasbourg University, FRANCE*
[c]*EOST-LHyGeS, Strasbourg University, FRANCE*

Abstract

Exploiting high temperatures geothermal resources in sedimentary and basement rocks, rifts or flexural basins to produce electricity is now possible because of the development of Enhanced Geothermal System (EGS) technology. However it remains challenging because the presence of fluid and permeability at 4-5km depth is necessary. A multi-scale and multi-disciplinary approach to increase our knowledge of the transition zone between the sedimentary cover and the basement have been undertaken to provide fundamental knowledge for the assessment of its geothermal potential. In this paper, we report out the results of a study performed on an exhumed transition zone in the Ringelbach area in the Vosges Mountain, on the flank of the Rhine graben. In this analogue of a deeply buried transition zone of the Rhine Graben, a thin layer of Permian sandstones is still present on the top of the fractured and altered granitic basement providing the unique opportunity to study in-situ the physical properties of this transition zone. We focused here on electrical and seismic properties of the transition zone as they are the main physical parameters usually assessed with the help of geophysical methods during the exploration phase of a geothermal project.

We show that altered porous and potentially permeable granite targeted in deep geothermal exploration has a clear signature on both electrical conductivity and seismic measurements that can be measured at core scale, borehole scale, and

are still visible with surface geophysical methods such as refraction and reflection seismic and Controlled Source Electromagnetism at a few hundred meter depth. The results suggest that best discrimination between permeable and non permeable rocks may be provided by the joint interpretation of both resistivity and seismic velocities.

1. Introduction

Exploiting geothermal resources at temperatures between 120 and 200℃ in sedimentary and basement rocks, in rifts or in flexural basins, to produce electricity is now possible because of the development of Enhanced Geothermal

5   System (EGS) technology. Reaching such temperature range is a major challenge for mainland France and Europe as it usually requires drilling up to 4 to 6 km depth. Aside from temperature, two other conditions are required to allow the exploitation of the geothermal energy: the presence of fluid, which is the heat vector, and sufficient permeability to allow the production and re-injection

10   of the fluid. This translates into the reservoir being located in the deep layers of sedimentary basins and the upper part of the Paleozoic basement, including the transition zone between the two.

The reality is however even more complex as the geothermal potential of this zone is also strongly influenced by large heterogeneities comprising 1) the lithol-

15   ogy/mineralogy of the cover/basement, 2) the internal architecture of the transition zone, 3) the anisotropic or heterogeneous cooling history of the batholith, degree of paleoalteration, and evolution of hydrothermalism and 4) the presence of natural faults and fracture networks above and below the transition zone. It is therefore clear that the characterization of the transition zone and its het-

20   erogeneity in the deeper part of sedimentary basins constitutes one of the most challenging problems for the development of geothermal resources.

Geophysical prospection methods such as 3D seismic reflexion [1, 2] and Mag-

netotellurics [3, 4] or Controlled-Source Electromagnetics [5, 6, 7] are commonly used to provide both structural and physical information at several kilometers depth. Those methods should help identifying favorable areas and de-risking geothermal projects. However, it is not clear yet what would be the geophysical signature of the most permeable areas of the transition zone in terms of seismic or electrical properties.

We have undertaken a multi-scale and multi-disciplinary approach to increase our knowledge of this transition zone between the sedimentary cover and the basement and provide fundamental knowledge for the assessment of its geothermal potential. In this paper, we report out the results of a geophysical study performed in the Ringelbach site on an exhumed transition zone in the Vosges Mountain, on the flank of the Rhine graben. We focused on electrical and seismic properties of the transition zone as they are the main physical parameters usually assessed with the help of geophysical methods during the exploration phase of a geothermal project. We describe in a first part the Ringlebach analogue site, then present both seismic and electrical resistivity measurements collected at core scale, from borehole data, and then at the field scale. We finally discuss how those result may be extrapolated at larger depth.

2. Geological setting

Since 1975, the Ringelbach catchment has been the subject of interdisciplinary research on the major components of the temperate mid-mountain water cycle [8, 9, 10, 11]. The Ringelbach site is located on the eastern side of the Vosges Massif (NE France) (Figure 1) and consists of Hercynian porphyritic granite capped in its upper part by a residual cover of Triassic sandstones. The main granite is the medium-grained and porphyritic "granite des Crêtes" which consists of quartz, plagioclase, K-feldspar, biotite, and amphibole with minor titanite [12]. Two types of two-micas granitic intrusives crosscut this massif. The Triassic sandstone cover, which gently dips towards the north, is heteroge-

3

neous, formed by thick, hard medium-grained sandstone interstratified with a series of thin quartz-silty clay layers.

Two boreholes (F-HUR, F-HEI) were drilled within the area for hydrogeological purpose (Figure 1) ; the F-HEI borehole was doubled in its upper part (F-HEI, F-HEI2). Their detailed lithological and petrological descriptions are given in [12] and summarized in Figure 2. Neither of the two 150-m deep boreholes (F-HUR, F-HEI) reach the fresh granite. These two boreholes indicate that sandstone in the top of the Ringelbach site covers a 20- to 35-m-thick upper layer of loose clayey saprolite, developed on granite and characterized by entire alteration of ferroan-magnesian minerals liberating iron and of plagioclase to form clays and iron-hydroxides. The induration and foliation of this truncated arena layer increase toward its bottom. Underneath is a very thick layer of fissured, relatively weathered granite. This succession of subhorizontal layers is interpreted as a truncated pre-Triassic stratified weathering profile of the Hercynian granite [12], as also proposed for other European Hercynian regions [13]. Several faults divide the basin into three main blocks (Bunker, Hurlin, and Heidenkopf), which are progressively downthrown from southeast to northwest (Figure 1). Within each block, periglacial and postglacial weathering and erosion processes generated a more recent regolith on the slope surfaces, which is typically only a few meters thick.

3. Fracturation and water/rock alterations

Granites and their Triassic cover do not well outcrop. Triassic sandstones that outcrop at the top of the hill near the F-HUR borehole (Hurlin block), occur as reddish medium- to fine-grained sandstones containing some pebbles and crosscut by mm- to cm-thick fractures partially filled by euhedral quartz and minor barite. Under the microscope, sandstones are essentially formed of monocrystalline quartz with minor K-feldspar, polycrystallic quartz, lithic elements, largely cemented by at least two generations of authigenic quartz : a first generation of aureole quartz, and a second one sealing most of the residual

4

porosity. It is noteworthy that quartz filling fractures is luminescent, what is not the case of the two generations of quartz cements in the sandstone matrix. The *granite des Crêtes* rather well outcrops on the middle slope of the Bunker block, and has a quite fresh aspect (photo).FRACT? (Chrystel). Weathering is marked by alteration of amphibole and of plagioclase cores. In the two boreholes, granite in the fissured layer is highly affected by sub-vertical fractures. The general paragenetic sequence of fracture fillings and wallrock alteration provide evidence of an early cataclasis stage associated with micro-quartz cementation followed by different generations of carbonates including calcite, dolomite and (Fe, Mn) - bearing dolomite, and barite. Microthermometry of fluid inclusions in carbonates (F-HUR 138 m) allows measuring homogeneisation temperatures of 120-160°C; these temperatures are very similar to those obtained at Soultz (EPS1 borehole) or in granite of the Waldhambach quarry [14]. These temperatures suggest hydrothermal conditions at maximum burial cover/basement interface reached just before the graben opening.

4. Electrical properties

4.1. Core-scale measurements

Electrical formation factor and surface conductivity measurements have been performed on Ringelbach's granitic core samples taken from the F-HUR and F-HEI wells [15]. It shows that the higher porosity, the higher surface and pore fluid conductivity are (Figure 3). Since the amount of alteration clays controls the rock surface conductivity [16], we can conclude that the higher the degree of alteration of the granite is, the higher the conductivity is. In addition, the higher the porosity is, the higher the permeability of the samples is (Figure 4). Porous and permeable altered granitic formations found within the transition zone are therefore likely to exhibit elevated electrical conductivity compared to unaltered and tight granite.

4.2. Borehole logging

Figure 2 displays the logged resistivity data in the F-HUR well. Resistivity logs show overall high values ($>$ 250 Ohm.m) over the crystalline basement but also a high degree of variability (250 – 6000 Ohm.m) caused by variations in the degree of alteration/fracturing of the granite, as evidenced by the strong correlation between resistivity readings and the rock competency. The close relationship between elevated porosity/permeability and high electrical conductivity observed at the core scale can therefore be scaled up in the transition zone to the size of the logging spatial sampling (metric to decametric scale).

4.3. Field scale CSEM measurements

To characterize the large-scale electrical resistivity distribution of the transition zone, we acquired a 3D Controlled Source Electro-Magnetic (CSEM) survey over a 1000m x 1000m area cutting through the transition zone (from the Triassic sedimentary cover deep down into the crystalline basement). 50 Metronix ADU recording stations where deployed every 100m on a regular grid to record both components of the horizontal electric field. Due to the very high shallow resistivities, galvanic transmitters were not efficient so an $100000m^2$ horizontal transmitting loop located 1.5km from the receiver array was used instead (Figure 5). Square signals with fundamental frequencies ranging from 0.25Hz to 8192Hz where injected in the loop using a 22kW TXM22 transmitter, rising a current of 40A at 560V. Current in the loop and electric fields at the stations are recorded simultaneously with GPS synchronisation. Accurate position and orientations of each station electrodes as well as the transmitting loop position are recorded using differential GPS in order to be considered accurately in the 3D modeling process. After editing the data, a proper signal deconvolution is achieved by computing the transfer functions between electric fields and injected currents at each discrete frequency used. Transfer functions are calculated using Razorback robust processing software [17, 18] in order to remove uncoherent noise. Analysis of the spectrum of the electric field transfer function conducted to select for inversion 5 frequencies in the range 32Hz to 8192Hz for which

6

the electric field varies significantly, highlighting sensitivity to the underground resistivity variations. Due to the orientation of the transmitter, east-west electric field component is largely dominant so north-south is weak enough to be neglected. The selected data are inverted in 3D with POLYEM3D software [19, 20, 21]. This code is a 3D massively parallel electromagnetic modeling and imaging software dedicated to the inversion of CSEM and MT data in the frequency domain. A 3D mesh of 700,000 cells is build with a dense core domain with 30m horizontal spacing and 20m maximum vertical spacing up to 900m. Each inversion run with this mesh lasts typically a few hours on the CINES Bull supercomputer Occigen on 256 MPI processes for a few tenths iterations depending on the regularisation and optimisation technique used.

We start inversion with a very rough initial guess using an homogeneous half space at 2000 $\Omega.m$. Data fit is good, reducing the RMS residuals from 518% in the starting model to 38%. Real and imaginary parts of electric field for observed data and computed in the homogeneous half space and the final inverted model are presented for a few representative stations Figure 8. The very weak variation at low frequency suggests a low sensitivity of the lowest frequencies to large depth structure. However more significant variations at high frequencies show very good fit with both real and imaginary parts. Vertical slices at several depth as well as S-N and W-E profiles extracted from the final 3D resistivity cube are shown Figures 6 and 7. Slices are compared figure 6 with the current geological map of the area with the known fault. The surface resistivity extracted from interpolated ERT profiles of [22] is also presented. The 3D model is probably slightly distorted and preferentially streched N-S due to the asymmetrical illumination obtained with the use of the single transmiter located North. The model shows high overall resistivities but also very high contrasts, ranging between 300 $\Omega.m$ to more than 3000$\Omega.m$ deeper than 500m and above an unaltered granite block at the southern part of the survey. This resistive granite block is well delineated and corresponds well to the very resistive anomaly imaged by ERT profiles in [22]. The shallow high resistivity area also

7

matches the shape of the granite visible in the geological map, except for the

₁₇₀ Eastern part that is known to be more altered and appear to be less resistive. The resistive anomaly associated to the fresh granite block disappears at depths greater than 100m. Beside the resistive block and everywhere bellow 100m, the model shows a conductive layer associated with altered and fractured zones that extends well over more than 200m depth into the basement and is laterally

₁₇₅ extensive. Those variations suggest that the thickness of this conductive zone to the base of the sedimentary cover varies laterally (from zero to 200m depth), most likely due to a different alteration history and intensity of the granite. Those results show that the resistivity variations due to alteration observed at core and borehole scale are also visible at the field scale where it still exhibits

₁₈₀ contrasts of at least one order of magnitude between fresh and altered granite.

5. Seismic properties

5.1. Core-scale measurements

P-wave velocities measurements (Figure 3) have been performed on Ringelbach's core samples taken from the F-HUR and F-HEI wells [15]. It shows that

₁₈₅ the higher porosity, the lower the P-wave velocity is. As for the electrical conductivity, we can therefore expect that porous and permeable altered granitic formations found within the transition zone exhibit lower P-wave velocity compared to unaltered and tight granite.

5.2. Borehole logging

₁₉₀ Figure 2 displays the logged sonic velocities in the F-HUR well. Sonic logs show overall high values (> 4500 m/s) over the crystalline basement but also a high degree of variability (3000 – 5500 m/s) caused by variations in the degree of alteration/fracturing of the granite, as evidenced by the strong correlation between sonic readings and the rock competency. The close relationship between

₁₉₅ elevated porosity/permeability and low P-wave velocity observed at the core scale can therefore in the transition zone at least to the size of the logging spatial sampling (metric to decametric scale).

8

5.3. Field scale seismic measurements

To characterize the large-scale P-wave velocity distribution of the transition

₂₀₀ zone, we acquired a 1100m long seismic refraction/reflection profile over the Triassic sedimentary cover cutting through three fault zones identified in the area (figure 5). We used a 240 geophones array with 5m spacing and a shot every 10m operated with a 3000 Joules AP200 accelerated impact energy source. A 2D first arrival traveltime tomography inversion was performed. On the other

₂₀₅ hand, the same dataset was used to produced a high resolution reflexion profile with constant velocity migration. Tomography and migrated reflexion profile are represented Figure 9. Very high P-wave velocities are imaged, rising 4000-5000 m/s at larger depths and close to 2000 m/s in the first tenths meters. A clear velocity drop from 4000-5000 m/s down to 3500-4000 m/s is observed at the top

₂₁₀ of the crystalline basement (within the first 100m) when crossing these faults (Figure 9). Interestingly, numerous and continuous reflectors are clearly visible on the reflexion profile at about 200m depth. Those reflectors obviously present within the basement are possibly caused by some layering in the alteration, as evidenced by the layering observed on the sonic logs in the exploratory boreholes,

₂₁₅ or by a sharp transition between the end of the transition zone and the top of the fresh granite. On the other hand, those reflectors fade away when crossing the fault zones identified both by surface geology and velocity drop in the P-wave tomography, possibly indicating the presence of more strongly altered and fractured granite above the fault zones. Here again, those variations suggest that

₂₂₀ the thickness of the transition zone varies laterally (from 100 to 200m depth), most likely due to a different fracturation and alteration history in the granite. Those results show that the seismic variations due to alteration observed at core and borehole scale are also clearly visible at the field scale with possible contrasts of 30% between fresh and altered granite.

9

6. Discussion

6.1. Surface versus pore electrical conductivity

Waxman and Smits' (1968) equation [23] can be used to describe the relationship between surface, pore and total electrical conductivity of a clay-rich porous media as follows:

$$\sigma_0 = \frac{\sigma_w}{F} + \sigma_s \tag{1}$$

with σ_0 the rock conductivity, σ_s the surface conductivity, σ_w the fluid conductivity and F the rock formation factor.

We computed the total rock conductivity at 10 and 200℃ as function of the fluid salinity for altered and unaltered Ringelbach granite (Figure 11) using Sen and Goode (1992) relationship [24] for the brine conductivity and the following constants derived from the core sample analysis:

	Porosity	Formation Factor	Surface Conduction	Permeability
Fresh granite	1.8%	1900	2.3 mS/m	10^{-18} m^2
Altered granite	5.3%	480	20 mS/m	10^{-16} m^2

The less saline/colder the fluid, the more important the surface conduction is. For the Ringelbach case, groundwater in the surface boreholes is fresh (salinity ~100 mg/L) and as a consequence, the total conductivity of the granite is mainly due to surface conduction and hence a proxy of mineral alteration but not indicative of rock porosity. Conversely, the more saline/hotter the fluid, the more important pore fluid conduction is. For deep and hot geothermal brines like found in Soultz-sous-Forêts in the Rhine graben (salinity of 100 g/L and temperature of 200℃), pore fluid conductivity is dominating and the total rock conductivity is indicative of the rock porosity and hence potentially a proxy of the rock permeability.

6.2. Electrical and seismic properties of deep geothermal reservoirs

To validate the aforementioned electrical conductivity model for deep geothermal reservoirs, we present here electricial resistivity measurements made in the

10

Soulz-sous-Forêts granitic basement (Figure 11). As predicted, altered zones are electrically more conductive than unaltered granite, with a factor ranging from ten to thousand times. Similarly, in the Rittershoffen geothermal project, altered zones at the top of the granitic basement proved to be electrically conductive but notatibly, the main permeable fault zones coincide with the most electrically conductive zones [25]. The electrical conductivity of the granitic basement is therefore a parameter of choice to explore for deep porous and potentially permeable fault zones. The challenge remains to deploy electromagnetic techniques capable of remotely detecting and imaging such anomalies, deeply buried underneath a thick sedimentary cover.

On seismic measurements, the most altered zones within the basement in Soultz-sous-Forêts show significant decrease in P-wave and S-wave velocities (up to 30%). However, the less altered zones do not exhibit any significant anomalies, most likely due to the limited sensitivity of elastic properties to alteration. To compensate for that, a joint analysis of electrical and elastic properties is necessary. Indeed, when crossploting logged P-wave velocity as a function of resistivity (Figure 12), we can observe that the less altered granite have similar P-wave velocities but that their resistivity varies greatly (by a factor 100) allowing to discriminate between the different alteration facies. Here also, the challenge remains to deploy seismic techniques capable of remotely detecting and imaging such anomalies.

7. Conclusions

Our study of an exhumed transition zone in the Vosges Mountain shows that altered porous and potentially permeable granite targeted in deep geothermal exploration has a clear signature on both electrical conductivity and seismic measurements that can be measured at core scale, borehole scale, and are still visible with surface geophysical methods such as refraction and reflection seismic and Controlled Source Electromagnetism at a few hundred meter depth. It also showed that the best discrimination comes from the joint interpretation of these

11

datasets. The challenge remains to develop and deploy electromagnetic and
seismic imaging techniques having sufficient investigation depth and sufficient
resolution to detect and image the targets of interest, usually deeply buried
underneath a thick sedimentary cover. An relevant strategy would be to combine
both methods during exploration, in order to get benefit of the high sensitivity
of resistivity to permeability with CSEM while conserving the high resolution
of 3D seismic reflection.

References

[1] C. Schmelzbach, S. Greenhalgh, F. Reiser, J.-F. Girard, F. Bretaudeau,
L. Capar, A. Bitri, Advanced seismic processing/imaging techniques and
their potential for geothermal exploration, Interpretation 4 (4) (2016) SR1–
SR18.

[2] C. M. Krawczyk, M. Stiller, K. Bauer, B. Norden, J. Henninges, A. Ivanova,
E. Huenges, 3-d seismic exploration across the deep geothermal research
platform groß schönebeck north of berlin/germany, Geothermal Energy
7 (1) (2019) 1–18.

[3] G. A. Newman, E. Gasperikova, G. M. Hoversten, P. E. Wannamaker,
Three-dimensional magnetotelluric characterization of the coso geothermal
field, Geothermics 37 (4) (2008) 369–399.

[4] C. Arango, A. Marcuello, J. Ledo, P. Queralt, 3d magnetotelluric characterization of the geothermal anomaly in the llucmajor aquifer system (majorca, spain), Journal of Applied Geophysics 68 (4) (2009) 479–488.

[5] F. Bretaudeau, S. Penz, N. Coppo, P. Wawrzyniak, M. Darnet, 3d land csem inversion in noisy environment with a single transmiter: inversion approach and application for geothermal water prospection, in: International Symposium in Three-Dimensional Electromagnetics (3DEM), 2017.

[6] M. Darnet, P. Wawrzyniak, N. Coppo, S. Nielsson, E. Schill, G. Fridleifsson, Monitoring geothermal reservoir developments with the controlled-source electro-magnetic method—a calibration study on the reykjanes geothermal field, Journal of Volcanology and Geothermal Research 391 (2020) 106437.

[7] M. Darnet, N. Coppo, F. Bretaudeau, P. Wawrzyniak, S. Penz, B. Bourgeois, J.-C. Gourry, B. Sanjuan, Characterizing geothermal resources with passive and active electromagnetic methods in challenging em environments, in: 23rd Electromagnetic Induction Workshop: EMIW2016, 2016.

[8] J. Mercier, Structure et fonctionnement du milieu naturel en moyenne montagne–bassins de la petite fecht et du ringelbach (vosges, france), Recherches Géographiques à Strasbourg 19 (1982) 20–21.

[9] B. Ambroise, J. Perrin, D. Reutenauer, Multicriterion validation of a semidistributed conceptual model of the water cycle in the fecht catchment (vosges massif, france), Water Resources Research 31 (6) (1995) 1467–1481.

[10] J.-M. Baltassat, A. Legchenko, B. Ambroise, F. Mathieu, P. Lachassagne, R. Wyns, J. Mercier, J.-J. Schott, Magnetic resonance sounding (mrs) and resistivity characterisation of a mountain hard rock aquifer: the ringelbach catchment, vosges massif, france, Near Surface Geophysics 3 (4) (2005) 267–274.

[11] T. Schaffhauser, F. Chabaux, B. Ambroise, Y. Lucas, P. Stille, T. Reuschlé, T. Perrone, B. Fritz, Geochemical and isotopic (u, sr) tracing of water

pathways in the granitic ringelbach catchment (vosges mountains, france), Chemical Geology 374 (2014) 117–127.

[12] R. Wyns, M. Tegyey, étude géologique du cadre structural et des forages du bassin versant de recherche du ringlebach (soultzeren, haut-rhin), Tech. Rep. BRGM/RP-56540-FR, BRGM (French Geological Survey) (2012).

[13] R. Wyns, J.-M. Baltassat, P. Lachassagne, A. Legchenko, J. Vairon, F. Mathieu, Application of proton magnetic resonance soundings to groundwater reserve mapping in weathered basement rocks (brittany, france), Bulletin de la Société géologique de France 175 (1) (2004) 21–34.

[14] C. Dezayes, C. Lerouge, Reconstructing paleofluid circulation at the hercynian basement/mesozoic sedimentary cover interface in the upper rhine graben, Geofluids 2019.

[15] A. Belghoul, Caractérisation pétrophysique et hydrodynamique du socle cristallin, Ph.D. thesis, University of Montpellier II (2007).

[16] A. Revil, L. Cathles III, S. Losh, J. Nunn, Electrical conductivity in shaly sands with geophysical applications, Journal of Geophysical Research: Solid Earth 103 (B10) (1998) 23925–23936.

[17] R. Streich, M. Becken, O. Ritter, Robust processing of noisy land-based controlled-source electromagnetic data, Geophysics 78 (5) (2013) E237–E247.

[18] P. WAWRZYNIAK, F. Smaï, Razorback, an open source python library for robust processing of magnetotelluric data, Frontiers in Earth Science 8 (2020) 296.

[19] F. Bretaudeau, S. Penz, N. Coppo, P. Wawrzyniak, M. Darnet, Practical inversion of electric resistivity in 3d from frequency-domain land csem data, in: 23rd European Meeting of Environmental and Engineering Geophysics, Vol. 2017, European Association of Geoscientists & Engineers, 2017, pp. 1–5.

[20] F. Bretaudeau, J. Porté, P. Wawrzyniak, S. Penz, B. Bourgeois, POLYEM3D: A massively parallel versatile code for 3d modeling and inversion of land csem and mt data, in: Electromagnetic Induction Workshop, EMIW, 2018.

[21] F. Bretaudeau, F. Dubois, S.-G. Bissavetsy Kassa, N. Coppo, P. Wawrzyniak, D. M., Time-lapse resistivity imaging : Csem-data 3d double-difference inversion and application to the reykjanes geothermal field, Geophysical Journal International In Press.

[22] J.-M. Baltassat, B. Ambroise, F. Mathieu, Boucher, M., R. Wyns, Réinterprétation des investigations géophysiques du bassin versant du ringelbach à l'aide des données de forage et des mesures sur échantillon en laboratoire, Tech. Rep. BRGM/RP-66694-FR, BRGM (French Geological Survey) (2018).

[23] M. H. Waxman, L. Smits, et al., Electrical conductivities in oil-bearing shaly sands, Society of Petroleum Engineers Journal 8 (02) (1968) 107–122.

[24] P. N. Sen, P. A. Goode, Influence of temperature on electrical conductivity on shaly sands, Geophysics 57 (1) (1992) 89–96.

[25] C. Glaas, A. Genter, J. Girard, P. Patrier, J. Vidal, How do the geological and geophysical signatures of permeable fractures in granitic basement evolve after long periods of natural circulation? insights from the rittershoffen geothermal wells (france), Geothermal Energy 6 (1) (2018) 14.

15
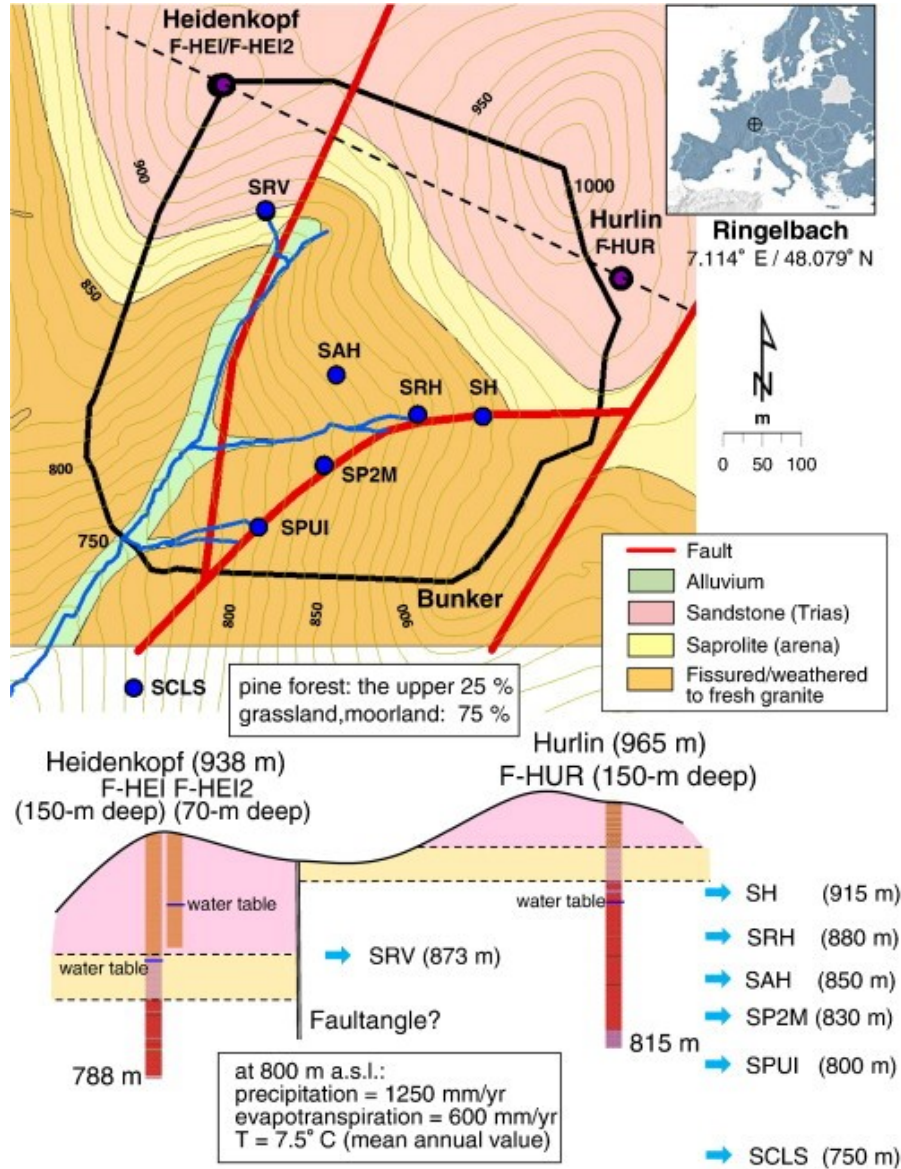
Figure 1: Topographic and geologic map of the Ringelbach catchment with the locations of the sandstone spring (pink circle), granitic springs (red circles) and boreholes (black circles). The dotted line indicates the position of the geological section presented below. F-HUR borehole: 150 m deep, through sandstone (0–28 m), granitic arena (28–48 m) and fissured granite; cored full length, casing down to 51 m; water table depth: 61.5 m ± 1.5 m. F-HEI borehole: 150 m deep, through sandstone (0–74 m), granitic arena (74–101 m) and fissured granite; cored below 101 m only, casing down to 101 m; water table depth: 77 m ± 1 m

16
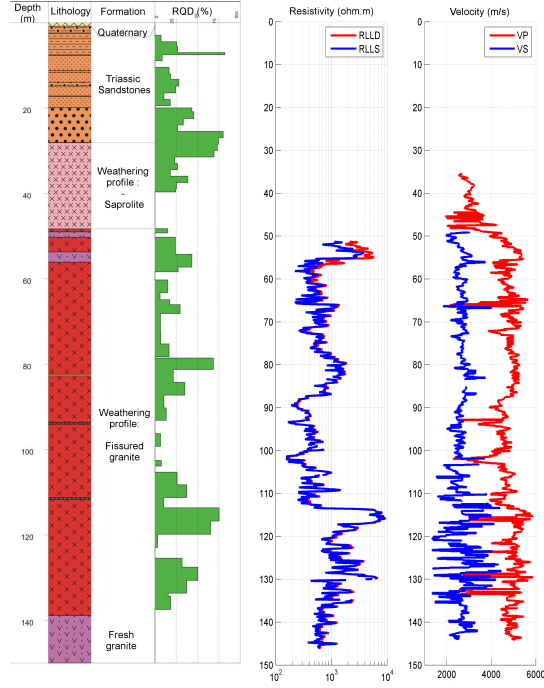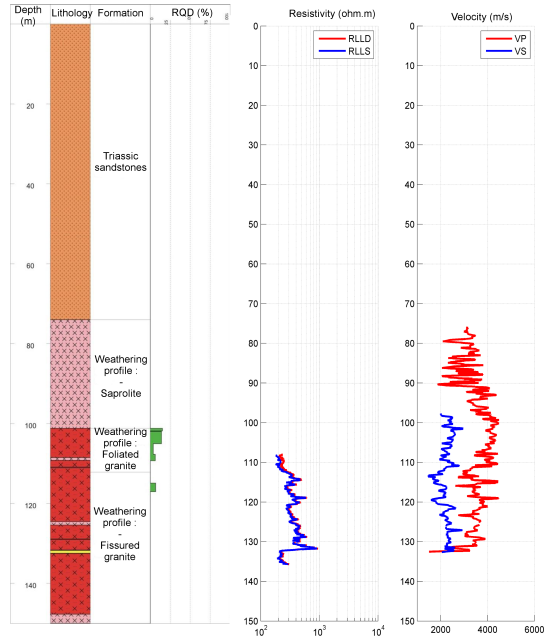
(a) F-HUR borehole

(b) F-HEI borehole

17

Figure 2: Lithological, RQD, logged resistivity and sonic velocity profiles of F-HEI (a) and F-HUR (b). RQD log is a proxy for the competency of the rock.
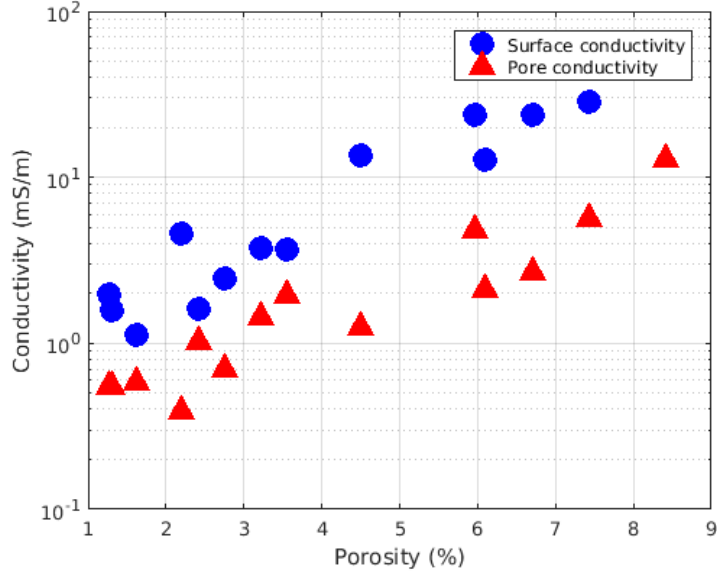
(a) Surface and pore conductivity versus porosity
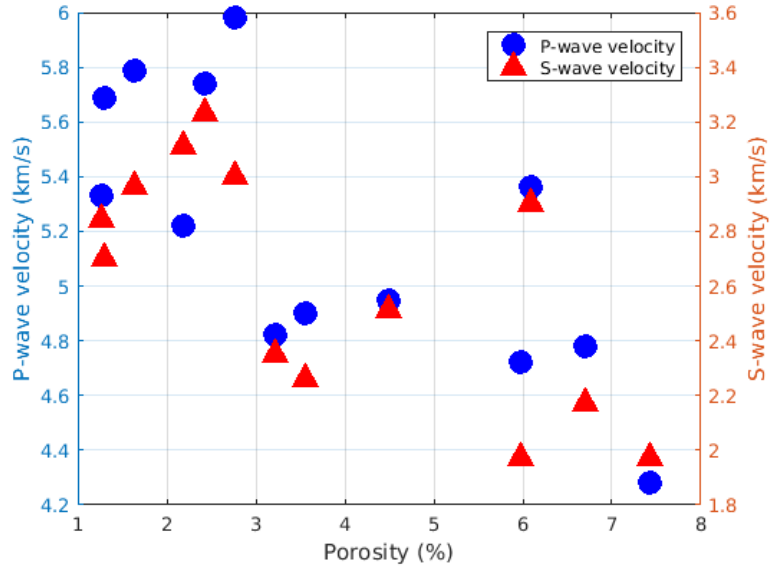
(b) P-wave velocity versus porosity

Figure 3: Variation with porosity of surface and pore conductivity (a) and P-wave velocity (b) of altered granite core samples extracted from the Ringlebach transition zone [15].
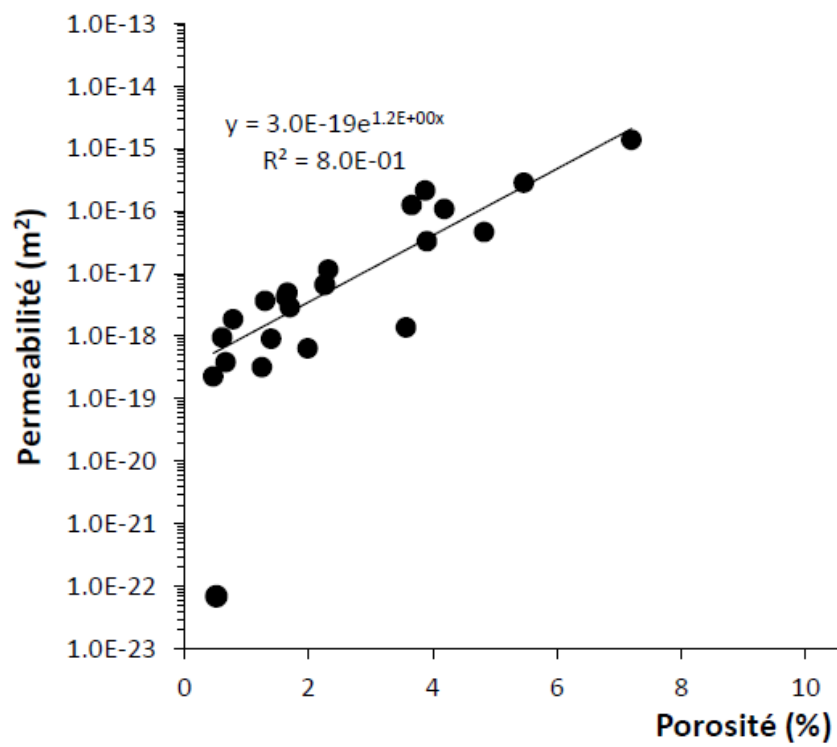
Figure 4: Permeability as a function of the porosity from Ringlebach's core samples [15].
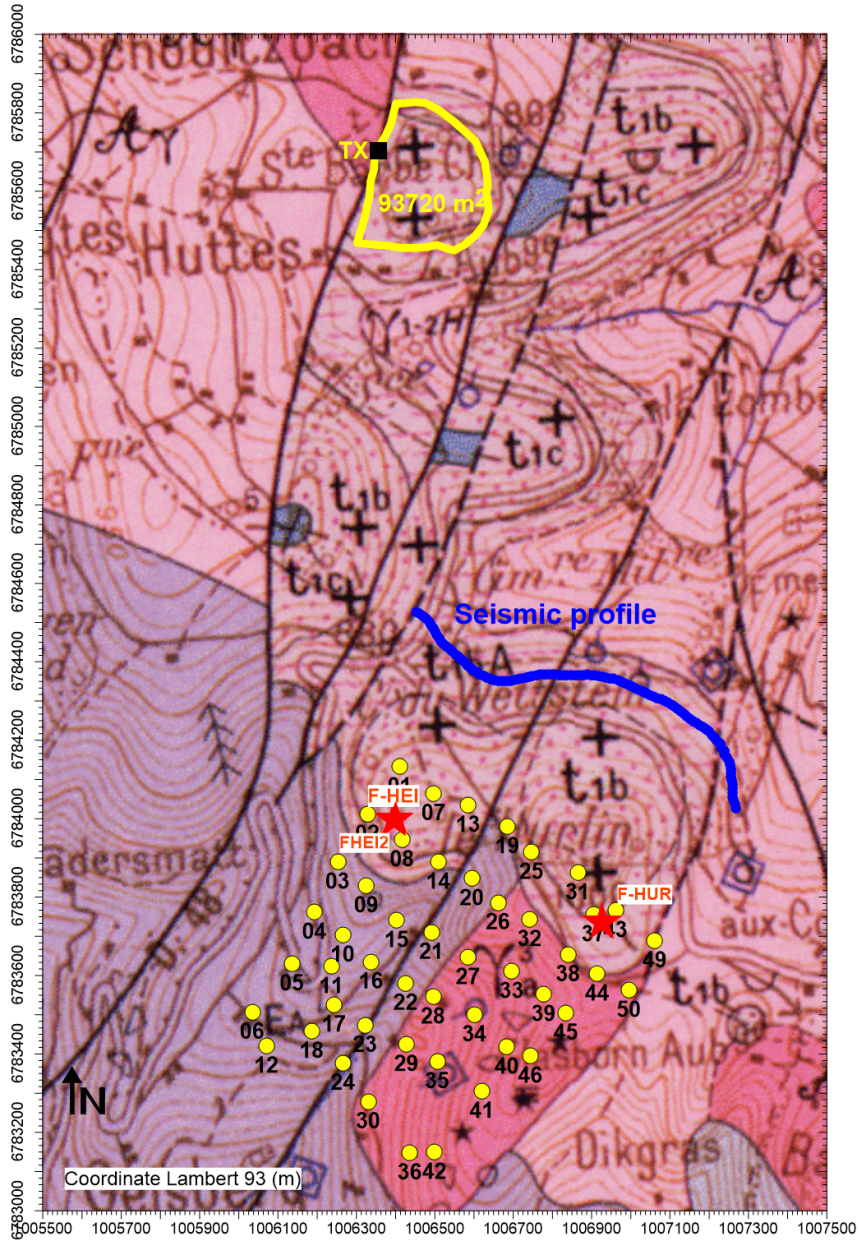
Figure 5: Location of the 3D CSEM grid (measurement station and transmitter loop in yellow), the reflexion/refraction seismic profile (in blue) and the boreholes (F-HEI, F-HUR). Background is the geological map of the area (t_{1b} in pink is Permian sandstone, purple and red γ are granite.
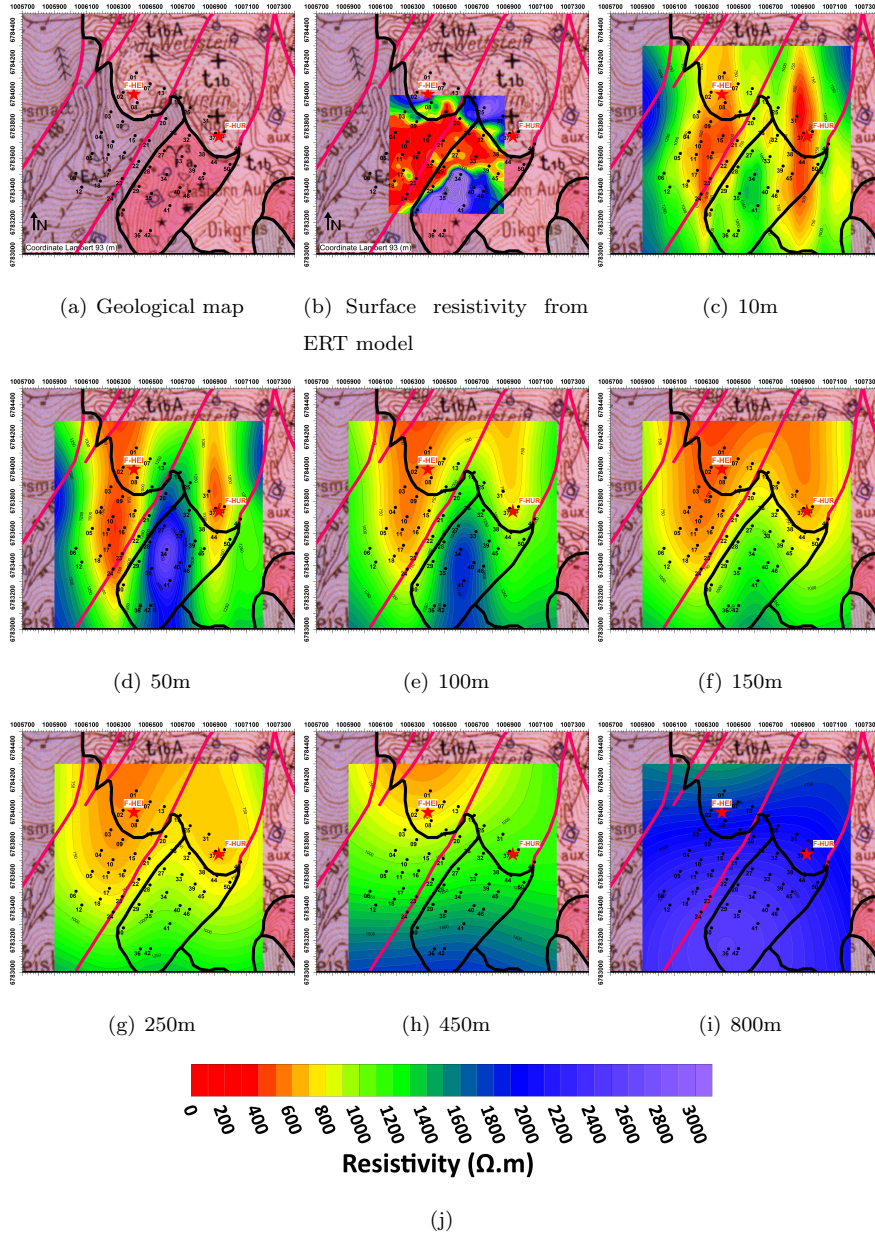
20

(a) Geological map

(b) Surface resistivity from ERT model

(c) 10m

(d) 50m

(e) 100m

(f) 150m

(g) 250m

(h) 450m

(i) 800m

(j)

Figure 6: Resistivity slices at different depth from the cube obtained from the inversion of 3D Controlled-Source Electro-Magnetic data over the Geological map.
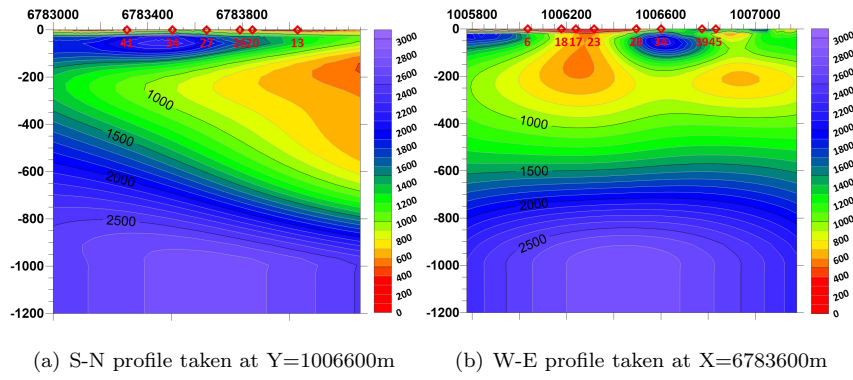
21

(a) S-N profile taken at Y=1006600m   (b) W-E profile taken at X=6783600m

Figure 7: S-N (a) and W-E (b) resistivity profiles from the cube obtained from the inversion of 3D Controlled-Source Electro-Magnetic data
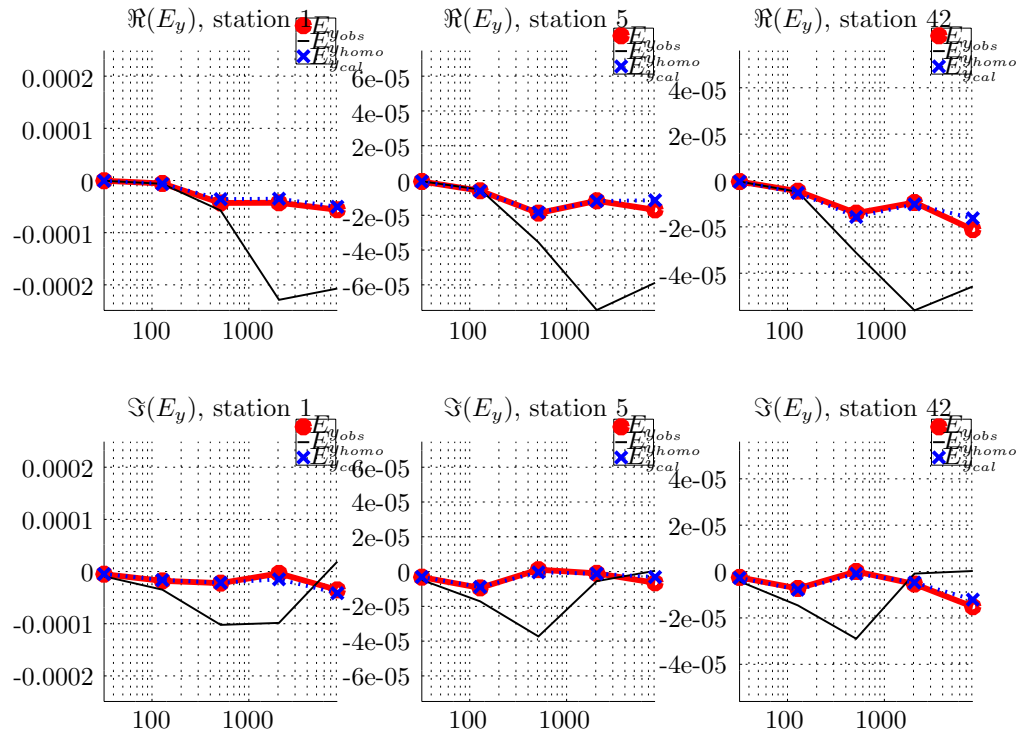
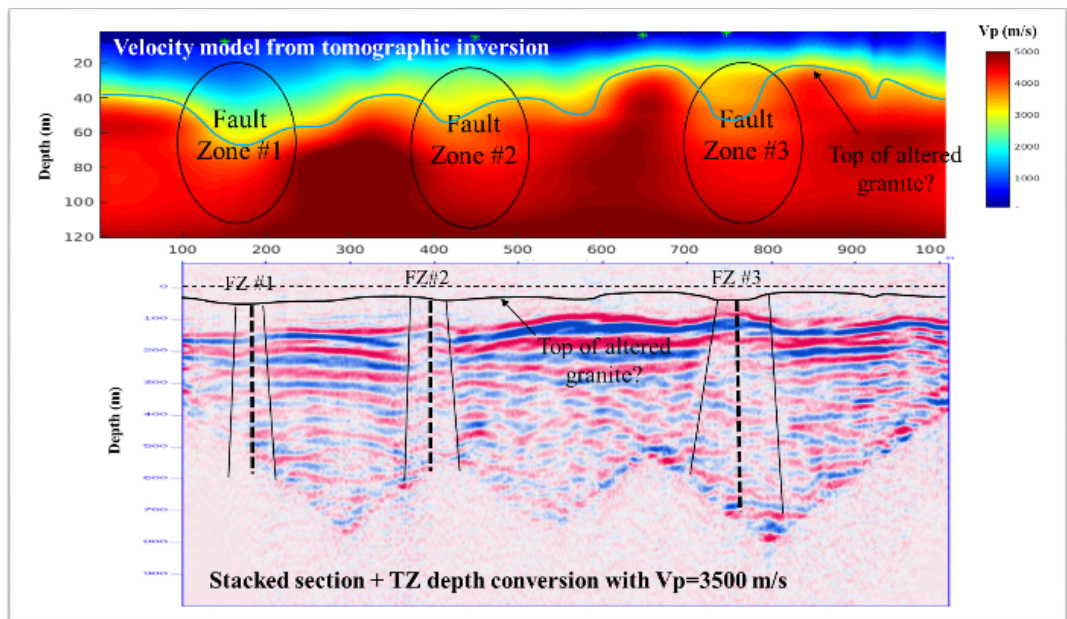Figure 8: Example of spectrums of electric field data (real and imaginary parts)

Figure 9: Top: Velocity model derived from the first arrival traveltime tomography. Bottom: constant velocity stacked migrated section in depth. The footprint of the faults is visible in the tomography section with a velocity drop and in the reflexion profile with a loss of coherency in the reflector.
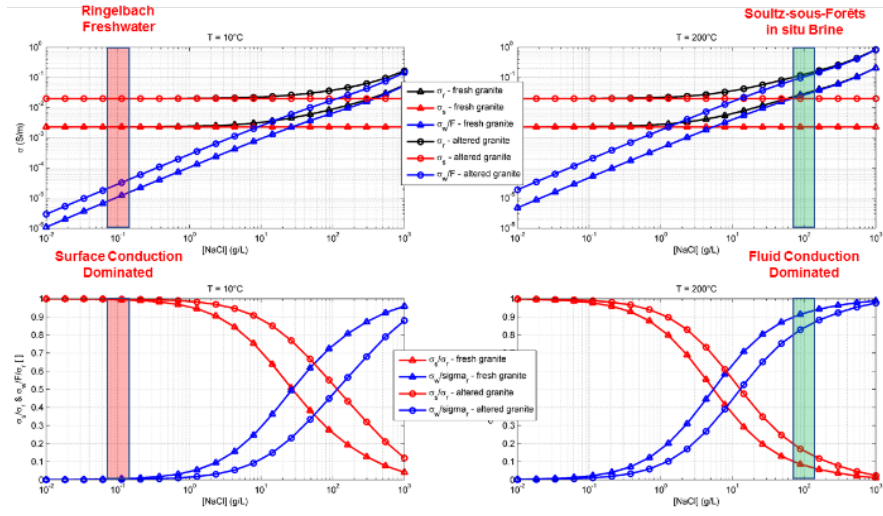
Figure 10: Top left: surface (red), pore fluid (blue) and total (black) conductivity of unaltered (triangle) and altered (circle) granite at 10 degC as a function of the brine salinity. Bottom left: ratio between the surface (red) and pore fluid (blue) versus the total rock conductivity for fresh (triangle) and altered (circle) granite at 10 degC as a function of the brine salinity. Top right: surface (red), pore fluid (blue) and total (black) conductivity of unaltered (triangle) and altered (circle) granite at 200 degC as a function of the brine salinity. Bottom right: ratio between the surface (red) and pore fluid (blue) versus the total rock conductivity for fresh (triangle) and altered (circle) granite at 200 degC as a function of the brine salinity.
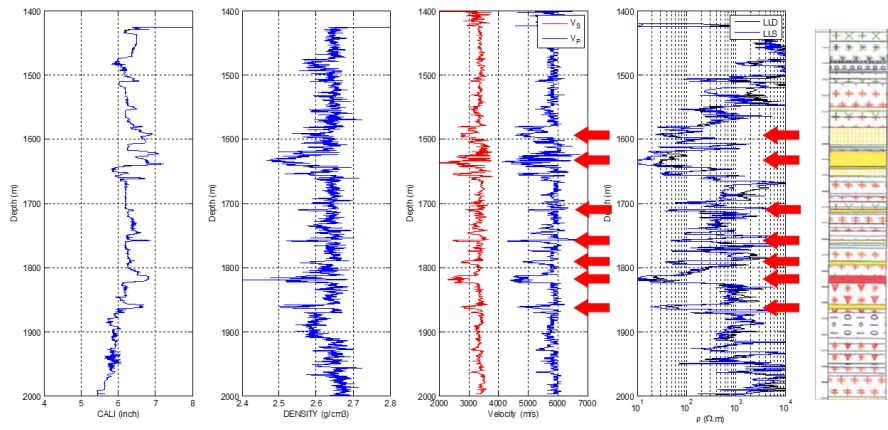
Figure 11: P-wave (blue) and S-wave (red) logs (left), shallow (blue) and deep (black) laterolog (middle) and lithological log (right) in the Soultz-sous-Forêts GPK1 well. Most altered granitic facies are marked with red arrows.
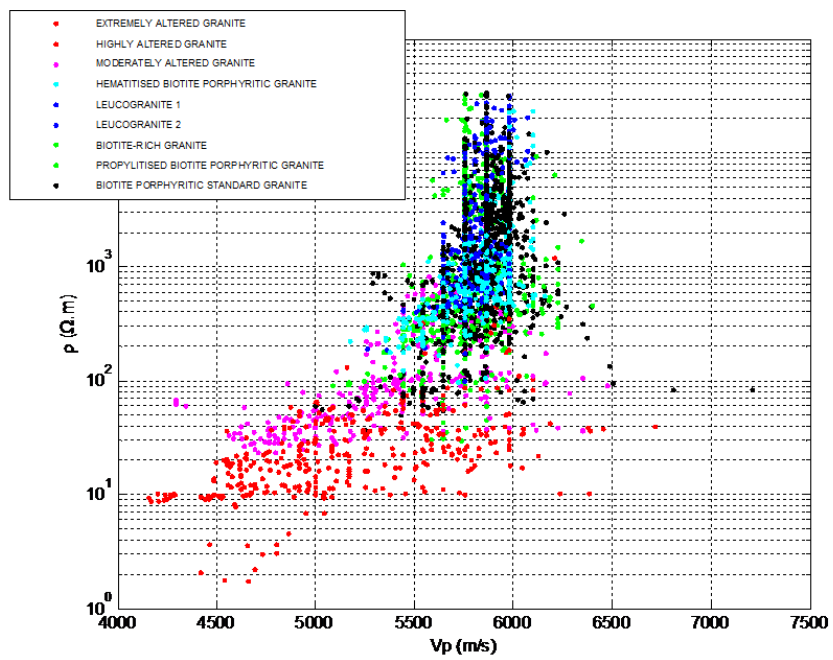
Figure 12: Logged resistivity as a function of the P-wave velocity of the granitic basement found in the Soultz-sous-Forêts GPK1 well. Colors indicate the different alteration facies.

Julien PORTE

Imagerie 3-D de la résistivité complexe à partir de données électromagnétiques à source contrôlée

Résumé

Les phénomènes de polarisation provoquée (PP) permettent l'accès à de nombreuses propriétés du sous-sol et se traduisent par une résistivité complexe (RC) variant avec la fréquence. Ces travaux portent sur l'implémentation d'une RC variant avec la fréquence à un code tridimensionnel (3D) de modélisation et d'inversion de données électromagnétiques à source contrôlée (CSEM). Le but est de permettre la prise en compte simultanée des effets PP et d'induction EM dans le processus d'imagerie du sous-sol, là où les méthodes PP négligent généralement les effets électromagnétiques (EM). Il est question ici d'établir en premier lieu la sensibilité des méthodes CSEM aux effets PP dans le domaine fréquentiel intervenant à l'échelle du terrain. Une stratégie d'inversion multi-étape basée sur la sensibilité aux effets PP est mise en avant afin de contraindre l'inversion efficacement. L'utilisation de polynômes de second ordre est proposée pour paramétriser la résistivité complexe et ses variations fréquentielles dans le problème inverse, ce qui permet de conserver ainsi une description générale et versatile du problème. La stratégie d'inversion suggérée a été développée à partir de travaux à une dimension (1D), puis testée sur divers exemples synthétiques. La transposition au problème 3D est ensuite réalisée, ainsi que son application sur données synthétiques. Il est montré qu'à partir de la stratégie d'inversion développée sur synthétique 1D ainsi que d'une paramétrisation polynomiale, un modèle de résistivité complexe imageant plusieurs cibles polarisables 3D en profondeurs a pu être extrait. La localisation ainsi que les informations PP ont pu être obtenues, permettant la discrimination des cibles chargeables de l'encaissant non chargeable, ainsi que de différencier leur signature spectrale. Dans une dernière partie, la méthodologie développée est appliquée sur données réelles. Ce travail participe à étendre le domaine d'application des méthodes PP par la prise en compte des informations EM dans l'imagerie.

Polarisation provoquée, Méthodes électromagnétiques, Méthodes inverses, Inversion multi-paramètre

Résumé en anglais

In some Earth materials, induced polarization (IP) phenomena are occurring when an electric perturbation is applied. They are described by a medium with a frequency dependent complex resistivity (CR). In this work, a frequency dependent CR is implemented in a tridimensional (3D) finite-difference modelling and inversion code for controlled-source electromagnetic data (CSEM). The purpose of this work is to recover simultaneously IP and EM information, as IP methods do not take into account EM induction. In order to constrain efficiently the multi-parameter problem, the inversion is tackled through a multi-stage procedure, based on the electrical field sensitivity to CR, which is evaluated in a first part of this work. A versatile parametrization of the frequency dependent CR is proposed by using second order polynomials. This strategy was developed and tested on 1D synthetic examples. The method was then transposed to the 3D case and applied to synthetic examples. Using the multi-stage workflow and the polynomial parameterization, it was demonstrated that the CR could be correctly retrieved for deep 3D targets as well as a part of their spectral behavior. The extracted IP information allowed discriminating the targets from the background and to separate their spectral behavior. In a last part, the developments of the thesis are applied to real CSEM datasets. This work helps extending the application domain of IP methods by taking EM information into account for the imaging.

Induced polarization, Electromagnetics methods, Inverse problem, Multi-parameter inversion